ABSTRACT

Title of dissertation: ON THEORETICAL ANALYSES OF QUANTUM SYSTEMS: PHYSICS AND MACHINE LEARNING

Shangjie Guo, Doctor of Philosophy, 2022

Dissertation directed by: Professor Ian B. Spielman
Professor Jacob M. Taylor
Professor Justyna P. Zwolak
National Institute of Standard and Technology

Engineered quantum systems can help us learn more about fundamental physics topics and quantum technologies with real-world applications. However, building them could involve several challenging tasks, such as designing more noise-resistant quantum components in confined space, manipulating continuously-measured quantum systems without destroying coherence, and extracting information about quantum phenomena using machine learning (ML) tools. In this dissertation, we present three examples from the three aspects of studying the dynamics and characteristics of various quantum systems. First, we examine a circuit quantum acoustodynamic system consisting of a superconducting qubit, an acoustical waveguide, and a transducer that nonlocally couples both. As the sound signals travel 10^5 times slower than the light and the coupler dimension extends beyond a few phonon emission wavelengths, we can model the system as a non-Markovian giant atom. With an explicit result, we show that a giant atom can exhibit suppressed relaxation within a free space and an effective vacuum coupling emerges between the qubit excitation and a confined acoustical wave packet. Second, we study closed-loop controls for open quan-

tum systems using weakly-monitored Bose-Einstein condensates (BECs) as a platform. We formulate an analytical model to describe the dynamics of backaction-limited weak measurements and temporal-spatially resolved feedback imprinting. Furthermore, we design a backaction-heating-prevention feedback protocol that stabilizes the system in quasi-equilibrium. With these results, we introduce closed-loop control as a powerful instrument for engineering open quantum systems. At last, we establish an automated framework consisting of ML and physics-informed models for solitonic feature identification from experimental BEC image data. We develop classification and object detection algorithms based on convolutional neural networks. Our framework eliminates human inspections and enables studying soliton dynamics from numerous images. Moreover, we publish a labeled dataset of soliton images and an open-source Python package for implementing our framework.

ON THEORETICAL ANALYSES OF QUANTUM SYSTEMS: PHYSICS AND MACHINE LEARNING

by

Shangjie Guo

Dissertation submitted to the Faculty of the Graduate School of the
University of Maryland, College Park in partial fulfillment
of the requirements for the degree of
Doctor of Philosophy
2022

Advisory Committee:
Professor Zohreh Davoudi, Chair
Professor Ian B. Spielman, Co-Advisor
Professor Jacob M. Taylor, Co-Advisor
Professor Justyna P. Zwolak, Co-Advisor
Professor Norbert Linke
Professor Xiaodi Wu, Dean's Representative

Dedication

To my family—my wife, mother, and father.

Acknowledgments

The list of people I want to thank for helping me finish my Ph.D. and this dissertation would be endless. Some persons listed here may not recall their importance in my advancement, but their effect was significant, and I will forget.

On more personal notes, I want to thank my research supervisors: Jacob M. Taylor, Ian B. Spielman, and Justyna P. Zwolak. It has been a substantial fortune for me to have three esteemed scholars in their own distinguished expertise, from theoretical and experimental physics to computer and data science. They have been incredible mentors who guided me through many challenges, sophisticated teachers who taught me science, philosophies, and much more, and sincere friends who helped me with their most excellent patience and compassion. Aside from their help in completing this dissertation, I am highly honored for all our work together.

I want to thank the Joint Quantum Institute, Department of Physics of the University of Maryland, and National Institute of Science and Technology for providing state-of-the-art learning and research environments for quantum students and scientists. I want to thank all the most remarkable people I have met here for their collaborations and insightful discussions with them: Tom, Yidan, Hilary, Amilson, Craig, Sophie, Fangli, Chris, Chiao, Daiwei, Steph, Steve, Emine, Qiyu, Jon, Minh, Brittany, Sohitri, Mingshu, Junheng, Yuruo, Jialin, Ming, and Xiao. I greatly appreciate them for being both professional scientists and patient friends.

I want to thank FinQ Tech Inc. for providing a professional quantum technology community for knowing great people and learning much more beyond my research scope.

I want to thank Quantum Center of Excellence of BP p.l.c. for offering a great opportunity to help adopt a variety of quantum technologies into real-world problems.

I would like to thank all my climbing and snowboarding friends and our cats, Uzi and

Apricot, for those good times we spent together, which brought me through tough times and helped me balance my life.

Last but most invaluable, I want to thank my family—my wife, mother, father, and grandma. Their supports are not only the foundation but also the most important motivation for me chasing fearlessly after my dreams. Because of that, I proudly dedicated this dissertation to them.

Table of Contents

Chapter 1: Introduction

Advancing quantum information science and engineering quantum technologies have both scientific and practical motivations [1–3]. Quantum devices not only help expand our knowledge horizon by studying quantum many-body phenomena [4–7], astronomical signals [8, 9], and even biology [10], but they may also provide values for solving classically challenging combinatorial optimization problems [11], simulating chemical reactions involving large molecules and materials [12], securing communication for confidential data [13], and sensing microscopic signals with high accuracy [14].

With these motivations, the primary purpose of this dissertation is to broaden our understanding of varieties of quantum systems dynamics in multiple aspects and accordingly help in converting science into advancing quantum technology. The scope of this dissertation includes: designing more noise-robust and compact quantum device components [15], engineering and preparing an innovative, continuously-observed quantum state [16], and identifying and extracting information about quantum phenomena with machine learning (ML) approaches [17].

The following chapters in this dissertation cover the topics above in more detail. In Chapter 2, we study an artificial superconducting atom coupled with a surface acoustical waveguide via a nonlocal piezoelectric component, such that the coupling region covers a many-emission-wavelength-long area [18]. We applied analytical tools and a Lorentzian toy model to simplify the system and compared our results with spectroscopy from numerical simulations. We observe that this non-Markovian giant atom exhibits suppressed relax-

ation and an effective vacuum coupling exists between a qubit excitation and a localized wave packet of sound, even in the absence of spatial emission constraints—thus realizing a quantum bound-in-continuum system.

Chapter 3 investigates a weakly monitored quasi one-dimensional (1D) Bose-Einstein condensate (BEC) and designs feedback protocols for cooling the atom cloud to quasi-equilibrium [19]. Using backaction-limited weak measurements and temporal-spatially resolved feedback imprinting, we create a theoretical tool for quantum feedback control of quantum systems, including BECs. We describe the intuitions and protocols of our feedback cooling that prevents excess heating caused by measurement backaction. Our findings demonstrate that closed-loop quantum control of BECs can offer a potent new tool for quantum engineering in cold-atom systems.

In Chapters 4 and 5, we start by noticing two difficulties in studying cold atom data from explicit images: first, we usually rely on human inspections for identifying features that bottleneck our research scale, and second, our preconceived notions about the existing patterns may constrain our capacity to analyze them. Therefore, we consider two different ML architectures for analyzing experimental cold atom data to automatically detect dark solitons appearing as local density depletions in BECs [20, 21]. Thus we eliminate human analysis requirements. Furthermore, we integrate ML models with physics-informed heuristics to distinguish solitonic excitations. Combining these models enables us to find the solitonic excitations, extract physical parameters, and categorize each solitonic excitation. For future ML research, we provide our labeled dataset of dark solitons in a public data repository [22, 23], and an open-source Python package for detecting solitonic excitation [24], which is pre-trained from our data and adaptable for any user-defined cold atom absorption image dataset.

Even though we developed these new techniques within the scope of specified types of quantum systems, they can be further generally implemented on other types of quantum

systems. The giant atom and its suppressed spontaneous emission can be re-engineered with any quantum non-Markovian system, such as optomechanical systems [25], cold atom systems [26], and the ones that have collective emissions via multiple coupling points [27]. The feedback cooling strategy may be implemented on any quantum device that allows partial measurements and rapid fine-resolution controls by altering its potential or interaction terms of Hamiltonian within the coherent time [28]. Finally, the classical ML can go beyond the scope of dark solitons and help us extract information from a quantum system from classical readout raw data either from direct images, a spectroscopy, or a series of pulse sequences [29–32].

In the remainder of this chapter, first we introduce the background and motivations from both physics and ML perspectives in the next two subsections, then we compare the benefits and limitations of them in the last subsection.

1.1 Physics backgrounds

The works presented in this dissertation contribute to various field topics of physics and quantum information science, including quantum non-Markovian systems [33], bound-state in the continuum [34], giant atoms [35], superconducting circuits [36], circuit quantum acousto-dynamics (QAD) [37], ultracold atoms and BECs [38], weak quantum measurement [39], real-time quantum feedback [40], nonlinear quantum dynamics [41], and solitons [42, 43].

The topic in the first half of this dissertation focuses on non-Markovian circuit QAD systems [37, 44, 45]. Within a quantum non-Markovian system, coherence travels via multiple mechanisms with different speeds and interferes nonlocally through space, and therefore these systems often show unconventional dynamical properties.

There are at least two exciting physics topics related to quantum non-Markovian sys-

tems: the bound-state in the continuum (BIC) and the giant atom. A BIC is a discretized eigenstate of a continuous system, which lives in an infinitely large Hilbert space [34, 46]. Those states are attractive to quantum scientists as they are fully decoupled from the environment in principle, even with no spatial confinements. A giant atom is another example of a quantum non-Markovian system [35]. It can be an artificial emitter with a spatial size comparable to or greater than its emission wavelength, an emitter with multiple coupling points separated for at least a few wavelengths, or a collection of emitters communicating via other channels than its emitting media. Unlike a typical point-like atom, those fabricated giant atoms show strong frequency-dependent couplings to the emission modes. Giant atoms are investigated for related physics concepts, including ultrastrong coupling and superradiance, and may serve as quantum device components due to their intrinsic robustness to noise and decoherence.

A common choice of mechanism combination to experimentally build a quantum non-Markovian system is phonons and photons. For example, an optomechanical system can be modeled in the non-Markovian regime as it couples laser modes with the vibrational modes of a crystal via radiation pressure [47]. This dissertation focuses on a circuit QAD system, which consists of a superconducting qubit, a surface acoustic wave waveguide, and an interdigital transducer (IDT) mounted on a piezoelectric substrate. Superconducting qubits are one of the most popular types of artificial atoms. They are often constructed by Josephson junction in experiments. Leveraging their nonlinear energy gaps, they make effective two-level systems. An IDT interlocks two comb-shaped arrays of electrodes printed on a piezoelectric substrate that can transduce electric signals to surface acoustic waves into the waveguide, where the spacing of the 'combs' provides spatial selectivity.

We find the non-Markovian circuit QAD systems intriguing and promising for a few reasons. First, since the wavelengths of sounds 10^5 times shorter than lights, these systems may deliver much more compact transmon-like qubits and on-chip quantum time-delay

relays and phononic transmission lines [48]. Second, their non-Markovianity enables creative engineering for dissipations and interactions beyond the limitations of typical superconducting systems or even natural atoms [49]. Third, circuit QAD converts signals between two forms, opening opportunities for quantum signal filtering and transducing. Lastly, these systems make a great platform to study giant atoms and make long-coherence quantum memories leveraging their reduced emission rate.

Ultracold atoms and BECs set the foundation for topics discussed in the second half of this dissertation [38]. An ultracold atom cloud is a group of atoms trapped with lasers and magnetic fields and cooled down until its quantum property merges. BEC is a phase of matter commonly realized with bosonic ultracold atom gas. BECs have become one of the most well-studied and mature macroscopical quantum systems. The states and dynamics of BECs could be expressed as wavefunctions evolving under Gross-Pitaevskii equations (GPE) [41].

BECs establish an ideal platform for our research in quantum physics from at least two aspects. First, many high-precision observing and controlling methods are achieved for BECs [50], allowing so-called analog quantum simulation and explorations of condensed matter physics and open quantum systems [51]. BEC also promises two prerequisites for studying quantum closed-loop feedback control: stroboscopic weak measurements with phase-contrast imaging and rapid real-time feedback by imprinting engineered external fields. Second, following the interactions among composing atoms shown as the nonlinear term in GPE, BECs make a great medium to study many-body interacting quantum systems, including topics like phase transitions [52], non-equilibrium [4], and thermalization [53]. This dissertation is particularly interested in dark solitons [54], the self-fortifying, localized wave packets as solutions of nonlinear dispersive systems.

Weak measurements refer to a generalized version of quantum measurements that do not entirely collapse the state and collect less information by associating engineered noises

to the measured results [55]. In order to conduct a weak measurement, we may couple the primary system with an ancilla, which gains incomplete information about the system. By tuning the coupling parameters, we could choose what type of information is needed. Then we may perform quantum measurement on the ancilla, estimate the information of the original system and complete a weak measurement. With the acquired measured result, the post-weakly-measured quantum states update according to descriptions of Kraus operators.

Rapid real-time feedback control for a quantum system is often achieved either by applying an external field or by changing the couplings between its component sub-system and therefore changing the potential or the interaction terms of its Hamiltonian [56]. For effectiveness, those feedbacks must be fast enough to beat the coherent time of the system. Furthermore, these feedbacks could learn from previous measurement results to determine the form of the external fields of coupling strengths. Such quantum feedback may help us extend the coherent time or apply innovative operations and channels.

Measurement and control comprise the two channels for a human agent to exchange information with a system. We may create quantum closed-loop feedback control by combining weak measurements and real-time feedback, creating a powerful tool to manipulate open quantum systems [50, 57, 58]. Closed-loop feedback control could allow new opportunities, including adaptive measurement and tomography [59], artificial interactions and dissipations [19], or open system quantum simulation [60].

A soliton is a singular, localized, and robust excitation emerging from the interactions among media components. It exists in nature, such as localized waves in a canal. It can also live as a quantum excitation in BEC [42, 43, 61], where we can benefit from sophisticated controls and little environmental noise to understand these many-body phenomena. Solitons are not only robust to local disruptions as topologically protected excitations, but they are resilient to each other as well. Two solitons both remain their waveforms unchanged after a collision. Therefore, solitons may serve as media for quantum communication and

long-living quantum memory.

Beyond the scientific values they deliver to many-body physics, solitons are essential to us for another interdisciplinary reason. Leveraging our well-established experimental apparatus, collecting the raw absorption imaging data of dark solitons in BECs is not a demanding job. These numerous physical data are significantly helpful for studying the intersection between ML-based data analysis techniques and quantum mechanical phenomena.

1.2 Machine learning backgrounds

As the field of ML algorithms has developed to a more mature stage in recent years, more applications are being found in scientific research, including quantum physics [17]. In the last few chapters of this dissertation, we used ML-based models as our primary approach to detect dark solitons. ML is an ideology that lets algorithms regulate themselves at a certain level through experience without precisely defined instructions. This idea resonates with many historical discoveries in physical science that originated from experimental observations, from Kepler's laws of planetary motion to the Michelson-Morley experiment and black-body radiation. As new physics becomes more delicate and requires more data to refine, we might eventually encounter a barrier that humans cannot comprehend these concepts. However, research today using ML for science might ultimately help overcome such barriers in the future.

Recent ML prosperity is partially fueled by the success of artificial neural networks (ANNs) [62]. The scheme of ANN is inspired by biological neural systems, which link the input and output with multiple layers of neurons, each described as a nonlinear activation function. Those layers are often referred to as dense layers. By updating the weights and biases of the linear functions that connect the inter-layer neurons with ground truth data, ANNs can predict unforeseen data with high accuracy in many use cases, such as in

computer vision.

Computer vision (CV) is a subfield for image processing in ML and computer science [63]. The goal of CV is to find mappings between image data and descriptions of these images. Some specific tasks of CV include classification, finding the catalog corresponding to the image; localization, finding the location of an object within an image; and object detection, finding multiple locations and catalogs of all target objects in the image.

Convolutional neural networks (CNNs) are among the most commonly used ML architectures for CV problems [64]. A CNN consists of particularly regularized ANN layers called convolutional layers, which apply filters to take the weighted average of a local range of pixels from the previous layer. Leveraging the fact that pixels in an image correlate more likely with its neighboring pixels than those on the other side of the image, convolution layers reduce many neuron connections from complete dense layers. Convolution layers often combine with pooling layers in a CNN. The pooling layers can reduce the size of an image by merging neighboring pixels into a single pixel. Pooling layers may lose some detailed information but can allow the following layers to learn about more extensive features in the original image.

We exploit CNN as our primary approach to analyze soliton data for two main reasons. First, CNN shows excellent performance for classification and object detection on the image data, to which our soliton data belong. Second, our target features are local and have specific shapes, where the convolution layers are designed for in principle. We trained CNN classifiers to classify images into three catalogs. We improved from that result and customized the objective detector model based on our data and tasks.

Achieving satisfactory ML performance often requires model customization based on the characteristics of features and problems. For example, we take five considerations into designing the object detection model: (1) As our soliton features mostly have a width greater than four pixels, we use cells with that width to divide the images into regions for

locating features. (2) As our target features are vertical, we design our output as arrays that map to vertical cells across the image. One Array for a binary decision of if a soliton exists within a cell or not. The other for the relative position of a soliton within the cell is detected. (3) For some convolutional layers, we used filters and kernels that have longer horizontal widths than vertical heights to allow characterizing horizontal profiles of the features; (4) We only used convolutional layers and pooling layers but no dense layers for the object detector because both input image and output array have special meanings associated. (5) We added a post-process that merges two soliton detections of nearest neighbor cells to prevent the edge case where a soliton exists at the boundary between two cells.

1.3 Comparing physics and machine learning

In this dissertation, we used analytical and numerical physics tools and data-driven ML models in the context of quantum mechanical physics. Since we might be standing at a historical transition point from human-intuition-based towards algorithmic scientific discoveries, it could be helpful to compare the benefits, limits, and common usages among analytical models, numerical simulations, and ML algorithms.

Analytical physics methods help simplify the expression of complex systems and reach an explicit closed-form solution for the interesting physical quantities. Those methods include but are not limited to applying well-known approximations, developing toy models, or designing phenomenological models.

However, these methods inevitably constrain the system within the regime where our simplified version behaves similar to the original one. Therefore, the achieved simple results often need additional validations to be generalized to regimes beyond the original designated ones. In addition, we often have limited choices for regimes and approximations for an existing experiment. One of the most used cases for the analytical methods is

in thought experiments. Once meaningful analytical solutions achieved from imagined scenarios may help us to seek feasible ways to implement them numerically or experimentally and produce new physics.

With given system configuration and initial and boundary conditions, simulating the time evolution of systems helps us learn numerical results of states, which is especially valuable when approximate methods are limited by the systems' complexities or the problems' generalities. Utilizing numerical simulation, we can prove if a specific experimental design would yield the desired outcomes, and we may study phase transitions by scanning through parameter spaces.

However, since numerical results do not have explicit form, we often need to run simulations extensively to scan through a specific set of configurations or get results at a long-time limit. In addition, the capability of simulation is restricted by the capacity of our digital computers. As most simulations require operations on matrices, we often find our dimension of simulated Hilbert space is limited at about 10^3 for a laptop. Simulating a quantum system with greater degrees of freedom could be challenging. Nevertheless, that might change in the next few decades if we could leverage quantum computers to simulate them.

ML helps derive the underlying pattern from a dataset or an oracle. Based on its philosophy of self-learning, ML models often neither have many assumptions about the system nor physics laws. They often have more trainable parameters than needed to describe and predict features or phenomena. The performance of ML models may heavily rely on their training dataset attributes such as the quantity of data, quality of labels, and noise from observations. The current ML techniques could be practically useful when the research goals focus on predicting the outcomes or enhancing the performance, and the chosen system is overly complicated such that adequate analytical models are few, yet collecting observations is relatively easy.

Meanwhile, there are a few concerns about using current ML techniques in scientific research. First, as its capability relies on the data, the dataset's quality needs to be examined thoroughly, or it may jeopardize the models' functionality and reliability. Second, it is hard to guarantee that a trained ML model can process data that may be beyond its training set distribution without any validations. The reliability of out-distribution data needs to be tested before use. Last but not least, these models usually work as black boxes with few physical interpretations, and it is hard to understand how they operate from human perspectives. However, all these concerns might be resolved with more profound research. For example, integrating physics-informed steps into ML models may enhance their reliability and interpretability, and implementing physics simulations may help validate dataset quality.

Chapter 2: Beyond spontaneous emission: Giant atom bounded in continuum

The quantum coupling of superconducting qubits to microwave photons opens the door to many exciting experimental possibilities. In this chapter, we consider the phononic situation, in which the qubit is piezoelectrically coupled to a surface acoustic wave antenna, allowing the qubit oscillations to propagate supersonically through space. This device can be treated as a giant atom with several phonon wavelengths long. We investigate an explicitly solvable toy model that captures these effects. This non-Markovian giant atom exhibits suppressed relaxation as long as an effective vacuum coupling exists between a qubit excitation and a localized wave packet of sound, even in the lack of a cavity for the sound waves, as demonstrated by the results our experiments. We used spectroscopy of numerical simulation in the discretized frequency domain to confirm our findings. Finally, we examine these ideas implemented in a realistic setting with existing surface acoustic wave devices.

2.1 Introduction

The coupling of resonant, compact systems to continuous media has a rich history, underlying phenomena ranging from musical instruments to complex machinery to the spontaneous emission of light from an atom [65, 66]. The strong coupling regime of such systems has also led to a plethora of applications in cavity quantum electrodynamics (QED)

[67], circuit QED [68, 69], and waveguide QED [69–72], all of which work in the regime where light propagation is fast relative to appropriate coupling time scales such as the coherence time. However, collective effects, such as Dicke superradiance, have shown that pre-existing coherence across multiple wavelengths of the medium excitations can dramatically alter the simple dynamics of such open quantum systems [73, 74].

In this chapter, we examine an example of such long-range coherence in the form of a superconducting qubit nonlocally coupled to a long, quasi-1D phononic waveguide. This system can be realized in, for example, surface acoustic wave (SAW) devices [75]. Working in the lumped element limit, the electrical antennae that couple to the mechanical waveguide have practically simultaneous coupling to distant regions of the system, while the motional degrees of freedom are constrained to propagate at the speed of sound. This leads to a variety of supersonic phenomena in the quantum acousto-dynamics (QAD) regime which has been heretofore largely unexplored.

Pioneering work in this domain have labeled this the "giant atom" regime of SAW devices [44, 48, 49, 76]. This model breaks locality in the lumped element limit and inevitably becomes non-Markovian, requiring a more detailed theoretical treatment [27, 33, 46, 77–82]. Furthermore, recent experiments show the robustness of systems that couple mechanical with electromagnetic parts in the quantum regime and open the opportunity to realize giant atoms in experiments [37, 49, 83–89].

We show that these devices have remarkable properties, particularly that of strong coupling without the presence of a cavity, in which a long-lived atomic excitation dynamic emerges due to the coupling to the electrical circuit directly, and the formation of long-lived states of sound in the unbounded continuum. We describe this as the bounded giant atom phenomenon.

While our simple theoretical model predicts this phenomenon directly, a more complicated numerical approach shows that specific additional phase matching condition must be

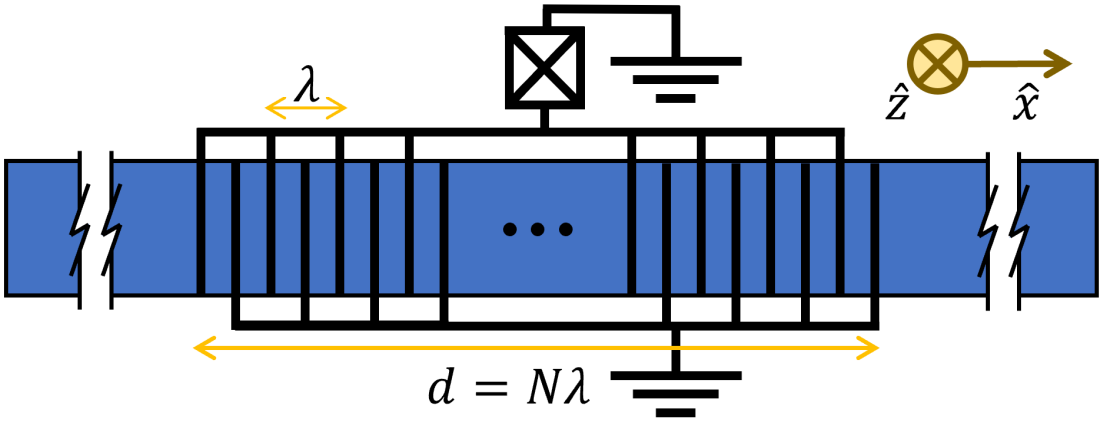

Figure 2.1: A sketch of a circuit QAD device viewed from the top. Black lines show electrodes and the blue area shows the surface of piezoelectric material substrate. The substrate extends deeply in $+z$ direction.

satisfied for experimental observation of the strong coupling of this emergent of bounded effect to the quantum bit. Furthermore, in this regime, boundary-based damping of the sound exponentially decreases with the atom size, leading to substantial improvements in coherence times. Our study suggests a pathway to more compact superconducting qubit designs that can leverage sound, rather than microwave photons. Key aspects of circuit QED-based architectures, such as using a photon in a resonator as an intermediary between two transmon qubits, and using dispersive coupling of a transmon to a waveguide have natural analogues using coupling to phonons instead. However, transducer efficiencies and parametric amplification, two key elements of circuit QED systems, are not at an appropriate level yet for replacement by sound. This suggests substantial research may be necessary before a sound-based architecture could be realized.

The rest of this chapter is organized as follows: In section II, we review the Weisskopf-Wigner theory for spontaneous emission [65], which provides the structure for our model later; throughout the chapter we refer to the superconducting qubit with antennae as a giant atom. We calculate the coupling between the artificial atom and phonons of the circuit QAD device, and we simplify it to a Lorentzian toy model in section III. In section IV, we derive our main results from the toy model and compare our results with the numerical

simulation. We conclude in section V and show future applications of the general method presented in this chapter.

2.2 Background

2.2.1 The General Theory

We consider a two-level giant atom with ground state $\rangle g|$ and excited state $\rangle e|$ with a frequency difference ν that non-locally couples to an infinitely-long 1-D bosonic field, governed by the following Hamiltonian in the rotating wave approximation:

$$\hat{H} = \frac{\nu}{2}\sigma_z + \int dK \left[\omega(K)\hat{a}_K^\dagger \hat{a}_K + g(K;N)\left(\hat{\sigma}_+ \hat{a}_K + \text{h.c.}\right)\right], \tag{2.1}$$

where $\hat{\sigma}_+(\hat{\sigma}_-)$, and $\hat{a}_K^\dagger(\hat{a}_K)$ are creation (annihilation) operators for atomic excitation and field, respectively. They satisfy $(\hat{\sigma}_-)^\dagger = \hat{\sigma}_+ = |e\rangle\langle g|$, $\sigma_z = |e\rangle\langle e| - |g\rangle\langle g|$, and $[\hat{a}_K, \hat{a}_{K'}^\dagger] = \delta(K-K')$. ν is the atomic transition frequency. We assume that the field has a linear dispersion $\omega(K) = c_s|K|$ with the speed of sound c_s, for momentum K. We set $\hbar = 1$ for simplicity.

We consider the coupling $g(K;N)$ to depend on the momentum K. As the Fourier transform of the position-dependent coupling, it is also parameterized by the spatial length of the atom N. One can expect that the parameter N will change the atom relaxation dynamics via tuning the shape of $g(K;N)$. We shall discuss two different models for $g(K;N)$ in section III.

We denote the vacuum state by $|g,0\rangle$, and limit our system to a single excitation Hilbert subspace with basis states $|e,0\rangle = \hat{\sigma}_+|g,0\rangle$ and $|g,K\rangle = \hat{a}_K^\dagger|g,0\rangle$, such that any time-dependent state can be described as $|\psi(t)\rangle = \alpha(t)|e,0\rangle + \int_{-\infty}^{+\infty} dK\beta_K(t)|g,K\rangle$, where $\alpha(t)$, and $\beta_K(t)$ are time-dependent amplitudes. In a frame rotating with frequency ν, we derive the equa-

tions of motion

$$\dot{\alpha}(t) = -2i \int_{-\infty}^{+\infty} dk g(k;N) \beta_k(t), \tag{2.2}$$

$$\dot{\beta}_k(t) = -i\delta(k)\beta_k(t) - ig(k;N)\alpha(t). \tag{2.3}$$

Note that as the coupling is real in position space in our case, such that $g(K;N) = g(-K;N)$, so the two branches for $K > 0$ and $K < 0$ contribute symmetrically and can be merged in equation 2.2. The momentum in the rotating frame is redefined as $k = |K| - \nu/c_s$, such that the field frequency becomes $\delta(k) = \omega(K) - \nu = c_s k$ for the near-resonance regime. Then, by taking the Laplace transform from the time domain into the complex frequency domain by $\tilde{\alpha}(s) = \mathscr{L}[\alpha(t)]$, and $\tilde{\beta}_k(s) = \mathscr{L}[\beta_k(t)]$, we get:

$$s\tilde{\alpha}(s) - \alpha(0) = -2i \int_{-\infty}^{+\infty} dk g(k;N) \tilde{\beta}_k(s) \ , \tag{2.4}$$

$$s\tilde{\beta}_k(s) - \beta_k(0) = -i\delta(k)\tilde{\beta}_k(s) - ig(k;N)\tilde{\alpha}(s) \ . \tag{2.5}$$

We set $\alpha(0) = 1$ and $\beta_k(0) = 0$ to investigate the relaxation of an atomic excitation. Then we have $\tilde{\beta}_k(s) = -ig(k;N)\tilde{\alpha}(s)/(s + i\delta(k))$ and the response function $\chi(s) \equiv \tilde{\alpha}(s)/\alpha(0)$ becomes

$$\chi(s) = \left(s + 2 \int_{-\infty}^{+\infty} dk \frac{|g(k;N)|^2}{s + i\delta(k)} \right)^{-1} . \tag{2.6}$$

From the residue theorem and initial conditions, we can derive that $\alpha(t) = \mathscr{L}^{-1}[\chi(s)]\alpha(0)$ $= \sum_n \mathrm{Res}[\chi(s), s_n] e^{s_n t}$ given that $g(k;N)$ is an analytic function, where s_n is the nth pole of $\chi(s)$ that satisfy the equation: $[\chi(s_n)]^{-1} = 0$ for $n \in \{1, 2, ..., n_{\max}\}$. $n_{\max}$ is the number of the poles of $\chi(s)$. Causality confines s_n to be in the left half complex plane or on the imaginary axis, i.e., $\mathrm{Re}(s_n) \leq 0$ [90]. Note that the inverse Laplace transform requires that

the contour path of integration is in the region of convergence of $\chi(s)$. This can be satisfied by integrating equation 2.6 with the condition $\mathrm{Re}(s) > 0$.

Armed with the solution for the poles s_n, we describe the atomic relaxation process as a composition of damped oscillation modes with effective vacuum Rabi oscillation frequencies $\mathrm{Im}(s_n)$ and decay rates $-2\mathrm{Re}(s_n)$. In the long-time limit, only the slowest damped modes can survive, and we thus define the long-time relaxation rate as $\gamma \equiv \mathrm{Min}_n[-2\mathrm{Re}(s_n)]$.

To understand the giant atom relaxation, we study how the poles of response function s_n change according to the atom size N. In the next section, we consider a realistic circuit QAD model and a simpler Lorentzian toy model to characterize $g(k;N)$ with N being a changing parameter, and study the response function $\chi(s)$ and its poles.

2.2.2 The Weisskopf-Wigner limit

Before moving into the giant atom case, we first review the Weisskopf and Wigner approach to the point-like atom case[65]. A point-like atom couples to all wavelengths emission equally, i.e., $g(k;N) = g_0$, independent of k. In this situation, one can calculate the real part of the equation $[\chi(s)]^{-1} = 0$, which results in

$$\gamma_1 \equiv -2\mathrm{Re}(s_1) = 4\pi|g_0|^2/c_s. \tag{2.7}$$

This textbook result shows when a point-like atom couples to an 1-D field, the atom decays with its spontaneous emission rate γ_1. In the giant atom case, we also define γ_1 as the weak-coupling relaxation rate for a unit cell (e.g., $N = 1$) for later discussion. Now we can proceed and study $g(k;N)$ for the circuit QAD and the toy models that simplify it.

2.3 The circuit QAD and toy models

2.3.1 The circuit QAD model

We examine a simplified 1-D model for the circuit QAD device shown in figure 2.1. A circuit QAD device comprises a superconducting artificial atom (as a Josephson junction parallelized with IDT as a capacitor) and a surface acoustic wave (SAW) cavity. The qubit couples to the cavity via an inter-digital transducer (IDT), where two interlocking comb-shaped arrays of electrodes are fabricated on the surface of a piezoelectric substrate. Such systems have been used to achieve strong coupling, where the vacuum Rabi coupling exceeds dephasing and damping [37, 84–86]. We can map the spatial atom size to the length of the IDT d, and the resonance emission wavelength to the IDT characteristic wavelength λ (the finger spacing of the IDT). We use the number of fingers of the IDT $N = d/\lambda$ as the atom size parameter for this circuit QAD model.

Since the electromagnetic wave travels about 10^5 faster than sound through the IDT, we take the lumped element limit for the circuit, and the electronic subsystem can be regarded as a two-level system that interacts with SAW at different positions simultaneously. Notice that this system inevitably becomes non-Markovian under this assumption, thus necessitating our use of the Laplace transform solutions in what follows, rather than more typical quantum optics approximations. We also assume the mass loading of all electrodes to be zero to remove additional mechanical resonances. And we approximate the uniform electric field between each pair of electrodes, such that $E(x,t) = [V(t)/\lambda]\,\mathrm{sgn}[\cos(\pi x/2\lambda)]$, where $V(t)$ is the voltage applied on the IDT. We also assume the substrate has no loss through intrinsic material dissipation or via acoustic energy radiated in directions perpendicular to $\hat{x}$

We take the atom transition frequency to equal the IDT resonance frequency, i.e.,

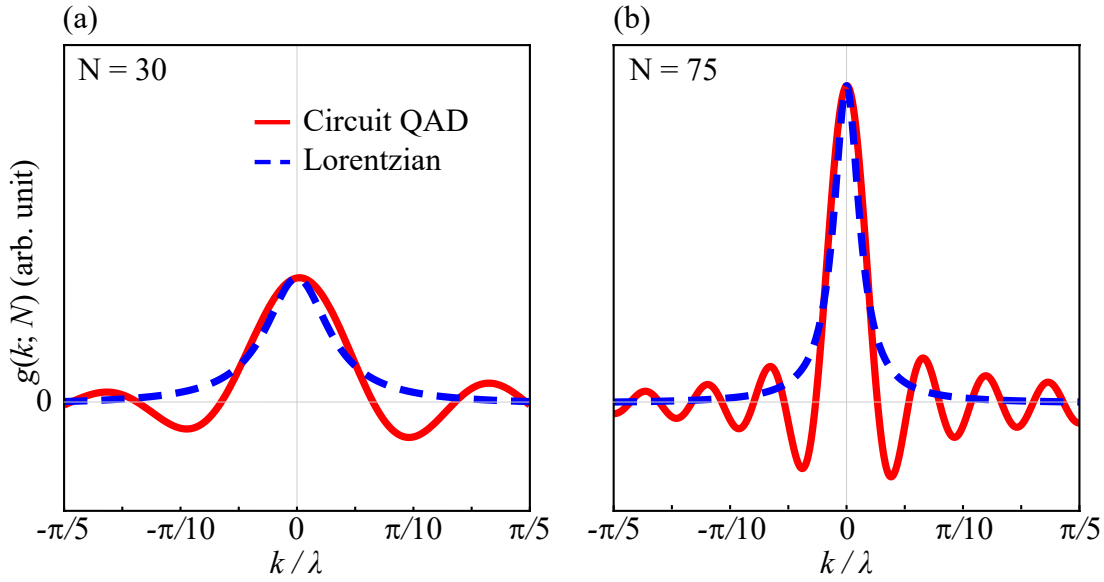

Figure 2.2: The momentum-dependent coupling $g(k;N)$ for (a) $N = 30$, (b) $N = 75$. Red solid lines correspond to circuit QAD model 2.8, blue dashed lines to Lorentzian toy model 2.15. The vertical axes for (a) and (b) share the same scale.

$\nu = 2\pi/T = 2\pi c_s/\lambda$, where c_s is the speed of SAW propagation, and T is the designed fundamental period of the SAW. We calculate the coupling $g(k;N)$ for circuit QAD device as [91]

$$g_{\mathrm{cQAD}}(k;N) = \sqrt{\frac{\gamma_1 c_s}{2\pi}}\,\frac{\sin(Nk\lambda/2)\cot(k\lambda/4)}{2+k\lambda/\pi}. \tag{2.8}$$

We illustrate $g_{\mathrm{cQAD}}(k;N)$ in figure 2.2 for $N = 30$, and 75. This model has a finite bandwidth about $2\pi/N\lambda$, with the on-resonance coupling proportional to N. Note that the poles of the response function 2.6 are hard to find analytically with this model. Therefore, we establish a toy model in the next subsection to capture the long-time dynamics and where we can analytically express its poles. Then, we compare the toy model to numerical results using the circuit QAD model in section IV. B.

2.3.2 Derivation of the circuit QAD model

In this subsection, we give both the derivation of equation 2.8 and a discussion of experimental feasibility of this model. Consider the system described by figure 2.1, where the IDT aligns to the [110] direction of a cubic crystal substrate. We assume the electrodes of the IDT do not change the mass density on the surface, and we model the Josephson junction as an LC circuit with inductance L_J and capacitance C_J. The Lagrangian of the system is [92]

$$\mathscr{L} = \frac{L_J}{2}\dot{Q}^2 - \frac{1}{2C_\Sigma}Q^2 - We_{14}\int_0^\infty dz \int_{-d/2}^{d/2} dx \left[\frac{\partial V}{\partial x}\left(\frac{\partial u_x}{\partial z} + \frac{\partial u_z}{\partial x}\right)\right] + \frac{W}{2}\times$$
$$\int_0^\infty dz \int_{-\infty}^\infty dx \left[\rho(\dot{u_x}^2 + \dot{u_z}^2) - c'_{11}\left(\frac{\partial u_x}{\partial x}\right)^2 - c_{11}\left(\frac{\partial u_z}{\partial z}\right)^2 - 2c_{12}\frac{\partial u_x}{\partial x}\frac{\partial u_z}{\partial z} - c_{44}\left(\frac{\partial u_x}{\partial z} + \frac{\partial u_z}{\partial x}\right)^2\right], \tag{2.9}$$

where variables $Q(t)$ and $\vec{u}(x,z,t) = \{u_x, u_z\}(x,z,t)$ are the charge and strain degrees of freedom, respectively. The total capacitance $C_\Sigma = C_J + C_{\text{IDT}}$, where the capacitance of IDT C_{IDT} can be calculated according to [93]. W is the width of the IDT. The material parameters ρ, c_{11}, c_{12}, c_{44}, e_{14} are the density, elements of elastic tensor, and piezoelectric tensor of the substrate. For the cubic crystal, we have $c'_{11} = (c_{11} + c_{12} + 2c_{44})/2$ [94]. To represent SAW modes, we take the ansatz [94]:

$$u_x(x,z,t) = \sum_{j=-\infty}^{\infty} C_j(t)\xi_j(z)\psi_j(x), \tag{2.10}$$

$$u_z(x,z,t) = \sum_{j=-\infty}^{\infty} C_j(t)\zeta_j(z)\psi_j(x), \tag{2.11}$$

where $\psi_j(x) = \sqrt{2/L}e^{-iK_j x}$, $\xi_j(z) = \sqrt{2/L}e^{-qK_j z - i\phi}$, and $\zeta_j(z) = \sqrt{2/L}re^{-qK_j z - i\phi}$ with periodic boundary conditions in x, and $\vec{u} = 0$ at $z \to \infty$. L, and $K_j = \pi j/L$ are the length of the system, and the momentum of modes, where $j \in \mathbb{Z}$. The fitting parameters $q, r \in \mathbb{C}$,

and $\phi \in \mathbb{R}$ can be derived from [94]. The electric field oscillates rapidly enough that the electric potential $V(x)$ is always quasi-static by the comparison of electron transmission. Therefore, we make the approximation:

$$\frac{\partial V}{\partial x} = \begin{cases} -\frac{2Q}{C_\Sigma \lambda}, & \text{for } \frac{2\eta - N}{2}\lambda \leq x < \frac{2\eta+1-N}{2}\lambda \\ +\frac{2Q}{C_\Sigma \lambda}, & \text{for } \frac{2\eta+1-N}{2}\lambda \leq x < \frac{2\eta+2-N}{2}\lambda \end{cases}, \tag{2.12}$$

where $\eta = 0, 1, 2, ..., N-1$. Substituting equation (2.10-2.12) into equation 2.9, we get

$$\mathscr{L} = \frac{L_J}{2}\dot{Q}^2 - \frac{1}{2C_\Sigma}Q^2 + \frac{W}{2L}\sum_{j=-\infty}^{\infty}\left[\frac{\rho'}{K_j}|\dot{C}_j|^2 - c' K_j |C_j|^2 - \frac{e'}{C_\Sigma}\frac{\sin\left(\frac{K_j\lambda N}{2}\right)\tan\left(\frac{K_j\lambda}{4}\right)}{K_j\lambda}QC_j\right]. \tag{2.13}$$

The new parameters $\rho' = \rho(1+|r|^2)/\mathrm{Re}[q]$, $c' = \{c'_{11} + c_{44}|r|^2 + (c_{44}+c_{11}|r|^2)|q|^2 + i[c_{12}(r^*q^* - rq) + c_{44}(rq^* - r^*q)]\}/\mathrm{Re}[q]$, and $e' = 8e_{14}\mathrm{Re}[(i - r/q)e^{-i\phi}]$ are effective density, elastic constant and piezoelectric constant, respectively. Then we define the momentum conjugates as: $V = L_J\dot{Q}$, $P_j = M_j\dot{C}_j$, where $M_j = W\rho'/(LK_j)$. And then we can calculate the quantized Hamiltonian by mapping $C_j \to \sqrt{\hbar/(2M_j\omega_j)}(\hat{a}_j + \hat{a}_j^\dagger)$, $P_j \to -i\sqrt{\hbar M_j\omega_j/2}(\hat{a}_j - \hat{a}_j^\dagger)$, $Q \to \sqrt{\hbar/(2L_J\nu)}(\hat{\sigma}_- + \hat{\sigma}_+)$, $V \to -i\sqrt{\hbar L_J\nu/2}(\hat{\sigma}_- - \hat{\sigma}_+)$. Then we have

$$\hat{H} = \hbar\nu\hat{\sigma}_+\hat{\sigma}_- + \sum_{j=-\infty}^{\infty}\hbar\omega_j\hat{a}_j^\dagger\hat{a}_j + \frac{\hbar g_0\sqrt{\pi}}{\sqrt{L}}\sum_{j=-\infty}^{\infty}\frac{\sin\left(K_j\lambda N/2\right)\tan\left(K_j\lambda/4\right)}{K_j\lambda/\pi}(\hat{\sigma}_- + \hat{\sigma}_+)(\hat{a}_j + \hat{a}_j^\dagger), \tag{2.14}$$

where $\nu \equiv 1/\sqrt{L_J C_\Sigma}$, $\omega_j \equiv c_s K_j$ (and $c_s = \sqrt{c'/\rho'}$), and $g_0 \equiv e'\sqrt{\pi W\nu/(C_\Sigma\sqrt{c'\rho'})}$. Taking the rotating wave approximation, the limit $L \to \infty$ then moving in to the rotating frame, we get the Hamiltonian equation 2.1 with equation 2.8.

In general, an artificial qubit (e.g. a DC SQUID as a generalization of Josephson junction) has tunable frequency from $0.1 \sim 10$ GHz. Taking the speed of sound as $3000 \sim 5000$

$\mathrm{m\,s^{-1}}$, the corresponding phonon wavelength range is $0.5 \sim 30$ μm. Engineering IDTs at this length scale has been achieved by multiple references such as Ref. [37]. Then we use parameters provided in Ref. [91] to estimate γ_1 and to validate the experimental feasibility of our model: $c_{11} = 12.26,\ c_{12} = 5.71,\ c_{44} = 6.00,\ c'_{11} = 14.99$ ($\times 10^{10}$ $\mathrm{N\,m^{-2}}$), $q = 0.5 + 0.48i,\ r = -0.68 + 1.16i,\ \phi = 1.05$, $\rho = 5307\ \mathrm{kg\,m^{-3}}$, $e_{14} = 0.157$ $\mathrm{C\,m^{-2}}$, and assume reasonable parameters as $\nu \approx 5$ GHz, $C_\Sigma = 2.5 \times 10^{-11}$ F, $W = 50$ μm. Then our numerical estimations of parameters are: $\rho' = 14902\ \mathrm{kg\,m^{-3}}$, $c' = 28.73 \times 10^{10}$ $\mathrm{N\,m^{-2}}$, $e' = -1.248\ \mathrm{C\,m^{-2}}$, $g_0 = -19.34\ \sqrt{\mu\mathrm{m}}\mathrm{MHz}$, $c_s = 4391\ \mathrm{m\,s^{-1}}$. $\gamma_1 = 4\pi g_0^2/c_s \approx 1.07$ MHz. As $\gamma_1 > \pi \times 10^{-5}\nu$ is possible, we conclude that experimental realization can be even easier than our analysis.

2.3.3 The Lorentzian toy model

To evaluate the integral in equation 2.6, we use a Lorentzian toy model $g_{\mathrm{Lor}}(k;N)$ defined as

$$g_{\mathrm{Lor}}(k;N) \equiv \sqrt{\frac{\gamma_1 c_s}{2\pi}}\ \frac{N}{(Nk\lambda/\pi)^2 + 1}, \tag{2.15}$$

instead of equation 2.8. Such a model satisfies the following criteria: it has a finite bandwidth about $2\pi/N\lambda$ and an on-resonance coupling proportional to N, it is non-local in position with the scale of $N\lambda$, and it decays exponentially in position and quadratically in momentum. In figure 2.2, we illustrate that the shape of the Lorentzian toy model matches the central peak of the circuit QAD model, while it does not capture the oscillation behavior at large $|k|$. This toy model greatly simplifies the calculations and allows us to analytically describe the poles of the response function $\chi(s)$, leading to our main results in section IV. A. We can then analyze corrections to this model from the QAD picture.

2.4 Results

2.4.1 Analytic solutions from the Lorentzian model

First, we substitute equation 2.15 into the equation defining the poles of the response function, $[\chi(s_n)]^{-1} = 0$, which yields

$$s_n + \frac{N^2 \gamma_1 \nu (N s_n + \nu)}{(\nu + 2N s_n)^2} = 0. \tag{2.16}$$

This equation can be reduced to a cubic polynomial of s_n. In figure 2.3(a-b), we set $\gamma_1 = \pi \times 10^{-5} \nu$ and plot the $-2\mathrm{Re}(s_n)$ and $\mathrm{Im}(s_n)$, which indicate the damping rates and the effective Rabi frequencies. We mark the solutions associated with the slowest damped modes with solid lines.

The explicit form for the roots of equation 2.16 is:

$$s_n = -\frac{\nu}{3N} + \frac{e^{-(2i\pi/3)n} \nu \left(\nu - 3\gamma_1 N^3\right)}{6A} + \frac{A e^{(2i\pi/3)n}}{6N^2}, \tag{2.17}$$

where $n = 1, 2, 3$, and $A = \sqrt[3]{-18\gamma_1 \nu^2 N^6 + \nu^3 N^3 + 3\sqrt{3}\sqrt{\gamma_1 \nu^3 N^9 \left(\gamma_1^2 N^6 + 11\gamma_1 \nu N^3 - \nu^2\right)}}$. We can find the transition point N_T by take the square root part of A equals zero, i.e. $\gamma_1^2 N_T^6 + 11\gamma_1 \nu N_T^3 - \nu^2 = 0$.

In figure 2.3(a-b), we observe a dramatic change of dynamics at the *transition point* N_T. When $N \ll N_T$, increasing the atom size only creates a larger coupling region and therefore accelerates the relaxation process. And at the transition point $N = N_T$, we find the imaginary parts of two poles merge, while their real parts split. And when $N \approx N_T$, the atom decays quickly into the 1-D waveguide, as all the modes have large damping rates. However, when $N > N_T$, the effective relaxation rate γ drops almost exponentially with N, while the effective Rabi frequency becomes non-zero and increases. Note that

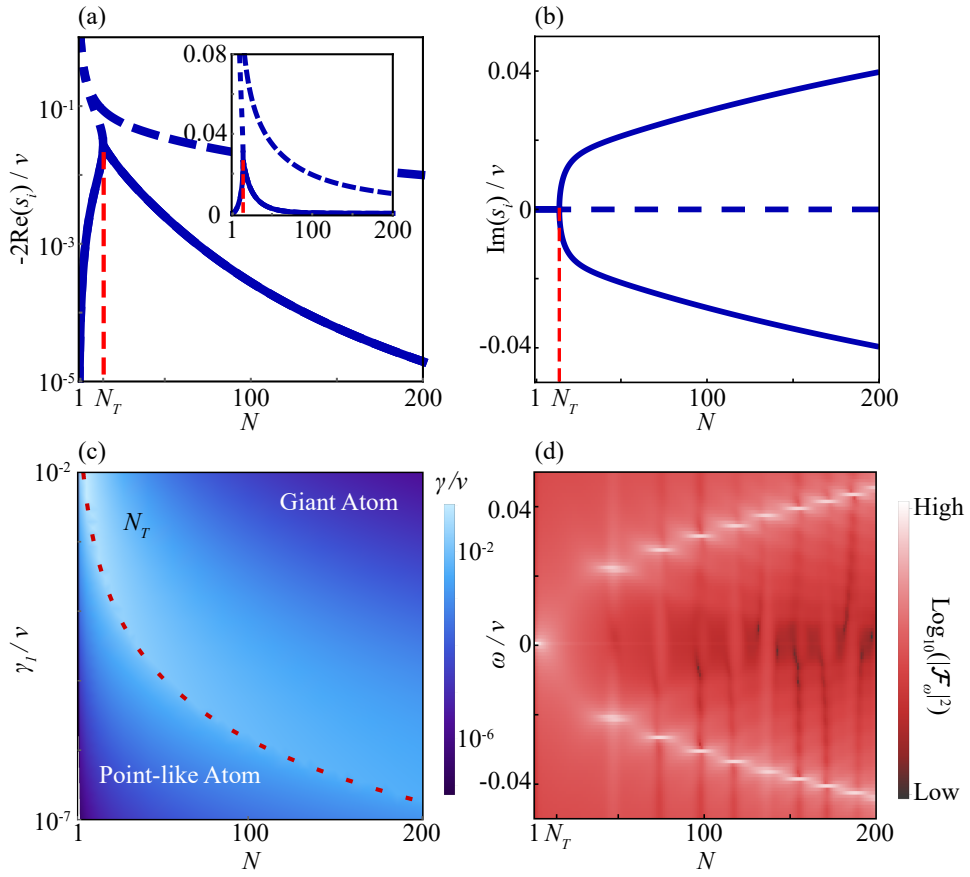

Figure 2.3: (a-c) Transition from the point-like atom to the giant atom, with the Lorentzian toy model: (a) The blue lines represent decay rates $-2\mathrm{Re}(s_n)$ versus atom size N in the semi-log scale, where s_n are roots for equation 2.16. The solid blue lines are the effective relaxation rate $\gamma \equiv \mathrm{Min}_n[-2\mathrm{Re}(s_n)]$, and the dashed blue ones represent other roots. The red dotted line shows the transition point N_T. The inset is plotted in a linear scale. (b) The effective Rabi oscillation frequency $\mathrm{Im}(s_n)$, corresponding to (a). (c) The effective relaxation rate γ in the N-γ_1 parameter plane. The red dashed line shows the transition point N_T, which separates two regimes for point-like atom and giant atom. (d) The power spectrum $|\mathscr{F}_\omega[\alpha(t;N)]|^2$ of the simulated time evolution with the circuit QAD model, in the log scale. We note that the discrete resonances observed arise from the phase matching condition in the circuit QAD model that is absent in the Lorentzian model. All figures are in rotating frame with frequency ν, and all log scales are in $\log_{10}$ base.

both phenomena are the results of the atom excitation state overlapping with bound states. This result shows that a bounded giant atom regime exists at $N \gg N_T$, where some of the atomic excitation energy is localized and oscillates between atomic excitation and a stationary phonon wave packet. We also find that in the limit $N \to \infty$, equation 2.16 reduces to $s_n \to \pm(i/2)\sqrt{N\gamma_1 \nu}$. As $\mathrm{Re}(s_n) \to 0$, a part of the excitation lives in bound states in this

limit. We can derive the transition point N_T from the roots of equation 2.16:

$$N_T = \sqrt[3]{\frac{(5\sqrt{5}-11)\nu}{2\gamma_1}} \approx 0.448 \times \sqrt[3]{\nu/\gamma_1}. \tag{2.18}$$

For $\gamma_1 = \pi \times 10^{-5}\nu$, we have $N_T \approx 14.2$. In figure 2.3(c), we show the effective relaxation rate γ in the N-γ_1 parameter plane. We find two slow relaxation regions corresponding to the point-like atom case and the bounded giant atom case, which are on either side of N_T.

2.4.2 Numerical results from the circuit QAD model

Although it is hard to analytically evaluate the integral in equation 2.6 with the circuit QAD model, we can discretize the Hamiltonian and simulate the dynamics of the system via solution of the Schrodinger equation for the case of a single initial excitation, i.e., $\rangle\psi(t=0)| = \rangle e,0|$. We choose the cutoff momentum $k_c = \pm 0.1\pi/\lambda$ and the density of states $dk = 2\pi \times 10^{-4}/\lambda$, and time step $dt = 0.1T$. We keep $\gamma_1 = \pi \times 10^{-5}\nu$ to compare with analytic results from the last subsection.

In figure 2.4(a), we show the time evolution of the atomic excitation, $|\alpha(t)|^2$. As expected, we find that for some $N \gg N_T$, such as $N = 45$, and 75, a fraction of the energy remains in the system after the phonons travel through the atom, i.e., $t_b = NT$, and this energy oscillates between mechanical and atomic excitation. Next, we choose a final time t_f, such that $|\alpha(t_f)|^2 \approx 0$ for all the N values we chose, and plot the magnitude of the phonon wavefunction $|\Psi(x,t_f)|^2$ in figure 2.4(b). Again, we find that for $N = 45$, and 75, a portion of energy remains confined within the range of the IDT after a long time.

We also show the logarithm of the power spectrum $|\mathscr{F}_\omega[\alpha(t;N)]|^2$ in figure 2.3(d), where $\mathscr{F}_\omega[f(t)]$ represents the Fourier transform of $f(t)$. We observe qualitative agreement between figure 2.3(b) and 2.3(d) in terms of the locations of peaks when peaks are observed, but with discrete frequencies rather than continuous as a function of N. For ex-

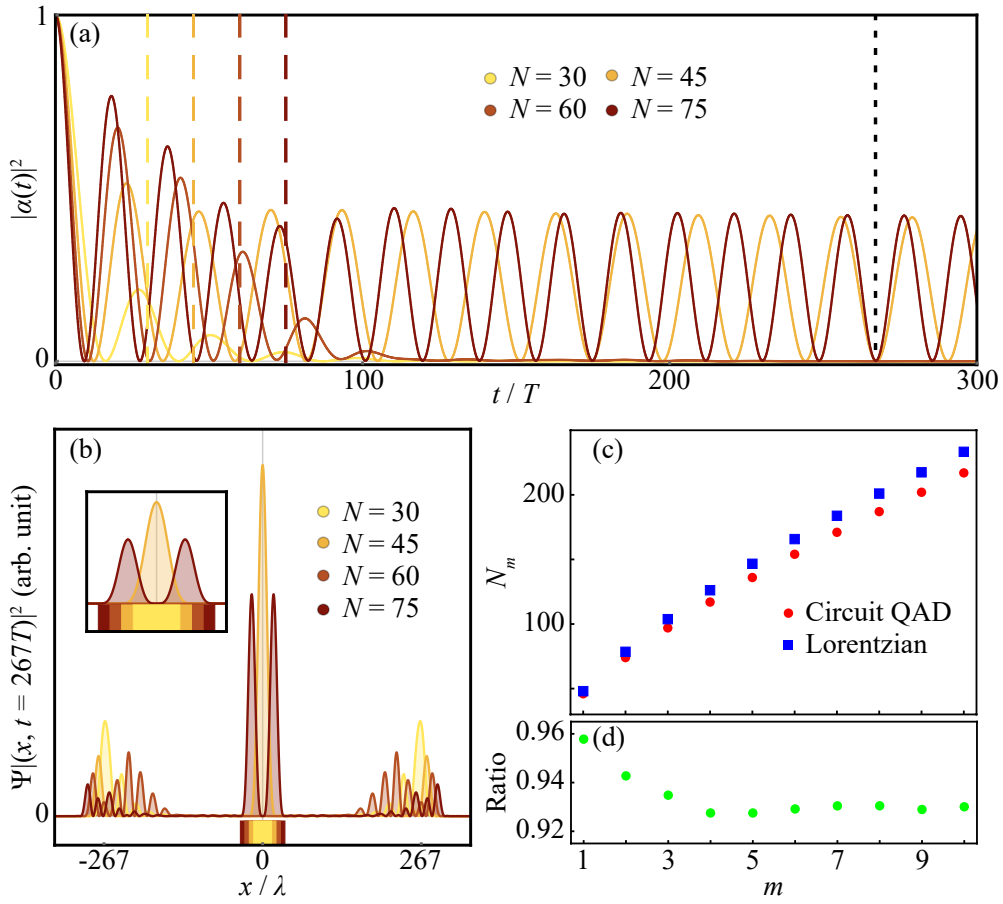

Figure 2.4: (a-b) Simulation for the circuit QAD model for different atom sizes N: (a) The time evolution of atom excitation amplitude $|\alpha(t)|^2$, for different N. The dashed lines show the time that the phonons travel through the atom length $t_b = NT$. For N above the onset of normal mode splitting and phase matched, the system settles into a long-lived state after a short time. (b) The magnitude of phonon wave function $|\Psi(x,t_f)|^2$ frozen at $t_f = 267T$ (also indicated by the black dashed line on figure 2.4(a)), for different N. We chose t_f such that $|\alpha(t_f)^2| \approx 0$ for all N values shown. The inset shows the same plot zoomed in near the atom region identified by the bars of color below the axis for different N. (c) The Lorentzian theory prediction and the circuit QAD simulation result of the bounded atom size N_m. (d) The ratio between $N_{m,\mathrm{cQAD}}/N_{m,\mathrm{Lor}}$.

ample, from figure 2.4(a-b), we also find that for some other $N \gg N_T$, such as $N = 60$, the atom still decays fast into the continuum and no peak is seen in the power spectrum. This behavior is caused by a mismatch between the atom length $N\lambda$ and the effective "vacuum Rabi wavelength" $\lambda_R(N) = 2\pi c_s/\mathrm{Max}_n[\mathrm{Im}(s_n(N))]$, as the circuit QAD model introduces a hard spatial boundary to the atom. Therefore, the circuit QAD model requires the atom size N_m to satisfy an additional phase matching condition $N_m\lambda \approx m\lambda_R(N_m)$ for the bounded giant atom phenomenon, where $m \in \mathbb{N}$. We have discussed the first two cases, $N_1 = 45$ and

$N_2 = 75$, and we further observe $1 \sim 2$ peaks that correspond to m in figure 2.4(b). In figure 2.4(c), we show a comparison between a numerical simulation of the circuit QAD model (by finding largest resonances on the power spectrum, i.e., the brightest points on figure 2.3(d)), and analytic calculations of N_m using the Lorentzian model (by solving the equation $N_m\lambda = 2\pi c_s m/\mathrm{Max}_n[\mathrm{Im}(s_n(N_m))]$). Again, we find a qualitative agreement between two models. We also plot the ratio between $N_{m,\mathrm{cQAD}}$ and $N_{m,\mathrm{Lor}}$, which is stabilized around 0.93 for $m \geq 3$.

Here we present an intuitive picture of understanding how phase matching conditions for bounded giant atoms arise even in a continuous model. Consider the case where the atom is set to the excited state at $t = 0$: During the first half of the effective vacuum Rabi oscillation $t = (0, T/2)$ the nominal outgoing phonon wavefunction becomes approximately $\psi_1(x) \propto \exp(-a|x|)$, where a is some geometrical parameter with a $1/x$ unit. During the second half of the period, this undergoes destructive interference with the newly emitted phonon state $\psi_2(x) \propto -\exp(-ab|x|)$ while ψ_1 moves outward a distance $\lambda_R/2$. The second portion has a π phase shift and some loss b due to energy being emitted in the first half. Therefore, the total emission in the far field ($|x| \gg N\lambda$) within the whole cycle is: $\psi(x) \propto \exp(-a|x + \lambda_R/2|) - \exp(-ab|x|)$. For the Lorentzian model in the giant atom regime, $b \sim a\lambda_R/2$ and these can cancel.

2.4.3 Top-hat model and bound states in continuum

If $\gamma = 0$, then there exists at least one bound state in the 1-D continuum. Such a state is known as a bound state in continuum (BIC) [34, 81, 95] or a decoherence-free state[76, 96–98]. A BIC is an eigenstate of the Hamiltonian with eigenenergy within the continuum of the spectrum. Its existence usually requires symmetry protection or fine-tuning [34]. We

illustrate the bound state in the continuum using the top-hat toy model

$$g_{\mathrm{TH}}(k;N) \equiv \begin{cases} \sqrt{\frac{\gamma_1 c_s}{2\pi}}\, N & |k| \leq \frac{2\pi}{N\lambda} \\ 0 & |k| > \frac{2\pi}{N\lambda} \end{cases}. \tag{2.19}$$

Note that though this toy model may seem simple, it is unphysical as it requires infinite spatial extent. Here, we report that a pair of purely imaginary solutions exist in our top-hat toy model. With equation 2.19, we can write the equation $[\chi(s_n)]^{-1} = 0$ as

$$\pi s_n + iN^2\gamma_1 \log\left(\frac{Ns_n - i\nu}{Ns_n + i\nu}\right) = 0, \tag{2.20}$$

where the complex function $\log(z)$ is the multiple-valued. Now we seek for purely imaginary solution $s_n = i\omega_n$, and we separate the real and imaginary part of equation 2.20, which results in

$$2\pi\omega_n + N^2\gamma_1 \log\left[\left(\frac{\nu - N\omega_n}{\nu + N\omega_n}\right)^2\right] = 0, \quad \text{with } |\omega_n| > \frac{\nu}{N}. \tag{2.21}$$

Although equation 2.21 is transcendental, there always exists a pair of solutions for all N: We define the left-hand side of equation 2.21 as $f(\omega_n)$, when $\omega_n \to \pm\nu/N$, $f(\omega_n) \to \mp\infty$; when $\omega_n \to \pm\infty$, $f(\omega_n) \to \pm\infty$. As f is analytic, there exist a $\omega_1 < -\nu/N$ and a $\omega_2 > \nu/N$, such that $f(\omega_n) = 0$.

2.5 Discussion and conclusion

In this chapter, we have generalized the Weisskopf-Wigner theory from a point-like atom to a bounded giant atom that interacts with the medium instantaneously over a continuous spatial length $N\lambda$, with a simple Lorentzian toy model. When the coherence of the

atom travels through the antenna much faster than the emission, we have observed that if its size N satisfies both (1) the atom size N is larger than the transition size N_T and (2) the phase matching condition $N\lambda \approx m\lambda_R(N)$, a giant atom dynamic emerges, which is characterized by suppressed relaxation and effective vacuum Rabi oscillation with a phononic wave packet bound to the antenna, even in the absence of a cavity. To verify our results, we have compared it with the exact numerics of a realistic circuit QAD coupling model. We have specifically studied the circuit QAD apparatus, but our analysis can be applied similarly to other quantum electro-mechanical systems with a large coupling spatial range [26, 47, 99]. For example, an optomechanical system where a membrane and a microwave waveguide coupled via radiation pressure could have similar effects.

Chapter 3: Feedback cooling for weakly monitored Bose-Einstein condensates

Combined with real-time feedback control, weak measurement opens up a new avenue for developing unique non-equilibrium quantum materials. We provide a theoretical framework for quantum feedback control of single component BECs by combining backaction-limited weak measurements with spatially resolved feedback. We demonstrate in this chapter how to construct a feedback cooling approach to minimize runaway heating caused by measurement backaction. We offer an analytical model and compare it to numerical simulations that averaged an ensemble of quantum trajectories to demonstrate its usefulness. Our finding reveals that closed-loop quantum control of BECs is a novel and potent tool for quantum engineering in cold-atom systems. Our feedback cooling strategy provides opportunities for many potential applications, such as novel states preparation and phase transition engineering.

3.1 Introduction

Laser-cooled quantum gas experiments have shown excellent control over the low-energy Hamiltonian regulating system dynamics, allowing for the study of interacting many-body quantum systems with high accuracy in the laboratory. The ultracold atom has therefore emerged as an essential platform in the field of so-called "analog quantum simulation" [51, 100–104], where studies have successfully studied condensed-matter phe-

nomena such as the superfluid-Mott insulator transition [52], the BEC-BCS crossover [105, 106], and spin-orbit coupling in ultracold atoms [107]. Systems with long-range interactions [108] or non-equilibrium dynamics [109, 110] have also been realized in cutting-edge studies.

In contrast, quantum simulation of open systems, i.e., systems that interact with their environments, has remained unexplored [60]. The sophisticated application of feedback control to many-body quantum systems is a novel method for achieving this aim in quantum simulation. Quantum simulations of open systems promise to understand fundamental physics and enable a wide range of applications in research and development. Observation of a variety of novel phenomena in dynamical steady state, where a potentially more considerable class of states is feasible than in thermal equilibrium, might be made possible, for example, through feedback management of many-body systems [111, 112]. Existing proposals include preparation of many-body states via potential engineering [28, 113–115], nonthermal steady states [53, 116], stable non-Abelian vortices [117], or even time crystals [118].

In this chapter, we use a BEC model system to demonstrate the flexibility of weak measurements in conjunction with spatially resolved feedback for quantum simulation of time-dependent effective Hamiltonians [119–121]. Using the framework of quantum control theory, we establish a theory of weak measurement and classical feedback in weakly interacting quantum systems [40]. We study the steady-state phases of BEC exposed to weak measurement and classical feedback through an applied potential using our generic formalism, which allows for the development of density feedback protocols.

We further develop a signal filtering and cooling system to reduce heating, and we demonstrate that the condensate stays intact even when subjected to feedback and measurement feedback. Our finding opens the door to the development of novel dynamical and spatially dependent effective interactions in quantum gases via closed-loop feedback

control, as shown here.

Previous works have examined quantum control protocols for BECs [50, 57, 58, 122–127]. Thus feedback strategies have focused on driving a condensate to its ground state by manipulating the positions and amplitudes of harmonic trapping potentials [50, 57, 58, 122, 123], or to deterministically prepare a target state [124, 127], possibly for quantum memory applications [125, 126]. In this work, the implementation of designed effective Hamiltonians with potentially unknown dynamical stable states takes us beyond particular state control and into designing effective Hamiltonians.

This chapter is structured as follows: In section 3.2 we set up the scope and format used in this chapter and introduce a toy model illustrating the prominent features of the control protocol. In section 3.3 we elaborate and formulate our feedback cooling protocol, describe our theoretical approaches, and characterize the resulting steady states. We show that feedback cooling can effectively mitigate heating due to measurement backaction. We conclude and compare with other of our work in section 3.4.

3.2 Toy model

Our goal is to build feedback methods that reduce quantum projection noise as much as possible. Here we establish a toy model of quasi one-dimensional (1D) single component BEC to demonstrate weak measurement and feedback concepts.

3.2.1 Weak measurement

We use phase-contrast imaging [128] to model dispersive imaging of a quasi 1D single component BEC of length L. We consider time and space resolved measurements of atomic density $\hat{n}(x,t)$ using a Gaussian measurement model designed in Ref. [129]. Stroboscopic

weak measurements with strength φ result in the measurement signal

$$\mathscr{M}(x,t) = \langle \hat{n}(x,t) \rangle + \frac{m(x)}{\varphi}, \tag{3.1}$$

where $m(x)$ describes spatiotemporal quantum projection noise associated with the measurement. The measurement is characterized by Fourier domain Gaussian statistics $\overline{\tilde{m}_k} = 0$ and $\overline{\tilde{m}_k \tilde{m}_{k'}} = L\Theta(|k|-k_c)\overline{dW_k dW_{k'}}/2dt^2$, where dW_k is a Wiener increment with $\overline{dW_k} = 0$ and $\overline{dW_k dW_{k'}} = dt\,\delta_{kk'}$ for a time increment dt [130]. The Heaviside function Θ enforces a momentum cutoff at $k_c = 2\pi/\lambda$, accounting for the fact that the physical measurement process can only resolve information with length scales larger than $\lambda/2\pi$. With this protocol, the observer does not immediately acquire information of the condensate phase.

We use the aggregate measurement result $\mathscr{M}$, a function of x, to guide the engineering of the feedback signals in the form of a single-particle potential $V[\mathscr{M}]$. We consider this potential to be local in space in this work.

We describe the condensate in the mean-field approximation using an order parameter $\psi(x)$, which is a classical field describing the BEC dynamics. The total density is $n(x) = \psi^\dagger(x)\psi(x)$ and the order parameter is normalized to the number of particles, $N = \int dx\, n(x)$. From Eq. (3.1) the measurement results at the mean-field level therefore depend on the field amplitude via $\langle \hat{n}(x) \rangle \to |\psi(x)|^2$. Measurement backaction leads to stochastic evolution of the order parameter, which results in condensate heating [55, 129] in the absence of a cooling protocol, which we describe in Sec. 3.3.

The combined measurement and quantum control process is described by a stochastic equation of motion

$$d\psi(x) = d\psi(x)|_{\mathrm{H}} + d\psi(x)|_{\mathrm{M}} + d\psi(x)|_{\mathrm{F}}, \tag{3.2}$$

for the condensate order parameter $\psi(x)$. Here

$$d\psi(x)|_{\mathrm{H}} = -\frac{i}{\hbar}\left[\hat{\mathscr{H}}(x) - \mu\right]\psi(x)dt, \tag{3.3}$$

$$d\psi(x)|_{\mathrm{M}} = \left[-\frac{\varphi^2 k_{\mathrm{c}}}{4\pi} + \varphi m(x)\right]\psi(x)dt, \tag{3.4}$$

$$d\psi(x)|_{\mathrm{F}} = -\frac{i}{\hbar}V[\mathscr{M}](x)\psi(x)dt, \tag{3.5}$$

denote contributions from unitary (i.e., closed system) evolution, measurement backaction, and feedback, respectively and μ represents the chemical potential. For simplicity we set $\hbar = 1$.

The measurement backaction is described by equation (3.4). Backaction noise $m(x)$ is determined by measuring the density of the condensate. The potential term $V[\mathscr{M}]$ is used in Equation (3.5) to describe the feedback. A deterministic term comprising information of the condensate dynamics is combined with a stochastic term due to quantum projection noise in the feedback potential. As a result, both $d\psi|_{\mathrm{F}}$ and $d\psi|_{\mathrm{M}}$ play a role in stochastic condensate dynamics. The density of noncondensed particles stays low when each individual measurement is relatively weak. As a result, we suppose that throughout its evolution, $\psi(x)$ is well characterized by the lowest order Hartree-Fock theory. In Sec. 3.3.2, we validate this assumption.

3.2.2 Feedback

In this section, we examine a simple measurement and feedback model for single component BEC systems. We take a weak density measurement and then apply a proportionate feedback potential

$$V[\mathscr{M}](x,t) = g_0\mathscr{M}(x,t), \tag{3.6}$$

where the gain parameter g_0 denotes the feedback strength. Inserting Eq. (3.1) into Eq. (3.6) gives a feedback potential with two contributions. The first is an effective mean-field interaction

$$V^{\text{eff}}(x,t) = g_0 n(x,t), \tag{3.7}$$

and the second is a stochastic contribution

$$V^{\text{fluct}}(x,t) = \frac{g_0 m(x)}{\varphi}. \tag{3.8}$$

By direct substitution of $V[\mathscr{M}]$ into Eq. (3.5), the dynamical Eqs. (3.3)-(3.5) reduce to two equations $d\psi(x) = d\psi(x)|_{\text{H}'} + d\psi(x)|_{\text{M}'}$ with modified unitary evolution and stochastic terms,

$$d\psi(x)|_{\text{H}'} = -i\left[\hat{\mathscr{H}}^{\text{eff}}(x) - \mu\right]\psi(x)dt \tag{3.9}$$

$$d\psi(x)|_{\text{M}'} = \left[-\frac{\varphi^2 k_{\text{c}}}{4\pi} + \left(\varphi - i\frac{g_0}{\varphi}\right)m(x)\right]\psi(x)dt. \tag{3.10}$$

The effective Hamiltonian $\hat{\mathscr{H}}^{\text{eff}}(x)$ is modified by V^{eff}, and the noise in the stochastic evolution is modified due to the contribution of $V^{\text{fluct}}(x,t)$.

We will utilize this toy model to design a measurement and feedback cooling protocol in the following sections. Due to runaway heating caused by the repetitive and uncompensated application of the stochastic potential in Eq. (3.10) [129], the more straightforward approach given in this section is ineffective. In section 3.3, we introduce a cooling procedure that avoids runaway heating, thus completing our quantum control toolbox.

3.3 Feedback cooling

Measurement backactions could introduce phononic excitations into the condensate. Feedback cooling aims to reduce the number of excitations by applying feedback based on information from the measured signal, eventually stabilizing the condensate and avoiding runaway heating. In this section, we create a feedback cooling protocol for condensates that could remove energy and entropy from the condensate after one cycle of measurement and feedback processes. We design such a protocol using a single discrete measurement as the building block. The final result demonstrates that the condensate fraction and entropy approach stable states throughout this procedure, though the Grossí ÓPitaevskii equation (GPE) energy functional continues to grow throughout the process slowly.

3.3.1 Single measurement protocol

Typically, the continuous measurement limit is established a priori by using $dt \to 0$. Eq. (3.1) specifies that the variance of the measurement record is proportional to $1/dt$, which means that this record diverges in this limit. However, an indefinitely fast physical measurement does not exist in reality. A "single measurement" is obtained by integrating Eq. (3.1) over a small time window. When we take this type of measurement into consideration, we can quantify a measurement protocol that can extract the maximum amount of information from condensates while reducing the negative impacts from backaction.

Now consider the time-integrated version of Eq. (3.1) over an interval Δt, giving a single measurement of density. The measurement result is $\mathscr{M}(x) = n(x) + \bar{m}(x)/\kappa$, where $\kappa = \sqrt{\Delta t}\varphi$ is the measurement strength. $\bar{m}(x)$ is the spatial quantum projection noise where $\tilde{\bar{m}}_k$ has the same Fourier space statistics previously discussed, with $\overline{\tilde{\bar{m}}_k} = 0$ and $\overline{\tilde{\bar{m}}_k \tilde{\bar{m}}_{k'}} = L\delta_{kk'}\Theta(|k|-k_c)/2$. Directly after measurement, the wavefunction updates to $\psi_{|M}(x) \approx$

$\psi(x) + \kappa\bar{m}(x)\psi(x)$. Thus, there exists an optimal measurement strength

$$\kappa_* \approx \sqrt{\frac{1}{2\max[n(x)]}}, \tag{3.11}$$

such that the measurement outcome is equivalent to the post-measurement density $n_{|\mathrm{M}}$ exactly, i.e., $\mathscr{M}(x) = n_{|\mathrm{M}}(x)$. In principle, the optimal measurement strength is determined by the local density; however, this is difficult to apply practically in experiments. Instead, we approximate κ_* to be constant, and we then utilize this coupling value to provide feedback cooling for the system.

If we can find a potential $V_{\mathrm{c}|\mathrm{M}}(x)$ that projects the post measurement state to the ground state, $\psi_{|\mathrm{M}}(x)$ would satisfy the stationary GPE

$$\mu\,\psi_{|\mathrm{M}} = \left[\hat{H}_0 + u_0 n_{|\mathrm{M}} + V_{\mathrm{c}|\mathrm{M}}\right]\psi_{|\mathrm{M}}. \tag{3.12}$$

To compose our feedback cooling protocol, first, we instantly apply the potential $V_{\mathrm{c}|\mathrm{M}}(x)$ for the post-measurement state *would* be the ground state of the total Hamiltonian if we assume a uniform phase. Next, we approach the initial state by slowly–adiabatically–ramping off the applied potential. We approximate $V_{\mathrm{c}|\mathrm{M}}$ using the Thomas-Fermi (TF) approximation of Eq. (3.12), yielding $V_{\mathrm{c}|\mathrm{M}}(x) = \mu - u_0 n_{|\mathrm{M}}(x)$. We then make the substitution $u_0 n_{|\mathrm{M}}(x) \to g_{\mathrm{c}}\mathscr{M}(x)$ where g_{c} is the cooling gain, an externally adjustable parameter for which the expected value of u_0 is found to be optimal. This gives our feedback cooling potential function

$$V_{\mathrm{c}|\mathrm{M}}(x,t) = \left[\mu - g_{\mathrm{c}}\mathscr{M}_{t_{\mathrm{m}}}(x)\right] f\left(t - t_{\mathrm{m}}\right), \tag{3.13}$$

where t_{m} is the time of the measurement and $f(t)$ is a ramp off function where $f(0) = 1$ and $f(t \to \infty) = 0$. Practically, we can use $f(t - t_{\mathrm{m}}) \approx 1 - \gamma(t - t_{\mathrm{m}})$ where γ is the ramp-off rate.

3.3.2 Bogoliubov theory for single measurement protocol

In this section, we present an analytical expression for the phonon distribtion after single measurement-feedback protocol mentioned above utilizing Bogoliubov theory [131] and periodic boundary conditions. Small excitations above the ground state of a spinless BEC with density n after the Bogoliubov transformation has been performed are characterized by the Hamiltonian

$$\hat{H}_{\rm ph} = \sum_k \varepsilon_k \hat{b}_k^\dagger \hat{b}_k, \tag{3.14}$$

where $\hat{b}_k^\dagger$ ($\hat{b}_k$) is the creation (annihilation) operator of a Bogoliubov phonon with momentum k and energy $\varepsilon_k = \mu\xi|k|\sqrt{\xi^2k^2+2}$. To render our analytic analysis easier, we concentrate on the weak measurement regime, in which only at most one phonon mode is occupied, resulting in wavefunctions of the form $|\psi\rangle = \alpha|{\rm vac}\rangle + \sum_k \beta_k|k\rangle$, where $|k\rangle = \hat{b}_k^\dagger|{\rm vac}\rangle$, and $|{\rm vac}\rangle$ is the phonon vacuum.

Measurement backaction is described by the Kraus operator

$$\hat{K} = \exp\left\{-\frac{\kappa^2}{2}\int dx\left[\delta\hat{n}(x) - \frac{\bar{m}_{t_m}(x)}{\kappa}\right]^2\right\}, \tag{3.15}$$

with the density difference operator $\delta\hat{n}(x) \equiv \hat{n}(x) - n$. In the phonon basis $\delta\hat{n}(x)$ can be expressed as a sum $\delta\hat{n}(x) = \sqrt{n/L}\sum_k (c_k e^{-ikx}\hat{b}_k + {\rm h.c.})$ of phonon creation and annihilation operators, with $c_k = [1+2/(\xi k)^2]^{-1/4}$.

In this representation, the feedback cooling operator derived from (3.13) is

$$\hat{V}_{\rm c|M}(t) = \int dx\, V_{\rm c|M}(x,t)\hat{n}(x). \tag{3.16}$$

Assuming adiabatic evolution, with ramp-off rate $\gamma \to 0$, and using first-order perturbation

approximation, the operator describing the cooling protocol is

$$\hat{R}_{|\mathrm{m}} = 1 + \sum_k \frac{g_\mathrm{c} c_k \sqrt{n}}{\kappa \varepsilon_k \sqrt{L}} \left[\tilde{\hat{m}}_{t_\mathrm{m}}(k) \hat{b}_k - \mathrm{h.c.} \right]. \tag{3.17}$$

This expression is valid for $g_\mathrm{c} c_k \sqrt{n} \ll \kappa \varepsilon_k \sqrt{L}$. The probability of finding a phonon in state $|k\rangle$ after a measurement-feedback cycle is

$$\bar{P}_k = \overline{|\langle k|\hat{R}_{|\mathrm{m}}\hat{K}|\mathrm{vac}\rangle|^2} = \frac{n\kappa^2 c_k^2}{2} \left(1 - \frac{g_\mathrm{c}}{\kappa^2 \varepsilon_k}\right)^2 \Theta(|k| - k_\mathrm{c}). \tag{3.18}$$

We draw two most important conclusions from this result: (1) Setting $g_\mathrm{c} = 0$ gives the probability $n\kappa^2 c_k^2/2$ that the measurement created a phonon in state $|k\rangle$; and (2) the phonon mode with energy $\varepsilon_{k,\mathrm{opt}} = g_\mathrm{c}\kappa^{-2}$ can be perfectly cooled with this protocol. Eq. (3.18) is compared to our stochastic GPE simulation with a linear ramp-off function $f(t)$ in Figure 3.1(a). The analytic approach accurately reproduces the numerically anticipated phonon distribution immediately after a single measurement (red curve). However, the results with cooling show extra periodic patterns due to the finite ramp-off time of the simulation. We also notice that our perturbation theory becomes inapplicable for the parameters on the gray area where single phonon energy is small.

In the thermodynamic limit $L \gg \xi$, the per-particle energy after one measurement-feedback cycle

$$\Delta E = \frac{1}{2\pi n} \int dk\ \varepsilon_k \bar{P}_k = A(g_\mathrm{c} - g_{\mathrm{c}*})^2 + \Delta E_* \tag{3.19}$$

is parabolic. With $\xi \gg 1/k_\mathrm{c}$, the minimal per-particle energy increase $\Delta E_*/\mu = \kappa^2 \phi_\mathrm{c}^2(\pi\phi_\mathrm{c} -$

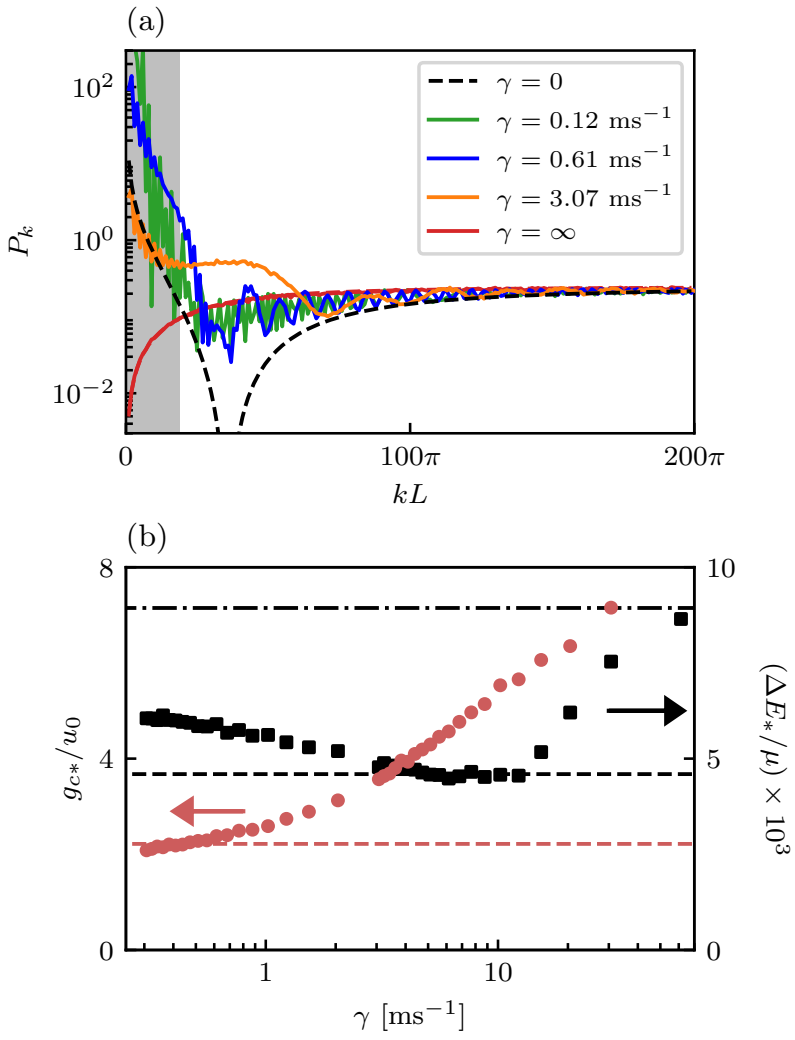

Figure 3.1: Comparison between Bogoliubov theoretical results and stochastic GPE simulations for a single measurement-feedback cycle, where the system initially in the BEC ground state. (a) Phonon population. Black, green, blue, orange, and red curves indicate $\gamma = 0\,\mathrm{ms}^{-1}$, $\gamma = 0.12\,\mathrm{ms}^{-1}$, $\gamma = 0.61\,\mathrm{ms}^{-1}$, $\gamma = 3.07\,\mathrm{ms}^{-1}$ and $\gamma = \infty$. Dashed curves result from Bogoliubov theory [Eq. (3.18) with $g_c = u_0$ and $g_c = 0$, corresponding to $\gamma = 0$ and $\gamma = \infty$ respectively], while solid curves derive from GPE simulations (3000 trajectories). The Bogoliubov and GPE results coincide for $\gamma = \infty$ (red). The grey region marks wavenumbers for which first order perturbation theory fails. (b) Gain g_{c*} (red circles) for which the energy increase ΔE_* (black squares) is minimized, plotted as a function of γ. For each point, we fit Eq. (3.19) to the GPE simulation result with A, g_{c*}, and ΔE_* as free parameters. Horizontal dashed lines indicate the Bogoliubov prediction of ΔE_* and g_{c*}, and dash-dotted line shows energy increase without feedback cooling (i.e., $\gamma = \infty$).

$6\sqrt{2})/(6\pi^2\xi)$ occurs for a gain

$$\frac{g_{c*}}{u_0} = \frac{2\sqrt{2}\kappa^2 n\phi_c}{\pi}, \tag{3.20}$$

where $\phi_c = k_c\xi/\sqrt{2}$ parameterizes the cutoff and $A = (4\sqrt{2}\kappa^2\mu\xi)^{-1}$.

Figure 3.1 (b) compares the optimal energy increase predicted by Eq. (3.19), with that obtained from numerical simulations of the stochastic GPE (horizontal black dashed line and black squares, respectively), and the corresponding optimal gains are denoted by the red circles. In this figure, the GPE simulation exhibits three regimes: (1) For very rapid ramps $\gamma \to \infty$, the adiabatic assumption is invalid, and the GPE optimal gain is larger than anticipated from the analytic model. (2) In the adiabatic ramping regime where $\gamma \to 0$, we find both g_{c*} and ΔE_* converge, with ΔE_* greater than our predicted value. This results from phonon-phonon scattering processes redistributing phonons between modes, which is not included in our Bogoliubov theory. And, (3) in the intermediate regime (γ between $3\,\mathrm{ms}^{-1}$ and $10\,\mathrm{ms}^{-1}$) our theory performs optimally and ΔE_* coincides with the analytic prediction, albeit with much higher gain. We note that the optimal gain $g_c = u_0$ obtained in Sect. 3.3.1 is close to that predicted by Eq. (3.20), where for the parameters in Fig. 3.1, $g_{c*} \approx 2.8 u_0$.

3.4 Discussion and conclusion

Hamiltonian engineering for Bose gases has been achieved at the level of the single-particle Hamiltonian via synthetic gauge fields [132, 133], spin-orbit coupling [107, 134, 135], and spin-dependent potentials [136, 137]. Going beyond previous works [57, 129], we created a cooling strategy to prevent the condensate from overheating during the monitoring-feedback process. For optimal experimental implementation, further improvement of the cooling process is required. For example, Eq. (3.18) predicts that the k dependent gain $g_c(k) = n\kappa^2\varepsilon_k$ would result in near-perfect cooling for all momentum states. Actual measurements include limited resolution, inefficient detectors, and technical noise. The realistic cooling performance might be improved by tweaking the details of this feedback technique according to these imperfections.

This work enables real-time feedback control, allowing us to explore both quasi-steady-state behavior and dynamics in the same experiment. Furthermore, it provides the option for developing feedback-controlled systems in stabilized modes. As illustrated in our publication in Appendix B, Hamiltonians can be tuned and engineerable for customized, spatially dependent effective interaction terms. Nonlocal or time-dependent interactions, which have no analog in closed systems, might be included in future work. Our protocols have the potential to be applied to higher dimensions and to stabilize topological defects like non-Abelian vortex anyons, which are unstable in closed systems [117].

Chapter 4: Machine-learning enhanced dark soliton detection in Bose-Einstein condensates

The majority of information obtained from cold-atom studies comes with images, while the interpretation of these images is constrained by our expectations about the patterns presented in the data. In this chapter, we investigate the well-defined problem of finding dark solitons, which appear as local density depletions in a BEC. In order to study soliton dynamics across a broad range of parameters, it is necessary to analyze big datasets, which means that the currently available human-inspected approach for soliton identification and classification is a substantial bottleneck. We combine CNN with traditional fitting techniques to categorize and extract quantitative information from atomic physics data. Using deep CNNs to detect localized excitations in atomic BECs, we provide an automated classification and positioning method for recognizing localized excitations in atomic BECs, therefore eliminating the requirement for manual evaluation. In addition, we publish our labeled dataset of dark solitons, which is the first of its kind, available for future machine learning research.

4.1 Introduction

ML-based image classification has found applications across a wide range of scientific disciplines, including analyzing of experimental data in high-energy physics [138–140], searching for dark matter and energy [141, 142] identifying excitations in quantum dots

experiments [143–146] predicting properties of materials [147–149] to studying molecular representations and properties [150–152]. In particular, the field of atomic physics has made use of ML for identifying topological phase transitions [153], assisting absorption imaging techniques [154], describing particles in disordered environments [155], and discovering quantum vortices in BECs [156].

We focus on solitons in cold-atom Bose-Einstein condensates. Since the first observation of solitons in canals [157], they have been found in many physical systems involving fluid dynamics, such as rivers and seas [158, 159]; BECs [54, 160]; optical fibers [161, 162]; astronomical plasmas [163]; and even human blood vesicles [164, 165]. Solitons are resilient solitary waves that preserve their size, shape, and travel speed as they are traveling [166, 167]. These characteristics are the result of a dynamic interaction between nonlinearity and dispersion. For their application, solitons in optical fibers have found practical uses in long-distance, high-speed transmission lines because of their inherent stability [168, 169].

While the natural environment does not permit the controlled study of quantum solitons, BECs provide an ideal medium in which one or multiple solitons may be generated on demand with all of their features, such as location and velocity, tailored to meet the needs of the experiment [43, 170]. When doing soliton studies in BECs, raw data in the form of images offer information on characteristics, including positions, of solitons inside the BEC. However, the inability to effectively and accurately determine the number of solitons and their positions is the bottleneck that prevents us from understanding their dynamics. It is possible to refine the position of a soliton provided a reasonable current estimation using typical least-squares fitting techniques if the number of solitons is known before the fitting process begins. As of right now, the number of solitons is decided manually [43], and this human involvement makes it difficult to do an automated analysis of massive datasets.

Here we describe a reliable automatic soliton identification and positioning system in

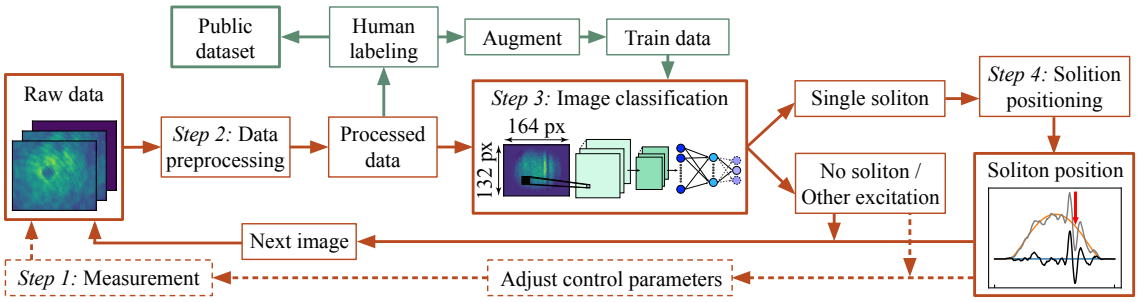

Figure 4.1: Schematic of the soliton detection and positioning system. Red boxes and solid arrows represent the flow of the complete system. The dashed red boxes and arrows represent additional components required for a closed-loop implementation. The green boxes and arrows represent additional out-of-loop steps of preparing the classifier and establishing the training dataset.

this chapter. This system receives input picture data and outputs information on whether or not a single soliton is present in addition to the location of that single soliton if one is there. Given that solitons are generally distinguishable by human analysis of images, this topic has a natural connection with computer vision and the categorization of images using CNNs [171]. Our algorithm is composed of a data preprocessor that transforms raw data into a CNN-compatible format; a CNN image classifier that assesses whether or not a single soliton has been spotted; and, when relevant, a position regressor that locates the soliton inside the BEC (see figure 4.1 for a schematic of the analysis flow).

As part of our research, we construct a dataset of 6,257 labeled experimental images of BECs with and without solitonic excitations, which is now accessible via the National Institute of Standards and Technology (NIST) Science Data Portal [22] and at data.gov. Next, we demonstrate that our automated system outperforms our current human image classifier by autonomously reproducing the data analysis described in Ref. [43] and completing a similar task.

The following content of this chapter is organized as follows: in section 4.2, we discuss the dataset and illustrate the workflow of the soliton detector and its training process. Then in section 4.3, we discuss the quality of the labeled dataset and demonstrate the quantified performance of our system. Finally in section 4.4, we conclude and discuss possible future

directions.

4.2 Soliton detection and position system

Here we explain our automated approach to soliton recognition and localization in images of BECs. Our four-step approach, which is described in detail in later subsections and shown in figure 4.1, is outlined as follows.

Step 1: Measurement. From experimental measurements, the atomic density distribution is represented by three raw images that are merged to form one image of the atomic density distribution. The experimental design is discussed in depth in our article C.

Step 2: Data preprocessing. As shown in figure 4.1, the image frame is rotated with respect to the BEC cloud orientation, and the region of interest is focused on where atoms are confined, which is a tiny fraction of the complete series of images ($3\times648\times488$ pixels). The data is rotated and cropped accordingly before going through the classification stage to make the soliton pinpointing process without unnecessary information.

Step 3: Image classification. The pre-trained CNN classifier detects whether or not a single soliton can be found in a given picture using the input image. If this is the case, step four is carried out; otherwise, the analysis is terminated and yields no soliton or other excitation results based on CNN prediction.

Step 4: Soliton positioning. The soliton location with respect to the BEC center of images that contain only one soliton is computed using a least-squares fit based on a one-dimensional (1D) model function.

4.2.1 Data preprocessing

6257 images were collected for CNN training from several experiments conducted in a single lab over a two-month period. The raw images were captured using a 648×488 pixel

camera. And pixels in the horizontal and vertical directions are labeled with the letters i and j, respectively.

Absorption imaging is a technique that integrates three raw images into a single atomic density record. In the first image $I^{\mathrm{A}}_{i,j}$, the BEC is shined by a probe laser, and the resultant intensity measures the probe to the BEC's shadow. The second image $I^{\mathrm{P}}_{i,j}$ records only the pure probe intensity, and the third image $I^{\mathrm{BG}}_{i,j}$ is a dark frame that only contains any potential background signal with no probe lights. We extract the 2D column density

$$\sigma_0 n_{i,j} \approx -\ln\left[\frac{I^{\mathrm{A}}_{i,j} - I^{\mathrm{BG}}_{i,j}}{I^{\mathrm{P}}_{i,j} - I^{\mathrm{BG}}_{i,j}}\right] \tag{4.1}$$

from these three images, where the resonant cross-section $\sigma_0 = 3\lambda^2/(2\pi)$ is calculated from the wavelength λ of the probe laser. And we express density in terms of the dimensionless product $\sigma_0 n_{i,j}$ for our data. Figure 4.1 displays an example of the probe beam with atoms and the final density in the 'Raw data' and 'Step 3: Image classification' frames, respectively.

After examining all of our data, we found that the BEC only covers a minor portion of the image in our raw data, and that the long axis of the BEC is rotated by about 43 degrees with regard to the camera in our raw data. (Except for very few shots that failed to capture the BEC, which are removed from our dataset.) To facilitate CNN training, the images are rotated to align the BEC with the image frame and cropped to eliminate the significant part of the image that does not include information about the BEC. The BEC's location and form might alter across multiple realizations of the same experiment; thus, we use a fitting technique to identify the BEC's position and size.

Then, we fit all 2D images to depth-integrated 3D Thomas-Fermi distributions [172],

giving us the global 2D distribution of BEC:

$$n_{i,j}^{\mathrm{TF}} = n_0 \max\left\{\left[1-\left(\frac{i-i_0}{R_i}\right)^2-\left(\frac{j-j_0}{R_j}\right)^2\right],0\right\}^{3/2}+\delta n. \tag{4.2}$$

This function expresses the 3D BEC density distribution summed along the imaging axis. We use six parameters in this fit: the BEC center coordinates $[i_0, j_0]$; the peak density of BEC n_0; the Thomas-Fermi radii $[R_i, R_j]$; and an offset δn from subtle changes in probe intensity between images.

A successful fitting needs appropriate initial guesses for all fit parameters. The guesses for i_0 and j_0 were determined by summing the picture in the vertical and horizontal dimensions to create two 1D projections, from which we chose the average location of the five greatest values as our first estimations. We took the largest value in the image as the guess for n_0 and used $[R_i, R_j] = [66, 55]$ pixels, based on our estimation as the typical radii over the whole dataset. The guess for the offset δn is zero. The results of these fits are included in our released dataset.

We determined the 164×132 pixel of the cropping region by examining the radii $[R_i, R_j] = [66(5), 58(3)]$ obtained from fits to 6257 images. We then centered the cropping region at $[i_0, j_0]$ as determined from the fits of each image separately. The process was validated on an additional 10^4 images that are not captured but included in this release. Dark solitons show as vertically aligned density depletions in the preprocessed images, and they could be distinguished by their appearance (see the top-left panel in figure4.2(b)).

4.2.2 Labeling

Three independent human labelers participate in categorizing the preprocessed data, classifying the images into three categories: “no soliton”, “single soliton”, and “other excitations”. The “no soliton” class includes images that unambiguously show no solitons; the

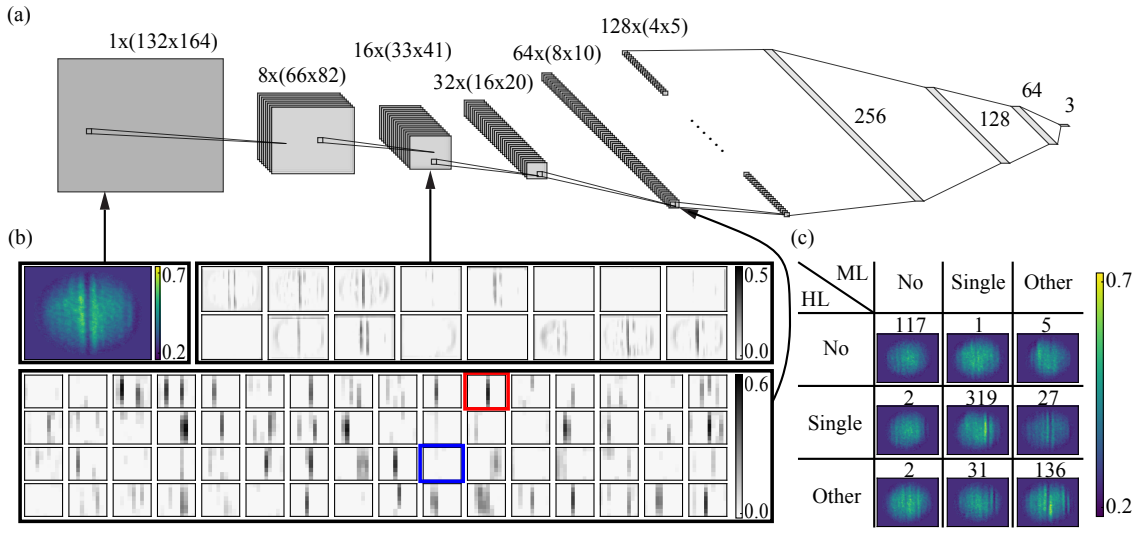

Figure 4.2: (a) CNN classifier structure. The first rectangular-shaped component represents a preprocessed input image. The left-most five architecture sets of rectangular-shaped components represent convolutional layers with their filter number and image size specified, each followed by a ReLU activation function and a max-pooling layer. The following three line-shaped components represent fully connected layers with specified neuron numbers, each followed by a ReLU activation function and a dropout layer. The last component represents a dense output layer with a softmax activation function. (b) Visualization of the input image, second, and fourth max-pooling layers for a correctly classified single soliton image. The top left panel shows the input image, the 16 images in the top right panel show the output of the second max-pooling layer, and 64 images in the bottom panel show the output of the fourth max-pooling layer. The red boxed output indicates one of the filters that capture the single soliton feature. The blue boxed filter would be activated if more than one soliton is present (see figure 4.3 for no soliton and other excitation case). (c) Confusion matrix of the classification result of test dataset, comparing between human allocated labels (HL) and ML classifier prediction (ML). The images show sample data for correct (diagonal) and misclassified (off-diagonal) cases. The numbers above show the number of images associated with a certain circumstance.

"single soliton" class depicts images with one and only one soliton; and "other excitations' class covers all other image that can neither be described as 'no soliton' nor 'single soliton.' A separate "two soliton" class is not included in our presentation since the limited number of images with two solitons may result in inadequate training.

Due to human capacity and limited focus span, we separate the labeling process into eight batches, with the size of each batch determined by how long each labeler was able to maintain their focus. Once we finish the labeling process of a batch of images, we compare the three resultant labels and save only images in the total agreement. The overall labeling agreement ratio was 87 % (table 4.1 shows a comparison of the labeling agreement scenarios across all three classes), consistent across all batches. The remaining images are further investigated and debated until a final agreement is achieved. The distribution of

Table 4.1: Human labeling result. The first two columns (Full) indicate image counts and percentages of each class. The last two columns (3-agree) compare the tallies and ratio in all data per class for the images with labels that human labelers initially agreed on.

Dataset	Full		3-agree	
Class	Count	Percentage [%]	Count	Agreement ratio [%]
No soliton	1 237	19.8	1 184	95.7
Single soliton	3 468	55.4	3 077	88.7
Other excitations	1 552	24.8	1 184	76.3
Total	6 257	100.0	5 445	87.0

images among classes is as follows: 19.8 % in no soliton class, 55.4 % in single soliton class, and 24.8 % in other excitations class. Figure 4.2(c) shows representative labeled images from each class. This labeled dataset was used to train the CNN classifier and assess the accuracy and reliability of the classifier and positioning protocol.

4.2.3 Image classification

We design our CNN classifier based on the input image size (164×132) and the number of possible output labels (3), shown in figure 4.2(a). This CNN consists of five convolutional layers and four fully connected layers. Each convolutional layer is followed by a rectified linear unit (ReLU) activation function defined as $f(x) = \max(0,x)$, then a max-pooling layer, which down-samples the input ($km \times ln$) array, partitiones into a set of non-overlapping rectangles of equal ($k \times l$) size, into a smaller ($m \times n$) array with entries representing the maximum value of the corresponding sub-region. The final max-pooling layer is flattened and fully connected to a complete neural network with three dense layers (256, 128, and 64 neurons, respectively) and then an output layer (three neurons), all fully connected to the subsequent layers. All dense layers are followed by ReLU activation functions and dropout layers that randomly eradicate neural connections with a possibility of 0.5 during the training phase to regulate and facilitate overfitting. Finally, the output vector $\vec{\xi} = (\xi_1, \xi_2, \xi_3)$ is normalized by the softmax activation function, giving the output

Table 4.2: Classification performance summary for training with the full training dataset with performance measured using cross-validation (first column), testing on the full test dataset (second column), and testing on a subset of the test dataset that labelers initially agreed on (last column).

	Cross-validation	Full test set	Labelers initially agreed subset
Accuracy [%]	89.6(5)	89.4	91.6
Weighted F1	0.896(6)	0.894	0.916
No soliton F1	0.938(10)	0.959	0.983
Single soliton F1	0.920(4)	0.913	0.935
Other excitations F1	0.806(6)	0.807	0.782

predictions $P_m(\vec{\xi}) = \exp(\xi_m)/\sum_n \exp(\xi_n)$.

We split the labeled dataset into two subsets, with 640 images (10.2 % of the dataset) being put aside as the test dataset, and the remaining 5 617 images (89.8 %) are utilized for training throughout the model architecture construction process.

Considering that our training dataset's unbalanced, i.e., different classes contain dramatically varying numbers of images, we use an augmentation approach to balance the dataset. We implement our augmentations with three physically acceptable transformations: horizontal and vertical reflections and a 180-degree rotation. All three transformations were performed to the no soliton and other excitations classes, resulting in a four-fold increase in the size of these classes. We applied one randomly determined transformation per picture for the single soliton class, thereby doubling the amount of data for this class. After augmentations, the number of data within the three classes has a $0.28 : 0.38 : 0.34$ fractional distribution.

To model a slight rotation angle that may exist in different realizations, we rotate images by a random angle in the range ± 1 degree every time they are used during the training process.

The classifier learns to distinguish between the BEC and the background during the first few training attempts. Therefore, we applied an elliptical mask with radii $[R_i, R_j]$ to each image, removing any technical noise outside of the BEC to speed up the training process. In the end, we preconditioned the data by uniformly scaling the image values to the $[0, 1]$

range to make them appropriate for CNN input.

Since our testing dataset is not augmented and remains unbalanced, we evaluate the performance of trained CNN models using the weighted F1 score [173]. When two models have comparable weighted F1 scores, we first compare their accuracies as a tie-breaker, and if accuracies are also a tie, we use the F1 score of the single soliton class to pick a winner. Here we use the F1 score of the single soliton class to resolve any remaining ties since we will be comparing to single-soliton dynamics data in the next sections 4.3.1.

To identify the best-performing model, we conducted a semi-structured search over the model parameter space. We employed k-fold cross-validation to determine the generalizability of trained models throughout this phase. The training set was divided into $k = 5$ smaller sets ('folds') for each set of hyperparameters defining the CNN model, four sets of which were used for training and one for validation. After training the model with all five cross-validation combinations, the mean score was calculated and compared to scores obtained from networks with previous hyperparameters settings. We prioritize the following parameters: the number of filters in each convolutional layer, the number of dense layer neurons, the optimizer, the kernel sizes of the convolution layers, the dropout rate, and the batch size. The parameters are optimized in this order, and the tuning history is given in table 4.3. Once we had chosen the best-performing model, we utilized 95 percent of the training set randomly picked for the final training. As our final trained model, we used the model that is halted before five consecutive non-improving epochs.

Figure 4.2(b) depicts typical intermediate convolutional layers of the trained model, using an input that can be successfully categorized as a single soliton by the CNN classifier. We see that certain filters, such as the one highlighted with a red box, can effectively capture the information contained for a single soliton. By contrast, the identical intermediate layers are shown in figure 4.3(a) and (b) for the correctly classified sample images from the no soliton and other excitations classes, respectively. In both cases, we emphasize two filters:

Table 4.3: Tuning history of model parameters. We present the number of filters used in all convolutional layers (Filters), the number of nodes in fully connected layers (Dense), the kernel sizes in all convolutional layers (K), the dropout rate (D), the batch size (B), and the optimizer used in training (SGD: Stochastic gradient descent, SGD+M: SGD with moment, SGD+M+D: SGD+M with decay). On the training set, the mean performance is averaged using five-fold cross-validation. The F1 score is weighted according to three categories. The best model is highlighted in grey. Parameters that change at each iteration is emphasized in italic.

Filters	Dense	K	D	B	Optimizer	Weighted F1 [%]	Accuracy [%]	Binary F1 [%]
8×8×8	256×128	5	0.5	32	Adam	65(23)	74(15)	71(18)
8×*16*×*32*	256×128	5	0.5	32	Adam	56(23)	61(25)	63(19)
8×16×32×*64*	256×128	5	0.5	32	Adam	67(24)	75(16)	72(20)
8×16×32×64×*128*	256×128	5	0.5	32	Adam	78(20)	82(14)	81(16)
8×16×32×64×128	256×128×*64*	5	0.5	32	Adam	48(20)	62(13)	56(16)
8×16×32×64×128	256×64	5	0.5	32	Adam	58(25)	69(17)	65(20)
8×16×32×64×128	256×64×*16*	5	0.5	32	Adam	61(19)	75(16)	69(17)
8×16×32×64×128	*512×128*	5	0.5	32	Adam	47(20)	54(22)	56(16)
8×16×32×64×128	512×128×*32*	5	0.5	32	Adam	67(24)	76(16)	72(20)
8×16×32×64×128	256×128×64	5	0.5	32	*Adamax*	86(6)	89(1)	88(3)
8×16×32×64×128	256×128×64	5	0.5	32	*SGD*	70(6)	87(2)	76(4)
8×16×32×64×128	256×128×64	5	0.5	32	*SGD+M*	64(22)	74(15)	70(18)
8×16×32×64×128	256×128×64	5	0.5	32	*SGD+M+D*	39(4)	60(9)	49(2)
8×16×32×64×128	256×128×64	5	*0.6*	32	Adamax	77(5)	90(0)	85(3)
8×16×32×64×128	256×128×64	5	*0.7*	32	Adamax	51(17)	68(15)	61(16)
8×16×32×64×128	256×128×64	5	*0.8*	32	Adamax	44(13)	62(13)	54(12)
8×16×32×64×128	256×128×64	*3*	0.5	32	Adamax	86(1)	90(1)	88(1)
8×16×32×64×128	256×128×64	*7*	0.5	32	Adamax	88(1)	89(1)	90(1)
8×16×32×64×128	256×128×64	*9*	0.5	32	Adamax	89(0)	89(0)	90(0)
8×16×32×64×128	256×128×64	*11*	0.5	32	Adamax	78(20)	82(14)	82(17)
8×16×32×64×128	256×128×64	9	0.5	*16*	Adamax	79(21)	83(13)	82(17)
8×16×32×64×128	256×128×64	9	0.5	*8*	Adamax	78(20)	82(13)	81(17)

the red box indicates a filter activated by images with a single soliton, while the blue box indicates a filter activated by images from the other excitation class. Neither highlighted filter is active for a picture belonging to the no soliton class. This result demonstrates that our model has been adequately trained to recognize and find distinctive characteristics of each class in an unforeseen image.

Figure 4.2(c) and the second column of table 4.2 show the prediction results of our final trained soliton CNN classifier. In conclusion, our model achieves weighted $F_1 \approx 0.9$ and accuracy $\approx 90\,\%$, in excess of the $87.0\,\%$ human labeler agreement ratio. The predominant classifier errors happen between images from single soliton and other excitations class: 6.9 % of single soliton images is wrongly allocated to the other classes ($P_1 < 0.2$), and 4.3 % has no clear assignment ($0.2 \leq P_1 < 0.8$).

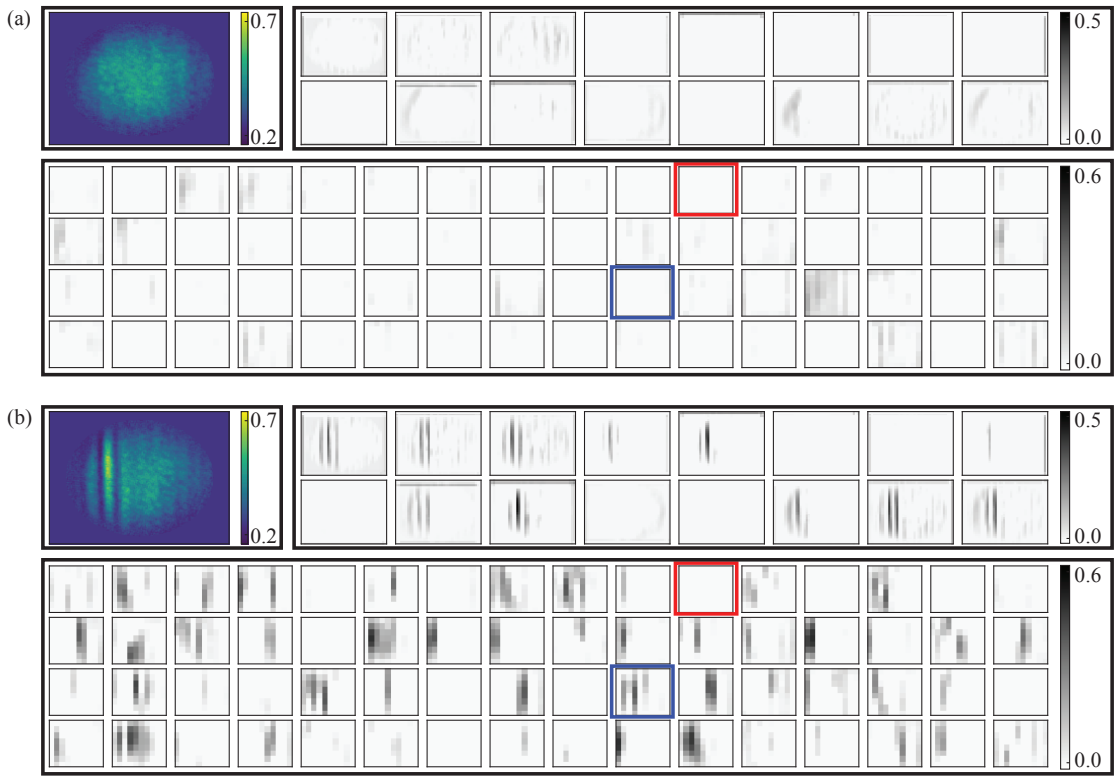

Figure 4.3: Visualization of the activation of the input, second, and fourth max-pooling layers for a correctly categorized image from (a) no soliton and (b) other excitations class. In both figures, the top left panels depict the input images, while the top right panels depict the 16 output images of the max-pooling layer. The bottom panels depict the 64 output images of the fourth max-pooling layer. The red box denotes one of the filters learned to capture the single soliton feature in figure 4.2(b). If an image from "other excitation" is present, the blue boxed filter is likely activated.

Figure 4.4(b) demonstrates that the classifier performs well for both the no soliton and single soliton classes in this case. The classifier functions with better results tested against human-initially-agreed data than when tested against human-initially-disagreed data, indicating that specific images that have been disagreed upon may be confusing (see also the last column in table 4.2 for more information). In addition, we detect an abnormally high misclassification rate for human accepted data in the other excitations class, which we attribute to the human labelers' adoption of this class when confronted with a difficult choice between two options. Figure 4.4(a) also shows that the incorrectly categorized data is clustered around the corners of the figure, indicating a high degree of confidence in that error.

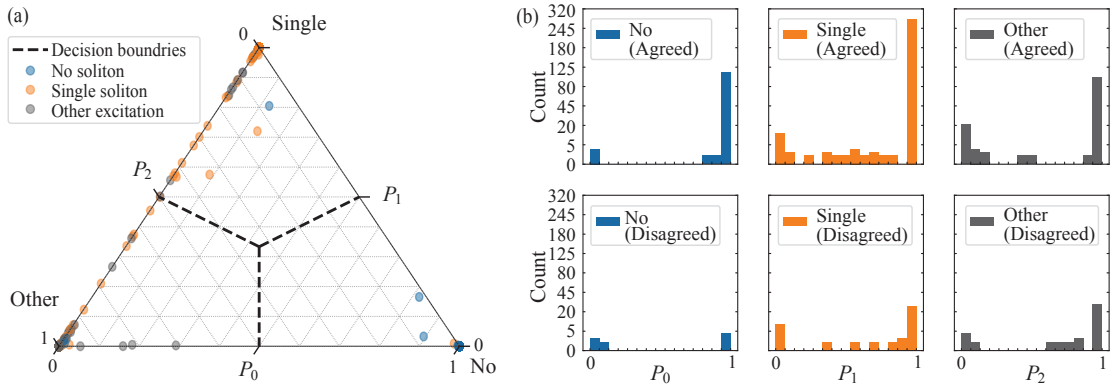

Figure 4.4: Soliton data classification results. (a) Distribution of CNN output for test data, colored by human labels. The scattered dots with various labels overlay each other in random order. (b) Histogrammed probabilities. The upper panels histogram the classifier outputs from human-initially-agreed data, while the lower panels histogram those from human-initially-disagreed data. The vertical axes are depicted in square root scales to highlight the small amount of misclassified data.

4.3 Results

4.3.1 Soliton detector

To evaluate the performance of the fully automated soliton detection and positioning system, we use two sets of images containing oscillating dark solitons, which comprise the data published in figure 2 of Ref. [43] and are presented in figure 4.5. They were launched using standard and improved protocols, with 60 and 59 images, respectively.

In the first test, we employ the improved-protocol data-set, with typical summed data n_i shown in the top panel from figure 4.5(a). As the solitons in these images are very apparent, we believe the CNN will simply categorize them. Out of 59 images, 52 are labeled as a single soliton, while the remaining seven images are classified as different excitations, according to one human labeler. Single solitons are then pinpointed by the position regressor (described in Section 2.5 of Appendix C). The middle and bottom rows in figure 4.5(a) depict the soliton positions changing with time from manual and CNN identification, respectively. We fit $i(t) = A\sin(\omega t + \Phi) + i_0$ to the soliton positions, and we compare the fitting parameters from those acquired by our automated protocol and the

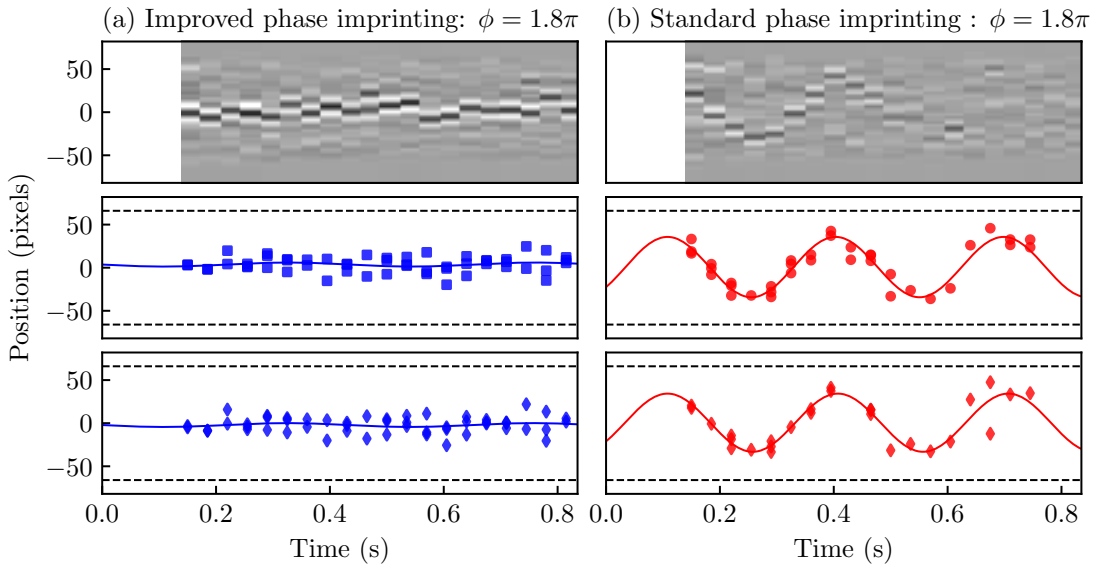

Figure 4.5: Oscillation of dark solitons constructed by applying $1.8(1)\pi$ phase employing the (a) improved and (b) standard protocol described in [43]. The top panels exhibit samples for the residuals Δ_i, obtained after removing the fit from the 1D profile. The middle and bottom panels show the soliton positions and sinusoidal fits based on human identification and the outputs of our automated protocol, respectively. Dashed lines at $j = \pm 66$ pixels in all four panels illustrate the boundaries of BECs.

earlier manual method. As can be noticed by comparing the middle and bottom panels of figure 4.5(a), the results of the automated technique are practically indistinguishable from the human inspections. The physical parameters from the CNN classifier ($A = 2(2)$ pixels and $\omega/2\pi = 2.3(7)$ Hz) are within one standard deviation of those acquired from manual identification ($A = 2(2)$ pixels and $\omega/2\pi = 2.3(6)$ Hz).

In the second test, we employ images containing solitons created by the conventional phase imprinting process. As remarked in the top panel of figure 4.5(b), solitons in these images are shallower compared to those in figure 4.5(a), causing them potentially more challenging to distinguish from the no soliton and other excitations classes. Out of 60 images in this test, 22 are predicted by the CNN as no soliton, and 11 as other excitations. The remaining 27 are categorized as a single soliton and forwarded to the position regressor. The lower panels in figure 4.5(b) show soliton position as a function of evolution time, obtained from manual [43] and CNN identification, respectively. Since [43] examined the

soliton oscillation amplitude resulting from the two imprinting techniques, the authors did not restrict themselves to images with a single soliton. Instead, when more than one soliton is generated, the authors recognized all the solitons but monitored just those connected with a given trajectory. Our CNN classifier is trained to select images with single soliton excitations. Therefore, the middle panel in figure 4.5(b) includes 12 additional observations than the bottom panel. Even with fewer data points, however, the fitting parameters from the CNN classifier ($A = 34(3)$ pixels and $\omega/2\pi = 3.34(9)$ Hz) are within one standard deviation of those obtained for human identification ($A = 35(2)$ pixels and $\omega/2\pi = 3.39(5)$ Hz).

The whole analysis resulting in both oscillation charts took under 148 seconds per series on a 2014 MacBook Pro. The estimated performance relevant for in-situ operation is 2.4 seconds per image, a relatively tiny overhead on top of the measurement time (around 12 seconds). In many circumstances, however, the analysis of an image would take place with the capture of the following image.

4.3.2 Soliton dataset

As with most ML topics, the availability of the training data is critical for the excellent performance of the trained classifier. Therefore, we further published our labeled soliton dataset used in this analysis along with our protocol.

Three labelers independently labeled the whole dataset to confirm the trustworthiness of our assigned labels, as detailed in section 4.2.1. Our whole soliton image collection consists of 6 257 labeled images. The dataset comprises 1 237, 3 468, and 1 552 images for no soliton, single soliton, and other excitations classes.

While most of the images the assigned labels were consistent amongst labelers, there are some images that at least one labeler disagreed with others. These images are fur-

ther discussed until an agreement is achieved. As can be observed in table 4.1, the most problematic case is to judge between images from the single soliton and other excitations classes. This is likely caused by the phase imprinting approach used to imprint solitons may also cause other excitations that show as density fluctuation or fringes in the BEC. Examples of such fluctuation may be observed in the off-diagonal images in figure 4.2(c). Additional explanation of the misclassified and mislabeled data can be found in Appendix A.3. of our publication C.

Our dataset comprises the full-frame raw images, the cropped and rotated images as utilized in this work, as well as the set of the fitted integrated 2D Thomas-Fermi distribution parameters. This dataset is adequate to reproduce our findings but also to evaluate fitted alternative models with different cropping sizes or image resolutions [22].

4.4 Discussion and conclusion

In this chapter, we offer an automated dark soliton identification and positioning system that combines ML-based image classification with traditional fitting approaches to track soliton dynamics in experimental images of BECs. We demonstrate that this system works on par with more conventional techniques that depend on human input for soliton identification, offering the potential to analyze soliton dynamics in big datasets. We also make public the first dataset collecting images from a dark soliton BEC experiment, which allows the data science community to create more advanced analytic tools and to comprehend nonlinear many-body physics better.

The performance of the classifier, as assessed by the weighted F1 score, leaves space for improvement. While adjusting the hyperparameters helped greatly enhance the initial performance, more data is essential to push this boundary. However, human labeling is not only labor-intensive but, as the examination of the misclassified image graphs demon-

strated, is also not always reliable. Our system provides a necessary tool to automatically expand the dataset's size. Such an enlarged dataset, in turn, will enable refining the soliton classifier and performing model uncertainty quantification [174, 175], which currently is not accounted for. Together, these refinements may enable reliable in-situ deployment.

This investigation was preconditioned on the assumption of a certain structure in the data, resulting in our three classifications. Therefore, other approaches, such as active learning ML [176], may be more suitable for this task. An enlarged dataset may also permit unsupervised learning algorithms [177] to perhaps uncover more categories within the data without presumptions. This unsupervised learning of soliton data might be a prototype for ML-based discovery using cold-atom data.

Chapter 5: Combining machine learning with physics: A framework for tracking and sorting multiple dark solitons

Cold atom imaging data may suffer information losses due to the inadequacies of the measurement and preparation processes, including not limited to phase imprinting, time-of-flight, and interferometry. Therefore, our simulation approaches may fail to attempt to comprehend them. In this case, we face a challenge to develop more sophisticated data analysis methods for investigating complex processes that may involve dynamics and interactions among excitations.

In this chapter, we integrate ML models with physics-based heuristics to identify multiple solitons from absorption images of BEC and automate the image analysis process. First, we improve from our previous result (Chapter 4) and develop a CNN-based object detector to locate the solitonic excitations. Then we design physics-informed models for extracting physical characteristics and categorizing each solitonic feature into one of three more refined categories: kink soliton, solitonic vortex, or "partial" soliton. In addition, we provide an open-source Python package to implement solitonic excitation detection protocol from both the pre-trained model using our data and any user-defined cold atom absorption image data.

5.1 Introduction

In the context of quantum technologies, machine learning (ML) methods improved data analysis as well as more resilient performance. Research has shown that technologies have progressed in the following areas: automated detection of states, excitations, and phases [178–182], automated parameter space search and optimization [30, 31, 183–186]; automated quantum control [187, 188], phase transition classification and interpolation [153, 189, 190], simulation acceleration [191], quantum noise characterization [192], and quantum tomography [193–195]. Taken together, these findings demonstrate how ML algorithms can detect and categorize ambiguous data, exploring huge parameter spaces effectively, and discovering optimum solutions.

On the other hand, physics-based heuristics and classic statistical procedures have been vastly implemented in the research of quantum technologies [25, 196, 197]. Compared to ML techniques, which sometimes function as "black boxes," traditional fitting tools provide human-appreciable standards. In addition, ML methods may encounter overfitting problems that limit their usage to data similar to the training dataset. Overfitting often happens when the number of fit parameters exceeds the number of independent data points in a given sample size calculation. Compared to ML models, statistical tools use a substantially lower number of fitting parameters, making them more resilient to overfitting and reliable on data with diverse features. We suspect a good technique for scientific research may combine both ML and traditional methods since they could benefit the results in different ways.

Our goal in this chapter is to provide a hybrid two-module feature identification framework that brings together the flexibility of ML with the interpretability and resilience of traditional fitting methods. Research has proven the effectiveness of such hybrid methods in a variety of subjects, including landslide prediction [198], medical image processing [199],

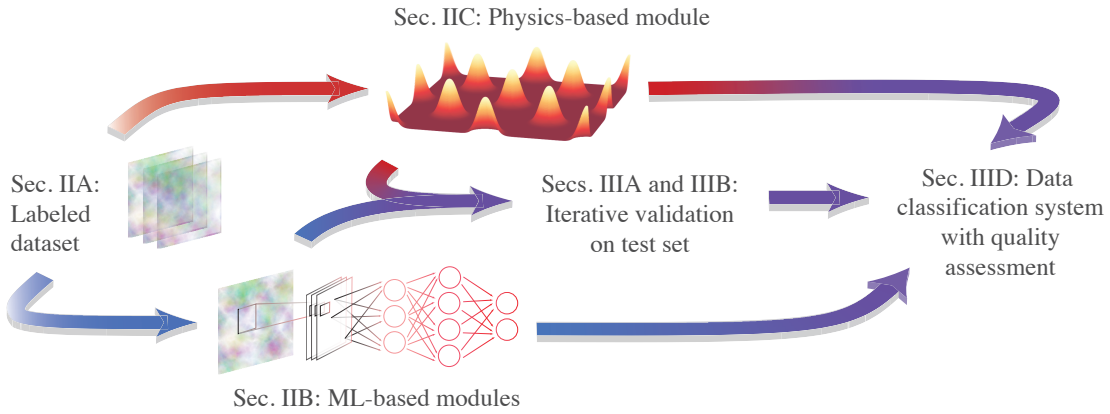

Figure 5.1: Framework overview. The colored arrows link the preparation (Secs. 5.2.1, 5.2.2, and 5.2.3), validation (Secs. 5.3.1), and implementation (Sec. 5.4.1) phases of this framework. The red path indicates the preparation and application of the physics-based approximation module of the framework. The blue path indicates the ML modules.

and cyber-attack detection [200].

As shown in Figure 5.1, our framework starts with a labeled dataset, which enables training the ML module and configuring the physics-based module. We then independently develop each module iteratively to enhance the performance and check the data quality by cross-validating two modules. Finally, we combine the modules into a single system as the new predicting tool for any unforeseen data.

A notable example of experimental physics that can benefit from this framework is laser-cooled BEC. BEC is an excellent platform for researching quantum physics that covers a wide range of applications, from achieving collective many-body physics [52] to developing accurate atomic clocks [201]. However, some techniques for preparing and measuring these systems, such as phase imprinting [197] and time-of-flight expansions [202], might cause information loss in the measured image data. Therefore, these data provide an excellent test-bed to challenge our hybrid framework.

Within the scope of the BEC study, we are particularly interested in the problem of identifying dark kink solitons (or referred to as dark solitons interchangeably), which are spatially localized excitations that present as depletions in atomic density traversing through BECs [197, 203, 204]. Using our established dark soliton dataset [22, 182] (sample data

shown in Figure 5.2). We aim to extract high-quality solitons from an existing dataset, regardless of the background noise and the number of solitons within each image.

The dark solitons in BECs appear as vertical density depletions in time-of-flight images [top image in Figure 5.2 (b)(i)]. Depending on the technique we used to induce them, dark solitons may be placed in between two shoulder-like density peaks [see the bottom plot in Figure 5.2 (b)(i)]. In our experiments, dark solitons are expected to oscillate in the horizontal direction or remain stationary, preserving their shape as they travel. Preparation of solitons can be delicate and may yield various forms of solitonic excitations, such as solitonic vortices [205], and bring additional chains of wiggles onto the cloud. As a result, spatial characteristics of dark solitons in these images are hard to determine, especially when multiple solitons exist. In order to better understand the conditions to excite solitonic excitations and to study their dynamics and interactions, both automated detection protocol and quantitative analysis are necessary.

Using our framework, we develop a protocol that can serve both needs. As the first component of our framework, our ML module leverages existing computer vision algorithms to locate features. The objectives of computer vision include image classification [64], both supervised and unsupervised, object detection [206] and semantic segmentation [207], synthetic image generation [208]. One of the most successful computer vision algorithms is CNN, which has been shown to perform remarkably well on most of the tasks listed above. Improving from our previous work described in Chapter 4, we employ a CNN-based object detector (OD) to go beyond simple classification and provide the location of all solitonic excitations in a given image. In addition to our ML module, our physics-based modules utilize traditional fitting methods to quantitatively describe the characters of dark solitons and to differentiate types of solitonic excitations.

There are three main advantages to using this hybrid protocol. First, though our hybrid framework is developed primarily from a training dataset whose images had either zero

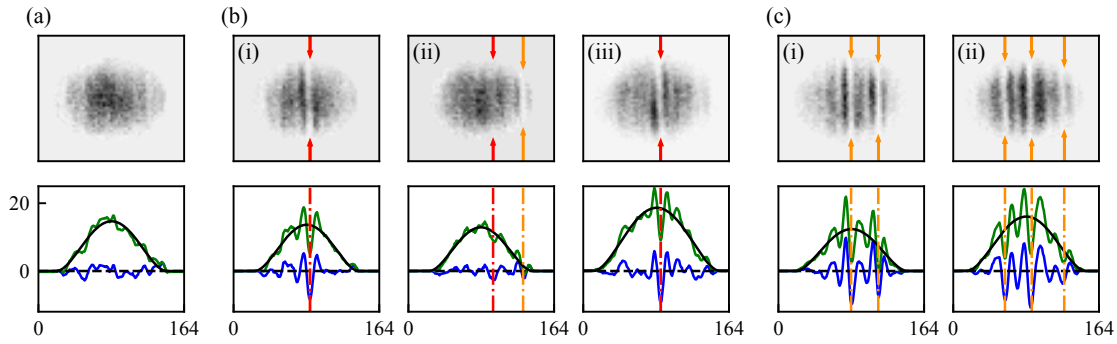

Figure 5.2: Representative data from labeled dataset. The top panels illustrate pre-processed images from our dataset, while the bottom panels illustrate harizontal profiles of the entire image (green), TF fits (black), and the density fluctuations (blue). The red lines and arrows denote the location of the deepest depletion in the density fluctuations, and the orange lines and arrows indicate the sites of the solitons discovered in our OD. (a) An image in the no excitation class. (b) Three images from the single excitation class: (i) a single kink soliton, (ii) an off-centered kink soliton, and (iii) a solitonic vortex. (c) Two images from the other excitations class.

or one soliton, it can perform well on more complex data comprising multiple excitations. Second, detailed examinations of the coefficients from the physics-based module enables us to differentiate between certain solitonic excitations and others (kink and solitonic vortex [203–205, 209]). Third, integrating findings from the ML and physics modules enabled us to automatically generate an enlarged, reliable dataset, including details such as the soliton locations and the types and qualities of detected solitons. This dataset is described in detail in Ref. [23] and is available for download from the NIST data repository [22].

The remainder of this chapter is structured as follows: Sec. 5.2 introduces the dataset, both modules, and describes their training and initialization. Sec. 5.3 describes the validations of both modules. In Sec. 5.4, we describe the open-source Python package that implement our protocol: SolDet [24], and its performance on new data that may include multiple solitonic excitations. Lastly, in Sec. 5.5 we conclude and discuss possible future directions.

5.2 Data and modules

In addition to traditional physics-based methods, it has been proved that solitonic excitations can also be discovered and described using ML approaches [179, 182, 210]. Our framework leverage a curated dark soliton dataset (section 5.2.1), and uses an OD (section 5.2.2) to provide an initial estimate of the positions of all solitonic excitations, and then uses a skewed Mexican hat fit function (section 5.2.3) to accurately describe the density profiles of all solitonic excitations.

5.2.1 Data

To initialize the proposed framework, we draw on a collection of about 5,400 experimental images of BECs with and without solitonic excitations that are curated from our previous dataset. The details for data collection and curation are described in Ref. [23].

Figure 5.2 shows a selection of six images from the labeled dataset taken from the labeled dataset. The dataset includes labels for three classes of images: "no excitation," which are images that do not contain any excitations; "single excitation," which are images that contain one solitonic excitation; and "other excitations," which are images that do not fall into any of the preceding classes but contain excitations (including those with multiple solitonic excitations, high degrees of noise, and those human labelers could not agree upon). Additionally, the dataset contains information about the human-examined horizontal location of excitations within the single excitation class.

Specifically, figure 5.2(a) shows an image from the no excitation class, which does not have the prominent stripes. In figure 5.2(b), we show three cases of the single excitation class, each of which has a single dark vertical fringe: (b-i) an iconic dark kink soliton; (b-ii) an off-center single kink soliton; and (b-iii) a solitonic vortex. In figure 5.2(c), we show three elements of the single excitation class, each of which has a single dark vertical fringe

(see section 5.2.3). Two members of the other excitations class, each bearing more than one dark vertical fringe, are shown in (c).

5.2.2 ML module: Object detector

In chapter 4 we developed a dark soliton detection and location system based on the CNN [182]. The proposed system may assess the atom cloud into three possible classes. However, the ML part does not provide any information about the excitation locations. Instead, the positioning stage uses the deepest depletion location throughout the image to initialize a least-square fit based on a 1D model function to achieve the best result. In Figure 5.2 (b), we present three examples of how to implement this locating method: The 1D profile is initially created by summing along the vertical axis (green lines), then the background is eliminated (blue lines) using the Thomas Fermi fit (solid black lines), then the soliton is found at the deepest depletions (red dashed lines and arrows).

There are two drawbacks to using this algorithm: (1) it is possible that the soliton does not represent the deepest depletion for all human-labeled single soliton images (as in Fig. 5.2(b-ii)), and (2) we add a bias for depletions at different points of the atom clouds as we remove the atom backdrop as we remove the atom background (as in Fig. 5.2(c)).

Inspired by the detection of vortices in BECs [179], we develop an object detection (OD) neural network. The OD enhances the performance of the CNN classifier in two ways: (1) it identifies soliton positions rather than classifying images into three classes; and (2) even though trained with single-soliton data, OD is capable of locating multiple excitations in the same image.

OD consists of only six convolution layers and four max-pooling layers, with no fully connected layers. Such that the OD has 70 times fewer trainable parameters than the CNN classifier (7×10^4 versus $\sim 10^6$ parameters), as the fully connected layers contain many

parameters. OD also uses less training data than the CNN classifier. As a result, OD is significantly more cost-efficient for training and predicting.

In the OD process, each image (164×132 pixels) is divided into 41 vertical cells (4×132 pixels each). Here we choose a cell size of 4 pixels for each of the output cells since the width of the soliton is approximately 3-5 pixels. This ensures that each output describes at most one soliton, and no cell contains more than one distinct solitonic excitation at a time. The OD produces two vectors of length $L = 41$ as the output $\widetilde{\mathbf{Y}}$, each element in the vector is the range $\in [0,1]$. Each cell's predicted probability of containing a soliton is described by the first vector $\widetilde{Y}_{\ell,1}$, and the second vector $\widetilde{Y}_{\ell,2}$ describes the normalized relative position of the soliton center within that cell, where 0 or 1 correspond to the left or right edge of the cell, respectively. OD considers any cell with $\widetilde{Y}_{\ell,1}$ more than 0.5 as holding an excitation, and it calculates the location of the excitation from $\widetilde{Y}_{\ell,2}$. And if $\widetilde{Y}_{\ell,1}$ is less than 0.5, it ignores $\widetilde{Y}_{\ell,2}$.

To facilitate the training process and to compare the OD predictions with the labels of training data represented by Y, we utilize the cost function

$$F = \sum_{\ell=1}^{41} \begin{cases} -w_1 \log(\widetilde{Y}_{\ell,1}) + w_2 (Y_{\ell,2} - \widetilde{Y}_{\ell,2})^2, & \text{if } \mathrm{Y}_{\ell,1} = 1 \\ -\log(1 - \widetilde{Y}_{\ell,1}), & \text{if } \mathrm{Y}_{\ell,1} = 0 \end{cases} \tag{5.1}$$

for each training data, where the label $Y_{\ell,1}$ identifies the existence of excitation in a cell with 100% confidence, i.e., 0 or 1. The coefficients w_1, w_2 are hyper-parameters that control each term's relative significance.

When the OD misidentifies solitons, the log terms raise the cost function, whereas the quadratic term contributes when a soliton is mislocated inside a cell. Because our training set only contains images with one soliton, cells with $Y_{\ell,1} = 1$ are considerably less common than cells with $Y_{\ell,1} = 0$. As a consequence, we use $w_1, w_2 = 10$ to assure the three terms

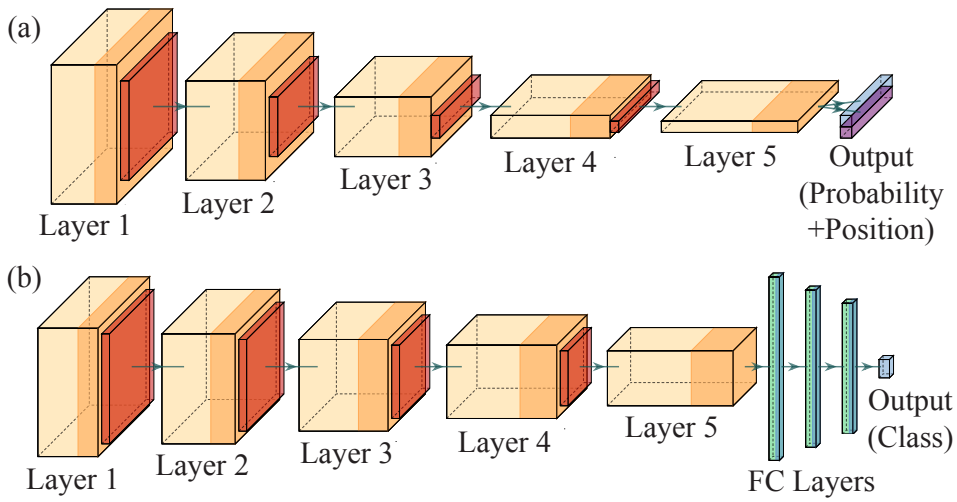

Figure 5.3: Architecture llustrations of (a) OD and (b) CNN classifier. Yellow-orange boxes indicate convolutional layers, orange-red boxes indicate max-pooling layers, the horizontal lengths of the boxes indicate the number of filters, and the remaining two dimensions indicate the image sizes. The blue and purple horizontal rectangles in (a) represent the output vectors. And the vertical blue-green rectangles in (b) represent three fully connected layers and the output layer. The lengths of edges are logarithmically scaled.

in equation 5.1 have comparable weights. In each training iteration, we update the OD outcome $\widetilde{\mathbf{Y}}$ by minimizing the cost function summed across all training images.

A single soliton may sit on the boundary between two cells and span over them since the cell size is comparable to the soliton size. To avoid double-counting, when two excitations in neighboring cells are detected, they will be merged into one, and the position is taken as the average of previous ones. If our training data has a soliton position similar to the predicted one, we consider the OD's detection successful (within 3 pixels in our implementation). And ailing to detect a labeled solitonic excitation and reporting an excitation that is not there are the two possible failure modes.

Same as the CNN classifier, OD is built and trained using the TensorFlow (v.2.5.0) Keras Python API [211]. Fig. 5.3(a) and (b) show the visualization of the network architecture for the OD and the CNN classifier, respectively. The model parameters of OD are presented in Tab. 5.1. The model parameters for the CNN classifier are presented in Ref. [182]. As seen in Fig. 5.3, there are three main differences between the two architec-

Table 5.1: The OD architecture parameters. Middle rows are for the convolutional layers and bottom rows are for max-pooling layers.

Layer	1	2	3	4	5	output
Filter	8	16	32	64	128	2
Kernel	5×5	5×5	5×5	1×5	1×5	1×5
Padding	same	same	same	same	same	same
Activation	ReLu	ReLu	ReLu	ReLu	ReLu	sigmoid
Pool size	4×2	4×2	4×1	2×1	N/A	N/A
Strides	4×2	4×2	4×1	2×1	N/A	N/A
Padding	valid	valid	same	same	N/A	N/A

tures: (1) the OD outputs 41 local probabilities and positions while the CNN classifier only outputs 1 of 3 possible classes; (2) the CNN classifier contains three fully-connected layers, which dramatically increase the number of trainable parameters, while OD does not; (3) the OD has asymmetric pool size and strides for vertical and horizontal directions, which are customized to the features in our dataset; the pool size and strides are symmetric for the CNN classifier. As a result, the OD has more than an order of magnitude fewer trainable parameters (7×10^4) than the CNN classifier (10^6).

5.2.3 Physics-based module: Quality estimator

In this subsection, we describe our physics-based module, which employs a confined least-squares fitting to estimate soliton parameters and generates a quality estimate indicating the likelihood that a given feature is a dark soliton.

First, we obtain the horizontal 1-D profile of fluctuation on an atom cloud (blue curves in the bottom row of Fig. 5.2): To compress 2D images to 1D, we first sum the pixel values vertically (green curves). Then, we fit the summed 1D distribution to a Thomas-Fermi (TF) model modeled as

$$n^{\mathrm{TF}}(i) \;\; = n_0 \max\left\{\left[1-\left(\tfrac{i-i_0}{R_0}\right)^2\right], 0\right\}^2 + \delta_n, \tag{5.2}$$

where i is the horizontal pixel index, and n_0, i_0, R_0, and δ_n are fitting parameters representing peak density, center position, TF radius, and an overall offset, respectively. The fit (represented by the black curves) acts as a cloud background from which we removed the 1D profiles, leaving behind the 1D density fluctuations (blue curves). Within the 1D fluctuations, the deepest depletion in single soliton data is shown by the red dashed lines.

We fit the Ricker wavelet [212], i.e., an inverted "Mexican hat" function

$$f(i) = \quad \delta_n - \; n^{\mathrm{TF}}(i_c) A \exp\left[-\tfrac{1}{2}\left(\tfrac{i-i_c}{\sigma}\right)^2\right] \times \left[1 - a\left(\tfrac{i-i_c}{\sigma}\right)^2 + b\left(\tfrac{i-i_c}{\sigma}\right)\right], \tag{5.3}$$

to the 1D density fluctuations described section 5.2.1, where $n^{\mathrm{TF}}(i_c)$ is evaluated with $\delta_n = 0$. The function takes six parameters: normalized amplitude A, center position i_c, soliton width σ, symmetrical shoulder height a, asymmetrical shoulder height b, and an offset δ. When a and b are both zero, this function is a simple Gaussian; however, if a is non-zero, the distribution gains symmetric shoulders, and if b is non-zero, the shoulders gain asymmetricity. Because our excitations show as density depletions, the second term in equation 5.3 is negative.

Our constrained least-squares fit requires initial estimations to be successful. The guess for the center location i_c must be provided. And it also yields the initial estimate for A as the 1D density fluctuations assessed at i_c. The starting settings $\sigma = 4$, $a = 0.2$, $b = 0$, and $\delta = 0$ are found by observations average over the labeled dataset. The following two restrictions are used to achieve trustworthy fits: To avoid numerical fitting mistakes, i_c must stay within three pixels of the provided initial guess, and $10^{-13} < A < 10^4$, and $10^{-13} < a < 10^4$ to prevent numerical fitting errors.

We now calculate a quality estimate for the likelihood of a candidate excitation being solitonic from the fitting parameter. A fitting parameter vector $\Theta = [A, i_c, \sigma, a, b]$ is chosen from a prior distribution with $k = 5$ dimensions that spans the observations of dark solitons.

We remove δ since it correlates with the other five parameters and would not enhance the quality estimate performance.

We assume that the fitting parameters follow the multivariate normal distribution as a reasonable choice for our purpose. Since parameters in Theta are not precisely following a normal distribution, we used a Yeo-Johnson power transformation [213] to turn each of them into 1D Gaussian distributions with zero mean and unit variance. Although we cannot precisely match the processed parameter distributions to Gaussian distributions with this treatment, we can change them into balanced distributions with single peaks and long tails. And at last, we compute the covariance matrix Σ_k for the transformed 5D distribution.

To measure the quality of a detected candidate excitation in an image, we:

1. Fit the subtracted background 1D profile to Mexican hat function 5.3 giving Θ.
2. Use the established Yeo-Johnson power transformation on Θ to obtain Θ'.
3. Return our quality estimate: $M(\Theta') = 1 - \chi_k^2\left(D^2(\Theta')\right)$, the likelihood between 0 and 1 that the excitation being dark soliton.

Assuming no previous knowledge of the distribution of fit results for non-solitonic excitation features, the chi-squared cumulative distribution function $\chi_k^2(p)$ relates the Mahalanobis distance [214] $D^2(\Theta') = \Theta'^{\dagger}\Sigma_k^{-1}\Theta'$ to the likelihood that an outcome is drawn from the specified distribution. $D(\Theta')$ is unbounded above and decreases to zero as Θ' approaches $\langle\Theta'\rangle$, the average over the prior distribution.

5.3 Results

5.3.1 ML modules

We train both the CNN classifier [182] and the OD using the dataset introduced in section 5.2.1 and Ref. [23]. We implement five-fold cross-validation to evaluate the perfor-

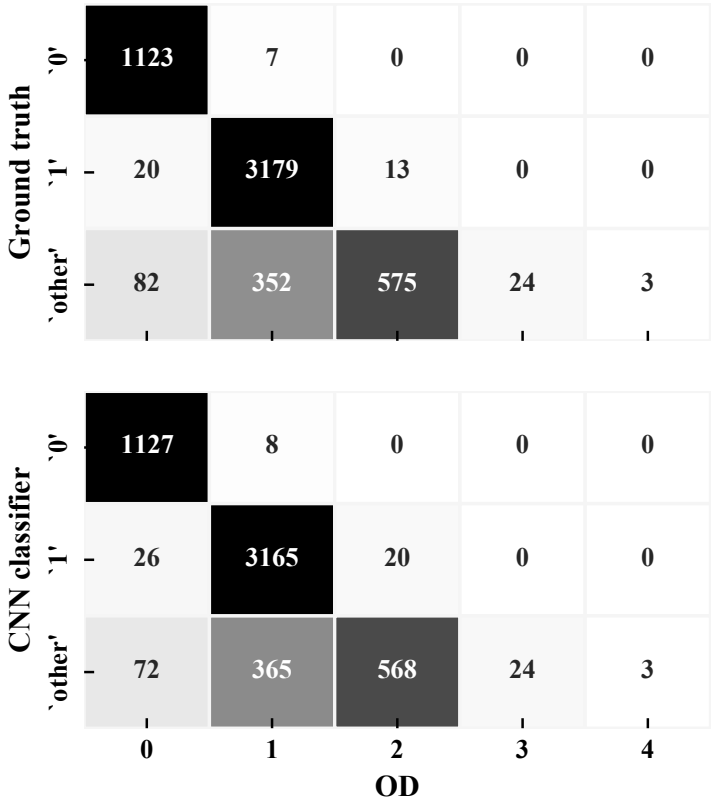

Figure 5.4: Performance of the OD in comparison to the ground truth (top) and CNN classifier prediction (bottom), The ticks ”0”, ”1”, and ”other” denote no, single, and other excitation classes for the ground truth and CNN classifier, respectively. Horizontal ticks indicate the total number of OD-detected´ⓒexcitations in an image.

mance of both modules. This means that we use 80 percent of the data to train a certain module and the remaining 20 percent to test it, and we repeat this procedure five times to cover the whole labeled dataset.

The classification outcomes are represented in the two cumulative confusion matrices displayed in Fig. 5.4. The top panel compares the result of OD to the original labels, which demonstrates almost perfect demarcation between classes with no excitations and classes with single excitations. This class of candidate solitonic excitations is further subdivided by the OD, which counts anything from 0 to 4 candidate solitonic excitations inside it. This outcome is because non-solitonic excitations and multiple solitons can happen within this class. The bottom panel shows the analogous comparison to CNN categorization labels is

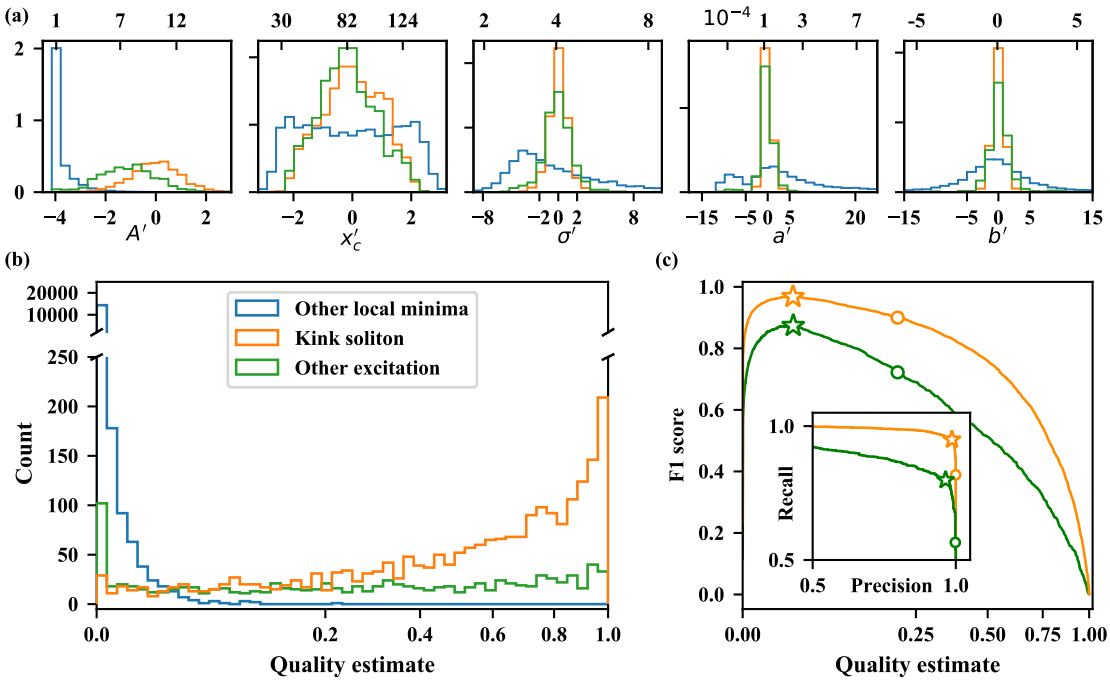

Figure 5.5: Performance of the quality estimator on no excitation and single excitation classes. The following color scheme is used in all cases: kink solitons (orange), all other solitonic excitations (green), and all non-solitonic local minima (blue). (a) Fit coefficient distributions after power transformation, with untransformed variables indicated on the ticks of top axis. (b) Quality estimate distribution. (c) The performance of the quality estimate is defined by the F1 score; the stars denote the ideal F1 value, while the circles denotes the classification threshold. Performance/recall curves are shown in the inset.

essentially identical to the top panel's, demonstrating the accuracy of the CNN predictions. Together, these ML algorithms successfully classify and locate excitations in the data.

5.3.2 Quality estimator

To validate our quality estimator, we started with a subset of the single excitation class known as dark kink solitons [23]. Figure 5.5(a) shows the power-transformed distribution of Mexican hat fit coefficients Θ', with the non-transformed coordinates noted on the top axis for comparison. After the transformation, we see that the training data (orange) are nearly normally distributed for all five parameters. And the distributions of the remaining excitations from the single excitation class are similar to dark kink solitons (green).

In comparison, we collect the Θ' distribution from every local minimum in the training

set *except* for solitonic excitations (blue). We observe that these distributions are qualitatively different from dark kink soliton ones. Here the "local minimum" refers to an area of at least 7 pixels wide, i.e., a minimum at pixel i must obey $n^{1D}_{i\pm j} < n^{1D}_{i\pm(j+1)}$ for $j = 0,1,2$. These distributions exhibit the capability of the quality estimator to differentiate between solitonic excitations and other features within our data.

We then compare the quality estimates M derived from the human-assured dark kink soliton positions from the single excitation class as the orange curve in Fig. 5.5(b). As expected, most kink solitons are related to higher M values. The other solitonic excitations (green) concentrated to small M value; While almost all non-soliton local minima (blue) have a M value smaller than 0.1. As a side remark, we see that the kink soliton distribution has a tiny peak at near-zero M that includes an insignificant proportion of the kink soliton dataset (about 1.3 percent). This peak is more notable for the other excitations, which is expected considering that the power transformer is initialized with only dark kink soliton data.

In Fig. 5.5(c), we show the quality estimator's performance measured in terms of F1 scores for kink solitons (orange) and all other solitonic excitations (green). It is theoretically possible to optimize the F1 score for kink solitons for the $M = 0.05$ threshold (stars). To reduce the number of false positives, we assign a feature to be solitonic when $M > 0.2$ (circles). Although this option results in a slight change in the F1 score, it results in a significant gain in accuracy with only a minor drop in the recall, as seen by the inset. We also remark that the quality estimate's performance on the other solitonic excitations is mediocre, though it is better than a random guess.

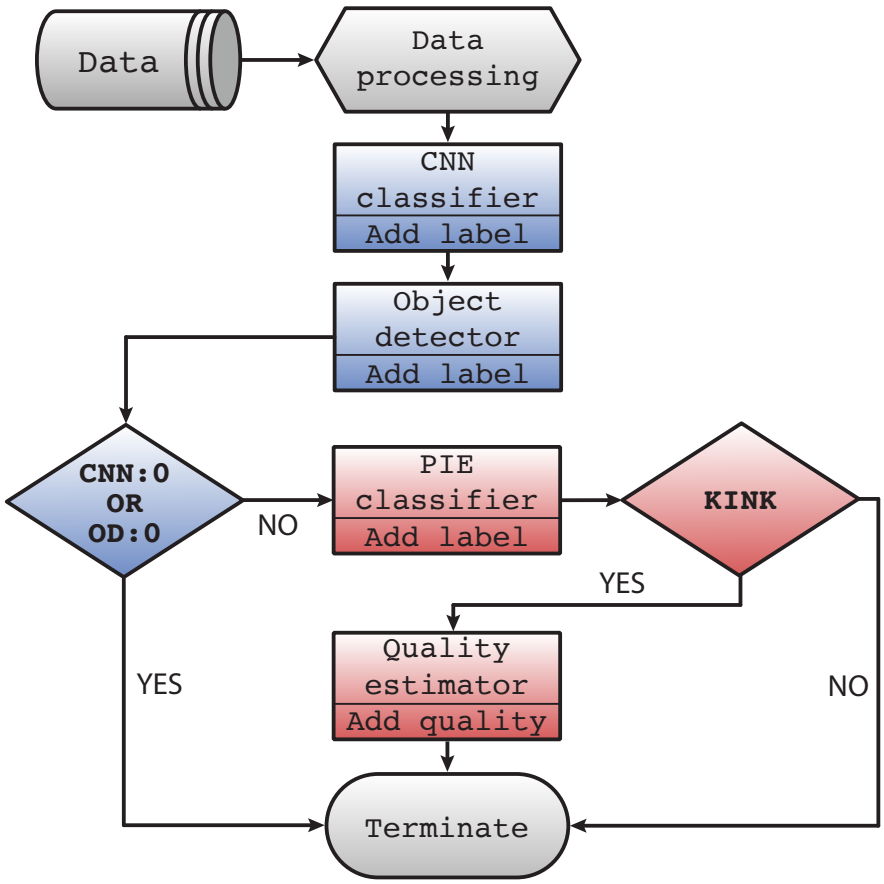

Figure 5.6: The SolDet flowchart. The black line represents the dataflow of SolDet and includes the information added by each module (rectangles). Blue blocks denote machine learning modules, while red blocks denote physics-based modules.

5.4 SolDet: Open-source Python package for solitonic excitation detection

In this chapter, we introduce our open-source software package SolDet, including both the ML modules (CNN classifier and object detection) and the fitting physics-based modules (Quality estimator and physics-informed excitation (PIE) classifier, described in section II.C.1 in Appendix D), and its performance of the new dataset. The previous sections show that the ML modules can successfully categorize images and reliably find one or more candidate kink solitons in a given image. Then, those candidates can be further sorted into subclasses by the physics-based modules, which can also assess the quality of the kink soli-

ton. As a result, the ML and physics-based modules can contribute to the work of soliton identification, and the SolDet framework uses their complementary qualities to maximize its effectiveness. We note that soliton detection is only one kind of feature identification in quantum gases, and thus SolDet is created to be generally applicable to other kins of quantum phenomena. The SolDet contains a CNN classifier, an object detector, a PIE classifier, and a quality estimator trained and initialized using our public soliton dataset [22].

As shown in figure 5.6, SolDet is a multi-module kink soliton identification tool, and its component blocks function in the following order:

Data processing Preprocess raw data into 164×132 image format enclosing the elliptical atom clouds [182]. This preprocessing is specifically designed for our task and the experimental parameters.

CNN classifier Apply a trained CNN classifier to processed data, yield labels among no excitation, single excitation, or other excitations.

Object detection Apply trained OD to processed data, yield a list of positions of solitonic excitations.

CNN:0 OR OD:0 If either the CNN classifier or OD finds no soliton, SolDet terminates.

PIE classifier Apply the PIE classifier to each OD detected solitonic excitation and yield the excitation types.

Quality estimator The quality estimator is applied to each excitation identified as "kink soliton" by the PIE classifier.

This approach is designed for a laboratory setting that requires real-time identification, and for the automatic labeling of large datasets, as in Section 5.4.2 and Ref. [23].

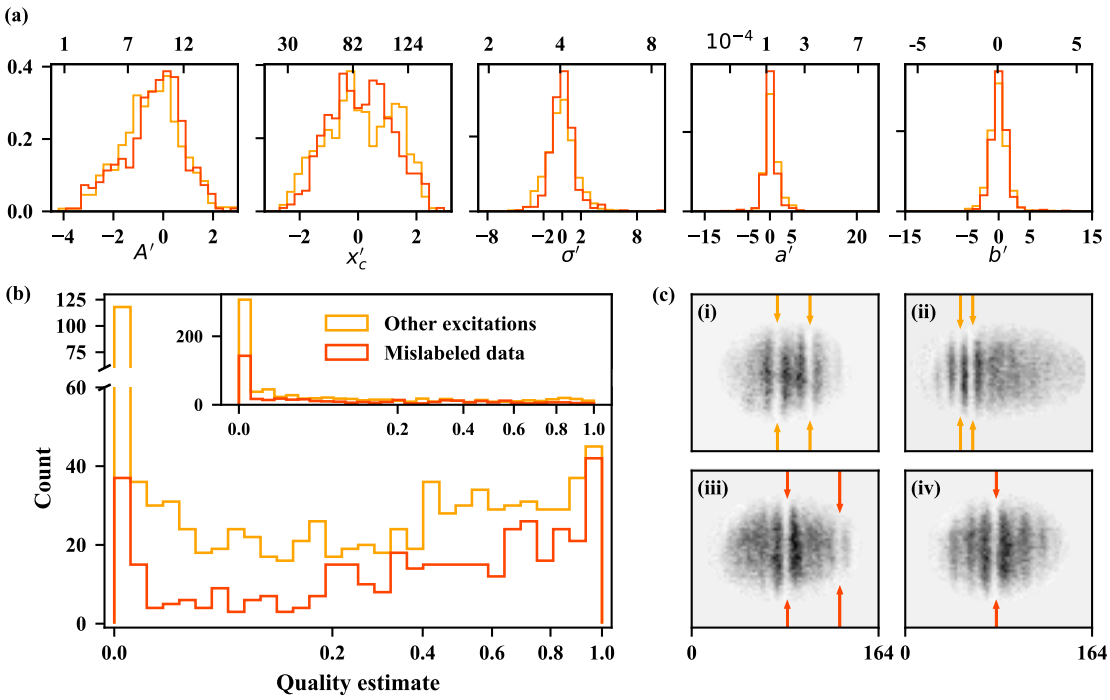

Figure 5.7: Quality estimation performance for other excitation (orange) and mislabeled (red) classes. (a) Power transformed fit coefficient distributions, with the original variables indicated on the top axis. (b) Distribution of quality estimates of all kink solitons (main), and other type of solitonic excitations (inset) (c) Representative pictures from the other excitation (i-ii) and mislabeled (iii-iv) classes, with arrows indicating the OD+PIE detected kink soliton. The quality estimates for these samples are as follows: $M_{(i)} = [0.74, 0.86]$, $M_{(ii)} = [0.00, 0.01]$, $M_{(iii)} = [0.92, 0.02]$ (all from left to right), and $M_{(iv)} = 0.82$.

5.4.1 Application to other excitation and misclassified data

In this part, we extend our use of the SolDet framework to the other excitation classes and the misclassified data from our curation process. The images in these categories include images with several solitonic excitations, such as the one in Fig. 5.2(c), and images with complex architecture that make human classification problematic. As a result, these datasets are excellent testbeds for SolDet since they have defeated past labeling efforts.

After the CNN classification stage, the framework first utilizes the OD to discover soliton candidates, then sorts them by the PIE classifier. Here we only focus on those features that have been recognized as kink solitons. Figure 5.7(a) shows the frequency distribution of power transformed Mexican hat fit outcomes Θ', which produces distributions that

are both qualitatively similar to those seen in figure 5.5(a), indicating labeled single solitons. In panel (b), the histograms of quality estimates for kink solitons discovered in these two groups are different. The distribution is about uniform for the other excitations class ($M > 0.4$). However, for mislabeled data, the distribution follows the same pattern as figure 5.5(b).

Consider the distinctions between the two courses to understand this difference further. OD result shows that most other excitation class images contain two or more excitations (78 %). The separation between the features may affect this result as the fluctuations next to the soliton can affect Mexican hat fitting. The two well-separated excitations in figure 5.7(c-i) I have a relatively high quality estimate ($M_{(i)} = [0.74, 0.86]$). In contrast, solitons in figure 5.7(c-ii) are assigned lower values ($M_{(ii)} = [0.00, 0.01]$) despite both excitations resembling kink solitons. Since most of these data involve multiple excitations, the overall quality estimate distribution can be influenced.

By contrast, the mislabeled class contains images that are possibly mislabeled during the manual labeling phase (for more information on the data curation procedure, see Ref.citeFritsch21-DSD). Most of those images contain one solitonic feature that might be a dark kink soliton, or a clear kink soliton associated with other ambiguous features. Humans cannot easily decide between the single soliton and other excitation classes for these data. The OD detected one excitation in about 83 % of these data. And therefore, the quality estimate distributions for both kink soliton and other excitations [the inset in Fig. 5.7(b)] are similar to the ones in figure 5.5(b). The figure 5.7(c-iii,iv) depicts two example images from this group, with $M_{(iii)} = [0.92, 0.02]$ and $M_{(iv)} = 0.82$.

The performance on these qualitatively distinct test datasets demonstrates SolDet's capability. SolDet autonomously locates many excitations inside BECs combining CNN classifier and OD modules, exceeding the previous deepest-depletion-based methods. The PIE classifier offers further systematic confirmation that the desired sort of excitation previ-

ously required human assessment. Finally, the quality estimate quantifies the excitation quality, enhancing the classification's reliability. Together, these tools provide a solid and trustworthy analytical framework capable of handling substantially more complex data.

5.4.2 Application to new dataset

In this section, we leverage SolDet to help analyze our new dataset containing more than 10^4 images with no labels and have neither been labeled nor used in the training process. This dataset includes images shown in Fig. 5.10 as examples of no solitons, single and multiple solitonic excitations, and obfuscating structures that may hinder human labeling. Our goal is to enlarge the dataset with SolDet.

In figure 5.8, we illustrate the results from SolDet components applied to the unlabeled new dataset. In figure 5.8(a), we summarize the results in the three cumulative confusion matrices of the outcomes of the CNN classifier and OD. We notice that the distribution is nearly indistinguishable from the matrix shown in Fig. 5.4 validating the usage of SolDet for data beyond our original labeled dataset and the qualities of both OD and CNN predictions. As expected, the ML models agree with each other for no excitations and single excitations classes, while OD further subdivides the other excitations class, counting anywhere from 0 to 4 candidate solitonic excitations within it.

In figure 5.8(b), we show the distribution of fine-grained categories as the result of the PIE classifier, for all OD detection, OD and CNN classifier agreed detections, and the ones they agree to single soliton. We find that the distribution of excitation types is similar to those in the training dataset, showing that our PIE classifier performance and data quality are consistent.

In figure 5.9 (a-b), we compare the distributions of Mexican hat fitting parameters Θ' for both the new data and the training data. We found these distributions are quantitatively

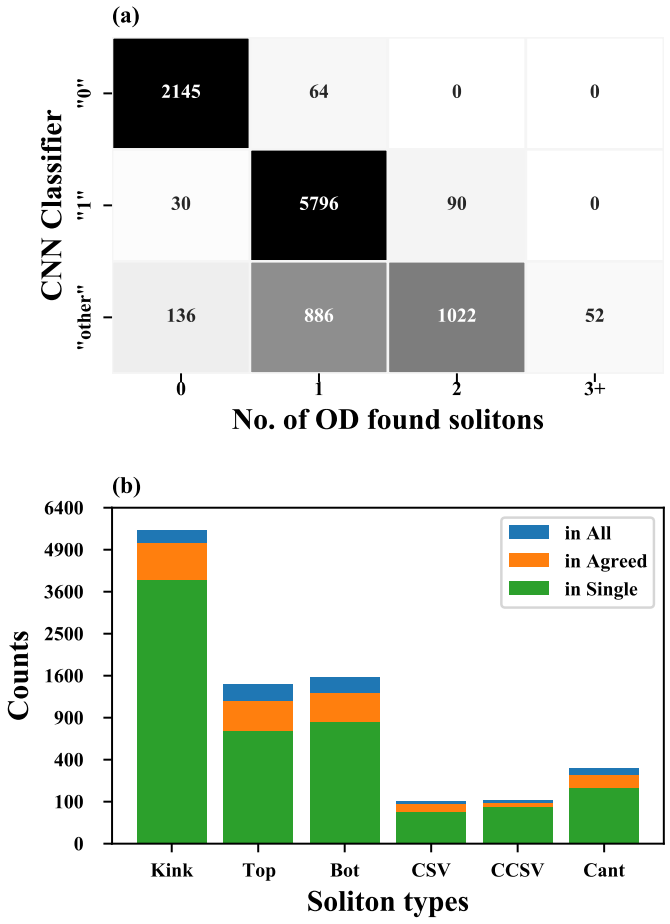

Figure 5.8: Statistics of SolDet classification on new dataset. (a) Confusion matrix between ML modules: CNN classifier results and the number of solitonic features OD has found. (b) The distribution of PIE classifier result for all OD found excitations (blue), detection that OD/CNN classifier agreed on (Orange), and the agreed detection that is predicted as single soliton (green). Types on horizontal axis represent: kink soliton (kink), top (Top) and bottom (Bot) "partial" soliton, Clockwise (CSV) and counter-clockwise (CCSV) solitonic vortex, and canted soliton (Cant). Vertical axis is square-root scaled.

the same, especially when we only consider the detected kink solitons (red). Figure 5.9 (d) histograms the quality estimate for these detected kink solitons. We observe that most kink solitons, especially those on single detection images, accumulate on the high-quality estimate side of the figure, which coincides with figure 5.9 (c) for labeled kink solitons. Together, these results suggest that the effectiveness of the OD/PIE combination is comparable to manual identification for locating potential kink solitons in the new dataset, according to the quality estimate.

In figure 5.10, we depict 30 examples for a variety of classification and position re-

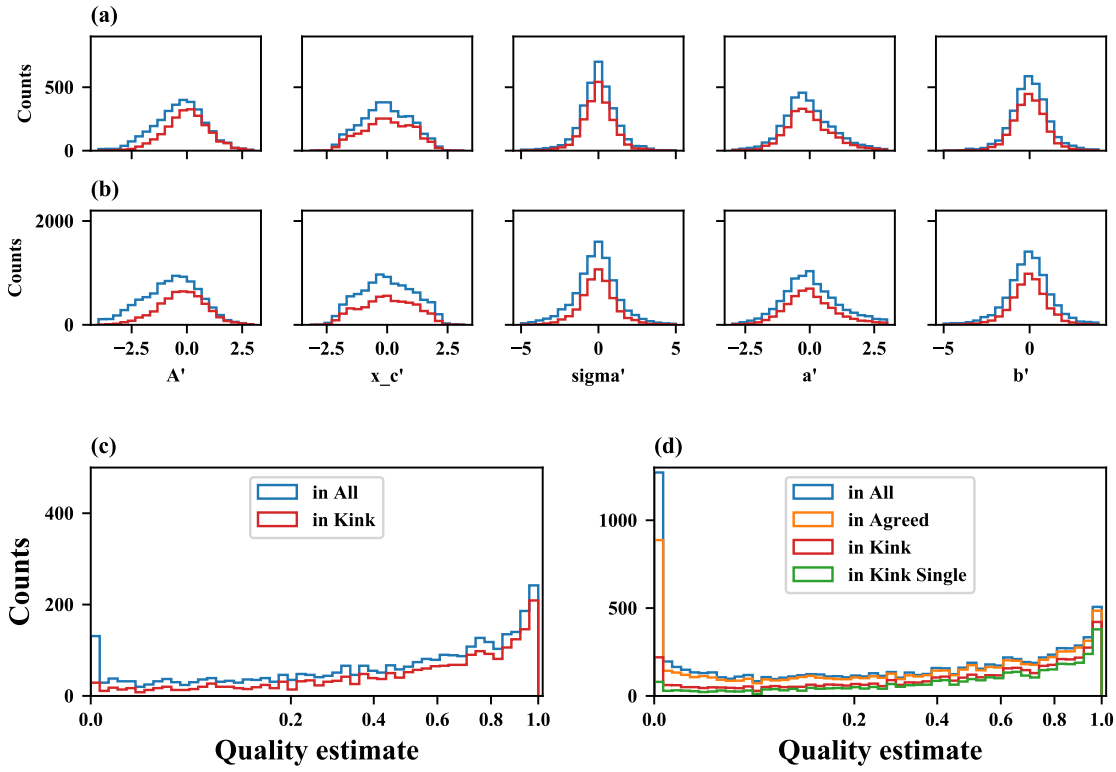

Figure 5.9: Comparison of quality estimates between labeled data and new data. (a-b) Distributions of Mexican hat fitting parameters Θ' for labeled (a) and new dataset (b). And (c-d) distributions of quality estimate for labeled (c) and the new dataset (d). All solitonic excitation labeled by humans (for labeled) or predicted by OD (for new) are colored in blue. The ones predicted by both CNN classifier and OD are in orange. Within them, the excitations that are marked as kink solitons are in red. And these kink solitons in images that are predicted as single excitation are in green.

sults in the new dataset. We present images with zero or one solitonic feature in the first three rows. We observe SolDet can accurately interpret most data, especially for "no soliton" (figure 5.10 (a)) and "kink soliton" with high quality estimates (figure 5.10 (i)), which are the focus of this work. For other solitonic excitation cases (figure 5.10 (b-f)), we observe SolDet can also provide reasonable guideline classifications for them, leaving some room for improvement. Since our primary goal is to provide kink soliton data with confidence, Our PIE classifier is set to have strict thresholds for a feature to be identified as kink solitons. Therefore, some other solitonic excitations might also include data that can be interpreted as kink solitons.

Figure 5.10 (a) present two images classified as no solitons, as we observe no clear ver-

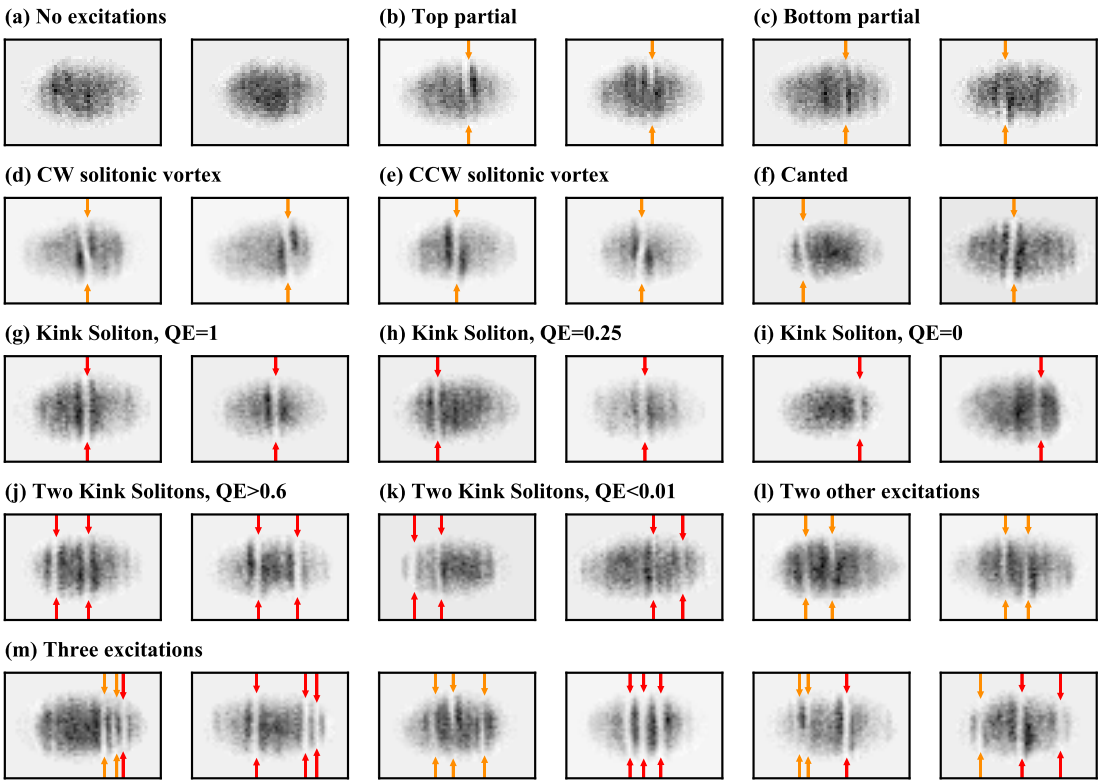

Figure 5.10: Iconic data in the new dataset. The red arrows show the detection of kink soliton excitations, whereas the orange arrows indicate the detection of other kinds of solitonic excitations.

tical depletions anywhere on the atom cloud. Figure 5.10 (b-c) present four images classified as top/bottom "partial" solitons, as we observe the vertical depletions do not fully penetrate the whole atom cloud. Figure 5.10 (d-e) present four images classified as clockwise/counterclockwise solitonic vortices, as we observe the uneven vertical distributions for the two shoulders around the depletion. At last, figure 5.10 (f) presents two images classified as canted kink solitons where the deletions do not fully align with the vertical axes of the images.

As shown in figure 5.10 (g-i), we notice that even for features that are classified as kink solitons by OD and PIE classifier, the quality may vary. In figure 5.10 (g), we show two examples with a perfect quality estimate $M_{(g)} = 1$ as we see apparent and deep depletion penetrating the whole cloud. In figure 5.10 (h), we show two examples with borderline

$M_{(h)} = 0.25$. Furthermore, in figure 5.10 (i), we show two examples with low quality estimates $M_{(i)} = 0$, as we see blurred shallow depletions at the OD detected positions. Therefore, we further assign the quality estimate for these features to indicate the qualitative confidence in addition to our ML results. Our new dataset contains much more high-quality kink solitons rather than low-quality ones, as shown in Fig. 5.9(d).

Images in the last two rows are classified as other excitations by the CNN classifier and have more than two soliton candidates identified by the OD. Figure 5.10 (j) depicts images containing two high quality kink soliton with $M_{(j)} = [[0.80, 0.70], [0.92, 0.71]]$, as we observe two clear kink solitons. Notice that we are particularly interested in this type of data as they are related to soliton collisions. In comparison, figure 5.10 (k) shows images containing two low-quality kink solitons, all with quantity estimates close to zero, as they show two obscure depletions on the data. Moreover, in figure 5.10 (l), we show images containing two other excitations. Specifically, the first image contains a bottom partial soliton and a top partial soliton, and the second one contains a top partial soliton and a bottom partial soliton, described from left to right.

In figure 5.10 (m), we sample some data that OD suggests three or more excitations. Specifically, the types for excitations in that row are $T_{(m)} =$ [[Bottom, Bottom, Kink], [Kink, Kink, Kink], [Bottom, Top, Bottom], [Kink, Kink, Kink], [Clockwise solitonic vertex, Top, Kink], [Bottom, Kink, Kink]], and the quantity estimates for kink soliton in them are $M_{(m)} = [[0.00], [0.81, 0.17, 0.00], [], [0.06, 0.27, 0.01], [0.86], [0.51, 0.01]]$. Both types and quantity estimates are described from left to right. Even with background noise and other excitations, we identify three high-quality kink solitons with SolDet in the second, fifth, and last images, as we can validate them by observing clear depletions throughout the clouds that are far from other features.

We conclude that applying SolDet to unforeseen experimental data containing multiple dark solitons can yield high reliability and quality results. As a result, SolDet provides

us with an enlarged, automatically-labeled dataset with fine-grained solitonic excitation categories and quantitative estimates of kink soliton qualities, opening the opportunity for more profound research into cold atom physics and computer science.

5.5 Discussion and conclusion

This chapter established a high-level framework that integrates ML approaches with physics-based analysis, resulting in an integrated platform for evaluating experimental data suitable for other applications. SolDet, as our implementation of this framework, is designed to focus on the identification, classification, and tracking of dark kink soliton features in cold atom image data.

Using a public dark soliton dataset [23], we show the training process and the performance of SolDet. Our analysis shows SolDet can successfully automate locating and classifying solitonic features on BEC absorption images, even in the cases of multiple solitons or in noisy backgrounds. The patterns are learned effectively on most testing images using SolDet starting from OD, which is trained with only the no excitation and single soliton data. In conclusion, our hybrid framework is a powerful data analysis tool for discovering features from the soliton dataset.

For future directions, the new version dataset also contains a label indicating the amount of time that has passed since the excitations are formed, which opens the door to further research into the relationship between system control parameters and the SolDet generated labels. It could also be interesting to use the PIE classifier results to train an OD that directly yields solitonic excitation types information. From the ML point of view, we expect to add modules based on unsupervised [215], active learning [216], and synthetic data generation with generative models [217] to the SolDet framework would improve the performance and help identify previously unknown features.

Chapter 6: Discussion and conclusion

This dissertation discusses three quantum mechanical system topics that could help extend knowledge of quantum information science and advance quantum technologies in many aspects, such as building compact quantum memory with long coherence time, initializing quantum systems to a variety of states, designing tunable many-body interactions, creating engineered cooling and heating channels, formulating error correction feedback loops, and reading out quantum information into the form of classical data.

With our generalized theory for giant atoms, we opened a new field of physics of artificial systems that have never been observed in nature. Usually, a natural atom takes a much smaller space than its emission wavelength. We take one step further from the existing Wigner-Weisskopf spontaneous decay theory by softening its point-like atom assumption. We investigated a new phase diagram that includes the parameter of atom size. Moreover, we also learned that for a circuit QAD device, observing the giant atom physics requires an additional constraint that the ratio of the atom size and characteristic emission wavelength need to be close to an integer.

Based on this work, many benefits and opportunities for engineering quantum systems become available. For example, engineering emission rate and excitation amplitude, creating relaxation dynamics beyond exponential decay, unlocking circuit QAD as a new apparatus to study BIC physics, and most importantly, providing a new route to achieve long coherent time qubits.

We open opportunities to engineer closed-loop feedback control for quantum systems

with our feedback cooling result. As the closed-loop feedback has been advantageous for many classical systems, from controlling the temperature of rooms to navigating satellites, we believe there would be many use cases in quantum engineering. These opportunities may include developing synthetic interactions, dissipations, and other dynamics; preparing novel states; inducing phase transition; implementing error correction and mitigation protocols; extending coherent time; understanding quantum chaos; simulating open quantum systems; and creating new quantum matters.

In addition, continuously monitoring quantum systems without destroying their quantum mechanical properties may help us better understand the effect and nature of quantum measurements, study the dynamical behaviors of equilibrium and non-equilibrium states, and observe quenched quantum systems. This research also paves the way for adaptive weak measurements to help quantum tomography and error corrections. For example, we may stop measuring or lower the measurement rate as we become more confident about our current state estimate.

In Chapters 4 and 5, we prove that ML techniques can extract information that we previously could not acquire from raw measured data. In other words, we can train ML models with a simpler dataset and apply it to more sophisticated data, and it could yield reasonable results. From a data processing perspective, we believe more opportunities can be investigated for quantum topics, such as automated phase recognition, parameter space scanning for novel states, auto-tuning for best control parameters of the experimental setting, generating artificial data to interpolate and extrapolate data that experimentally hard to prepare, estimating experiment or simulation results by learning from real or simulated oracles.

With this project, we developed an automatic protocol to process new raw cold atom absorption image data for solitonic excitations. We established a soliton dataset that consists of more than 1.6×10^4 images with a complete description of soliton types, positions,

and quality estimates. Furthermore, we introduced a general framework that combines ML and physics-informed modules.

With the automated protocol, we unlock the opportunity to study solitonic excitation dynamics without human inspections. These dynamics may include oscillations, stabilization, collisions of solitons, and rotations of solitonic vortices. It may also help improve techniques for imprinting, controlling, and measuring multiple solitonic excitations, reducing noise and phonons, and understanding the physics of so-called "partial solitons".

To our best knowledge, the dark solitonic excitations dataset that we collected from our cold atom lab is the very first of its kind. Leveraging this dataset, researchers can develop new ML techniques for controlling and measuring solitons and BECs. This dataset may open the door to ML-assisted quantum control, studying solitonic features, unsupervised learning of physical excitations, and investigating the noise patterns and phonons for cold atom experiments.

We also introduced a framework that combines physics-informed models to assist ML. By doing so, we can enhance the overall performance and cross-validate ML results more reliably. We believe this framework may help many more quantum physics research that relies on data, such as tomography and quantum error correction.

We find at least two profound aspects that ML can improve quantum information science, with or without assistance from physics-informed modules. First, ML could help reconstruct information about the quantum state, process, or channels from measured results. ML models are proficient in finding patterns from large amounts of classical data associated with some noise, similar to our resource for observing a quantum system. This aspect may include examples like learning quantum information with adaptive measurements and shadow tomography, recognizing errors and states from weak measurements results, optimizing post-selection strategies, and estimating partial derivatives of a variational quantum operation.

Second, ML could help create high-fidelity quantum states, equilibrium, operations, and dynamics by applying ML to quantum device control channels. ML shows the capability of predicting future dynamics and stochastic correlated noise. Quantum systems are often fragile to noise from environments, including the surrounding controlling and measuring apparatus components. Using ML may help minimize the effect of a specific type of noise and help us to achieve better global control. Some examples may cover exploring feedback strategies for steady states with weak measurement results; engineering better pulse sequences for high-fidelity rapid quantum operations and state preparations; ML-assisted zero noise extrapolations; and ML-assisted quantum error decoding.

Appendix A: Publication for Chapter 2: Beyond spontaneous emission: Giant atom bounded in the continuum

Beyond spontaneous emission: Giant atom bounded in the continuum

Shangjie Guo,[1,2] Yidan Wang,[1] Thomas Purdy,[3,4] and Jacob Taylor[1,2,3]
[1]*Joint Quantum Institute, University of Maryland, College Park, Maryland 20742, USA*
[2]*Joint Center for Quantum Information and Computer Science, NIST/University of Maryland, College Park, Maryland 20742, USA*
[3]*National Institute of Standards and Technology, Gaithersburg, Maryland 20899, USA*
[4]*Pittsburgh Quantum Institute, University of Pittsburgh, Pittsburgh, PA 15260, USA*

(Received 11 May 2020; accepted 6 August 2020; published 8 September 2020)

The quantum coupling of individual superconducting qubits to microwave photons leads to remarkable experimental opportunities. Here we consider the phononic case where the qubit is coupled to an electromagnetic surface acoustic wave antenna that enables supersonic (electromagnetic) propagation of the qubit oscillations. This can be considered as a giant atom that is many phonon wavelengths long. We study an exactly solvable toy model that captures these effects, and find that this non-Markovian giant atom has a suppressed relaxation, so long as an effective vacuum coupling exists between a qubit excitation and a localized wave packet of sound, even in the absence of a cavity for the sound waves. Finally, we consider practical implementations of these ideas in current surface acoustic wave devices.

DOI: 10.1103/PhysRevA.102.033706

I. INTRODUCTION

The coupling of resonant, compact systems to continuous media has a rich history, underlying phenomena ranging from musical instruments to complex machinery to the spontaneous emission of light from an atom [1,2]. The strong coupling regime of such systems has also led to a plethora of applications in cavity quantum electrodynamics (QED) [3], circuit QED [4,5], and waveguide QED [5–8], all of which work in the regime where light propagation is fast relative to appropriate coupling time scales such as the coherence time. However, collective effects, such as Dicke superradiance, have shown that preexisting coherence across multiple wavelengths of the medium excitations can dramatically alter the simple dynamics of such open quantum systems [9,10].

Here we examine an example of such long-range coherence in the form of a superconducting qubit nonlocally coupled to a long, quasi-one-dimensional (quasi-1D) phononic waveguide. This system can be realized in, for example, surface acoustic wave (SAW) devices [11]. Working in the lumped element limit, the electrical antennae that couple to the mechanical waveguide have practically simultaneous coupling to distant regions of the system, while the motional degrees of freedom are constrained to propagate at the speed of sound. This leads to a variety of supersonic phenomena in the quantum acoustodynamics (QAD) regime which has been heretofore largely unexplored.

Pioneering works in this domain have labeled this the "giant atom" regime of SAW devices [12–15]. This model breaks locality in the lumped element limit and inevitably becomes non-Markovian, requiring a more detailed theoretical treatment [16–24]. Furthermore, recent experiments show the robustness of systems that couple mechanical with electromagnetic parts in the quantum regime and open the opportunity to realize giant atoms in experiments [12,25–32].

We show that these devices have remarkable properties, particularly that of strong coupling without the presence of a cavity, in which a long-lived atomic excitation dynamic emerges due to the coupling to the electrical circuit directly, and the formation of long-lived states of sound in the unbounded continuum. We describe this as the bounded giant atom phenomenon.

While our simple theoretical model predicts this phenomenon directly, a more complicated numerical approach shows that a specific additional phase matching condition must be satisfied for experimental observation of the strong coupling of this emergent of bounded effect to the quantum bit. Furthermore, in this regime, boundary-based damping of the sound exponentially decreases with the atom size, leading to substantial improvements in coherence times. Our study suggests a pathway to more compact superconducting qubit designs that can leverage sound, rather than microwave photons. Key aspects of circuit QED-based architectures, such as using a photon in a resonator as an intermediary between two transmon qubits and using dispersive coupling of a transmon to a waveguide, have natural analogs using coupling to phonons instead. However, transducer efficiencies and parametric amplification, two key elements of circuit QED systems, are not at an appropriate level yet for replacement by sound. This suggests substantial research may be necessary before a sound-based architecture could be realized.

The rest of this paper is organized as follows: In Sec. II, we review the Weisskopf-Wigner theory for spontaneous emission [1], which provides the structure for our model later; throughout the paper we refer to the superconducting qubit with antennae as a giant atom. We calculate the coupling between the artificial atom and phonons of the circuit QAD

device, and we simplify it to a Lorentzian toy model in Sec. III. In Sec. IV, we derive our main results from the toy model and compare our results with the numerical simulation. We conclude in Sec. V and show future applications of the general method presented in this paper.

II. BACKGROUND

A. The general theory

We consider a two-level giant atom with ground state $|g\rangle$ and excited state $|e\rangle$ with a frequency difference ν that non-locally couples to an infinitely long 1D bosonic field, governed by the following Hamiltonian in the rotating wave approximation:

$$\hat{H} = \frac{\nu}{2}\sigma_z + \int dK[\omega(K)\hat{a}_K^\dagger \hat{a}_K + g(K;N)(\hat{\sigma}_+\hat{a}_K + \text{H.c.})], \tag{1}$$

where $\hat{\sigma}_+$ ($\hat{\sigma}_-$) and $\hat{a}_K^\dagger$ ($\hat{a}_K$) are creation (annihilation) operators for atomic excitation and field, respectively. They satisfy $(\hat{\sigma}_-)^\dagger = \hat{\sigma}_+ = |e\rangle\langle g|$, $\sigma_z = |e\rangle\langle e| - |g\rangle\langle g|$, and $[\hat{a}_K, \hat{a}_{K'}^\dagger] = \delta(K - K')$. ν is the atomic transition frequency. We assume that the field has a linear dispersion $\omega(K) = c_s|K|$ with the speed of sound c_s, for momentum K. We set $\hbar = 1$ for simplicity.

We consider the coupling $g(K;N)$ to depend on the momentum K. As the Fourier transform of the position-dependent coupling, it is also parametrized by the spatial length of the atom N. One can expect that the parameter N will change the atom relaxation dynamics via tuning the shape of $g(K;N)$. We shall discuss two different models for $g(K;N)$ in Sec. III.

We denote the vacuum state by $|g, 0\rangle$, and limit our system to a single excitation Hilbert subspace with basis states $|e, 0\rangle = \hat{\sigma}_+|g, 0\rangle$ and $|g, K\rangle = \hat{a}_K^\dagger|g, 0\rangle$, such that any time-dependent state can be described as $|\psi(t)\rangle = \alpha(t)|e, 0\rangle + \int_{-\infty}^{+\infty} dK\beta_K(t)|g, K\rangle$, where $\alpha(t)$ and $\beta_K(t)$ are time-dependent amplitudes. In a frame rotating with frequency ν, we derive the equations of motion

$$\dot{\alpha}(t) = -2i\int_{-\infty}^{+\infty} dk\, g(k;N)\beta_k(t), \tag{2}$$

$$\dot{\beta}_k(t) = -i\delta(k)\beta_k(t) - ig(k;N)\alpha(t). \tag{3}$$

Note that as the coupling is real in position space in our case, such that $g(K;N) = g(-K;N)$, the two branches for $K > 0$ and $K < 0$ contribute symmetrically and can be merged in Eq. (2). The momentum in the rotating frame is redefined as $k = |K| - \nu/c_s$, such that the field frequency becomes $\delta(k) = \omega(K) - \nu = c_s k$ for the near-resonance regime. Then, by taking the Laplace transform from the time domain into the complex frequency domain by $\tilde{\alpha}(s) = \mathcal{L}[\alpha(t)]$, and $\tilde{\beta}_k(s) = \mathcal{L}[\beta_k(t)]$, we get

$$s\tilde{\alpha}(s) - \alpha(0) = -2i\int_{-\infty}^{+\infty} dk\, g(k;N)\tilde{\beta}_k(s), \tag{4}$$

$$s\tilde{\beta}_k(s) - \beta_k(0) = -i\delta(k)\tilde{\beta}_k(s) - ig(k;N)\tilde{\alpha}(s). \tag{5}$$

We set $\alpha(0) = 1$ and $\beta_k(0) = 0$ to investigate the relaxation of an atomic excitation. Then we have $\tilde{\beta}_k(s) = -ig(k;N)\tilde{\alpha}(s)/[s + i\delta(k)]$ and the response function $\chi(s) \equiv \tilde{\alpha}(s)/\alpha(0)$ becomes

$$\chi(s) = \left(s + 2\int_{-\infty}^{+\infty} dk \frac{|g(k;N)|^2}{s + i\delta(k)}\right)^{-1}. \tag{6}$$

When $g(k;N)$ is an analytic function, we can derive that $\alpha(t) = \mathcal{L}^{-1}[\chi(s)]\alpha(0) = \sum_n \text{Res}[\chi(s), s_n]e^{s_n t}$ from the residue theorem and our initial conditions, where s_n is the nth pole of $\chi(s)$ that satisfies the equation $[\chi(s_n)]^{-1} = 0$ for $n \in \{1, 2, \ldots, n_{\max}\}$. $n_{\max}$ is the number of the poles of $\chi(s)$. Causality confines s_n to be in the left half complex plane or on the imaginary axis, i.e., $\text{Re}(s_n) \leqslant 0$ [33]. Note that the inverse Laplace transform requires that the contour path of integration is in the region of convergence of $\chi(s)$. This can be satisfied by integrating Eq. (6) with the condition $\text{Re}(s) > 0$.

Armed with the solution for the poles s_n, we describe the atomic relaxation process as a composition of damped oscillation modes with effective vacuum Rabi oscillation frequencies $\text{Im}(s_n)$ and decay rates $-2\,\text{Re}(s_n)$. In the long-time limit, only the slowest damped modes can survive, and we thus define the long-time relaxation rate as $\gamma \equiv \text{Min}_n[-2\,\text{Re}(s_n)]$.

To understand the giant atom relaxation, we study how the poles of response function s_n change according to the atom size N. In the next section, we consider a realistic circuit QAD model and a simpler Lorentzian toy model to characterise $g(k;N)$ with N being a changing parameter, and study the response function $\chi(s)$ and its poles.

B. The Weisskopf-Wigner limit

Before moving into the giant atom case, we first review the Weisskopf and Wigner approach to the pointlike atom case [1]. A pointlike atom couples to all wavelength emissions equally, i.e., $g(k;N) = g_0$, independent of k. In this situation, one can calculate the real part of the equation $[\chi(s)]^{-1} = 0$, which results in

$$\gamma_1 \equiv -2\,\text{Re}(s_1) = 4\pi|g_0|^2/c_s. \tag{7}$$

This textbook result shows that, when a pointlike atom couples to a 1D field, the atom decays with its spontaneous emission rate γ_1. In the giant atom case, we also define γ_1 as the weak-coupling relaxation rate for a unit cell (e.g., $N = 1$) for later discussion. Now we can proceed and study $g(k;N)$ for the circuit QAD and the toy models that simplify it.

III. THE CIRCUIT QAD AND TOY MODELS

A. The circuit QAD model

We examine a simplified 1D model for the circuit QAD device shown in Fig. 1. A circuit QAD device comprises a superconducting artificial atom [as a Josephson junction parallelized with an interdigital transducer (IDT) as a capacitor] and a surface acoustic wave (SAW) cavity. The qubit couples to the cavity via an IDT, where two interlocking comb-shaped arrays of electrodes are fabricated on the surface of a piezoelectric substrate. Such systems have been used to achieve strong coupling, where the vacuum Rabi coupling exceeds dephasing and damping [26–28,30]. We can map the spatial atom size to the length of the IDT d, and the resonance emission wavelength to the IDT characteristic wavelength λ (the finger spacing of the IDT). We use the number of fingers of

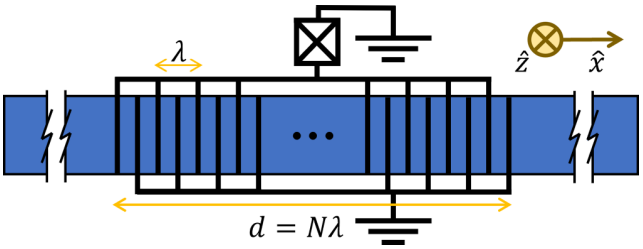

FIG. 1. A sketch of a circuit QAD device viewed from the top. Black lines show electrodes and the blue area shows the surface of piezoelectric material substrate. The substrate extends deeply in the $+z$ direction.

the IDT, $N = d/\lambda$, as the atom size parameter for this circuit QAD model.

Since the electromagnetic wave travels about 10^5 faster than sound through the IDT, we take the lumped element limit for the circuit, and the electronic subsystem can be regarded as a two-level system that interacts with SAW at different positions simultaneously. Notice that this system inevitably becomes non-Markovian under this assumption, thus necessitating our use of the Laplace transform solutions in what follows, rather than more typical quantum optics approximations. We also assume the mass loading of all electrodes to be zero to remove additional mechanical resonances. We approximate the uniform electric field between each pair of electrodes, such that $E(x,t) = [V(t)/\lambda]\,\mathrm{sgn}[\cos(\pi x/2\lambda)]$, where $V(t)$ is the voltage applied on the IDT. We also assume the substrate has no loss through intrinsic material dissipation or via acoustic energy radiated in directions perpendicular to $\hat{x}$

We take the atom transition frequency to equal the IDT resonance frequency, i.e., $\nu = 2\pi/T = 2\pi c_s/\lambda$, where c_s is the speed of SAW propagation and T is the designed fundamental period of the SAW. We calculate the coupling $g(k;N)$ for the circuit QAD device as [34]

$$g_{\mathrm{cQAD}}(k;N) = \sqrt{\frac{\gamma_1 c_s}{2\pi}}\,\frac{\sin(Nk\lambda/2)\cot(k\lambda/4)}{2 + k\lambda/\pi}. \tag{8}$$

In Appendix A, we give both the derivation of Eq. (8) and a discussion of experimental feasibility of this model. We illustrate $g_{\mathrm{cQAD}}(k;N)$ in Fig. 2 for $N = 30$, and 75. This model has a finite bandwidth about $2\pi/N\lambda$, with the on-resonance coupling proportional to N. Note that the poles of the response function (6) are hard to find analytically with this model. Therefore, we establish a toy model in the next subsection to capture the long-time dynamics and where we can analytically express its poles. Then, we compare the toy model to numerical results using the circuit QAD model in Sec. IV B.

B. The Lorentzian toy model

To evaluate the integral in Eq. (6), we use a Lorentzian toy model $g_{\mathrm{Lor}}(k;N)$ defined as

$$g_{\mathrm{Lor}}(k;N) \equiv \sqrt{\frac{\gamma_1 c_s}{2\pi}}\,\frac{N}{(Nk\lambda/\pi)^2 + 1}, \tag{9}$$

instead of Eq. (8). Such a model satisfies the following criteria: it has a finite bandwidth about $2\pi/N\lambda$ and an on-resonance coupling proportional to N, it is nonlocal in position with the scale of $N\lambda$, and it decays exponentially in position and quadratically in momentum. In Fig. 2, we illustrate that the shape of the Lorentzian toy model matches the central peak of the circuit QAD model, while it does not capture the oscillation behavior at large $|k|$. This toy model greatly simplifies the calculations and allows us to analytically describe the poles of the response function $\chi(s)$, leading to our main results in Sec. IV A. We can then analyze corrections to this model from the QAD picture.

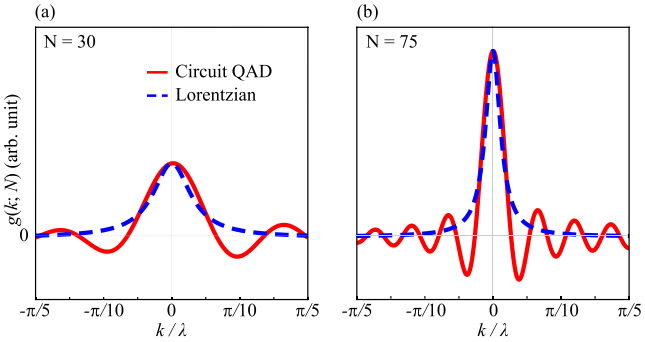

FIG. 2. The momentum-dependent coupling $g(k;N)$ for (a) $N = 30$, (b) $N = 75$. Red solid lines correspond to circuit QAD model (8), blue dashed lines to Lorentzian toy model (9). The vertical axes for (a) and (b) share the same scale.

IV. RESULTS

A. Analytic solutions from the Lorentzian model

First, we substitute Eq. (9) into the equation defining the poles of the response function, $[\chi(s_n)]^{-1} = 0$, which yields

$$s_n + \frac{N^2\gamma_1\nu(Ns_n + \nu)}{(\nu + 2Ns_n)^2} = 0. \tag{10}$$

This equation can be reduced to a cubic polynomial of s_n, and we give the explicit form of its solutions in Appendix B. In Figs. 3(a) and 3(b), we set $\gamma_1 = \pi \times 10^{-5}\nu$ and plot the $-2\,\mathrm{Re}(s_n)$ and $\mathrm{Im}(s_n)$, which indicate the damping rates and the effective Rabi frequencies. We mark the solutions associated with the slowest damped modes with solid lines.

In Figs. 3(a) and 3(b), we observe a dramatic change of dynamics at the *transition point* N_T. When $N \ll N_T$, increasing the atom size only creates a larger coupling region and therefore accelerates the relaxation process. At the transition point $N = N_T$, we find the imaginary parts of two poles merge, while their real parts split. When $N \approx N_T$, the atom decays quickly into the 1D waveguide, as all the modes have large damping rates. However, when $N > N_T$, the effective relaxation rate γ drops almost exponentially with N, while the effective Rabi frequency becomes nonzero and increases. Note that both phenomena are the results of the atom excitation state overlapping with bound states. This result shows that a bounded giant atom regime exists at $N \gg N_T$, where some of the atomic excitation energy is localized and oscillates between atomic excitation and a stationary phonon wave packet. We also find that, in the limit $N \to \infty$, Eq. (10) reduces to $s_n \to \pm(i/2)\sqrt{N\gamma_1\nu}$. As $\mathrm{Re}(s_n) \to 0$, a part of the excitation

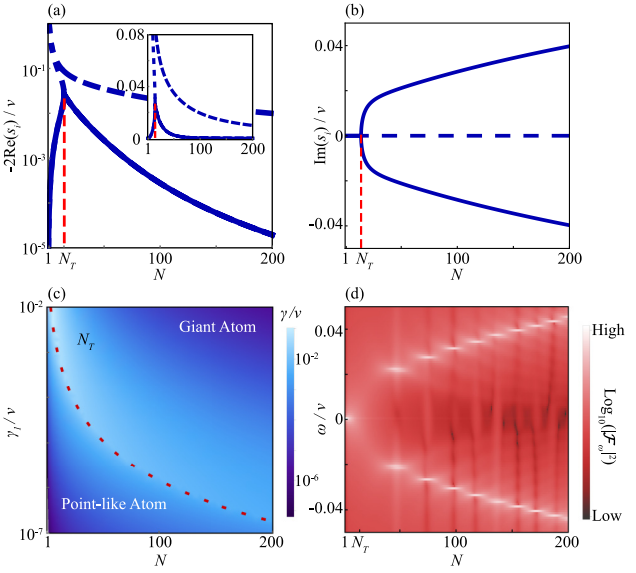

FIG. 3. (a)–(c) Transition from the pointlike atom to the giant atom, with the Lorentzian toy model: (a) The blue lines represent decay rates $-2\,\mathrm{Re}(s_n)$ versus atom size N in semilogarithmic scale, where s_n are roots for Eq. (10). The solid blue lines are the effective relaxation rate $\gamma \equiv \mathrm{Min}_n[-2\,\mathrm{Re}(s_n)]$, and the dashed blue ones represent other roots. The red dotted line shows the transition point N_T. The inset is plotted in a linear scale. (b) The effective Rabi oscillation frequency $\mathrm{Im}(s_n)$, corresponding to (a). (c) The effective relaxation rate γ in the N-γ_1 parameter plane. The red dashed line shows the transition point N_T, which separates two regimes for pointlike atom and giant atom. (d) The power spectrum $|\mathcal{F}_\omega[\alpha(t;N)]|^2$ of the simulated time evolution with the circuit QAD model, in logarithmic scale. We note that the discrete resonances observed arise from the phase matching condition in the circuit QAD model that is absent in the Lorentzian model. All figures are in rotating frame with frequency ν, and all logarithmic scales are in $\log_{10}$ base.

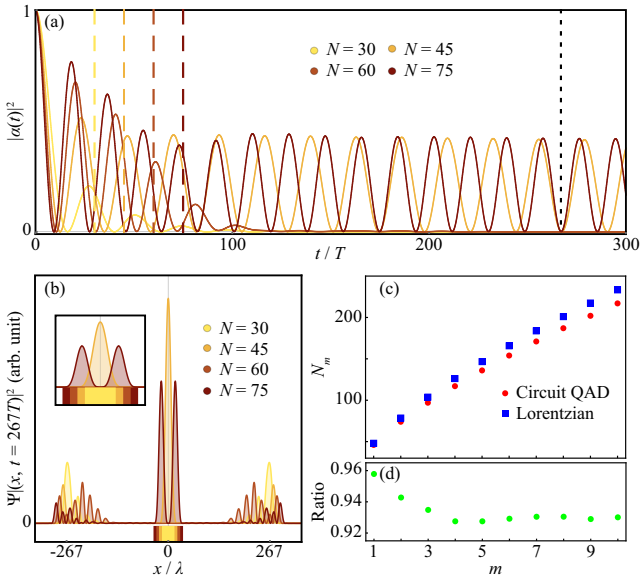

FIG. 4. (a)–(b) Simulation for the circuit QAD model for different atom sizes N: (a) The time evolution of atom excitation amplitude $|\alpha(t)|^2$, for different N. The dashed lines show the time that the phonons travel through the atom length $t_b = NT$. For N above the onset of normal mode splitting and phase matched, the system settles into a long-lived state after a short time. (b) The magnitude of phonon wave function $|\Psi(x,t_f)|^2$ frozen at $t_f = 267T$ [also indicated by the black dashed line on Fig. 4(a)], for different N. We chose t_f such that $|\alpha(t_f)^2| \approx 0$ for all N values shown. The inset shows the same plot zoomed in near the atom region identified by the bars of color below the axis for different N. (c) The Lorentzian theory prediction and the circuit QAD simulation result of the bounded atom size N_m. (d) The ratio between $N_{m,\mathrm{cQAD}}/N_{m,\mathrm{Lor}}$.

lives in bound states in this limit. We can derive the transition point N_T from the roots of Eq. (10):

$$N_T = \sqrt[3]{\frac{(5\sqrt{5}-11)\nu}{2\gamma_1}} \approx 0.448 \times \sqrt[3]{\nu/\gamma_1}. \tag{11}$$

For $\gamma_1 = \pi \times 10^{-5}\nu$, we have $N_T \approx 14.2$. In Fig. 3(c), we show the effective relaxation rate γ in the N-γ_1 parameter plane. We find two slow relaxation regions corresponding to the pointlike atom case and the bounded giant atom case, which are on either side of N_T.

B. Numerical results from the circuit QAD model

Although it is hard to analytically evaluate the integral in Eq. (6) with the circuit QAD model, we can discretize the Hamiltonian and simulate the dynamics of the system via solution of the Schrodinger equation for the case of a single initial excitation, i.e., $|\psi(t=0)\rangle = |e,0\rangle$. We choose the cutoff momentum $k_c = \pm 0.1\pi/\lambda$, the density of states $dk = 2\pi \times 10^{-4}/\lambda$, and time step $dt = 0.1T$. We keep $\gamma_1 = \pi \times 10^{-5}\nu$ to compare with analytic results from the last subsection.

In Fig. 4(a), we show the time evolution of the atomic excitation, $|\alpha(t)|^2$. As expected, we find that for some $N \gg N_T$, such as $N = 45$ and 75, a fraction of the energy remains in the system after the phonons travel through the atom, i.e., $t_b = NT$, and this energy oscillates between mechanical and atomic excitation. Next, we choose a final time t_f, such that $|\alpha(t_f)|^2 \approx 0$ for all the N values we chose, and plot the magnitude of the phonon wave function $|\Psi(x,t_f)|^2$ in Fig. 4(b). Again, we find that for $N = 45$ and 75 a portion of energy remains confined within the range of the IDT after a long time.

We also show the logarithm of the power spectrum $|\mathcal{F}_\omega[\alpha(t;N)]|^2$ in Fig. 3(d), where $\mathcal{F}_\omega[f(t)]$ represents the Fourier transform of $f(t)$. We observe qualitative agreement between Figs. 3(b) and 3(d) in terms of the locations of peaks when peaks are observed, but with discrete frequencies rather than continuous as a function of N. For example, from Figs. 4(a) and 4(b), we also find that for some other $N \gg N_T$, such as $N = 60$, the atom still decays fast into the continuum and no peak is seen in the power spectrum. This behavior is caused by a mismatch between the atom length $N\lambda$ and the effective "vacuum Rabi wavelength" $\lambda_R(N) = 2\pi c_s/\mathrm{Max}_n[\mathrm{Im}\{s_n(N)\}]$, as the circuit QAD model introduces a hard spatial boundary to the atom. Therefore, the circuit QAD model requires the atom size N_m to satisfy an additional phase matching condition $N_m\lambda \approx m\lambda_R(N_m)$ for the bounded

giant atom phenomenon, where $m \in \mathbb{N}$. We have discussed the first two cases, $N_1 = 45$ and $N_2 = 75$, and we further observe 1–2 peaks that correspond to m in Fig. 4(b). In Fig. 4(c), we show a comparison between a numerical simulation of the circuit QAD model [by finding largest resonances on the power spectrum, i.e., the brightest points on Fig. 3(d)], and analytic calculations of N_m using the Lorentzian model (by solving the equation $N_m\lambda = 2\pi c_s m/\mathrm{Max}_n[\mathrm{Im}\{s_n(N_m)\}]$). Again, we find a qualitative agreement between two models. We also plot the ratio between $N_{m,\mathrm{cQAD}}$ and $N_{m,\mathrm{Lor}}$, which is stabilized around 0.93 for $m \geqslant 3$.

Here we present an intuitive picture of understanding how phase matching conditions for bounded giant atoms arise even in a continuous model. Consider the case where the atom is set to the excited state at $t = 0$: During the first half of the effective vacuum Rabi oscillation $t = (0, T/2)$ the nominal outgoing phonon wave function becomes approximately $\psi_1(x) \propto \exp(-a|x|)$, where a is some geometrical parameter with a $1/x$ unit. During the second half of the period, this undergoes destructive interference with the newly emitted phonon state $\psi_2(x) \propto -\exp(-ab|x|)$ while ψ_1 moves outward a distance $\lambda_R/2$. The second portion has a π phase shift and some loss b due to energy being emitted in the first half. Therefore, the total emission in the far field ($|x| \gg N\lambda$) within the whole cycle is $\psi(x) \propto \exp(-a|x + \lambda_R/2|) - \exp(-ab|x|)$. For the Lorentzian model in the giant atom regime, $b \sim a\lambda_R/2$ and these can cancel.

V. DISCUSSION AND CONCLUSION

In this work, we have generalized the Weisskopf-Wigner theory from a pointlike atom to a bounded giant atom that interacts with the medium instantaneously over a continuous spatial length $N\lambda$, with a simple Lorentzian toy model. When the coherence of the atom travels through the antenna much faster than the emission, we have observed that if its size N satisfies both (1) the atom size N is larger than the transition size N_T and (2) the phase matching condition $N\lambda \approx m\lambda_R(N)$, a giant atom dynamic emerges, which is characterized by suppressed relaxation and effective vacuum Rabi oscillation with a phononic wave packet bound to the antenna, even in the absence of a cavity. To verify our results, we have compared it with the exact numerics of a realistic circuit QAD coupling model. We have specifically studied the circuit QAD apparatus, but our analysis can be applied similarly to other quantum electromechanical systems with a large coupling spatial range [35–37]. For example, an optomechanical system where a membrane and a microwave waveguide coupled via radiation pressure could have similar effects.

Note added. Recently, we learned of a similar result in Ref. [38].

ACKNOWLEDGMENTS

We thank D. Carney, C. Flowers, J. Kunjummen, F. Liu., Y. Nakamura, A. Noguchi, K. Sinha, E. Tiesinga, A. Gorshkov, and K. Srinivasan for insightful discussions. Y.W. acknowledges support by ARL CDQI, ARO MURI, NSF PFC at JQI, AFOSR, the DoE BES QIS program (Award No. DE-SC0019449), the DoE ASCR Quantum Testbed Pathfinder program (Award No. DE-SC0019040), DoE ASCR Accelerated Research in Quantum Computing program (Award No. DE-SC0020312), and the NSF PFCQC program.

APPENDIX A: DERIVATION OF THE CIRCUIT QAD MODEL

Consider the system described by Fig. 1, where the IDT aligns to the [110] direction of a cubic crystal substrate. We assume the electrodes of the IDT do not change the mass density on the surface, and we model the Josephson junction as an LC circuit with inductance L_J and capacitance C_J. The Lagrangian of the system is [39]

$$\mathcal{L} = \frac{L_J}{2}\dot{Q}^2 - \frac{1}{2C_\Sigma}Q^2 + \frac{W}{2}\int_0^\infty dz \int_{-\infty}^{\infty} dx \left[\rho\left(\dot{u_x}^2 + \dot{u_z}^2\right) - c'_{11}\left(\frac{\partial u_x}{\partial x}\right)^2 - c_{11}\left(\frac{\partial u_z}{\partial z}\right)^2 - 2c_{12}\frac{\partial u_x}{\partial x}\frac{\partial u_z}{\partial z} - c_{44}\left(\frac{\partial u_x}{\partial z} + \frac{\partial u_z}{\partial x}\right)^2\right] - We_{14}\int_0^\infty dz \int_{-d/2}^{d/2} dx \left[\frac{\partial V}{\partial x}\left(\frac{\partial u_x}{\partial z} + \frac{\partial u_z}{\partial x}\right)\right], \tag{A1}$$

where variables $Q(t)$ and $\vec{u}(x, z, t) = \{u_x, u_z\}(x, z, t)$ are the charge and strain degrees of freedom, respectively. The total capacitance $C_\Sigma = C_J + C_{\mathrm{IDT}}$, where the capacitance of IDT C_{IDT} can be calculated according to [40]. W is the width of the IDT. The material parameters ρ, c_{11}, c_{12}, c_{44}, e_{14} are the density, elements of elastic tensor, and piezoelectric tensor of the substrate. For the cubic crystal, we have $c'_{11} = (c_{11} + c_{12} + 2c_{44})/2$ [41]. To represent SAW modes, we take the ansatz [41]

$$u_x(x, z, t) = \sum_{j=-\infty}^{\infty} C_j(t)\xi_j(z)\psi_j(x), \tag{A2}$$

$$u_z(x, z, t) = \sum_{j=-\infty}^{\infty} C_j(t)\zeta_j(z)\psi_j(x), \tag{A3}$$

where $\psi_j(x) = \sqrt{2/L}e^{-iK_j x}$, $\xi_j(z) = \sqrt{2/L}e^{-qK_j z - i\phi}$, and $\zeta_j(z) = \sqrt{2/L}re^{-qK_j z - i\phi}$ with periodic boundary conditions in x, and $\vec{u} = 0$ at $z \to \infty$. L and $K_j = \pi j/L$ are the length of the system and momenta of the modes, where $j \in \mathbb{Z}$. The fitting parameters $q, r \in \mathbb{C}$ and $\phi \in \mathbb{R}$ can be derived from [41]. The electric field oscillates rapidly enough that the electric potential $V(x)$ is

always quasistatic by the comparison of electron transmission. Therefore, we make the approximation

$$\frac{\partial V}{\partial x} = \begin{cases} -\frac{2Q}{C_\Sigma \lambda} & \text{for } \frac{2\eta-N}{2}\lambda \leqslant x < \frac{2\eta+1-N}{2}\lambda, \\ +\frac{2Q}{C_\Sigma \lambda} & \text{for } \frac{2\eta+1-N}{2}\lambda \leqslant x < \frac{2\eta+2-N}{2}\lambda, \end{cases} \tag{A4}$$

where $\eta = 0, 1, 2, \ldots, N-1$. Substituting Eqs. (A2)–(A4) into Eq. (A1), we get

$$\mathcal{L} = \frac{L_J}{2}\dot{Q}^2 - \frac{1}{2C_\Sigma}Q^2 + \frac{W}{2L}\sum_{j=-\infty}^{\infty}\left[\frac{\rho'}{K_j}|\dot{C}_j|^2 - c' K_j |C_j|^2 - \frac{e'}{C_\Sigma}\frac{\sin\left(\frac{K_j\lambda N}{2}\right)\tan\left(\frac{K_j\lambda}{4}\right)}{K_j\lambda} Q C_j\right]. \tag{A5}$$

The new parameters $\rho' = \rho(1+|r|^2)/\,\mathrm{Re}[q]$, $c' = \{c'_{11} + c_{44}|r|^2 + (c_{44}+c_{11}|r|^2)|q|^2 + i[c_{12}(r^*q^* - rq) + c_{44}(rq^* - r^*q)]\}/\,\mathrm{Re}[q]$, and $e' = 8e_{14}\,\mathrm{Re}[(i-r/q)e^{-i\phi}]$ are effective density, elastic constant, and piezoelectric constant, respectively. Then we define the momentum conjugates as $V = L_J\dot{Q}$, $P_j = M_j\dot{C}_j$, where $M_j = W\rho'/(LK_j)$. Then we can calculate the quantized Hamiltonian by mapping $C_j \to \sqrt{\hbar/(2M_j\omega_j)}(\hat{a}_j + \hat{a}_j^\dagger)$, $P_j \to -i\sqrt{\hbar M_j\omega_j/2}(\hat{a}_j - \hat{a}_j^\dagger)$, $Q \to \sqrt{\hbar/(2L_J\nu)}(\hat{\sigma}_- + \hat{\sigma}_+)$, $V \to -i\sqrt{\hbar L_J\nu/2}(\hat{\sigma}_- - \hat{\sigma}_+)$. Then we have

$$\hat{H} = \hbar\nu\hat{\sigma}_+\hat{\sigma}_- + \sum_{j=-\infty}^{\infty}\hbar\omega_j\hat{a}_j^\dagger\hat{a}_j + \frac{\hbar g_0\sqrt{\pi}}{\sqrt{L}}\sum_{j=-\infty}^{\infty}\frac{\sin\left(K_j\lambda N/2\right)\tan\left(K_j\lambda/4\right)}{K_j\lambda/\pi}(\hat{\sigma}_- + \hat{\sigma}_+)(\hat{a}_j + \hat{a}_j^\dagger), \tag{A6}$$

where $\nu \equiv 1/\sqrt{L_J C_\Sigma}$, $\omega_j \equiv c_s K_j$ (and $c_s = \sqrt{c'/\rho'}$), and $g_0 \equiv e'\sqrt{\pi W\nu/(C_\Sigma\sqrt{c'\rho'})}$. Taking the rotating wave approximation, the limit $L \to \infty$ then moving in to the rotating frame, we get the Hamiltonian (1) with Eq. (8).

In general, an artificial qubit [e.g., a DC superconducting quantum interference device (SQUID) as a generalization of Josephson junction] has tunable frequency of 0.1–10 GHz. Taking the speed of sound as 3000–5000 m s^{-1}, the corresponding phonon wavelength range is 0.5–30 μm. Engineering IDTs at this length scale has been achieved by multiple references such as Ref. [30]. Then we use parameters provided in Ref. [34] to estimate γ_1 and to validate the experimental feasibility of our model: $c_{11} = 12.26$, $c_{12} = 5.71$, $c_{44} = 6.00$, $c'_{11} = 14.99$ ($\times 10^{10}$ N m^{-2}), $q = 0.5 + 0.48i$, $r = -0.68 + 1.16i$, $\phi = 1.05$, $\rho = 5307$ kg m^{-3}, $e_{14} = 0.157$ C m^{-2}, and assume reasonable parameters as $\nu \approx 5$ GHz, $C_\Sigma = 2.5 \times 10^{-11}$ F, $W = 50$ μm. Then our numerical estimations of parameters are $\rho' = 14902$ kg m^{-3}, $c' = 28.73 \times 10^{10}$ N m^{-2}, $e' = -1.248$ C m^{-2}, $g_0 = -19.34$ $\sqrt{\mu\mathrm{m}}$ MHz, $c_s = 4391$ m s^{-1}, $\gamma_1 = 4\pi g_0^2/c_s \approx 1.07$ MHz. As $\gamma_1 > \pi \times 10^{-5}\nu$ is possible, we conclude that experimental realization can be even easier than our analysis.

APPENDIX B: EXPLICIT SOLUTIONS OF THE LORENTZIAN MODEL

Here we provide the explicit form for the roots of Eq. (10):

$$s_n = -\frac{\nu}{3N} + \frac{e^{-(2i\pi/3)n}\nu(\nu - 3\gamma_1 N^3)}{6A} + \frac{Ae^{(2i\pi/3)n}}{6N^2}, \tag{B1}$$

where $n = 1, 2, 3$, and $A = \sqrt[3]{-18\gamma_1\nu^2N^6 + \nu^3N^3 + 3\sqrt{3}\sqrt{\gamma_1\nu^3N^9(\gamma_1^2N^6 + 11\gamma_1\nu N^3 - \nu^2)}}$. We can find the transition point N_T by taking the square root part of A equal zero, i.e., $\gamma_1^2N_T^6 + 11\gamma_1\nu N_T^3 - \nu^2 = 0$.

APPENDIX C: TOP-HAT MODEL AND BOUND STATES IN CONTINUUM

If $\gamma = 0$, then there exists at least one bound state in the 1D continuum. Such a state is known as a bound state in continuum (BIC) [22,42,43] or a decoherence-free state [13,44–46]. A BIC is an eigenstate of the Hamiltonian with eigenenergy within the continuum of the spectrum. Its existence usually requires symmetry protection or fine tuning [42]. We illustrate the bound state in the continuum using the top-hat toy model

$$g_{\mathrm{TH}}(k;N) \equiv \begin{cases} \sqrt{\frac{\gamma_1 c_s}{2\pi}}N, & |k| \leqslant \frac{2\pi}{N\lambda}, \\ 0, & |k| > \frac{2\pi}{N\lambda}. \end{cases} \tag{C1}$$

Note that though this toy model may seem simple, it is unphysical as it requires infinite spatial extent. Here, we report that a pair of purely imaginary solutions exist in our top-hat toy model. With Eq. (C1), we can write the equation $[\chi(s_n)]^{-1} = 0$ as

$$\pi s_n + iN^2\gamma_1 \ln\left(\frac{Ns_n - i\nu}{Ns_n + i\nu}\right) = 0, \tag{C2}$$

where the complex function $\ln(z)$ is multiple valued. Now we seek a purely imaginary solution $s_n = i\omega_n$, and we separate the real and imaginary parts of Eq. (C2), which results in

$$2\pi\omega_n + N^2\gamma_1 \ln\left[\left(\frac{\nu - N\omega_n}{\nu + N\omega_n}\right)^2\right] = 0, \quad \text{with } |\omega_n| > \frac{\nu}{N}. \tag{C3}$$

Although Eq. (C3) is transcendental, there always exists a pair of solutions for all N: We define the left-hand side of Eq. (C3) as $f(\omega_n)$: when $\omega_n \to \pm\nu/N$, $f(\omega_n) \to \mp\infty$; when $\omega_n \to \pm\infty$, $f(\omega_n) \to \pm\infty$. As f is analytic, there exist a $\omega_1 < -\nu/N$ and a $\omega_2 > \nu/N$, such that $f(\omega_n) = 0$.

[1] V. Weisskopf and E. Wigner, Berechnung der natürlichen Linienbreite auf Grund der Diracschen Lichttheorie, Z. Phys. **63**, 54 (1930).

[2] P. W. Milonni, Why spontaneous emission? Am. J. Phys. **52**, 340 (1984).

[3] H. Walther, B. T H Varcoe, B.-G. Englert, and T. Becker, Cavity quantum electrodynamics, Rep. Prog. Phys. **69**, 1325 (2006).

[4] T. Niemczyk, F. Deppe, H. Huebl, E. P. Menzel, F. Hocke, M. J. Schwarz, J. J. Garcia-Ripoll, D. Zueco, T. Hümmer, E. Solano, A. Marx, and R. Gross, Circuit quantum electrodynamics in the ultrastrong-coupling regime, Nat. Phys. **6**, 772 (2010).

[5] X. Gu, A. F. Kockum, A. Miranowicz, Y. Liu, and F. Nori, Microwave photonics with superconducting quantum circuits, Phys. Rep. **718**, 1 (2017).

[6] H. Zheng, D. J. Gauthier, and H. U. Baranger, Waveguide QED: Many-body bound-state effects in coherent and Fock-state scattering from a two-level system, Phys. Rev. A **82**, 063816 (2010).

[7] Y.-L. L. Fang and H. U. Baranger, Waveguide QED: Power spectra and correlations of two photons scattered off multiple distant qubits and a mirror, Phys. Rev. A **91**, 053845 (2015).

[8] F. Dinc, I. Ercan, and A. M. Brańczyk, Exact Markovian and non-Markovian time dynamics in waveguide QED: Collective interactions, bound states in continuum, superradiance and subradiance, Quantum **3**, 213 (2019).

[9] R. H. Dicke, Coherence in spontaneous radiation processes, Phys. Rev. **93**, 99 (1954).

[10] M. Gross and S. Haroche, Superradiance: An essay on the theory of collective spontaneous emission, Phys. Rep. **93**, 301 (1982).

[11] S. Datta, *Surface Acoustic Wave Devices* (Prentice-Hall, Englewood Cliffs, NJ, 1986).

[12] G. Andersson, B. Suri, L. Guo, T. Aref, and P. Delsing, Non-exponential decay of a giant artificial atom, Nat. Phys. **15**, 1123 (2019).

[13] A. F. Kockum, G. Johansson, and F. Nori, Decoherence-Free Interaction between Giant Atoms in Waveguide Quantum Electrodynamics, Phys. Rev. Lett. **120**, 140404 (2018).

[14] L. Guo, A. Grimsmo, A. F. Kockum, M. Pletyukhov, and G. Johansson, Giant acoustic atom: A single quantum system with a deterministic time delay, Phys. Rev. A **95**, 053821 (2017).

[15] A. Ask, M. Ekström, P. Delsing, and G. Johansson, Cavity-free vacuum-Rabi splitting in circuit quantum acoustodynamics, Phys. Rev. A **99**, 013840 (2019).

[16] K. Sinha, P. Meystre, E. A. Goldschmidt, F. K. Fatemi, S. L. Rolston, and P. Solano, Non-Markovian Collective Emission from Macroscopically Separated Emitters, Phys. Rev. Lett. **124**, 043603 (2020).

[17] Y. Wang, M. J. Gullans, A. Browaeys, J. V. Porto, D. E. Chang, and A. V. Gorshkov, Single-photon bound states in atomic ensembles, arXiv:1809.01147.

[18] G. Calajó, Y.-L. L. Fang, H. U. Baranger, and F. Ciccarello, Exciting a Bound State in the Continuum through Multiphoton Scattering Plus Delayed Quantum Feedback, Phys. Rev. Lett. **122**, 073601 (2019).

[19] P.-O. Guimond, A. Roulet, H. N. Le, and V. Scarani, Rabi oscillation in a quantum cavity: Markovian and non-Markovian dynamics, Phys. Rev. A **93**, 023808 (2016).

[20] L. Qiao and C.-P. Sun, Atom-photon bound states and non-Markovian cooperative dynamics in coupled-resonator waveguides, Phys. Rev. A **100**, 063806 (2019).

[21] C. Gonzalez-Ballestero, F. J. García-Vidal, and E. Moreno, Non-Markovian effects in waveguide-mediated entanglement, New J. Phys. **15**, 073015 (2013).

[22] S. Garmon, T. Petrosky, L. Simine, and D. Segal, Amplification of non-Markovian decay due to bound state absorption into continuum, Fortschr. Phys. **61**, 261 (2013).

[23] H.-P. Breuer, E.-M. Laine, J. Piilo, and B. Vacchini, Colloquium: Non-Markovian dynamics in open quantum systems, Rev. Mod. Phys. **88**, 021002 (2016).

[24] F. Dinc and A. M. Brańczyk, Non-Markovian super-superradiance in a linear chain of up to 100 qubits, Phys. Rev. Research **1**, 032042(R) (2019).

[25] L. R. Sletten, B. A. Moores, J. J. Viennot, and K. W. Lehnert, Resolving Phonon Fock States in a Multimode Cavity with a Double-Slit Qubit, Phys. Rev. X **9**, 021056 (2019).

[26] B. A. Moores, L. R. Sletten, J. J. Viennot, and K. W. Lehnert, Cavity Quantum Acoustic Device in the Multimode Strong Coupling Regime, Phys. Rev. Lett. **120**, 227701 (2018).

[27] K. J. Satzinger, Y. P. Zhong, H.-S. Chang, G. A. Peairs, A. Bienfait, M.-H. Chou, A. Y. Cleland, C. R. Conner, É. Dumur, J. Grebel, I. Gutierrez, B. H. November, R. G. Povey, S. J. Whiteley, D. D. Awschalom, D. I. Schuster, and A. N. Cleland, Quantum control of surface acoustic-wave phonons, Nature (London) **563**, 661 (2018).

[28] A. Noguchi, R. Yamazaki, Y. Tabuchi, and Y. Nakamura, Single-photon quantum regime of artificial radiation pressure on a surface acoustic wave resonator, Nat. Commun. **11**, 1183 (2020).

[29] A. Noguchi, R. Yamazaki, Y. Tabuchi, and Y. Nakamura, Qubit-Assisted Transduction for a Detection of Surface Acoustic Waves near the Quantum Limit, Phys. Rev. Lett. **119**, 180505 (2017).

[30] R. Manenti, A. F. Kockum, A. Patterson, T. Behrle, J. Rahamim, G. Tancredi, F. Nori, and P. J. Leek, Circuit quantum acoustodynamics with surface acoustic waves, Nat. Commun. **8**, 975 (2017).

[31] T. Aref, P. Delsing, M. K. Ekström, A. F. Kockum, M. V. Gustafsson, G. Johansson, P. J. Leek, E. Magnusson, and R. Manenti, Quantum acoustics with surface acoustic waves, in *Superconducting Devices in Quantum Optics* (Springer International, Cham, 2016), p. 217.

[32] A. Frisk Kockum, P. Delsing, and G. Johansson, Designing frequency-dependent relaxation rates and Lamb shifts for a giant artificial atom, Phys. Rev. A **90**, 013837 (2014).

[33] G. De Nittis and M. Lein, *Linear Response Theory: An Analytic-Algebraic Approach* (Springer, Berlin, 2017).

[34] M. J. A. Schuetz, E. M. Kessler, G. Giedke, L. M. K. Vandersypen, M. D. Lukin, and J. I. Cirac, Universal Quantum Transducers Based on Surface Acoustic Waves, Phys. Rev. X **5**, 031031 (2015).

[35] R. Singh and T. P. Purdy, Detecting Thermal Acoustic Radiation with an Optomechanical Antenna, arXiv:1911.09607.

[36] S. Kim, X. Xu, J. M. Taylor, and G. Bahl, Dynamically induced robust phonon transport and chiral cooling in an optomechanical system, Nat. Commun. **8**, 205 (2017).

[37] A. González-Tudela, C. S. Muñoz, and J. I. Cirac, Engineering and Harnessing Giant Atoms in High-Dimensional Baths: A Proposal for Implementation with Cold Atoms, Phys. Rev. Lett. **122**, 203603 (2019).

[38] L. Guo, A. F. Kockum, F. Marquardt, and G. Johansson, Oscillating bound states for a giant atom, arXiv:1911.13028.

[39] D. Royer and E. Dieulesaint, *Elastic Waves in Solids I: Free and Guided Propagation* (Springer, Berlin, 1996).

[40] R. Igreja and C. J. Dias, Analytical evaluation of the interdigital electrodes capacitance for a multi-layered structure, Sens. Actuators A: Phys. **112**, 291 (2004).

[41] R. Stoneley, The propagation of surface elastic waves in a cubic crystal, Proc. R. Soc. A **232**, 447 (1955).

[42] C. W. Hsu, B. Zhen, A. D. Stone, J. D. Joannopoulos, and M. Soljacic, Bound states in the continuum, Nat. Rev. Mater. **1**, 16048 (2016).

[43] F. H. Stillinger and D. R. Herrick, Bound states in the continuum, Phys. Rev. A **11**, 446 (1975).

[44] D. Suter and G. A. Álvarez, Colloquium: Protecting quantum information against environmental noise, Rev. Mod. Phys. **88**, 041001 (2016).

[45] D. A. Lidar, I. L. Chuang, and K. B. Whaley, Decoherence-Free Subspaces for Quantum Computation, Phys. Rev. Lett. **81**, 2594 (1998).

[46] V. Paulisch, H. J. Kimble, and A. González-Tudela, Universal quantum computation in waveguide QED using decoherence free subspaces, New J. Phys. **18**, 043041 (2016).

Appendix B: Publication for Chapter 3: Feedback induced magnetic phases in binary Bose-Einstein condensates

Feedback induced magnetic phases in binary Bose-Einstein condensates

Hilary M. Hurst [1,2] Shangjie Guo,[3] and I. B. Spielman [1]

[1]*Joint Quantum Institute, National Institute of Standards and Technology, and University of Maryland, Gaithersburg, Maryland 20899, USA*
[2]*Department of Physics and Astronomy, San José State University, San José, California 95192, USA*
[3]*Joint Quantum Institute and Department of Physics, University of Maryland, College Park, Maryland 20742, USA*

(Received 14 July 2020; accepted 6 November 2020; published 7 December 2020)

Weak measurement in tandem with real-time feedback control is a new route toward engineering novel nonequilibrium quantum matter. Here we develop a theoretical toolbox for quantum feedback control of multicomponent Bose-Einstein condensates (BECs) using backaction-limited weak measurements in conjunction with spatially resolved feedback. Feedback in the form of a single-particle potential can introduce effective interactions that enter into the stochastic equation governing system dynamics. The effective interactions are tunable and can be made analogous to Feshbach resonances—spin independent and spin dependent—but without changing atomic scattering parameters. Feedback cooling prevents runaway heating due to measurement backaction and we present an analytical model to explain its effectiveness. We showcase our toolbox by studying a two-component BEC using a stochastic mean-field theory, where feedback induces a phase transition between easy-axis ferromagnet and spin-disordered paramagnet phases. We present the steady-state phase diagram as a function of intrinsic and effective spin-dependent interaction strengths. Our result demonstrates that closed-loop quantum control of Bose-Einstein condensates is a powerful tool for quantum engineering in cold-atom systems.

DOI: 10.1103/PhysRevResearch.2.043325

I. INTRODUCTION

Quantum gas experiments have exquisite control over the low-energy Hamiltonian governing system dynamics, providing demonstrated opportunities to study interacting many-body quantum systems with great precision. As a result, ultracold atoms have emerged as a leading platform in "analog quantum simulation" [1–6], where experiments have successfully explored condensed-matter phenomena such as the superfluid-Mott insulator transition [7], the BEC-BCS crossover [8,9], and spin-orbit coupling [10]. Cutting-edge experiments now realize systems with long-range interactions [11] or novel nonequilibrium dynamics [12,13]. In contrast, quantum simulation of open systems remains relatively unexplored [14], and careful application of feedback control to many-body quantum systems is a different approach toward this goal.

Feedback control of many-body systems could enable observation of a wide range of new phenomena in the dynamical steady state, where a potentially larger class of states is possible than in thermal equilibrium [15,16]. Existing proposals include preparation of many-body pure states via reservoir engineering [17–20], nonthermal steady states [21,22], stable non-Abelian vortices [23], or time crystals [24]. Here, we showcase the flexibility of weak measurements coupled with spatially resolved feedback for the quantum simulation of time-dependent effective Hamiltonians using a two-component Bose-Einstein condensate (BEC) as a model spinor system [25–27].

We develop a theory of weak measurement and classical feedback in weakly interacting quantum systems framed in the context of quantum control theory [28]. Using our general formalism, we investigate the steady-state phases of a two-component BEC subject to weak measurement and classical feedback via a spin-dependent applied potential, enabling both density- and spin-dependent feedback protocols.

Spatially local feedback can result in spin-dependent effective interaction terms in the stochastic equation governing condensate dynamics. Depending on the interplay of intrinsic and effective (i.e., feedback induced) spin-dependent interactions, the condensate steady-state phase is either an easy-axis ferromagnet or spin-disordered paramagnet. The effective interaction is tunable via the gain of the feedback signal, enabling a reversible, feedback induced phase transition. The transition is reminiscent of what is achieved by tuning intrinsic interactions via a spin-dependent Feshbach resonance [29]; however, here the atomic scattering lengths remain unchanged. We develop a signal filtering and cooling scheme to minimize heating and show that the condensate remains intact under feedback and measurement backaction. Our result opens the door to engineering dynamical and/or spatially dependent effective interactions in quantum gases via closed-loop feedback control.

Previous works have considered quantum control protocols for BECs [30–38]. Feedback schemes thus far presented have focused on driving a condensate to its ground state by altering the position and strength of a harmonic trapping potential

[30–34], or to deterministically prepare a target state [35,38], possibly for quantum memory applications [36,37]. Here we move beyond the realm of specific state control toward implementation of designer effective Hamiltonians or Liouvillian functions with possibly unknown dynamical steady states.

The paper is structured as follows: In Sec. II, we present our main formal results, including the stochastic equation describing condensate dynamics, and introduce a toy model illustrating the salient features of the control protocol. We show that locally applied feedback induces a phase transition between easy-axis ferromagnetic and disordered paramagnetic phases in a two-component condensate.

In Sec. III, we elaborate on our feedback cooling protocol and characterize the resulting steady state via condensate fraction, von Neumann entropy, and energy. We show that heating due to measurement backaction can be effectively mitigated by feedback cooling. In Sec. IV, we discuss the feedback induced steady-state phases in more detail and elucidate the nature of the phase transition in our system. We conclude in Sec. V.

II. SUMMARY OF RESULTS

A. General formalism

We model dispersive imaging of a quasi-one-dimensional (1D) multicomponent Bose-Einstein condensate of length L via spin-resolved phase-contrast imaging [39] and we label individual components by an index s. We consider time- and space-resolved measurements of atomic density $\hat{n}_s(x,t)$ in each component using the Gaussian measurement model developed in detail in Ref. [40]. Stroboscopic weak measurements with strength φ result in the measurement signal

$$\mathcal{M}_s(x,t) = \langle \hat{n}_s(x,t)\rangle + \frac{m_s(x)}{\varphi}, \tag{1}$$

where $m_s(x)$ describes spatiotemporal quantum projection noise associated with the measurement. The measurement is characterized by Fourier domain Gaussian statistics $\overline{\tilde{m}_{s,k}} = 0$ and $\overline{\tilde{m}_{s,k}\tilde{m}_{s,k'}} = L\Theta(|k| - k_c)\overline{dW_{s,k}dW_{s',k'}}/2dt^2$, where $dW_{s,k}$ is a Wiener increment with $\overline{dW_{s,k}} = 0$ and $\overline{dW_{s,k}dW_{s',k'}} = dt\delta_{ss'}\delta_{kk'}$ for a time increment dt [41]. The Heaviside function Θ enforces a momentum cutoff at $k_c = 2\pi/\lambda$, accounting for the fact that the physical measurement process can only resolve information with length scales larger than $\lambda/2\pi$. The observer does not directly obtain information about the condensate phase using this protocol.

Here, we do not impose any additional resolution limits on the measurement results. In any real experiment, an additional momentum-space transfer function modeling the imaging system's exit pupil should be applied to $\mathcal{M}_s(x,t)$ to account for imperfect imaging resolution [42]. This process will depend on the specific details of the imaging system, therefore we consider it beyond the scope of this work.

We use the aggregate measurement result $\mathcal{M}$, a function of x and s, to generate feedback signals in the form of a single-particle potential $\check{V}[\mathcal{M}]$, where $\check{\cdot}$ indicates an operator in component space. In this work, we consider a potential which is local in space.

We describe the condensate in the mean-field approximation using a complex spinor order parameter $\Psi(x) = [\psi_1(x), \psi_2(x), \ldots]^T$, where $\psi_s(x)$ is a classical field describing the dynamics of component s. The total density is $n(x) = \Psi^\dagger(x)\check{\mathbb{1}}\Psi(x)$ and the order parameter is normalized to the number of particles, $N = \int dx\, n(x)$. From Eq. (1), the measurement results at the mean-field level therefore depend on the field amplitude via $\langle \hat{n}_s(x)\rangle \to |\psi_s(x)|^2$. Measurement backaction leads to stochastic evolution of the order parameter, which results in condensate heating [40,43] in the absence of a cooling protocol, which we describe in Sec. III.

The combined measurement and quantum control process is described by a stochastic equation of motion,

$$d\Psi(x) = d\Psi(x)|_{\mathrm{H}} + d\Psi(x)|_{\mathrm{M}} + d\Psi(x)|_{\mathrm{F}}, \tag{2}$$

for the condensate order parameter $\Psi(x)$. Here,

$$d\psi_s(x)|_{\mathrm{H}} = -\frac{i}{\hbar}[\hat{\mathcal{H}}_{ss'}(x) - \mu\delta_{ss'}]\psi_{s'}(x)dt, \tag{3}$$

$$d\psi_s(x)|_{\mathrm{M}} = \left[-\frac{\varphi^2 k_c}{4\pi} + \varphi m_s(x)\right]\psi_s(x)dt, \tag{4}$$

$$d\psi_s(x)|_{\mathrm{F}} = -\frac{i}{\hbar}V_{ss'}[\mathcal{M}](x)\psi_{s'}(x)dt \tag{5}$$

denote contributions from unitary (i.e., closed-system) evolution, measurement backaction, and feedback, respectively, and μ is the chemical potential. We adopt the implied summation convention over repeated indices and set $\hbar = 1$.

Using this general formalism, we study a condensate of ^{87}Rb atoms from which we select two hyperfine states, yielding a two-component condensate [27,44] with components denoted by $s = \uparrow, \downarrow$. The Hamiltonian in Eq. (3) is the usual Gross-Pitaevskii equation (GPE) describing closed-system dynamics, which takes the explicit form

$$\hat{\mathcal{H}}_{ss'}\psi_{s'} = [\hat{H}_0 + u_0 n]\mathbb{1}_{ss'}\psi_{s'} + u_2 S_z \sigma^z_{ss'}\psi_{s'}, \tag{6}$$

for two-component condensates, with (x,t) indices suppressed for clarity. Here, $S_z(x) = \Psi^\dagger(x)\check{\sigma}^z\Psi(x)$ indicates the spin density and $\check{\boldsymbol{\sigma}} = (\check{\sigma}^x, \check{\sigma}^y, \check{\sigma}^z)$ is a vector of the Pauli operators. The single-particle Hamiltonian is $\hat{H}_0 = \hat{p}^2/2m_a$ for atoms of mass m_a. The intrinsic spin-independent u_0 and spin-dependent u_2 interaction strengths serve to define $\xi = 1/\sqrt{2m_a\mu}$ and $\xi_s = \xi\sqrt{u_0/2|u_2|}$, the healing length and spin-healing length, respectively.

Equation (4) describes measurement backaction. Separate measurements of each condensate component result in independent backaction noise $m_s(x)$. Equation (5) describes feedback, applied via the potential term $\check{V}[\mathcal{M}]$. The feedback potential combines a deterministic part containing information about the condensate dynamics with a stochastic part due to quantum projection noise. Therefore, both $d\Psi|_{\mathrm{F}}$ and $d\Psi|_{\mathrm{M}}$ contribute to stochastic condensate dynamics. When each individual measurement is very weak, the density of noncondensed particles remains low. Therefore, we assume $\Psi(x)$ to be well described by a lowest-order Hartree-Fock theory throughout its evolution. This assumption is validated in Secs. III B and III C.

B. Key feedback concepts

Our aim is to develop feedback schemes which add new effective interaction terms to the Hamiltonian while minimizing quantum projection noise. We illustrate the core concept of feedback using a toy model. The toy model is a simplified version of the feedback protocols developed in later sections, which nonetheless illustrates a key result: weak measurements combined with feedback can be used to engineer new effective Hamiltonians.

1. Toy model

Here we construct a minimal model of measurement and feedback for single-component systems, and therefore suppress the component index s. We weakly measure the density, then apply a proportional feedback potential,

$$V[\mathcal{M}](x,t) = g_0 \mathcal{M}(x,t), \tag{7}$$

where the gain parameter g_0 denotes the feedback strength. Inserting Eq. (1) into Eq. (7) gives a feedback potential with two contributions. The first is an effective mean-field interaction,

$$V^{\rm eff}(x,t) = g_0 n(x,t), \tag{8}$$

and the second is a stochastic contribution,

$$V^{\rm fluct}(x,t) = \frac{g_0 m(x)}{\varphi}. \tag{9}$$

By direct substitution of $V[\mathcal{M}]$ into Eq. (5), the dynamical Eqs. (3)–(5) reduce to two equations $d\Psi(x) = d\Psi(x)|_{\rm H'} + d\Psi(x)|_{\rm M'}$ with modified unitary evolution and stochastic terms,

$$d\psi(x)|_{\rm H'} = -i[\hat{\mathcal{H}}^{\rm eff}(x) - \mu]\psi(x)dt, \tag{10}$$

$$d\psi(x)|_{\rm M'} = \left[-\frac{\varphi^2 k_{\rm c}}{4\pi} + \left(\varphi - i\frac{g_0}{\varphi}\right)m(x)\right]\psi(x)dt. \tag{11}$$

The effective Hamiltonian $\hat{\mathcal{H}}^{\rm eff}(x)$ has the same form as the spin-independent term in Eq. (6), but with u_0 replaced by an effective interaction constant $u_0^{\rm eff} = u_0 + g_0$. Likewise, the noise in the stochastic evolution is modified due to the contribution of $V^{\rm fluct}(x,t)$. This simple model illustrates how feedback can be used to create new effective Hamiltonians with modified interaction terms.

Returning to the two-component case, we consider the spin-dependent feedback potential,

$$\check{V}[\mathcal{M}](x,t) = g_0 \mathcal{M}_n(x,t)\check{\mathbb{1}} + g_2 \mathcal{M}_z(x,t)\check{\sigma}^z, \tag{12}$$

describing separate contributions to the density and spin sectors controlled by independent gain parameters g_0 and g_2, respectively. Measurement signals $\mathcal{M}_s$ are used to calculate total density and spin density, given by $\mathcal{M}_n = \mathcal{M}_\uparrow + \mathcal{M}_\downarrow$ and $\mathcal{M}_z = \mathcal{M}_\uparrow - \mathcal{M}_\downarrow$, respectively. Following the same algebraic arguments, the feedback potential (12) leads to effective interaction strengths $u_0^{\rm eff} = u_0 + g_0$, $u_2^{\rm eff} = u_2 + g_2$, along with modified stochastic noise on each component ψ_s.

In the following, we use this guiding principle to develop a measurement and feedback scheme which controls the magnetic properties of a two-component condensate without changing the internal interaction parameters. The simplified protocol presented in this section is impractical due to runaway heating [40], from the repeated and uncompensated application of the stochastic potential in Eq. (11). In Sec. III, we introduce a feedback cooling protocol that prevents runaway heating and thus completes our toolbox for quantum feedback control.

2. Signal filtering

In the toy model above, the feedback potential is governed only by local-in-time measurement results. Because Eqs. (3)–(5) describe continuous time evolution, the effect of $V^{\rm fluct}(x,t)$ in Eq. (9) would seem to diverge as $dt \to 0$. However, any measurement signal $\mathcal{M}_i(x,t)$ can be filtered in time to provide a running best estimate of the measured observable i (where $i = n, z$, etc.).

The resulting estimator ε_i is derived from $\mathcal{M}_i$ via the low-pass filter

$$\tau_i \dot{\varepsilon}_i(x,t) + \varepsilon_i(x,t) = \mathcal{M}_i(x,t), \tag{13}$$

i.e.,

$$\varepsilon_i(x,t) = \frac{1}{\tau_i}\int_{-\infty}^{t} dt'\, \mathcal{M}_i(x,t') e^{-(t-t')/\tau_i}, \tag{14}$$

where τ_i is the filter time constant and $\mathcal{M}_i(x,t)$ indicates the unfiltered measurement signal. This process filters the contribution of projection noise present at timescales below τ_i, making τ_i the effective measurement time associated with the estimator ε_i.

We derive all of our feedback potentials using estimators ε_i instead of measurement signals $\mathcal{M}_i$, thereby controlling the noise applied to the system via feedback. In our feedback scheme, we use separate estimators of the total density, spin density, or density in component s, denoted ε_n, ε_z, ε_s, respectively, which can have different filter time constants τ_n, τ_z, and τ_s.

C. Feedback induced magnetic phases

We now focus on feedback-tuned spin-dependent interactions with $g_2 \neq 0$ and $g_0 = 0$. Guided by our toy model, we expect the steady-state phase diagram of a two-component BEC to resemble the ground-state phase diagram for u_2. The ground-state density $n(x)$ and spin density $S_z(x)$ are shown in Fig. 1(a). For $u_2 > 0$, the ground state is an easy-plane ferromagnet with $S_z(x) = 0$, while for $u_2 < 0$, the ground state is an easy-axis ferromagnet, consisting of spin-polarized domains [25,44–46], separated by a domain wall.

Using the measurement and feedback procedure outlined in Sec. II B 1, we apply a forcing potential

$$\check{V}_{\rm f}(x,t) = g_2 \varepsilon_z(x,t)\check{\sigma}^z, \tag{15}$$

along with a cooling potential $\check{V}_{\rm c}$, to be described in Sec. III. Equation (15) changes the effective spin-dependent interaction strength via the gain g_2, based on the estimator of the spin density ε_z. The effective Hamiltonian for this protocol is

$$\check{\mathcal{H}}_{\rm eff} \approx [\hat{H}_0 + u_0 n]\check{\mathbb{1}} + \check{V}_c + [u_2 S_z + g_2 \varepsilon_z]\check{\sigma}^z. \tag{16}$$

The phase diagram is now a function of two variables: spin-dependent interaction strength u_2 and signal gain g_2, which

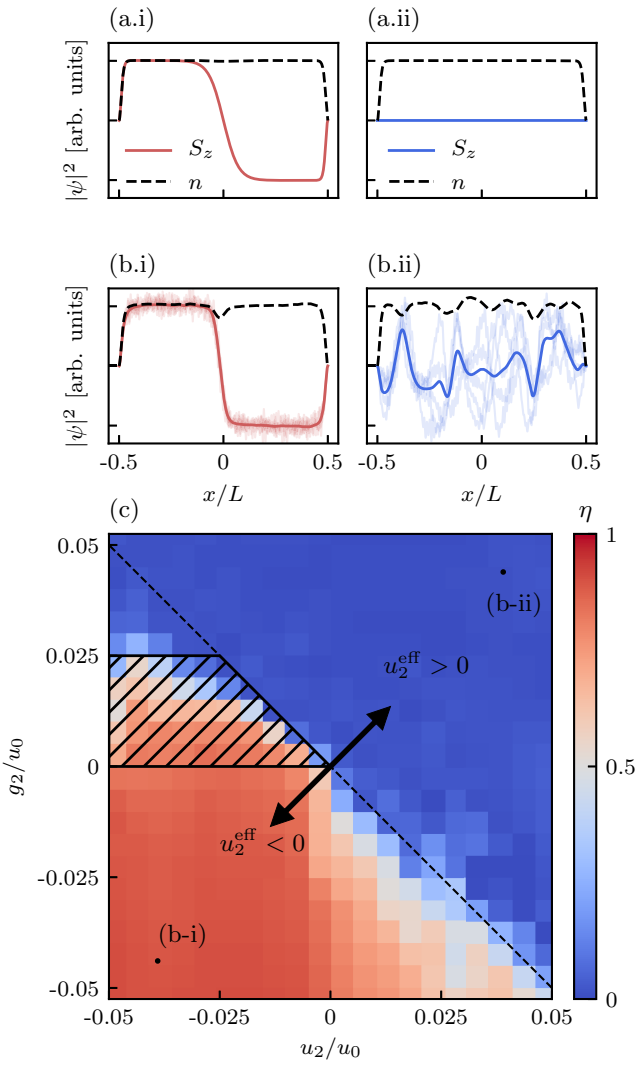

FIG. 1. (a) Ground-state density (black dashed curve) and spin density (solid curve) for (a.i) $u_2 < 0$ and (a.ii) $u_2 > 0$. (b) Steady-state density (black dashed curve) and spin density (solid curve) for (b.i) $u_2^{\rm eff} \lesssim 0$ and (b.ii) $u_2^{\rm eff} \gtrsim 0$, averaged over 100 ms. Semitransparent curves indicate S_z without time averaging. (c) Steady-state phase diagram as a function of u_2/u_0 and g_2/u_0 (defined in text), showing magnetically ordered, easy-axis ferromagnet (red/lower left) or spin-disordered paramagnet (blue/upper right) phases. The black dashed line indicates the expected phase boundary at $u_2^{\rm eff} = 0$, and the hatched region indicates bistability depending on the initial phase. The system enters an easy-axis ferromagnet if the initial condition is (a.i), and a spin-disordered paramagnet if the initial condition is (a.ii).

give an effective interaction strength $u_2^{\rm eff} \approx u_2 + g_2$. Examples of the two steady-state phases are shown in Fig. 1(b). Both phases have uniform density, but with very different spin character. For $u^{\rm eff} \lesssim 0$, the system is an easy-axis ferromagnet with well-defined, spin-polarized domains. For $u_2^{\rm eff} \gtrsim 0$, the system enters a spin-disordered paramagnetic phase, with large spin fluctuations. Figure 1(b) shows the spin density averaged over 100 ms (darker solid curve) and 10 individual time traces (semitransparent curves). The individual time traces show that the spin is essentially static in the ferromagnetic phase, but has large spatiotemporal fluctuations in the paramagnetic phase.

Figure 1(c) shows the steady-state phase diagram as a function of u_2/u_0 and g_2/u_0. As expected, the phase diagram is divided into two regimes delineated by $u_2^{\rm eff} = 0$ (black dashed curve). We quantify the steady-state phase using a time-separated correlation function of magnetization,

$$\eta = \frac{1}{\mathcal{A}} \int d\tau \int dt\, dx\, \frac{S_z(t+\tau, x) S_z(t, x)}{n(t+\tau, x) n(t, x)}, \tag{17}$$

where $\mathcal{A}$ is an overall normalization factor. A condensate with well-defined domains gives $\eta \gtrsim 0.5$; for the ground state with a single domain wall, $\eta \approx 1$. The disordered paramagnet phase with fluctuating magnetization has $\eta \approx 0$ because the local magnetization at any point x fluctuates strongly in time.

Like many magnetic systems, this system exhibits hysteretic behavior. When $g_2 < 0$, the easy-axis phase is robust to the initial condition of the system and over many different repetitions of the simulation with different noise realizations. The phase in the region where $u^{\rm eff} \lesssim 0$ with $u_2 < 0$ and $g_2 > 0$ is sensitive to the initial state, denoted by the hatched region in Fig. 1(c). In this region, the steady state of the system is an easy-axis ferromagnet only if it was initially in the ferromagnetic ground state with $u_2 < 0$, as in [Fig. 1(a.i)]. For the easy-plane ground state, as in Fig. 1(a.ii), domains do not form. We discuss this steady-state behavior for the easy-plane initial condition in Appendix B.

In the following sections, we examine the robustness of the feedback induced magnetic phases and feedback cooling. We show that despite repeated weak measurements and feedback, the condensate remains largely intact over the ∼4 s time period of the simulation. Furthermore, by changing the effective interaction via feedback, we demonstrate tunability between different steady-state phases. Spatially resolved, time-dependent feedback therefore provides a tool to dynamically change effective interactions in cold-atom systems.

III. FEEDBACK COOLING

Measurement backaction adds excitations to the condensate. The aim of feedback cooling is to apply feedback using information from the measurement signal to suppress the excitations, thereby stabilizing the condensate and preventing runaway heating. In this section, we develop a feedback cooling protocol for single and multicomponent condensates, which ensures the stability of the condensate during measurement and feedback. We connect the continuous measurement limit presented in Sec. II A to the experimental reality of discrete measurements. We then develop a feedback cooling protocol using a single discrete measurement as a building block. Finally, we show that during this protocol, the condensate fraction and entropy reach a steady state, but the GPE energy functional continues to slowly increase.

A. Single-measurement protocol

The continuous measurement limit is typically assumed *a priori* by taking $dt \to 0$. Since the variance of the measurement signal in Eq. (1) is $\propto 1/dt$, the variance in the

measurement record diverges in this limit. However, no physical measurement is infinitely fast. Integrating Eq. (1) over a small time window therefore yields a "single measurement." By considering this type of measurement, we can quantify a measurement protocol which extracts maximal information from the condensate while minimizing the negative effects of backaction. As in Sec. II B 1, here we consider measurements of a single-component condensate and drop the s index. It is straightforward to generalize this procedure to multicomponent condensates.

Consider a time-integrated version of Eq. (1) over an interval Δt, giving a single measurement of density. The measurement result is $\mathcal{M}(x) = n(x) + \bar{m}(x)/\kappa$, where the measurement strength $\kappa = \sqrt{\Delta t}\varphi$. The spatial quantum projection noise is $\bar{m}(x)$, where $\tilde{\bar{m}}_k$ has the same Fourier space statistics previously discussed, with $\overline{\tilde{\bar{m}}_k} = 0$ and $\overline{\tilde{\bar{m}}_k \tilde{\bar{m}}_{k'}} = L\delta_{kk'}\Theta(|k| - k_c)/2$. Directly after measurement, the updated wave function is $\psi_{|M}(x) \approx \psi(x) + \kappa\bar{m}(x)\psi(x)$. Thus, there exists an optimal measurement strength,

$$\kappa_* \approx \sqrt{\frac{1}{2\max[n(x)]}}, \tag{18}$$

such that the measurement outcome matches the postmeasurement density $n_{|M}$ exactly, i.e., $\mathcal{M}(x) = n_{|M}(x)$. In principle, the optimal measurement strength depends on the local density; however, as this is difficult to implement experimentally, we instead approximate κ_* to be constant. We then use this coupling value for feedback cooling.

If we could find a potential $V_{c|M}(x)$ for which the postmeasurement state is the ground state, $\psi_{|M}(x)$ would satisfy the stationary GPE,

$$\mu\psi_{|M} = \left[\hat{H}_0 + u_0 n_{|M} + V_{c|M}\right]\psi_{|M}. \tag{19}$$

In our feedback cooling protocol, we first apply the potential $V_{c|M}(x)$ for which the postmeasurement state *would* be the ground state (assuming a uniform phase). Then we approach the initial state by slowly—adiabatically—ramping off the applied cooling potential. We approximate $V_{c|M}$ using the Thomas-Fermi (TF) approximation of Eq. (19), giving $V_{c|M}(x) = \mu - u_0 n_{|M}(x)$. We then make the substitution $u_0 n_{|M}(x) \to g_c\mathcal{M}(x)$, where g_c is the cooling gain, an externally adjustable parameter (for which the expected value of u_0 is found to be optimal). This gives the feedback cooling potential function,

$$V_{c|M}(x,t) = [\mu - g_c\mathcal{M}_{t_m}(x)]f(t - t_m), \tag{20}$$

where t_m is the time of the measurement and $f(t)$ is a ramp-off function where $f(0) = 1$ and $f(t \to \infty) = 0$. In practice, we use $f(t - t_m) \approx 1 - \gamma(t - t_m)$, where γ is the ramp-off rate.

B. Bogoliubov theory for single-measurement protocol

Here we provide an analytical solution of the single-measurement-feedback protocol described above using Bogoliubov theory [47], with periodic boundary conditions. After making the Bogoliubov transformation, small excitations above the ground state of a weakly interacting spinless BEC with density n are described by the Hamiltonian

$$\hat{H}_{ph} = \sum_k \epsilon_k \hat{b}_k^\dagger \hat{b}_k, \tag{21}$$

where $\hat{b}_k^\dagger$ describes the creation of a Bogoliubov phonon with momentum k and energy $\epsilon_k = \mu\xi|k|\sqrt{\xi^2k^2 + 2}$. To facilitate our analytic treatment, we focus on the weak-measurement regime, in which, at most, one phonon mode is occupied, leading to wave functions of the form $|\psi\rangle = \alpha|\text{vac}\rangle + \sum_k \beta_k|k\rangle$, where $|k\rangle = \hat{b}_k^\dagger|\text{vac}\rangle$, and $|\text{vac}\rangle$ is the phonon vacuum.

Measurement backaction is described by the Kraus operator

$$\hat{K} = \exp\left\{-\frac{\kappa^2}{2}\int dx\left[\delta\hat{n}(x) - \frac{\bar{m}_{t_m}(x)}{\kappa}\right]^2\right\}, \tag{22}$$

with the density difference operator $\delta\hat{n}(x) \equiv \hat{n}(x) - n$. In the phonon basis, $\delta\hat{n}(x)$ can be expressed as a sum, $\delta\hat{n}(x) = \sqrt{n/L}\sum_k(c_k e^{-ikx}\hat{b}_k + \text{H.c.})$, of phonon creation and annihilation operators, with $c_k = [1 + 2/(\xi k)^2]^{-1/4}$.

In this representation, the feedback cooling operator derived from (20) is

$$\hat{V}_{c|M}(t) = \int dx\, V_{c|M}(x,t)\hat{n}(x). \tag{23}$$

Assuming adiabatic evolution, with ramp-off rate $\gamma \to 0$, and using first-order perturbation theory, the operator describing the cooling protocol is

$$\hat{R}_{|m} = 1 + \sum_k \frac{g_c c_k\sqrt{n}}{\kappa\epsilon_k\sqrt{L}}\left[\tilde{\bar{m}}_{t_m}(k)\hat{b}_k - \text{H.c.}\right]. \tag{24}$$

This expression is valid for $g_c c_k\sqrt{n} \ll \kappa\epsilon_k\sqrt{L}$. The probability of finding a phonon in state $|k\rangle$ after a measurement-feedback cycle is

$$\bar{P}_k = \overline{|\langle k|\hat{R}_{|m}\hat{K}|\text{vac}\rangle|^2} = \frac{n\kappa^2 c_k^2}{2}\left(1 - \frac{g_c}{\kappa^2\epsilon_k}\right)^2\Theta(|k| - k_c). \tag{25}$$

We draw two conclusions from this result: (1) Setting $g_c = 0$ gives the probability $n\kappa^2 c_k^2/2$ that the measurement created a phonon in state $|k\rangle$; and (2) the phonon mode with energy $\epsilon_{k,opt} = g_c\kappa^{-2}$ can be perfectly cooled with this protocol. Figure 2(a) compares Eq. (25) with our stochastic GPE simulation with a linear ramp-off function $f(t)$. The analytic calculation exactly reproduces the numerically predicted phonon distribution immediately following a single measurement (red curve), while the results with cooling have additional periodic features resulting from the finite ramp-off rates in the simulations. The shaded region denotes the parameters for which our perturbation theory is inapplicable.

In the thermodynamic limit $L \gg \xi$, the per-particle energy after one measurement-feedback cycle,

$$\Delta E = \frac{1}{2\pi n}\int dk\,\epsilon_k\bar{P}_k = A(g_c - g_{c*})^2 + \Delta E_*, \tag{26}$$

is parabolic. With $\xi \gg 1/k_c$, the minimal per-particle energy increase $\Delta E_*/\mu = \kappa^2\phi_c^2(\pi\phi_c - 6\sqrt{2})/(6\pi^2\xi)$ occurs for a

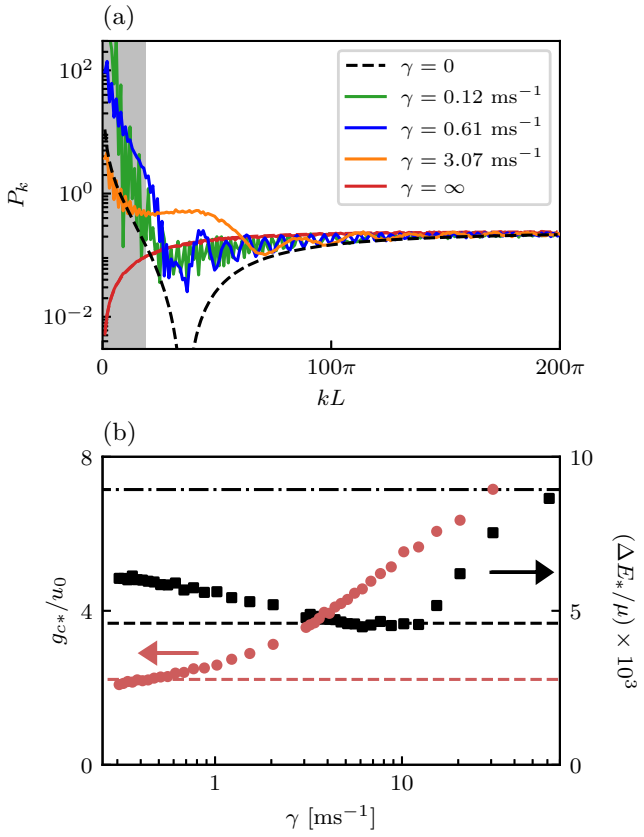

FIG. 2. Comparison between Bogoliubov theory and stochastic GPE simulation for a single-measurement-feedback cycle for a system initially in the ground state. (a) Phonon population. Black, green, blue, orange, and red curves indicate $\gamma = 0\,\mathrm{ms}^{-1}$, $\gamma = 0.12\,\mathrm{ms}^{-1}$, $\gamma = 0.61\,\mathrm{ms}^{-1}$, $\gamma = 3.07\,\mathrm{ms}^{-1}$, and $\gamma = \infty$. Dashed curves result from Bogoliubov theory [Eq. (25) with $g_c = u_0$ and $g_c = 0$, corresponding to $\gamma = 0$ and $\gamma = \infty$, respectively], while solid curves derive from GPE simulations (3000 trajectories). The Bogoliubov and GPE results coincide for $\gamma = \infty$ (red). The gray region marks wave numbers for which first-order perturbation theory fails. (b) Gain g_{c*} (red circles) for which the energy increase ΔE_* (black squares) is minimized, plotted as a function of γ. For each point, we fit Eq. (26) to the GPE simulation result with A, g_{c*}, and ΔE_* as free parameters. Horizontal dashed lines indicate the Bogoliubov prediction of ΔE_* and g_{c*}, and the dash-dotted line shows the energy increase without feedback cooling (i.e., $\gamma = \infty$).

gain,

$$\frac{g_{c*}}{u_0} = \frac{2\sqrt{2}\kappa^2 n\phi_c}{\pi}, \tag{27}$$

where $\phi_c = k_c\xi/\sqrt{2}$ parameterizes the cutoff and $A = (4\sqrt{2}\kappa^2\mu\xi)^{-1}$.

Figure 2(b) compares the optimal energy increase predicted by Eq. (26) with that obtained from numerical simulations of the stochastic GPE (horizontal black dashed line and black squares, respectively), and the corresponding optimal gains are denoted by the red circles. The GPE simulation exhibits three regimes: (1) For very rapid ramps $\gamma \to \infty$, the adiabatic assumption is invalid, and the GPE optimal gain is larger than anticipated from the analytic model. (2) In the adiabatic ramping regime where $\gamma \to 0$, we find that both g_{c*} and ΔE_* converge, with ΔE_* greater than our predicted value. This results from phonon-phonon scattering processes redistributing phonons between modes, which is not included in our Bogoliubov theory. (3) And in the intermediate regime (γ between $3\,\mathrm{ms}^{-1}$ and $10\,\mathrm{ms}^{-1}$), our theory performs optimally and ΔE_* coincides with the analytic prediction, albeit with much higher gain. We note that the optimal gain $g_c = u_0$ obtained in Sec. III A is close to that predicted by Eq. (27), where, for the parameters in Fig. 2, $g_{c*} \approx 2.8u_0$.

C. Continuous feedback cooling protocol

The single-measurement procedure described in Sec. III A is a building block for continuous feedback cooling. We periodically measure the condensate with measurement strength $\kappa = \kappa_*\sqrt{\Delta t/\tau}$, where κ_* is the ideal single-measurement strength in Eq. (18) and τ is the filtering time constant for the measurement signal. The cooling potential is derived from the density estimator $\varepsilon(x,t)$ [48] and is decreased between measurements, as described by Eq. (20).

The effect of the cooling potential is to drive $\psi(x)$ toward its ground state between measurements. This procedure leverages the optimal single-measurement strength and signal filtering to measure the condensate more weakly. We implement this protocol numerically and simulate condensate evolution under measurement and feedback using Eqs. (3)–(5).

Here we simulate an elongated condensate with $N = 10^5$ particles, healing length $\xi = 0.8$ m, and total system size $L = 80$ m, computed for $k_c = 2\pi/\lambda$ with $\lambda = 780$ nm. The interval between measurements is set to $dt = 200$ s to match typical image acquisition times in experiment, and the estimator time constant and cooling ramp-off rate were set to $\tau = 1/\gamma = 4.6$ ms. We characterize the quasisteady state by three metrics: condensate fraction, von Neumann entropy, and energy, and find that the condensate remains remarkably coherent throughout the feedback cooling protocol. Upon implementing continuous feedback cooling, the condensate fraction and von Neumann entropy reach a steady state, while the GPE energy functional slowly increases, as shown in Fig. 3.

We calculate the condensate fraction using the Penrose-Onsager criteria [49]. Per this criteria, upon diagonalizing the one-body density matrix $\hat{\rho}$ as $\hat{\rho}|n\rangle = N_n|n\rangle$, a condensate is present in mode $|n\rangle$ if its eigenvalue is $N_n \sim O(N)$, where N is the total number of particles. We obtain $\hat{\rho}$ from an ensemble of stochastic trajectories of pure states [50], starting from the GPE ground state. In Fig. 3(a), we show the four largest eigenvalues of $\hat{\rho}$, normalized by N, giving a measure of the fractional occupation in each mode. The condensate fraction is the largest eigenvalue, which stabilizes at ≈0.99, with a secondary mode having an occupation fraction of ≈0.01. The remaining eigenvalues are orders of magnitude smaller than the leading two; therefore, those modes have negligible occupation.

The second metric we use to characterize the steady state is the von Neumann entropy, defined as $S = \mathrm{Tr}[\hat{\rho}\ln\hat{\rho}]$. As shown in Fig. 3(b), S saturates at ≈0.01 of its maximum possible value $\log(D)$, where D is the Hilbert-space dimension.

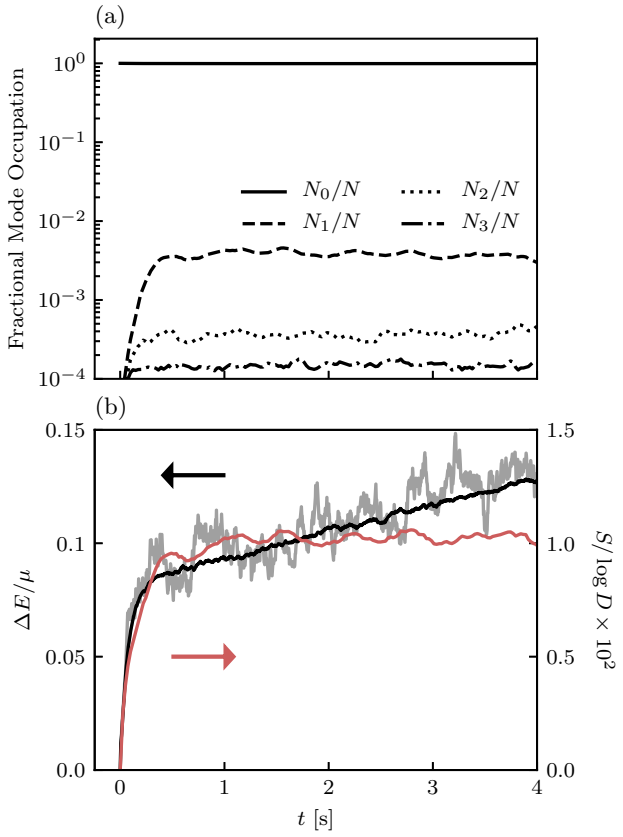

FIG. 3. Properties of a single-component condensate under feedback cooling with gain $g_c = u_0$ and measurement strength $\kappa_* = 2.2\times10^{-3}$. Statistical properties were calculated from 128 independent stochastic trajectories. (a) Fractional occupation of the first four modes in the single-particle density matrix. The condensate fraction (solid curve) is ≈0.99 in the quasisteady state. (b) The von Neumann entropy (red/light gray) and average energy (black) of the condensate. The gray curve is the energy for a single trajectory.

This is consistent with the final condensate fraction of ≈0.99. We extract an equilibration time $\tau_{\rm eq} \approx 200$ ms by fitting S to the function $S(t) \approx S_0(1 - e^{-t/\tau_{\rm eq}})$.

The third metric, energy, does not reach a constant value, rather it slowly increases even after the condensate fraction and entropy saturate, as shown in Fig. 3(b). Here we define energy in terms of the per-particle GPE energy without any feedback terms present. The final energy after 4 s of evolution is ∼0.15 μ, indicating a 15% increase from the ground-state value throughout the protocol. We determined that this energy increase is due to the gradual population of modes above the momentum cutoff which cannot be directly addressed by feedback cooling. However, this increase is slow enough to provide ample time (on the order of seconds) for additional experiments while the condensate is being measured.

Cooling for the two-component case proceeds similarly, but with cooling applied in the spin and density channels separately. Weak measurements add magnons (spin waves) in addition to phonons [27]. For the easy-axis ground state with $u_2 < 0$, the results are qualitatively the same as as the single-component case, with the final condensate fraction reduced to ≈0.85, indicating cooling is not quite as efficient for the two-component system. However, in the easy-plane case (i.e., $u_2 > 0$), cooling is not as effective at long times and the condensate enters a spin-disordered phase with large spin fluctuations and a lower condensate fraction of ≈0.35. The cooling protocol for two-component condensates is discussed in Appendix C.

IV. FEEDBACK INDUCED MAGNETIC PHASES

In this section, we elaborate on the steady-state magnetic phases and their measurement signatures. The phase diagram in Fig. 1(c) was computed for a gas of $N = 10^5$ ^{87}Rb atoms with healing length $\xi = 0.8$ m and total system length $L = 80$ m, with feedback both to control the effective interactions and cool the system. In all of our simulations, feedback cooling is continuously applied. We add the forcing feedback $\check{V}_{\rm f}(x,t) = g_2\varepsilon_z(x,t)\check{\sigma}^z$ in the time window from 1 to 3 s and allow the simulations to continue until the total run time reaches 4 s.

Figure 1(c) shows that the magnetic phase of the system reaches a steady state governed by the effective spin-dependent interaction strength $u_2^{\rm eff} = g_2 + u_2$ while the forcing potential is on, leading to the easy-axis ferromagnet and spin-disordered paramagnetic phases discussed in Sec. II C. The spin-dependent interaction strength u_2 and gain g_2 serve as tunable parameters.

The easy-axis ferromagnetic phase for $u_2^{\rm eff} < 0$ exhibits well-defined, spin-polarized domains. The order parameter η for this phase is the time-separated correlation function of the magnetization, given in Eq. (17). We find that $\eta \gtrsim 0.5$ indicates the existence of persistent domains. We can identify an effective spin-healing length $\xi_s \propto 1/\sqrt{|u_2^{\rm eff}|}$ in this phase, similar to the spin-healing length in closed two-component systems [44]. Changing $u_2^{\rm eff}$ via the feedback strength thus alters the spin-healing length in the steady state.

Figure 4 shows the effective spin-healing length, obtained by fitting the spin density $S_z(x)$ to a function with $N_{\rm d}$ domains, where

$$S_z(x) = \pm\mathcal{S}\,\Pi_{n=1}^{N_{\rm d}-1}\tanh\left(\frac{x-x_n}{\xi_s}\right). \tag{28}$$

Here, x_n are the positions of each domain wall, $\mathcal{S}$ is the overall amplitude of domains, and ξ_s is the spin-healing length. The $\pm$ sign in front accounts for the polarity of the domain signal (i.e., which domain is at the edge), as the measurement and feedback process spontaneously breaks a $\mathbb{Z}_2$ symmetry to determine the domain orientations [40,51].

The spin-healing length diverges upon approaching the transition at $u_2^{\rm eff} = 0$, indicating system behavior that is analogous to the expected phase transition from changing the interaction parameters. The markers in Fig. 4 are color-coded based on the value of the η, where we can see that for lower values, there is more variability in the data. This is because lower values of η generally correspond to a spin texture with multiple domains, where there is movement of the domain boundaries over time due to fluctuations parameterized by the nonzero entropy [40]. The black diamonds in Fig. 4 show the spin-healing length obtained for the corresponding

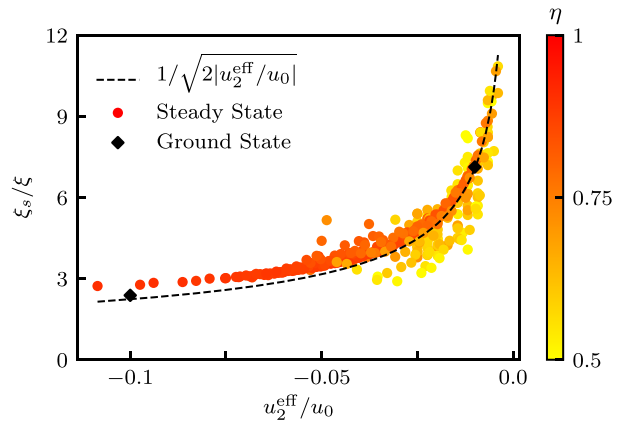

FIG. 4. Spin-healing length as a function of effective spin-dependent interaction strength $u_2^{\rm eff} = g_2 + u_2$ for data shown in the Fig. 1(c) phase diagram with $u_2^{\rm eff} < 0$. The colored markers indicate the calculated spin-healing length averaged over a 1.6 s window. The black markers indicate the spin-healing length for a ground-state system (i.e., no feedback) with u_2 equal to the marked value of $u_2^{\rm eff}$. The dashed curve indicates the predicted spin-healing length $\xi_s = \xi/\sqrt{2|u_2^{\rm eff}/u_0|}$ with no fitting parameters.

closed-system ground state, and the dashed curve is the computed functional dependence $\xi_s = \xi[u_0/2|u_2^{\rm eff}|]^{1/2}$ for $u_2^{\rm eff} < 0$, which shows excellent agreement with the simulations.

The disordered paramagnetic phase is characterized by a spatially and temporally fluctuating spin structure. An example of these fluctuations in real space is shown in Fig. 5(a). In the disordered paramagnetic phase, a spin-healing length is not well defined. The power spectral density (PSD) of the spin,

$$\mathrm{PSD}_z(k,t) = |\tilde{S}_z(k,t) - \bar{\tilde{S}}_z(k,t)|^2, \tag{29}$$

provides a measure of how much the spin fluctuates [44]. Here, $\bar{S}_z(x)$ is the time-averaged value of the spin density and $\tilde{S}_z(k,t)$ is the Fourier transform of $S_z(x,t)$.

Figure 5(a) shows $\mathrm{PSD}_z(k)$ in the steady-state magnetic phase averaged over 1 s. At low momenta, the signature for the disordered phase is significantly higher than for the easy-axis ferromagnetic phase. The large fluctuations in spin are thus a signature of the paramagnetic phase, which can be deduced from the measurement signals. Above the cutoff $k_c\lambda = 200\pi$ indicated by the black dashed line, we see additional spectral features at multiples of k_c, indicating higher-order resonances due to the measurement process. The population of modes above the cutoff leads to a gradual increase in energy and affects cooling, as discussed in Sec. III C.

V. OUTLOOK

Hamiltonian engineering for multicomponent Bose gases has been achieved at the level of the single-particle Hamiltonian via synthetic gauge fields [52,53], spin-orbit coupling [10,54,55], and spin-dependent potentials [56,57]. The ability to tune the character and strength of interactions beyond those already present in the system has heretofore been limited to using Feshbach resonances [29], which typically change only

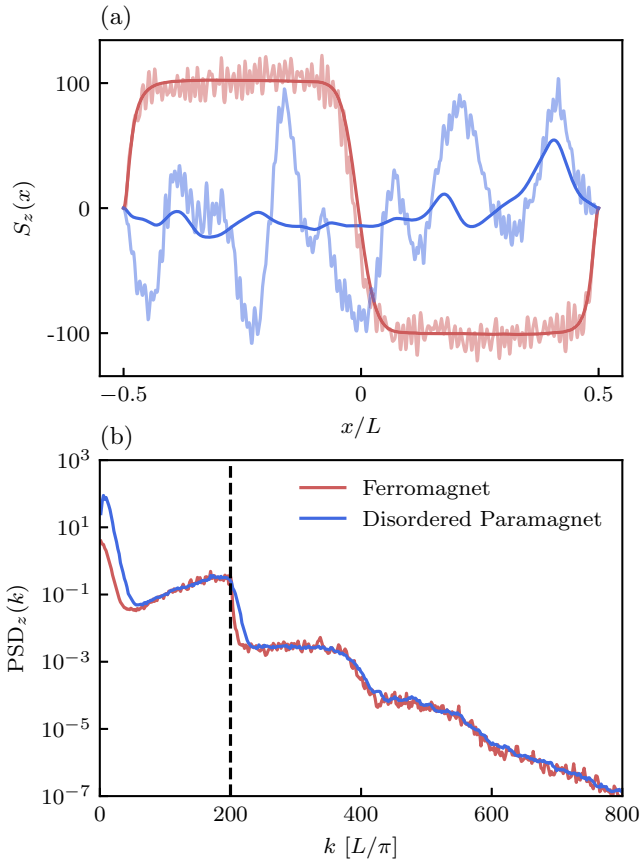

FIG. 5. (a) Real-space spin density $S_z(x)$ computed in the ferromagnetic and disordered paramagnetic phase. The solid curve shows the time-averaged signal over 1 s and the semitransparent curve indicates a single time trace. (b) The corresponding power spectral density of fluctuations in each phase. The vertical dashed line indicates the momentum cutoff k_c.

one interaction constant at a time, or via coupling to an external cavity field [58–60]. In contrast, our feedback technique can simultaneously change all the spin-dependent effective interaction strengths *in situ*: not possible with Feshbach resonances or cavity-mediated interactions.

Our result shows that spatially local feedback control based on a record of weak measurements is a viable route toward engineering effecting interactions in quantum gases. We demonstrated that a dynamical steady state can be engineered in a two-component Bose-Einstein condensate where the magnetic phase is determined by the interplay of the intrinsic and feedback induced interaction strengths.

Going beyond previous works [34,40], we implemented a cooling scheme which avoids runaway heating of the condensate during the feedback process. Further optimization of the cooling protocol will be important for experimental implementation. For example, Eq. (25) suggests that the k-dependent gain $g_c(k) = n\kappa^2\epsilon_k$ would lead to near-perfect cooling for all momentum states.

Actual imaging systems have additional limitations beyond backaction noise, including decreased resolution, detector inefficiencies, and technical noise. These effects can be incorporated into our formalism by applying an appropriate

transfer function to the measurement record $\mathcal{M}_s(x,t)$ prior to calculating the feedback signals. Broadly speaking, this process will introduce another, lower momentum cutoff set by the imaging resolution, thus limiting the information content in the applied feedback potential.

The typical spin-healing length (on the order of microns) is already accessible by modern imaging techniques, and therefore we expect that manipulating the spin texture via feedback is presently possible. We also expect that feedback cooling will be less efficient since the decreased detector resolution will limit the excitations that can be cooled. Future work should quantify the effectiveness of feedback cooling for real imaging systems. Additionally, more novel signal filtering schemes beyond the low-pass filter used here might help to address the parasitic effects of measurement resolution on cooling efficiency. We note that cooling only needs to be good enough to maintain a condensate over the timescale required to study the relevant spinor physics.

The feedback control method of engineering effective Hamiltonians is flexible and allows for the introduction of tailored, spatially dependent effective interaction terms. Future work could implement nonlocal or time-dependent interactions which have no analog in closed systems. Our protocols can be generalized to higher dimensions and could stabilize topological defects such as non-Abelian vortex anyons which are unstable in closed systems [23]. Finally, our methods enable real-time feedback control, so over the course of one experiment we can study both quasi-steady-state behavior and dynamics.

ACKNOWLEDGMENTS

This work was partially supported by NIST and NSF through the Physics Frontier Center at the JQI. H.M.H. acknowledges the financial support of the NIST NRC postdoctoral program. The authors are grateful to Jeremy Young and Emine Altuntas for useful discussions and to Luis Pedro Garcia-Pintos for a careful reading of the manuscript.

APPENDIX A: SIMULATION PARAMETERS

Here we briefly review the simulation method for Eqs. (3)–(5) and the parameters we use in this work. All simulations have $N = 10^5$ atoms and we consider a quasi-1D system of length $L = 80$ m with hard-wall boundary conditions such that $\Psi(x = -L/2) = \Psi(x = L/2) = 0$. Hard-wall boundaries can be implemented using flat-bottomed traps instead of a harmonic one [61]. The momentum cutoff is $k_c = 2\pi/\lambda$, with $\lambda = 780$ nm being the wavelength of imaging light. We simulate a single-component condensate in order to study steady-state behavior under feedback cooling in Sec. III. Elsewhere, we simulate a two-component condensate with an easy-axis magnetic ground state, i.e., $u_2 < 0$, or easy-plane ground state with $u_2 > 0$. In the main text, the results are presented using the easy-axis ground state with $u_2 = 0.01u_0$ as the initial condition.

The system is initialized in its ground state by solving the GPE in imaginary time. The natural units for this setup are the total system length L and the chemical potential $\mu = \hbar^2/2m\xi^2$ as the unit of energy, where $\xi = 0.8$ m is the healing length. Upon rescaling the variables to unitless quantities $x \to xL$, $t \to t(2m_a\xi^2/\hbar)$, $\psi_{\uparrow(\downarrow)} \to \sqrt{N/L}\psi_{\uparrow(\downarrow)}$, the Hamiltonian in Eq. (19) is

$$\check{\mathcal{H}} = \left[-\frac{\xi^2}{L^2}\frac{\partial^2}{\partial x^2} + n(x)\right]\check{\mathbb{1}} + \frac{u_2}{u_0}S_z(x)\check{\sigma}^z, \tag{A1}$$

where $\int dx\, n(x) = 1$. Therefore, the spinless case has one free parameter ξ/L and the two-component case has the additional free parameter u_2/u_0. For our parameters, we have $\xi/L = 0.01$ and we consider different values of u_2. We simulate the nonlinear dynamics using a second-order symplectic integration method [62]. In these units, it is natural to express u_2 and the gain strengths g_0, g_2, etc. in units of u_0.

In order to simulate a small measurement interval (approaching the continuous measurement limit), we consider a separation of timescales $dt \ll \tau$ such that the measurement interval dt of the system is much shorter than the signal filtering timescale τ for any observable. This enables us to write the evolution Eqs. (3)–(5) as continuous time stochastic differential equations.

APPENDIX B: STEADY-STATE PHASE DIAGRAM FOR EASY-PLANE INITIAL CONDITION

As indicated by the hatched region in Fig. 1(c), the steady-state phase diagram has a region of bistability depending on the initial state of the system. In this Appendix, we present the results for the phase diagram calculated using the easy-plane ground state as the initial condition, shown in Fig. 6. In the steady-state magnetic phase, the system forms domains for $u_2^{\text{eff}} < 0$ and $g_2 < 0$. An example of the density and spin density in this region is shown in Fig. 6(a.i), where we see that there are multiple domains in the spin texture. This is in contrast to the case presented in the main text where there is only one domain, due to the single domain being the ground state. The number of domains depends on many parameters including u_2, g_2, and the timescale over which feedback is turned on. We consider further investigation of these variables to be outside the scope of this work.

Unlike the easy-axis initial condition, the spin-disordered phase occurs for a wider range of parameters, most notably in the hatched region where $u_2^{\text{eff}} = 0$ but $g_2 > 0$. The spin texture in this regime is shown in Fig. 6(a.ii), which indicates relatively uniform density but a highly fluctuating spin texture. We suspect that the observed bistability could be due in part to the underlying cooling protocol for the two-component system, which can also affect the spin texture, as discussed in Appendix C.

APPENDIX C: TWO-COMPONENT FEEDBACK COOLING

The density is measured in each component s with strength $\kappa = \kappa_*\sqrt{\Delta t/\tau_n}$ where Δt is the measurement duration and τ_n is the low-pass filtering time constant for the total density. Measurements $\mathcal{M}_\uparrow$ and $\mathcal{M}_\downarrow$ are then combined to give a measurement of total density $(\mathcal{M}_\uparrow + \mathcal{M}_\downarrow)$ or spin density $(\mathcal{M}_\uparrow - \mathcal{M}_\downarrow)$, which is used in a low-pass filter to calculate the estimators ε_n and ε_z. Crucially, the filtering works best when ε_n and ε_z have different filtering time constants; we use $\tau_n = 4.6$ and $\tau_z = 46$ ms, respectively. This is due to the different

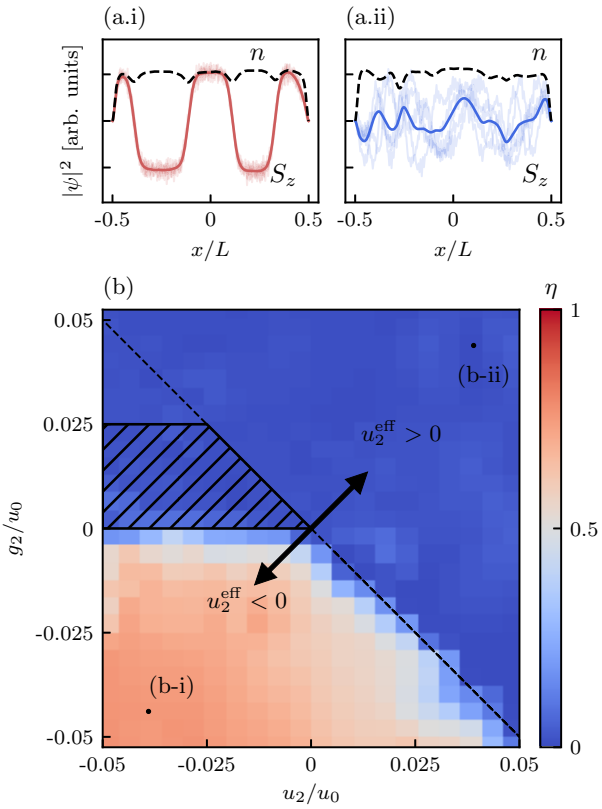

FIG. 6. (a) Steady-state density (black dashed curve) and spin density (solid curve) for (a.i) $u_2^{\rm eff} \lesssim 0$ and (a.ii) $u_2^{\rm eff} \gtrsim 0$, averaged over 100 ms. Semitransparent curves indicate S_z without time averaging. (b) Steady-state phase diagram as a function of u_2/u_0 and g_2/u_0 (defined in text), showing magnetically ordered, easy-axis ferromagnet (red/lower left) or spin-disordered paramagnet (blue/upper right) phases. The black dashed line indicates the expected phase boundary at $u_2^{\rm eff} = 0$, and the hatched region indicates bistability depending on the initial phase.

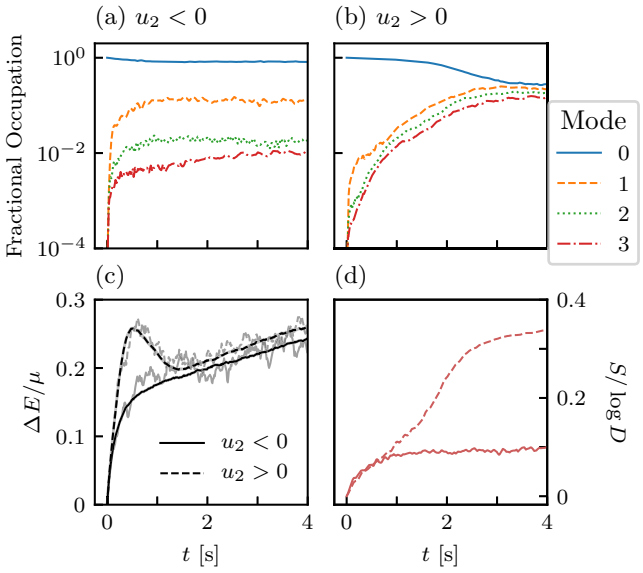

FIG. 7. Properties of a two-component condensate under measurement and feedback cooling. (a), (b) Fractional occupation of first four modes in the single-particle density matrix for (a) $u_2 < 0$ and (b) $u_2 > 0$. The eigenvalue of the four highest-occupied modes is pictured. The condensate fraction (solid curve) is ≈0.85 in the steady state for $u_2 < 0$ and ≈0.35 for $u_2 > 0$. (c) Average energy (black) for a condensate with $u_2 < 0$ (solid curve) and $u_2 > 0$ (dashed curve) calculated from 124 independent stochastic trajectories. As in the spinless case, energy computed from the GPE energy functional increases slowly. (d) The von Neumann entropy for a condensate with $u_2 < 0$ (solid curve) and $u_2 > 0$ (dashed curve).

types of excitations in the two-component case, which can be phonons or magnons. Phonons have faster time dynamics than magnons, which necessitates different time constants in each channel.

The spin-dependent cooling potential is

$$\check{V}_{\rm c}(x,t) = V_{{\rm c},n}[\varepsilon_n, t]\check{\mathbb{1}} + V_{{\rm c},z}[\varepsilon_z, t]\check{\sigma}^z. \tag{C1}$$

As in the spinless case, the potentials $V_{{\rm c},n}$ and $V_{{\rm c},z}$ are calculated after each measurement and then exponentially ramped off between measurements. Cooling in the density channel is done via the potential

$$V_{{\rm c},n}(x,t) = [\mu - g_{\rm c}\varepsilon_n(x,t)]e^{-\gamma_n(t-t_{\rm m})}, \tag{C2}$$

where $g_{\rm c}$ is the gain. This potential drives the total density toward a uniform state based on estimator ε_n with ramp-off rate γ_n. Cooling for the spin sector is via the spin-dependent potential

$$V_{{\rm c},z}(x,t) = g_{{\rm c},z}[\bar{\varepsilon}_z(x,t) - \varepsilon_z(x,t)]e^{-\gamma_z(t-t_{\rm m})}, \tag{C3}$$

where γ_z is the spin ramp-off rate, $g_{{\rm c},z}$ is the cooling gain for the spin sector, and $\bar{\varepsilon}_z$ indicates a running time average of ε_z. This potential drives the spin density $S_z(x)$ toward its time-averaged value, effectively cooling short-wavelength (high-momentum) spin fluctuations, but allowing long-wavelength spin textures such as domain walls to remain intact. In practice, we use $\gamma_n^{-1} = \tau_n$ and $\gamma_z^{-1} = \tau_z$, with the other parameters the same as for the spinless case. We calculate $\bar{\varepsilon}_z$ by averaging the original signal over a 120 ms time window. Cooling is most effective when the gain parameters are $g = u_0$ and $g_{{\rm c},z} = u_2$.

As in the spinless case, feedback cooling drives the two-component condensate to a quasisteady state. The condensate fraction and von Neumann entropy stabilize around constant values and the energy per particle increases slowly over the course of the simulation. We compute the energy from the GPE energy functional without any feedback terms present. The steady-state properties for cooling a two-component condensate are presented in Fig. 7. The results are qualitatively different for the case with $u_2 < 0$ (easy-axis ground state) and $u_2 > 0$ (easy-plane ground state).

The easy-axis case is similar to the spinless cooling results presented in the main text. In Fig. 7(a), we present the condensate fraction for $u_2 < 0$, which can also be calculated for multicomponent condensates [63]. The condensate fraction is ≈0.85 in the steady state, with one additional mode having occupation ≈0.15 and other modes having negligible occupation. The energy increase, shown in Fig. 7(c), is $\approx 0.25\mu$. The von Neumann entropy, shown in Fig. 7(d) (solid curve), increases to about 10% of its maximum value. These metrics indicate that the cooling protocol is effective for

two-component condensates with $u_2 < 0$. Furthermore, we find that at the end of the cooling protocol, the domain wall is still intact, showing that this spin-dependent cooling protocol is effective both at maintaining a high level of condensation and preserving the spin structure. The equilibration time extracted from the entropy is $\tau_{\rm eq} \approx 400\,{\rm ms}$.

In the case of an easy-plane initial condition (i.e., $u_2 > 0$), the cooling protocol is not as effective. In Fig. 7(b), we show the fractional occupation of the first four modes from the one-body density matrix. The condensate fraction (blue solid curve) decreases to ≈0.35, while the other modes also have fractional occupations of $O(0.1)$. This indicates that the Penrose-Onsager criterion for condensation is violated in this regime. Furthermore, we find that the entropy S increases considerably more than the easy-axis case, reaching a constant value of $\approx 0.4\log(D)$ after 2 s of time evolution. The entropy increase is likely being driven by an instability toward spin separation in the condensate. Under our current feedback protocol, the easy-plane ground state eventually enters a spin-disordered phase with large spin fluctuations, which accounts for the higher entropy and lower condensate fraction that we observe. Future work could develop a feedback cooling protocol specifically for $u_2 > 0$ systems to combat this instability more effectively.

[1] I. Bloch, J. Dalibard, and W. Zwerger, Many-body physics with ultracold gases, Rev. Mod. Phys. **80**, 885 (2008).

[2] J. I. Cirac and P. Zoller, Goals and opportunities in quantum simulation, Nat. Phys. **8**, 264 (2012).

[3] I. M. Georgescu, S. Ashhab, and F. Nori, Quantum simulation, Rev. Mod. Phys. **86**, 153 (2014).

[4] S. Hodgman, R. Dall, A. Manning, K. Baldwin, and A. Truscott, Direct measurement of long-range third-order coherence in Bose-Einstein condensates, Science **331**, 1046 (2011).

[5] C. Gross and I. Bloch, Quantum simulations with ultracold atoms in optical lattices, Science **357**, 995 (2017).

[6] T. V. Zache, T. Schweigler, S. Erne, J. Schmiedmayer, and J. Berges, Extracting the Field Theory Description of a Quantum Many-Body System from Experimental Data, Phys. Rev. X **10**, 011020 (2020).

[7] M. Greiner, O. Mandel, T. Esslinger, T. W. Hänsch, and I. Bloch, Quantum phase transition from a superfluid to a Mott insulator in a gas of ultracold atoms, Nature (London) **415**, 39 (2002).

[8] M. Bartenstein, A. Altmeyer, S. Riedl, S. Jochim, C. Chin, J. H. Denschlag, and R. Grimm, Collective Excitations of a Degenerate Gas at the BEC-BCS Crossover, Phys. Rev. Lett. **92**, 203201 (2004).

[9] T. Bourdel, L. Khaykovich, J. Cubizolles, J. Zhang, F. Chevy, M. Teichmann, L. Tarruell, S. J. J. M. F. Kokkelmans, and C. Salomon, Experimental Study of the BEC-BCS Crossover Region in Lithium 6, Phys. Rev. Lett. **93**, 050401 (2004).

[10] Y.-J. Lin, K. Jiménez-García, and I. B. Spielman, Spin-orbit-coupled Bose-Einstein condensates, Nature (London) **471**, 83 (2011).

[11] R. Landig, L. Hruby, N. Dogra, M. Landini, R. Mottl, T. Donner, and T. Esslinger, Quantum phases from competing short-and long-range interactions in an optical lattice, Nature (London) **532**, 476 (2016).

[12] J. P. Ronzheimer, M. Schreiber, S. Braun, S. S. Hodgman, S. Langer, I. P. McCulloch, F. Heidrich-Meisner, I. Bloch, and U. Schneider, Expansion Dynamics of Interacting Bosons in Homogeneous Lattices in One and Two Dimensions, Phys. Rev. Lett. **110**, 205301 (2013).

[13] T. Kohlert, S. Scherg, X. Li, H. P. Lüschen, S. Das Sarma, I. Bloch, and M. Aidelsburger, Observation of Many-Body Localization in a One-Dimensional System with a Single-Particle Mobility Edge, Phys. Rev. Lett. **122**, 170403 (2019).

[14] P. Solano, Y. Duan, Y.-T. Chen, A. Rudelis, C. Chin, and V. Vuletić, Strongly Correlated Quantum Gas Prepared by Direct Laser Cooling, Phys. Rev. Lett. **123**, 173401 (2019).

[15] A. Polkovnikov, K. Sengupta, A. Silva, and M. Vengalattore, Colloquium: Nonequilibrium dynamics of closed interacting quantum systems, Rev. Mod. Phys. **83**, 863 (2011).

[16] M. Heyl, Dynamical quantum phase transitions: A review, Rep. Prog. Phys. **81**, 054001 (2018).

[17] S. Diehl, A. Micheli, A. Kantian, B. Kraus, H. Büchler, and P. Zoller, Quantum states and phases in driven open quantum systems with cold atoms, Nat. Phys. **4**, 878 (2008).

[18] B. Kraus, H. P. Büchler, S. Diehl, A. Kantian, A. Micheli, and P. Zoller, Preparation of entangled states by quantum Markov processes, Phys. Rev. A **78**, 042307 (2008).

[19] F. Verstraete, M. M. Wolf, and J. I. Cirac, Quantum computation and quantum-state engineering driven by dissipation, Nat. Phys. **5**, 633 (2009).

[20] C. Laflamme, D. Yang, and P. Zoller, Continuous measurement of an atomic current, Phys. Rev. A **95**, 043843 (2017).

[21] M. Rigol, Breakdown of Thermalization in Finite One-Dimensional Systems, Phys. Rev. Lett. **103**, 100403 (2009).

[22] D. A. Abanin, E. Altman, I. Bloch, and M. Serbyn, Colloquium: Many-body localization, thermalization, and entanglement, Rev. Mod. Phys. **91**, 021001 (2019).

[23] T. Mawson, T. C. Petersen, J. K. Slingerland, and T. P. Simula, Braiding and Fusion of Non-Abelian Vortex Anyons, Phys. Rev. Lett. **123**, 140404 (2019).

[24] J. Zhang, P. Hess, A. Kyprianidis, P. Becker, A. Lee, J. Smith, G. Pagano, I.-D. Potirniche, A. C. Potter, A. Vishwanath *et al.*, Observation of a discrete time crystal, Nature (London) **543**, 217 (2017).

[25] M. Trippenbach, K. Góral, K. Rzazewski, B. Malomed, and Y. Band, Structure of binary Bose-Einstein condensates, J. Phys. B: At. Mol. Opt. Phys. **33**, 4017 (2000).

[26] Y. Kawaguchi and M. Ueda, Spinor Bose-Einstein condensates, Phys. Rep. **520**, 253 (2012).

[27] D. M. Stamper-Kurn and M. Ueda, Spinor Bose gases: Symmetries, magnetism, and quantum dynamics, Rev. Mod. Phys. **85**, 1191 (2013).

[28] J. Zhang, Y.-X. Liu, R.-B. Wu, K. Jacobs, and F. Nori, Quantum feedback: Theory, experiments, and applications, Phys. Rep. **679**, 1 (2017).

[29] M. Theis, G. Thalhammer, K. Winkler, M. Hellwig, G. Ruff, R. Grimm, and J. H. Denschlag, Tuning the Scattering Length with an Optically Induced Feshbach Resonance, Phys. Rev. Lett. **93**, 123001 (2004).

[30] S. A. Haine, A. J. Ferris, J. D. Close, and J. J. Hope, Control of an atom laser using feedback, Phys. Rev. A **69**, 013605 (2004).

[31] S. D. Wilson, A. R. R. Carvalho, J. J. Hope, and M. R. James, Effects of measurement backaction in the stabilization of a Bose-Einstein condensate through feedback, Phys. Rev. A **76**, 013610 (2007).

[32] S. S. Szigeti, M. R. Hush, A. R. R. Carvalho, and J. J. Hope, Continuous measurement feedback control of a Bose-Einstein condensate using phase-contrast imaging, Phys. Rev. A **80**, 013614 (2009).

[33] S. S. Szigeti, M. R. Hush, A. R. R. Carvalho, and J. J. Hope, Feedback control of an interacting Bose-Einstein condensate using phase-contrast imaging, Phys. Rev. A. **82**, 043632 (2010).

[34] M. Hush, S. Szigeti, A. Carvalho, and J. Hope, Controlling spontaneous-emission noise in measurement-based feedback cooling of a Bose-Einstein condensate, New J. Phys. **15**, 113060 (2013).

[35] A. C. J. Wade, J. F. Sherson, and K. Mølmer, Squeezing and Entanglement of Density Oscillations in a Bose-Einstein Condensate, Phys. Rev. Lett. **115**, 060401 (2015).

[36] E. O. Ilo-Okeke and T. Byrnes, Theory of Single-Shot Phase Contrast Imaging in Spinor Bose-Einstein Condensates, Phys. Rev. Lett. **112**, 233602 (2014).

[37] S. Wang and T. Byrnes, Quantum feedback control of atomic ensembles and spinor Bose-Einstein condensates, Phys. Rev. A **94**, 033620 (2016).

[38] A. C. J. Wade, J. F. Sherson, and K. Mølmer, Manipulation of collective quantum states in Bose-Einstein condensates by continuous imaging, Phys. Rev. A **93**, 023610 (2016).

[39] M. R. Andrews, D. M. Kurn, H.-J. Miesner, D. S. Durfee, C. G. Townsend, S. Inouye, and W. Ketterle, Propagation of Sound in a Bose-Einstein Condensate, Phys. Rev. Lett. **79**, 553 (1997).

[40] H. M. Hurst and I. B. Spielman, Measurement-induced dynamics and stabilization of spinor-condensate domain walls, Phys. Rev. A **99**, 053612 (2019).

[41] In this work, we use $\bar{\cdot}$ to denote a statistical average and $\langle\cdot\rangle$ to denote a quantum-mechanical expectation value. $\tilde{m}_{s,k}$ indicates the Fourier transform of $m_s(x)$.

[42] E. Hecht, *Optics* (Addison Wesley, United Kingdom, 1987).

[43] D. A. R. Dalvit, J. Dziarmaga, and R. Onofrio, Continuous quantum measurement of a Bose-Einstein condensate: A stochastic Gross-Pitaevskii equation, Phys. Rev. A **65**, 053604 (2002).

[44] S. De, D. L. Campbell, R. M. Price, A. Putra, B. M. Anderson, and I. B. Spielman, Quenched binary Bose-Einstein condensates: Spin-domain formation and coarsening, Phys. Rev. A **89**, 033631 (2014).

[45] R. Barnett, A. Turner, and E. Demler, Classifying Novel Phases of Spinor Atoms, Phys. Rev. Lett. **97**, 180412 (2006).

[46] Y. Kawaguchi and M. Ueda, Symmetry classification of spinor Bose-Einstein condensates, Phys. Rev. A **84**, 053616 (2011).

[47] L. Pitaevskii and S. Stringari, *Bose-Einstein Condensation* (Oxford University Press, Oxford, 2003).

[48] We calculate the estimator $\varepsilon(x,t)$ after each measurement using a discretized version of Eq. (13).

[49] O. Penrose and L. Onsager, Bose-Einstein condensation and liquid helium, Phys. Rev. **104**, 576 (1956).

[50] A. J. Daley, Quantum trajectories and open many-body quantum systems, Adv. Phys. **63**, 77 (2014).

[51] L. P. García-Pintos, D. Tielas, and A. del Campo, Spontaneous Symmetry Breaking Induced by Quantum Monitoring, Phys. Rev. Lett. **123**, 090403 (2019).

[52] Y.-J. Lin, R. L. Compton, K. Jiménez-García, J. V. Porto, and I. B. Spielman, Synthetic magnetic fields for ultracold neutral atoms, Nature (London) **462**, 628 (2009).

[53] N. Goldman, G. Juzeliūnas, P. Öhberg, and I. B. Spielman, Light-induced gauge fields for ultracold atoms, Rep. Prog. Phys. **77**, 126401 (2014).

[54] V. Galitski and I. B. Spielman, Spin-orbit coupling in quantum gases, Nature (London) **494**, 49 (2013).

[55] R. M. Kroeze, Y. Guo, and B. L. Lev, Dynamical Spin-Orbit Coupling of a Quantum Gas, Phys. Rev. Lett. **123**, 160404 (2019).

[56] K. Jiménez-García, L. J. LeBlanc, R. A. Williams, M. C. Beeler, A. R. Perry, and I. B. Spielman, Peierls Substitution in an Engineered Lattice Potential, Phys. Rev. Lett. **108**, 225303 (2012).

[57] H.-I. Lu, M. Schemmer, L. M. Aycock, D. Genkina, S. Sugawa, and I. B. Spielman, Geometrical Pumping with a Bose-Einstein Condensate, Phys. Rev. Lett. **116**, 200402 (2016).

[58] H. Ritsch, P. Domokos, F. Brennecke, and T. Esslinger, Cold atoms in cavity-generated dynamical optical potentials, Rev. Mod. Phys. **85**, 553 (2013).

[59] M. Landini, N. Dogra, K. Kroeger, L. Hruby, T. Donner, and T. Esslinger, Formation of a Spin Texture in a Quantum Gas Coupled to a Cavity, Phys. Rev. Lett. **120**, 223602 (2018).

[60] R. M. Kroeze, Y. Guo, V. D. Vaidya, J. Keeling, and B. L. Lev, Spinor Self-Ordering of a Quantum Gas in a Cavity, Phys. Rev. Lett. **121**, 163601 (2018).

[61] T. P. Meyrath, F. Schreck, J. L. Hanssen, C.-S. Chuu, and M. G. Raizen, Bose-Einstein condensate in a box, Phys. Rev. A **71**, 041604(R) (2005).

[62] L. M. Symes, R. I. McLachlan, and P. B. Blakie, Efficient and accurate methods for solving the time-dependent spin-1 Gross-Pitaevskii equation, Phys. Rev. E **93**, 053309 (2016).

[63] P. Mason and S. A. Gardiner, Number-conserving approaches to n-component Bose-Einstein condensates, Phys. Rev. A **89**, 043617 (2014).

Appendix C: Publication for Chapter 4: Machine-learning enhanced dark soliton detection in Bose-Einstein condensates

MACHINE LEARNING
Science and Technology

OPEN ACCESS

RECEIVED
31 December 2020

REVISED
19 February 2021

ACCEPTED FOR PUBLICATION
9 March 2021

PUBLISHED
15 June 2021

PAPER

Machine-learning enhanced dark soliton detection in Bose–Einstein condensates

Shangjie Guo[1], Amilson R Fritsch[1], Craig Greenberg[2], I B Spielman[1] and Justyna P Zwolak[2,*]

[1] Joint Quantum Institute, National Institute of Standards and Technology, and University of Maryland, Gaithersburg, MD 20899, United States of America
[2] National Institute of Standards and Technology, Gaithersburg, MD 20899, United States of America
* Author to whom any correspondence should be addressed.

E-mail: jpzwolak@nist.gov

Keywords: dark solitons, machine learning, convolutional neural network

Abstract

Most data in cold-atom experiments comes from images, the analysis of which is limited by our preconceptions of the patterns that could be present in the data. We focus on the well-defined case of detecting dark solitons—appearing as local density depletions in a Bose–Einstein condensate (BEC)—using a methodology that is extensible to the general task of pattern recognition in images of cold atoms. Studying soliton dynamics over a wide range of parameters requires the analysis of large datasets, making the existing human-inspection-based methodology a significant bottleneck. Here we describe an automated classification and positioning system for identifying localized excitations in atomic BECs utilizing deep convolutional neural networks to eliminate the need for human image examination. Furthermore, we openly publish our labeled dataset of dark solitons, the first of its kind, for further machine learning research.

1. Introduction

Machine-learning (ML)-based image classification has found application throughout science, from analysis of experimental data in particle physics [1–3], dark matter search experiments [4, 5] or quantum dots experiments [6–9] to predicting properties of materials [10–12] to studying molecular representations and properties [13–15]. In atomic physics, ML has been used to locate topological phase transitions [16], to complement absorption imaging technique [17], to characterize particles in disordered fields [18], and to detect quantum vortices in rotating BECs [19]. In this paper, by combining convolutional neural networks (ConvNets) with traditional fitting techniques, we first categorize many-body atomic physics data, and then extract quantitative information from this data.

Using cold-atom Bose–Einstein condensates (BECs), we focus on solitons, robust solitary waves that retain their size, shape, and speed at which they travel [20, 21]. These properties arise from an interplay between nonlinearity and dispersion that is present in many physical systems. Indeed, since their first observation in canals [22], solitons have been found in rivers and seas [23, 24]; BECs [25, 26]; optical fibers [27, 28]; astronomical plasmas [29]; and even human blood vesicles [30, 31]. Due to their inherent stability, solitons in optical fibers [32] have found commercial applications in long-distance, high-speed transmission lines [33].

While the natural environment does not allow for the controlled study of quantum solitons, BECs are an excellent medium where individual or multiple solitons can be created on-demand, with all their properties, such as position and velocity, tuned according to necessity [34, 35]. Most measurements in BEC experiments produce raw data in the form of images that, in our context, provide information about the solitons' positions within the BEC. The challenge is to efficiently and reliably identify the number of solitons and their locations. Traditional least-squares fitting techniques can locate solitons, provided that the soliton number is known in advance. Currently, the number of solitons is determined manually [35], and this human intervention inhibits the automated analysis of large datasets.

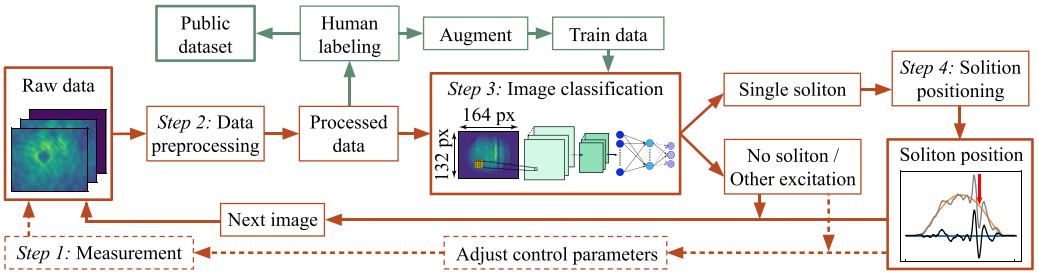

Figure 1. Schematic of the soliton detection and positioning system. Red boxes and arrows represent the flow of the full system. The dashed red boxes and arrows represent additional components required for a closed-loop implementation. The green boxes and arrows represent additional out-of-loop steps of preparing the classifier and establishing the training dataset.

Here, we describe our reliable automated soliton detection and positioning system that takes as input image data and outputs information whether a single soliton is present, and, if so, its location. Since solitons are easily identifiable by human examination of images, this problem naturally connects to the field of computer vision and ConvNet-based image classification [36]. Our algorithm consists of a data preprocessor that converts raw data into a ConvNet-compatible format; a ConvNet image classifier that determines if a single soliton has been detected; and a position regressor that locates the soliton within the BEC, when applicable (see figure 1 for a schematic of the analysis flow).

We show that our fully automated system performs comparably to our existing human image classifier, autonomously replicating the data analysis in Ref. [35]. In addition to developing a detection and positioning tool, we established a dataset of over 6000 labeled experimental images of BECs with and without solitonic excitations; this dataset is available via the National Institute of Standards and Technology (NIST) Science Data Portal [37] and at data.gov.

The remainder of this paper is organized as follows: in section 2, we illustrate the workflow of the soliton detector and its preparation process. Then in section 3, we demonstrate the system, quantify its performance, and discuss the quality of the labeled dataset. Finally in section 4, we conclude and discuss possible future directions.

2. Soliton detection and position system

In this section we describe our fully automated method of soliton detection and positioning in images of BECs. Our four-step protocol, detailed in the following sections and depicted in figure 1, is outlined as follows.

Step 1: Measurement. The measurement consists of three raw images that are combined to produce a single image of the atomic density distribution.

Step 2: Data preprocessing. As shown in figure 1, the BEC is rotated with respect to the image frame orientation, and the region of interest where atoms are captured is a small fraction of the full image. To simplify soliton positioning, the data is first rotated to align the BEC orientation with the image frame and then cropped prior to the classification step.

Step 3: Image classification. The pre-trained ConvNet classifier determines whether a lone soliton is present in a given image. If so, step four is executed, otherwise the image analysis terminates.

Step 4: Soliton positioning. The soliton position with respect to the BEC center is determined using a least-squares fit based on a one-dimensional (1D) model function.

2.1. Experimental setup and measurement

In our experiments, solitons are created and propagate the nonlinear media of a ^{87}Rb atomic BEC. We create BECs using well-established techniques for cooling and trapping atoms [38], allowing us to obtain $N = 2.4(2) \times 10^5$ atom[3] condensates in a time-averaged crossed optical dipole trap. Since solitons are only stable in quasi-1D systems [39], i.e., resulting from highly anisotropic trapping geometries, our potential is elongated, with trapping frequencies $[\omega_x, \omega_y, \omega_z] = 2\pi \times [9.1(1), 153(1), 94.5(6)]$ Hz.

We launch solitons using our recently developed 'improved' protocol, that simultaneously engineers the density and phase of the BEC wave function [35]. By contrast with the 'standard' protocol that only modifies

[3] We use a notation value(uncertainty) to express uncertainties, for example 1.5(6) cm would be interpreted as (1.5 ± 0.6) cm. All uncertainties herein reflect the uncorrelated combination of single-sigma statistical and systematic uncertainties.

the BEC phase and can only create solitons within a small range of initial velocities, our protocol can create solitons with arbitrary initial velocity. The potentials for density engineering and phase imprinting are both generated by far-detuned laser light, spatially patterned by a digital micromirror device (DMD). Our protocol is summarized as follows: After the BEC is created, we reduce its local density by applying a repulsive dimple potential. Next, the DMD is reprogrammed to display a step function that illuminates only half of the BEC, imprinting the soliton's phase profile. To minimize creating additional density perturbations, the dimple potential is reapplied and its magnitude slowly ramped to zero. We note that in our data there are additional solitonic excitations that, while representing different physical states (e.g. kink solitons, solitonic vortices, soliton rings and so forth [40]), can result in similar image and we identify simply as solitons in our analysis.

After solitons are created, we let them oscillate in the harmonic trapping potential for a variable evolution time. For evolution times much less than the trap period, additional density excitations from the soliton imprinting process are present. We then turn off the trapping potential and let the BEC evolve for a 15 ms time of flight, before absorption imaging the resulting density distribution [41].

2.2. Data preprocessing

We established a dataset of over 6.2×10^3 images for ConvNet training; these images were taken from multiple experiments performed in a single lab over a span of two months. The raw images were obtained with a 648×488 pixel camera (Point Grey FL3) with 5.6 μm square pixels, labeled by i and j. Including the $\approx 6\times$ magnification, each pixel has effective 0.93 μm size. The diffraction limit of the imaging system gives an optical resolution of ≈ 2.8 μm (roughly three pixels).

Absorption imaging combines three raw images into a single record of atomic density. In the first image $I^{\mathrm{A}}_{i,j}$, a probe laser illuminates the BEC and the resulting intensity records the probe with the BEC's shadow. The second image $I^{\mathrm{P}}_{i,j}$ records only the probe intensity, and the third image $I^{\mathrm{BG}}_{i,j}$ is a dark frame containing any ambient background signal. The 2D column density

$$\sigma_0 n_{i,j} \approx -\ln\left[\frac{I^{\mathrm{A}}_{i,j} - I^{\mathrm{BG}}_{i,j}}{I^{\mathrm{P}}_{i,j} - I^{\mathrm{BG}}_{i,j}}\right] \tag{1}$$

can be derived from these images, where the resonant cross-section $\sigma_0 = 3\lambda^2/(2\pi)$ is derived from the wavelength λ of the probe laser. The dimensionless product $\sigma_0 n_{i,j}$ is of order 1 in our data, so we express density in terms of this product. Figure 1 shows an example of the probe beam with atoms and the resulting density in the 'raw data' and 'image classifier' frames, respectively.

In our raw data, the BEC occupies only a small region of the image, and the long axis of the BEC is rotated by about 43 degrees with respect to the camera. To facilitate the ConvNet training, the images are rotated to align the BEC with the image frame and cropped to discard the large fraction of the image that does not contain information about the BEC. Since the BEC's position and shape can vary for different realizations of the same experiment, we implement a fitting approach to determine the position and size of the BEC.

Next, we fit every image to a column-integrated 3D Thomas–Fermi distribution [42], giving the 2D distribution:

$$n^{\mathrm{TF}}_{i,j} = n_0 \max\left\{\left[1 - \left(\frac{i-i_0}{R_i}\right)^2 - \left(\frac{j-j_0}{R_j}\right)^2\right], 0\right\}^{3/2} + \delta n. \tag{2}$$

This function describes the density distribution of 3D BECs integrated along the imaging axis. We use six parameters to fit: the BEC center coordinates $[i_0, j_0]$; the peak 2D density n_0; the Thomas–Fermi radii $[R_i, R_j]$; and an offset δn from small changes in probe intensity between images.

Successful fitting requires acceptable initial guesses for all fit parameters. We obtained guesses for i_0 and j_0 by summing the image along the vertical and horizontal directions to obtain two 1D projections, from which we select the average position of the five largest values as the initial guesses. We took the largest value of the image as the guess for n_0 and used $[R_i, R_j] = [66, 55]$ pixels, based on the typical radii over the whole dataset. The guess for the offset δn is zero. The result of these fits are included in our released dataset.

We determined the 164×132 pixel extent of the cropping region by examining the radii $[R_i, R_j] = [66(5), 58(3)]$ obtained from fits to 6.2×10^3 images. We then centered the cropping region at $[i_0, j_0]$ as determined from fits of each image separately. The process was validated on an additional 10^4 images not included in our dataset. In the preprocessed images, dark solitons appear as vertically aligned density depletions and are easily visually identified (see top-left panel in figure 2(b)).

2.3. Labeling

Three independent human labelers labeled the preprocessed data, categorizing the images into three classes: 'no soliton', 'single soliton', and 'other excitations'. The 'no soliton' class contains images that unambiguously

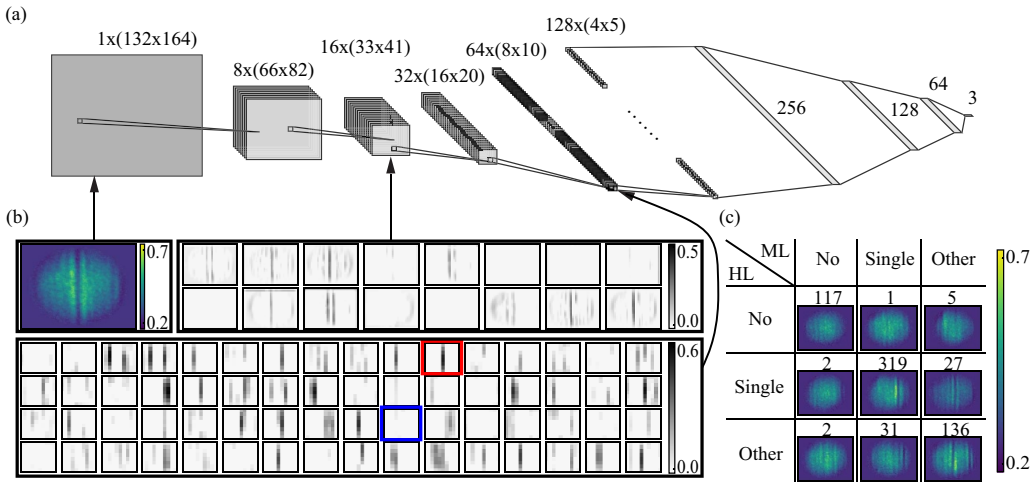

Figure 2. (a) ConvNet classifier structure. The first box represents a preprocessed input image. Each of the following left-most five architecture components represent a combination of a convolutional layer with a ReLU activation function and a max pooling layer, with their filter number and image size specified. Each of the following three components represents a combination of a fully connected layer with a ReLU activation, and a dropout layer, with their neuron number specified. The last component represents a fully connected output layer with softmax activation. (b) Visualization of the input, second, and fourth max pooling layer activation for a successfully classified single soliton image. The top left panel is the input image, the 16 images in the top right panel are the output of the max pooling layer, and 64 images in the bottom panel are the output of the fourth max pooling layer. The red boxed filter indicates one of the filters that captures the lone soliton feature. The blue boxed filter would activate if more than one soliton is present (see appendix A.1 for no soliton/other excitation). (c) Confusion matrix of the test set, comparing between human assigned labels (HL) and ML classifier prediction (ML). The images show sample successful (diagonal) and misclassified (off-diagonal) cases. The numbers above indicate how many images are assigned to a given class.

Table 1. Human labeling result. The first two columns (Full) show image counts and percentages of each class. The last two columns (3-agree) compare the counts and ratio in the all data of each class for the images with labels that humans initially agreed on.

Dataset	Full		3-agree	
Class	Count	Percentage [%]	Count	Agreement ratio [%]
No soliton	1237	19.8	1184	95.7
Single soliton	3468	55.4	3077	88.7
Other excitations	1552	24.8	1184	76.3
Total	6257	100.0	5445	87.0

contains no solitons; the 'single soliton' class describes images with one and only one soliton; and 'other excitations' class covers any image that can neither be interpreted as 'no soliton' nor 'single soliton'. We did not include a separate 'two soliton' class in our demonstration because the small number of images with two solitons led to ineffective training.

The labeling process was carried out in eight batches, with each batch size limited by the attention span of the labelers. Once a given batch was completed, the resulting labels were compared and images with full agreement were set aside. The overall labeling agreement rate was 87% (table 1 shows a comparison of the labeling agreement for all three classes), consistent across all batches. The remaining images were further analyzed and discussed until an agreement was reached. The final distribution of images between classes is as follows: 19.8% in the no soliton class, 55.4% in the single soliton class, and 24.8% in the other excitations class. Figure 2(c) shows representative labeled images from each class. This labeled dataset was employed to train the ConvNet classifier and to test the positioning protocol.

2.4. Image classification

Our ConvNet classifier, shown in figure 2(a), consists of five convolutional layers. Each layer is followed by a rectified linear unit (ReLU) function defined as $f(x) = \max(0, x)$, then a max pooling layer[4]. The final max pooling layer is flattened and fully connected to a deep neural network with three hidden layers (256, 128, and 64 neurons, respectively) and an output layer (three neurons). Each hidden layer is followed by the ReLU

[4] Max pooling is a form of non-linear down-sampling that converts the input $(km \times ln)$ array, partitioned into a set of non-overlapping rectangles of equal $(k \times l)$ size, into a smaller $(m \times n)$ array with entries representing the maximum value of the corresponding sub-region.

Table 2. Classification performance summary for the best classifier when training with the full training dataset with performance measured using cross-validation from the training, when testing on the full test dataset, and when testing on a subset of the test dataset with labels that labelers initially agreed on.

	Cross-validation	Full test set	Labelers initially agreed subset
Accuracy [%]	89.6(5)	89.4	91.6
Weighted F1	0.896(6)	0.894	0.916
No soliton F1	0.938(10)	0.959	0.983
Single soliton F1	0.920(4)	0.913	0.935
Other excitations F1	0.806(6)	0.807	0.782

activation function, and to reduce overfitting, a dropout layer that randomly eliminates neural connections with a frequency of 0.5 during each training stage. The output vector $\boldsymbol{\xi} = (\xi_1, \xi_2, \xi_3)$ is normalized by the softmax activation function, giving the final output probabilities $P_m(\boldsymbol{\xi}) = \exp(\xi_m)/\sum_n \exp(\xi_n)$.

The labeled dataset was divided into two subsets: 640 images (10.2% of the dataset) were set aside as testing set, while the remaining 5617 images (89.8%) were used for training during the model architecture development. Since our training dataset is unbalanced, i.e. its different classes have a significantly different number of images, we balance it using augmentation techniques. We augment using three physically acceptable transformations: horizontal and vertical reflections, as well as a 180 degree rotation. All three transformations were applied to the no soliton and other excitations classes, increasing their size by a factor of four. For the single soliton class we used one randomly chosen transformation per image, doubling the size of this class. After augmentations, the size of the three classes has a $0.28 : 0.38 : 0.34$ fractional distribution. To model a small rotation angle present in different realizations of our BEC, we randomly rotate images by an angle in the range ± 1 degree every time they are used during the training process. We applied an elliptical mask with radii $[R_i, R_j]$ to each image, eliminating all technical noise outside the BEC, to accelerate the training process[5]. Lastly, we preconditioned the data to have a range suitable for ConvNet input by uniformly scaling the image-values to the $[0, 1]$ range.

Since our testing dataset remains unbalanced, we assess the performance of trained models using the weighted F1 score [43]. When two models have similar weighted F1 scores, we first compare their accuracies as a tie-breaker, and if that fails we use the F1 score of the single soliton class[6].

We used a semi-structured search through the model parameter space, and the resulting performance for varying hyperparameters is detailed in the appendix A.2. Once we determined the best performing model, we used randomly selected 95% of training set for the final training. Training terminated when the F1 score of the remaining 5% did not increase for five epochs. We took the model prior to these five non-improving epochs as our final trained model.

Figure 2(b) shows representative intermediate convolutional layers of the trained model, with a correctly classified single soliton as the input. We observe that some filters, such as the one marked with a red box, successfully capture the information of a single soliton (further examples are presented in appendix A.1).

Figure 2(c) and the second column of table 2 show the results of our final soliton classifier. In summary, our model has weighted $F_1 \approx 0.9$ and accuracy $\approx 90\%$, in excess of the 87.0% human agreement ratio. The most frequent classifier errors conflate images from the single soliton class and the other excitations class: 6.9% of the single soliton images is wrongly assigned to the other classes ($P_1 < 0.2$), and 4.3% has no clear assignment ($0.2 \leqslant P_1 < 0.8$).

Figure 3(b) shows that the classifier works very well for the no soliton and single soliton classes. The classifier performs better when tested against human-initially-agreed data than human-initially-disagreed data, suggesting that some disagreed upon images may be truly ambiguous (Also see the last column in table 2). In addition, we observe an anomalously large misclassification rate for human agreed data in the other excitations class, resulting from the human labelers use of this class when facing a dilemma. Furthermore, the wrongly classified data are distributed near the corners of figure 3(a), indicating a high degree of confidence in the misclassification.

[5] In early training attempts, the classifier learned to separate the BEC from the background. Because the BEC resides within a well-defined ellipse, we accelerated convergence by applying the elliptical mask prior to training.

[6] We use the F1 score of the single soliton class as the final tie-breaker, because we ultimately compare to single-soliton dynamics data in section 3.1.

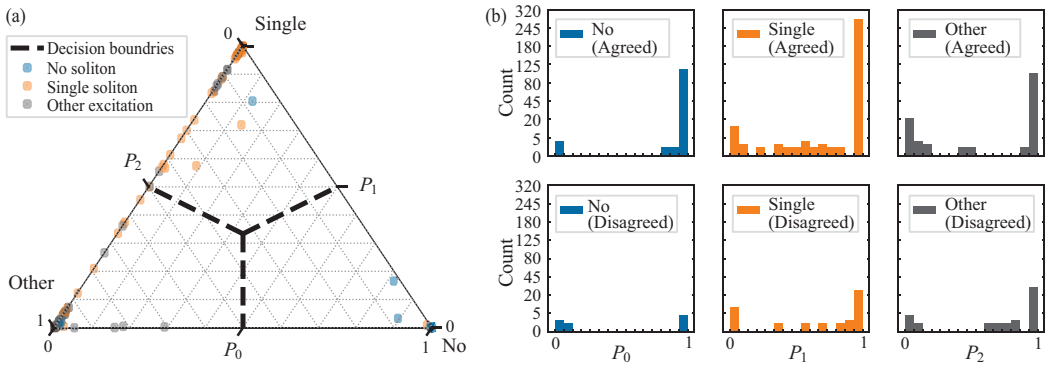

Figure 3. Soliton classification results. (a) Distribution of test data, colored by ground truth label. The scattered dots with different labels overlap each other in a randomized order. (b) Histogrammed probabilities. The upper panels histogram the classification probabilities from human-initially-agreed data, while the lower panels histogram those from human-initially-disagreed data. The vertical axes are in square root scale to emphasize the misclassified data.

2.5. Position regression

Once images containing only one soliton are identified, we locate the soliton position using a simple yet robust least-squares fitting procedure [43]. The first step consists of summing each 2D image along the j direction to obtain a 1D distribution $n_i = \sum_j n_{i,j}$. We fit the 1D distributions to the expected profile:

$$n_i^{1D} = n_0^{1D} \max\left\{\left[1 - \left(\frac{i - i_0}{R_i}\right)^2\right], 0\right\}^2 + \delta n^{1D}, \tag{3}$$

that is, equation (2) integrated along the j direction. The initial guess for n_0^{1D} was the max of the integrated distribution, and the remaining guesses were taken from the successful 2D fit. We subtract the fit from the integrated 1D profile to obtain the residuals $\Delta_i = n_i - n_i^{1D}$. Ideally, this procedure would result in a flat background containing a single dip, associated with the soliton, which we identified using a Gaussian fit[7]. We use the minimum of Δ_i as the initial guess for the Gaussian amplitude, the minimum position as the initial center, 3 pixels for the width, and zero for the offset. This fit yielded the soliton width, amplitude and position.

3. Results

3.1. Soliton detector

To test the performance of the fully automated soliton detection and positioning system, we use two sets of images containing oscillating dark solitons[8] that were launched using the standard and improved protocols described in section 2.1, with 60 and 59 images, respectively.

In the first test, we used the improved-protocol data-set, with representative summed data n_i presented in the top panel of figure 4(a). As the solitons in these images are well pronounced, we expected the ConvNet will easily classify them. Out of 59 images, 52 were classified as single soliton and the remaining seven were classified as other excitations, in agreement with a human labeler. Solitons were then located in the first group by the positioning regressor (see figure 1). The middle and bottom rows in figure 4(a) plot the soliton position from manual and ConvNet identification, respectively. We fit $i(t) = A\sin(\omega t + \Phi) + i_0$ to the soliton position data, and we compare the fitted parameters with those obtained from our previous manual approach. As can be seen by comparing the middle and bottom rows of figure 4(a), the performance of the automated protocol is basically indistinguishable from the manual approach. The physical parameters from the ML classifier ($A = 2(2)$ pixels and $\omega/2\pi = 2.3(7)$ Hz) were within one standard deviation of those obtained for manual soliton identification ($A = 2(2)$ pixels and $\omega/2\pi = 2.3(6)$ Hz).

In the second test, we used images with solitons generated by the standard phase imprinting protocol. As can be seen in the top panel of figure 4(b), solitons in these images can be shallower than those in figure 4(a), making them potentially more difficult to distinguish from the no soliton and other excitations classes. Out of the 60 images in this test, 22 were classified by the ConvNet as no soliton, and 11 as other excitations, in

[7] We found that the Gaussian gave the highest quality of fit as compared to other peaked functions.

[8] These two sets of images contribute to the data published in figure 2 of [35], and are presented here in figure 4.

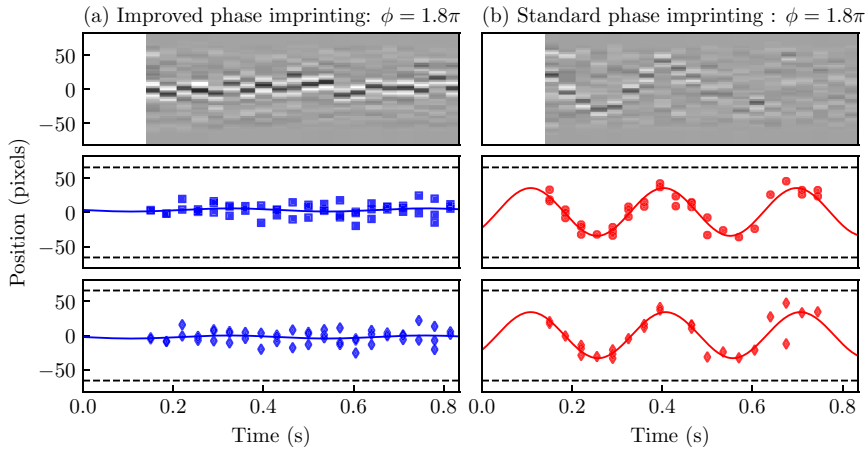

Figure 4. Oscillation of dark solitons created by applying $1.8(1)\pi$ phase using the (a) improved and (b) standard protocol described in [35]. Top panels show samples for the residuals Δ_i, obtained after subtracting the fit from the 1D profile. Middle and bottom panels show the soliton positions and sinusoidal fits (as described in the text) based on manually identified images and the outputs of the automated system, respectively. Dashed lines at $j = \pm 66$ pixels in all four panels represent the edges of the BEC.

agreement with a human labeler. The remaining 27 were classified as a single soliton and were sent to the position regressor. The lower panels in figure 4(b) show soliton position as a function of evolution time, obtained from manual [35] and ConvNet identification, respectively. Since [35] compared the soliton oscillation amplitude resulting from the two imprinting protocols, the authors did not limit themselves to images with a single soliton. Rather, when more than one soliton was created, the authors identified all the solitons but tracked only that associated with a specific trajectory. Since the ConvNet classifier was trained to select images with single soliton excitations, the middle panel in figure 4(b) includes 12 more points than the bottom panel. Even with fewer data points, however, the parameters from the ML classifier ($A = 34(3)$ pixels and $\omega/2\pi = 3.34(9)$ Hz) were within one standard deviation of those obtained for manual soliton identification ($A = 35(2)$ pixels and $\omega/2\pi = 3.39(5)$ Hz).

The complete analysis resulting in both oscillation plots took under 148 s per series on a 2014 MacBook Pro. The expected performance relevant for in-situ operation is ≈ 2.4 s per image, a relatively small overhead on top of the measurement time (about 12 s). In many cases, however, the analysis of an image would take place during the acquisition of the next image.

3.2. Soliton dataset

As with all ML techniques, the availability of the training data is essential for good performance of the trained classifier. To assure the reliability of the assigned labels, the full dataset was independently labeled by three labelers, as described in section 2.2. Our full soliton image dataset consists of 6 257 labeled images. There are 1237, 3468, and 1552 images for no soliton, single soliton, and other excitations classes, respectively.

While for 5445 (87.0%) of the images the assigned labels were consistent between labelers, for the remaining 812 images (13.0%) there was a disagreement with at least one labeler. These images needed to be further discussed until an agreement was reached. As can be seen in table 1, the most challenging was distinguishing between images with single soliton and other excitations. This is likely due to the fact that the phase-imprinting method used to imprint solitons can also create other excitations that appear as density modulations or fringes in the BEC. Examples of such modulation can be seen in the off-diagonal images in figure 2(c). Additional discussion of the misclassified and mislabeled data can be found in appendix A.3.

Our dataset includes the full-frame raw images, the cropped and rotated images as used in this study, as well as the set of the fitted integrated 2D Thomas–Fermi distribution parameters. This dataset is sufficient to reproduce our results but also to test fitted alternative models with varying cropping size or image resolution [37].

4. Conclusion and outlook

In this manuscript, we present an automated dark soliton detection and positioning system that combines ML-based image classification with standard fitting techniques to track soliton dynamics in experimental images of BECs. We show that the system performs on par with more traditional approaches that rely on human input for soliton identification, creating the opportunity to study soliton dynamics in large datasets.

We also make available the first dataset of images from a dark soliton BEC experiment, which provides an opportunity for the data science community to develop more sophisticated analysis tools and to further understand nonlinear many-body physics.

The performance of the classifier, as measured by the weighted F1 score, leaves room for improvement. While tuning the hyperparameters allowed us to substantially improve the initial performance, additional data is necessary to push the limits. However, human labeling is not only time-consuming but, as the analysis of the misclassified images revealed, is also not always reliable. Other approaches, such as active learning ML [44], may be more suitable for this task. Such enlarged dataset, in turn, will enable refining the soliton classifier and perform model uncertainty quantification [45, 46], which currently is not accounted for. Together, these refinements may enable reliable in-situ deployment.

This study was preconditioned on the assumption of specific structure in the images, leading to our three classes. Enlarged dataset will enable employing unsupervised learning strategies [47] to possibly discover additional classes consistent with the data without presumptions. This unsupervised learning of soliton-data is a prototype for ML based discovery with cold-atom data in general.

Data availability statement

The data that support the findings of this study are openly available at the following URL/DOI: https://doi.org/10.18434/mds2-2363.

Acknowledgments

This work was partially supported by NIST and NSF through the Physics Frontier Center at the JQI. We appreciate conversations with Yuchen Yue and Justin Elenewski.

Appendix

A.1. Additional visualization of intermediate convolutional layers

In addition to figure 2(b) in the main text (visualizing the single soliton case), figure A1 shows the same intermediate layers for the correctly classified sample images from the (a) no soliton and (b) other excitations classes. In both figures, we highlight two filters: red box indicates a filter that activates for an image with a single soliton, while the blue box indicates a filter that activates for an image from the other excitations class. For an image from the no soliton class (figure A1(a)), neither highlighted filter is activated. This confirms that filters in our model are trained to properly detect and locate features that are characteristic of each class in a previously unknown image.

A.2. Model parameter tuning

We used a naive semi-structure search approach to optimize our model parameter. During parameter tuning, we used k-fold cross-validation to assess the generalizability of trained models. For each set of hyperparameters defining the overall model (e.g. kernel size and number of layers, both convolutional and hidden), the training set was split into $k = 5$ smaller sets ('folds'), four of which were used for training and one for validation. Once the model was trained using all five cross-validation combinations, the mean score was recorded and compared against scores from networks with other hyperparameters. We arrange the parameters by their importance: filter number of each convolutional layers, dense layer node number, optimizer, convolution kernel size, dropout rate and batch size. The parameters are optimized in this order and the history of hyperparameter tuning is shown in table A1.

A.3. Misclassified data

As discussed in section 2.1, in BEC experiments trapped condensates are often held for a certain period of time after phase imprinting. This is necessary to smooth out the various other excitations resulting from the phase imprinting process. However, by looking only at a single image (single holding time), all the information about the soliton dynamics is lost, and other excitations can be confused with shallow solitons. In the final 640 images in the test dataset, there are 68 misclassified images in one of six possible ways. As can be seen in figure 2(c), for our model, the most confusion comes from distinguishing between the single soliton and other excitations classes. Upon reviewing the 58 images misclassified in this way, we find that out of 27 images classified as other excitations only two clearly contain lone solitons. The remaining 25 images are confusing and thus should belong to the other excitations class. Interestingly, for this case, the classifier seems to be nearly as likely to be wrong as confused (see middle columns in figure 3(b)). All 31 images classified as

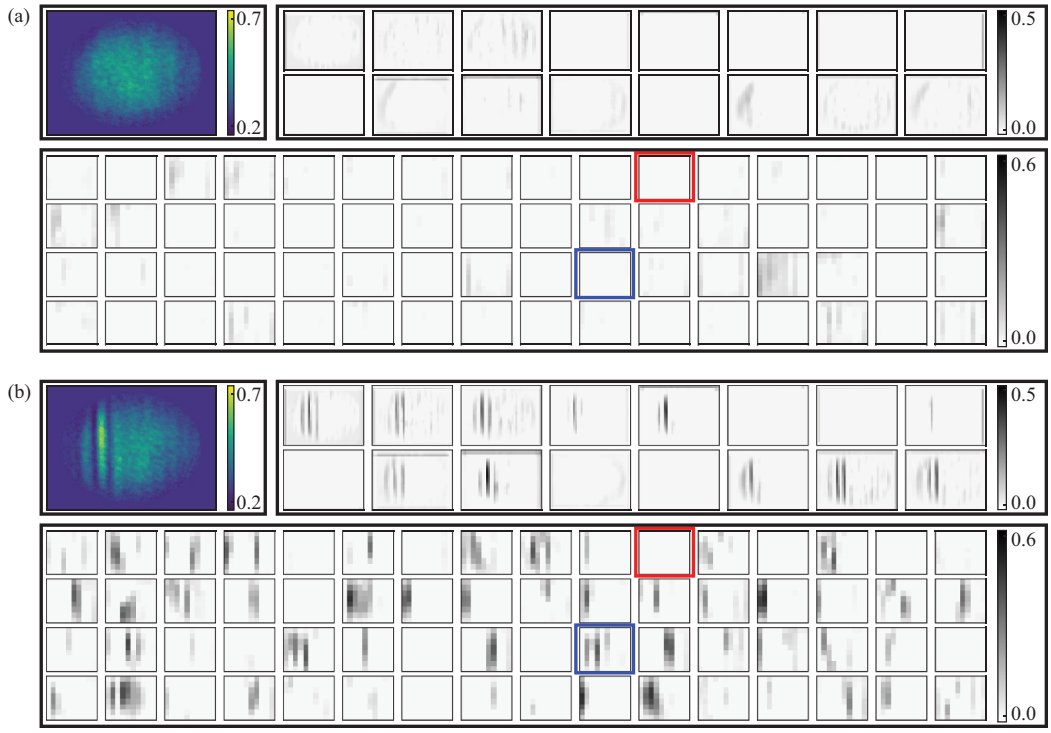

Figure A1. Visualization of the input, second, and fourth max pooling layer activation for a successfully classified (a) no soliton image and (b) other excitations one. In both cases, the top left panels are the input images, the 16 images in the top right panels represent the output of the max pooling layer, and 64 images in the bottom panels are the output of the fourth max pooling layer. The red box indicates one of the filters that captures the lone soliton feature (see figure 2(b)). The blue boxed filter activates if more than one soliton is present.

Table A1. Model parameter tuning history. For each model, we provide the number of filters for all convolutional layers (Filters), the number of nodes in the fully connected layers (Dense), as well as the kernel size of all convolutional layers (K), the dropout rate (D), the batch size (B), and the optimizer used of training (SGD: Stochastic gradient descent, SGD+M: SGD with moment, SGD+M+D: SGD+M with decay). The mean performance is averaged by 5-fold cross-validation on the training set. F1 score is weighted by three classes. Best model is highlighted. Parameters changed at each stage are highlighted in italic.

Filters	Dense	K	D	B	Optimizer	Weighted F1 [%]	Accuracy [%]	Binary F1 [%]
8 × 8×8	256 × 128	5	0.5	32	Adam	65(23)	74(15)	71(18)
8×*16*×*32*	256 × 128	5	0.5	32	Adam	56(23)	61(25)	63(19)
8 × 16×32×*64*	256 × 128	5	0.5	32	Adam	67(24)	75(16)	72(20)
8 × 16×32 × 64×*128*	256 × 128	5	0.5	32	Adam	78(20)	82(14)	81(16)
8 × 16×32 × 64×128	256 × 128×*64*	5	0.5	32	Adam	48(20)	62(13)	56(16)
8 × 16×32 × 64×128	256 × 64	5	0.5	32	Adam	58(25)	69(17)	65(20)
8 × 16×32 × 64×128	256 × 64×*16*	5	0.5	32	Adam	61(19)	75(16)	69(17)
8 × 16×32 × 64×128	*512×128*	5	0.5	32	Adam	47(20)	54(22)	56(16)
8 × 16×32 × 64×128	512 × 128×*32*	5	0.5	32	Adam	67(24)	76(16)	72(20)
8 × 16×32 × 64×128	256 × 128×64	5	0.5	32	*Adamax*	86(6)	89(1)	88(3)
8 × 16×32 × 64×128	256 × 128×64	5	0.5	32	*SGD*	70(6)	87(2)	76(4)
8 × 16×32 × 64×128	256 × 128×64	5	0.5	32	*SGD+M*	64(22)	74(15)	70(18)
8 × 16×32 × 64×128	256 × 128×64	5	0.5	32	*SGD+M+D*	39(4)	60(9)	49(2)
8 × 16×32 × 64×128	256 × 128×64	5	*0.6*	32	Adamax	77(5)	90(0)	85(3)
8 × 16×32 × 64×128	256 × 128×64	5	*0.7*	32	Adamax	51(17)	68(15)	61(16)
8 × 16×32 × 64×128	256 × 128×64	5	*0.8*	32	Adamax	44(13)	62(13)	54(12)
8 × 16×32 × 64×128	256 × 128×64	*3*	0.5	32	Adamax	86(1)	90(1)	88(1)
8 × 16×32 × 64×128	256 × 128×64	*7*	0.5	32	Adamax	88(1)	89(1)	90(1)
8 × 16×32 × 64×128	256 × 128×64	*9*	0.5	32	Adamax	89(0)	89(0)	90(0)
8 × 16×32 × 64×128	256 × 128×64	*11*	0.5	32	Adamax	78(20)	82(14)	82(17)
8 × 16×32 × 64×128	256 × 128×64	9	0.5	*16*	Adamax	79(21)	83(13)	82(17)
8 × 16×32 × 64×128	256 × 128×64	9	0.5	*8*	Adamax	78(20)	82(13)	81(17)

single solitons are true misclassification. For these images, the classifier is confidently wrong (see last columns in figure 3(b)). We suspect that it might be possible to improve the classifier by training with less penalty for classifying an ambiguous image to other excitations class. This also suggests that active learning strategy might be better for training model and labeling data than relaying on a dataset labeled by humans.

ORCID iDs

I B Spielman https://orcid.org/0000-0003-1421-8652
Justyna P Zwolak https://orcid.org/0000-0002-2286-3208

References

[1] Aurisano A *et al* 2016 A convolutional neural network neutrino event classifier *J. Instrum.* **11** 09001
[2] Acciarri R, Adams C, An R, Asaadi J and Auger M *et al* 2017 Convolutional neural networks applied to neutrino events in a liquid argon time projection chamber *J. Instrum.* **12** 03011
[3] Kagan M 2020 Image-based jet analysis (arXiv:2012.09719)
[4] Golovatiuk A, Giovanni D L and Ustyuzhanin A 2020 Deep learning for directional dark matter search *J. Phys.: Conf. Series* **1525** 012108
[5] Khosa C K, Mars L, Richards J and Sanz V 2020 Convolutional neural networks for direct detection of dark matter *J. Phys. G: Nucl. Part. Phys.* **47** 095201
[6] Kalantre S S, Zwolak J P, Ragole S, Xingyao W, Zimmerman N M, Stewart M D and Taylor J M 2017 Machine learning techniques for state recognition and auto-tuning in quantum dots *npj Quantum Inf.* **5** 1–10
[7] Mills A R, Feldman M M, Monical C, Lewis P J, Larson K W, Mounce A M and Petta J R 2019 Computer-automated tuning procedures for semiconductor quantum dot arrays *Appl. Phys. Lett.* **115** 113501
[8] Zwolak J P *et al* 2020 Autotuning of double-dot devices in situ with machine learning *Phys. Rev. Appl.* **13** 034075
[9] Usman M, Wong Y Z, Hill C D and Hollenberg L C L 2020 Framework for atomic-level characterisation of quantum computer arrays by machine learning *npj Comput. Mater.* **6** 1–8
[10] Cao Z, Dan Y, Xiong Z, Niu C, Xiang Li, Qian S and Jianjun H 2019 Convolutional neural networks for crystal material property prediction using hybrid orbital-field matrix and magpie descriptors *Crystals* **9** 191
[11] Karamad M, Magar R, Shi Y, Siahrostami S, Gates I D and Farimani A B 2020 Orbital graph convolutional neural network for material property prediction *Phys. Rev. Mater.* **4** 093801
[12] Gubernatis J E and Lookman T 2018 Machine learning in materials design and discovery: examples from the present and suggestions for the future *Phys. Revi. Mater.* **2** 120301
[13] Duvenaud D K, Maclaurin D, Iparraguirre J, Bombarell R, Hirzel T, Aspuru-Guzik A and Adams R P 2015 Convolutional networks on graphs for learning molecular fingerprints *Adv. Neural Inf. Process. Syst.* **28** 2224–32 (https://proceedings.neurips.cc/paper/2015/file/f9be311e65d81a9ad8150a60844bb94c-Paper.pdf)
[14] Butler K T, Davies D W, Cartwright H, Isayev O and Walsh A 2018 Machine learning for molecular and materials science *Nature* **559** 547–55
[15] Winter R, Montanari F, Noé F and Clevert D-A 2019 Learning continuous and data-driven molecular descriptors by translating equivalent chemical representations *Chem. Sci.* **10** 1692–701
[16] Rem B S, Käming N, Tarnowski M, Asteria L, Fläschner N, Becker C, Sengstock K and Weitenberg C 2019 Identifying quantum phase transitions using artificial neural networks on experimental data *Nat. Phys.* **15** 917–20
[17] Ness G, Vainbaum A, Shkedrov C, Florshaim Y and Sagi Y 2020 Single-exposure absorption imaging of ultracold atoms using deep learning *Phys. Rev. Appl.* **14** 014011
[18] Pilati S and Pieri P 2019 Supervised machine learning of ultracold atoms with speckle disorder *Sci. Rep.* **9** 5613
[19] Metz F, Polo J, Weber N and Busch T 2021 Deep learning based quantum vortex detection in atomic Bose-Einstein condensates *Mach. Learn.: Sci. Technol.* (available at: https://doi.org/10.1088/2632-2153/abea6a)
[20] Weller A, Ronzheimer J P, Gross C, Esteve J, Oberthaler M K, Frantzeskakis D J, Theocharis G and Kevrekidis P G 2008 Experimental observation of oscillating and interacting matter wave dark solitons *Phys. Rev. Lett.* **101** 130401
[21] Frantzeskakis D J 2010 Dark solitons in atomic Bose–Einstein condensates: from theory to experiments *J. Phys. A: Math. Theor.* **43** 213001
[22] Russel J S 1837 *Report of the Committee on Waves* 417–68 British reports VI plus plates 1–8
[23] Osborne A R and Burch T L 1980 Internal solitons in the Andaman sea *Science* **208** 451–60
[24] Lakshmanan M 2009 *Solitons, Tsunamis and Oceanographical Applications of* (New York: Springer) pp 8506–21
[25] Burger S, Bongs K, Dettmer S, Ertmer W, Sengstock K, Sanpera A, Shlyapnikov G V and Lewenstein M 1999 Dark solitons in Bose–Einstein condensates *Phys. Rev. Lett.* **83** 5198–201
[26] Denschlag J *et al* 2000 Generating solitons by phase engineering of a Bose–Einstein condensate *Science* **287** 97–101
[27] Hasegawa A and Tappert F 1973 Transmission of stationary nonlinear optical pulses in dispersive dielectric fibers. ii. normal dispersion *Appl. Phys. Lett.* **23** 171–2
[28] Mollenauer L F, Stolen R H and Gordon J P 1980 Experimental observation of picosecond pulse narrowing and solitons in optical fibers *Phys. Rev. Lett.* **45** 1095–8
[29] Stasiewicz K, Shukla P K, Gustafsson G, Buchert S, Lavraud B, Thidé B and Klos Z 2003 Slow magnetosonic solitons detected by the cluster spacecraft *Phys. Rev. Lett.* **90** 085002
[30] Hashizume Y 1985 Nonlinear pressure waves in a fluid-filled elastic tube *J. Phys. Soc. Japan* **54** 3305–12
[31] Yomosa S 1987 Solitary waves in large blood vessels *J. Phys. Soc. Japan* **56** 506–20
[32] Mollenauer L F and Gordon J P 2006 *Solitons in Optical Fibers* (Burlington, VA: Academic)
[33] Hasegawa A 2000 Soliton-based optical communications: an overview *IEEE J. Sel. Top. Quantum Electron.* **6** 1161–72
[34] Aycock L M, Hurst H M, Efimkin D K, Genkina D, Lu H-I, Galitski V M and Spielman I B 2017 Brownian motion of solitons in a Bose–Einstein condensate *Proc. Natl Acad. Sci.* **114** 2503–8
[35] Fritsch A R, Mingwu L, Reid G H, Piñeiro A M and Spielman I B 2020 Creating solitons with controllable and near-zero velocity in Bose–Einstein condensates *Phys. Rev.* A **101** 053629

[36] Rawat W and Wang Z 2017 Deep convolutional neural networks for image classification: a comprehensive review *Neural Comput.* **29** 2352–449
[37] Database: data.nist.gov [Internet] Dark solitons in BECs dataset 2020 (available at: https://doi.org/10.18434/mds2-2363)
[38] Lin Y-J, Perry A R, Compton R L, Spielman I B and Porto J V 2009 Rapid production of [sup 87]rb Bose-Einstein condensates in a combined magnetic and optical potential *Phys. Rev.* A **79** 63631
[39] Muryshev A, Shlyapnikov G V, Ertmer W, Sengstock K and Lewenstein M 2002 Dynamics of dark solitons in elongated Bose–Einstein condensates *Phys. Rev. Lett.* **89** 110401
[40] Muñoz Mateo A and Brand J 2015 Stability and dispersion relations of three-dimensional solitary waves in trapped Bose–Einstein condensates *New J. Phys.* **17** 125013
[41] Ketterle W, Durfee D S and Stamper-Kurn D M 1999 Making, probing and understanding Bose–Einstein condensates *Bose-Einstein Condensation in Atomic Gases, Proc. Int. School of Physics 'Enrico Fermi', Course CXL* ed M Inguscio, S Stringari and C E Wieman (Amsterdam: IOS Press) pp 67–176
[42] Castin Y and Dum R 1996 Bose-Einstein condensates in time dependent traps *Phys. Rev. Lett.* **77** 5315–19
[43] Pedregosa F *et al* 2011 Scikit-learn: machine learning in Python *J. Mach. Learn. Res.* **12** 2825–30
[44] Settles B 2009 Active learning literature survey *Technical Report* University of Wisconsin-Madison Department of Computer Sciences
[45] Abdar M *et al* 2020 A review of uncertainty quantification in deep learning: techniques, applications and challenges (arXiv:2011.06225)
[46] Thiebes S, Lins S and Sunyaev A 2020 Trustworthy artificial intelligence *Electron. Markets* 1–18
[47] Ji X, Henriques J F and Vedaldi A 2019 Invariant information clustering for unsupervised image classification and segmentation *2019 IEEE/CVF Int. Conf. on Computer Vision (ICCV) (Seoul, Korea, Oct 27–Nov 2 2019)* (IEEE) 9864–73

Appendix D: Preprint for Chapter 5: Combining Machine Learning with Physics: A Framework for Tracking and Sorting Multiple Dark Solitons

Combining Machine Learning with Physics: A Framework for Tracking and Sorting Multiple Dark Solitons

Shangjie Guo,[1] Sophia M. Koh,[2,3] Amilson R. Fritsch,[1] I. B. Spielman,[1] and Justyna P. Zwolak[3,*]

[1] *Joint Quantum Institute, National Institute of Standards and Technology, and University of Maryland, Gaithersburg, Maryland 20899, USA*

[2] *Department of Physics and Astronomy, Amherst College, Amherst, Massachusetts 01002, USA*

[3] *National Institute of Standards and Technology, Gaithersburg, Maryland 20899, USA*

(Dated: April 14, 2022)

In ultracold atom experiments, data often comes in the form of images which suffer information loss inherent in the techniques used to prepare and measure the system. This is particularly problematic when the processes of interest are complicated, such as interactions among excitations in Bose-Einstein condensates (BECs). In this paper, we describe a framework combining machine learning (ML) models with physics-based traditional analyses to identify and track multiple solitonic excitations in images of BECs. We use an ML-based object detector to locate the solitonic excitations and develop a physics-informed classifier to sort solitonic excitations into physically motivated sub-categories. Lastly, we introduce a quality metric quantifying the likelihood that a specific feature is a longitudinal soliton. Our trained implementation of this framework—SolDet—is publicly available as an open-source python package. SolDet is broadly applicable to feature identification in cold atom images when trained on a suitable user-provided dataset.

I. INTRODUCTION

Machine learning (ML) techniques promise improved data analysis and enhanced performance for today's quantum devices and technologies. Ultracold atomic gases are a nearly ideal system to deploy ML-driven analysis, where the automated exploration and interpretation of very large dataset—in the form of images—can lead to scientific enhancements and experimental optimization [1] as well as new discoveries. Here we focus on the general problem of feature identification, a commonly recurring task in the analysis of such data, from locating vortices [2–4] or tracking solitons [5, 6], identifying spin textures or magnetic domain walls [7–9] to locating topological singular points [10]. While data from these examples have been individually analyzed using task-specific algorithms (or even manual inspection), they are all feature identification problems that can be solved using a single ML-enhanced analysis framework. This manuscript introduces such a framework, and demonstrates its utility on the specific problem of identifying solitonic excitations in atomic Bose-Einstein condensates (BECs), as well as quantifying the quality of each identified feature.

Traditional statistical analysis using physics-based models, such as least-square fitting and hypotheses testing, have been go-to techniques for data analysis since the 1800's [11] and remain widely applied in quantum cold-atom image analysis [12–14]. The outcome of physics-model-based algorithms and fits are intuitive, physically meaningful, and can help identify patterns present in the data; even fits based on more heuristic functions can have coefficients that are derived in obvious ways from the data. By contrast, ML methods work as "black boxes," making their operation difficult to interpret. Conventional statistical methods use fixed algorithms in conjunction with preconceived models for data reduction. Overfitting occurs when the number of fit parameters is comparable or larger than the number of independent data points. In this context, the process of training an ML tool essentially co-designs the fitting algorithm and the data model, as encoded by a large number of internal parameters. Training ML models is itself a fitting process that can be susceptible to overfitting, for example when the training dataset has too little variability or the ML model has too many internal parameters. ML involves a class of data-driven techniques that do not rely on preexisting models, but also add additional opportunities for overfitting that can make them less reliable on new data than conventional techniques.

Here, we describe the hybrid two-module feature identification framework shown in Fig. 1, that combines the flexibility of ML techniques with the intuition and robustness of conventional fitting methods. Furthermore the separate outputs of these two very different modules allow us to assess data quality by cross-validation. Hybrid approaches have been employed in other settings, for example for landslide prediction [15], medical image processing [16], and cyber attack detection [17].

The framework begins with a labeled dataset that is used to train the ML module and initialize the physics-based module. Before trusting either module, we independently validate each module on a subset of the labeled data that was not used for training. Model-redesign may be needed until satisfactory performance of each module is reached. We then combine both modules into an integrated system able to analyze new data.

We demonstrate the performance of our framework using data from atomic BECs, quintessential quantum systems. Quantum research with BECs, and cold-

* jpzwolak@nist.gov

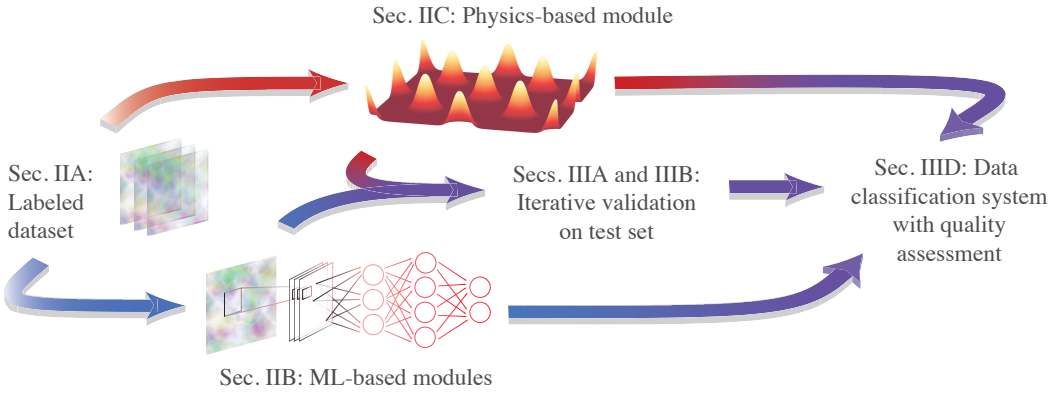

FIG. 1. Overview of the framework. The colored arrows link the preparation (Secs. II A, II B, and II C), validation (Secs. III A. III B), and application (Sec. III D) phases of the framework. The red path represents the preparation and implementation of the physics-based-approximation module of the framework. The blue path represents the ML modules.

atom quantum gases more broadly, is multifaceted with examples ranging from realizing collective many-body physics [18] to creating today's most accurate atomic clocks [19]. In the vast majority of these experiments, data is acquired in the form of noisy images that typically have undergone evolution—such as a time of flight—before measurement. This often obfuscates the computation of the quantities of interest. Cold quantum gases therefore make an ideal test-bed for our methodology that combines physically motivated, but heuristic, fitting functions with established computer vision techniques.

We focus on the specific problem of locating dark solitons—spatially compact excitations that manifest as reductions in the atomic density—as they move in BECs [13, 20, 21]. This allows us to leverage our established soliton dataset [22, 23] to train and validate our framework; representative elements of the dataset are shown in Fig. 2. These data consist of elliptical atom clouds (top row) where solitons appear as vertically aligned density depletions (bottom row). Not all vertically aligned density depletions are created equal: deep depletions mark the location of slowly moving kink solitons; shallow depletions are associated with rapidly moving kink solitons or "longitudinal" solitonic vortices (where the vortex core is aligned in the image plane); asymmetric depletions can result from "transverse" solitonic vortices [24] (were the vortex core is aligned perpendicularly to the image plane); and chains of stripes can result from highly excited phonon modes. Our framework is the first tool that can automatically locate all the solitonic excitations in each image and distinguish between longitudinal solitons and transverse solitonic vortices. Here we introduce the term "longitudinal soliton" to include both kink solitons and longitudinal solitonic vortices.

Our ML module leverages and extends established computer vision techniques. Computer vision is a broad field with applications ranging from image classification to semantic segmentation and object detection [25]. Object detection refers to the capability of software systems to locate and identify objects in an image. Convolutional neutral networks (CNNs) underlie solutions to all of these tasks, and unsurprisingly were employed in our previous work classifying soliton image data into three categories: no solitonic excitation, one solitonic excitation, and other excitations [22]. Our ML module goes beyond simple classification and uses a CNN based object detector (OD) to provide the location of all candidate excitations in a given image.

By contrast our physics-based module employs a least-squares fit of an inverted and skewed Mexican-hat function to 1D background-subtracted projections of soliton-candidates (shown in bottom row in Fig. 2). We initialized this module using our previously labeled single soliton data and employ a Yeo-Johnson transformation [26] to produce a multivariate normal distribution yielding the likelihood that an unknown feature is a soliton.

This approach yielded three immediate benefits. First, a careful analysis of the coefficients from the physics based module identified previously overlooked correlations that allow us to distinguish between some solitonic excitations (longitudinal solitons and transverse solitonic vortex [20, 21, 24, 27]). Second, combining the results of the ML and fitting modules allowed us to automatically create a larger, more reliable dataset that includes fine-grained information such as the soliton position and type of excitation. This dataset is described in Ref. [28] and published in the NIST data repository [23]. Third, our hybrid framework was prepared solely from a training dataset whose images contain either zero or one solitonic excitation, however, it is performant on complex data containing multiple excitations.

The remainder of this manuscript is structured as follows: Sec. II introduces both modules and describes their training and initialization. Sec. III describes the validation of both modules and their performance on new data that include multiple solitonic excitations. In Sec. III E, we describe an open-source Python reference implemen-

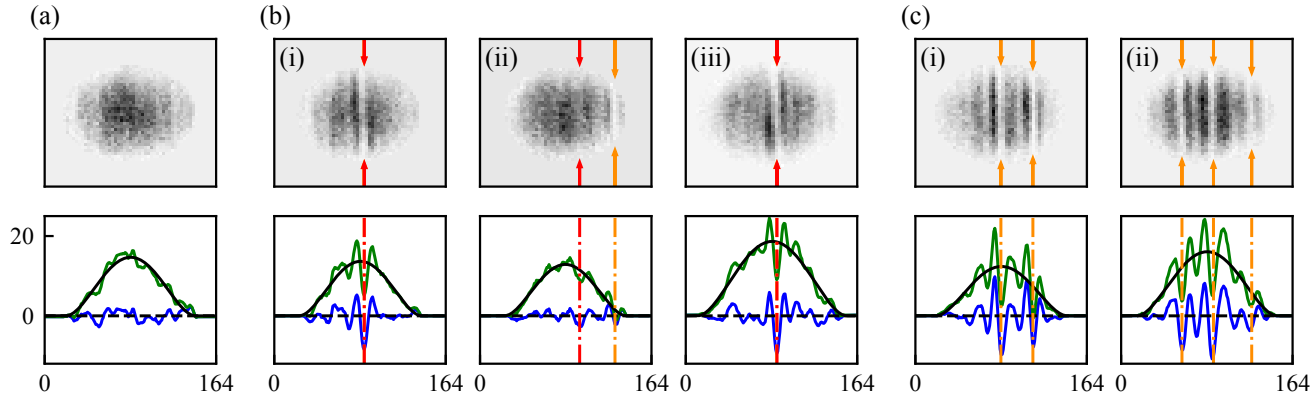

FIG. 2. Representative data. The top panels plot pre-processed images from our dataset and the bottom panels plot profiles: (green) profile of full image, (black) TF fits, (blue) density fluctuations. The red lines mark the location of the deepest depletion in the density fluctuations, while the orange lines mark the solitons locations found from our OD. (a) An element of the no-excitation class. (b) Three elements of the single excitation class: (i) a single longitudinal soliton, (ii) an off-center longitudinal soliton, and (iii) a solitonic vortex. (c) Two representative elements of the other excitations class.

tation of our framework: SolDet [29]. Lastly, in Sec. IV we conclude and discuss the potential applications of the framework as well as the possible future directions.

II. DATA AND MODULES

In addition to recent success of ML methods [22, 30, 31], solitonic excitations have also been located and characterized using traditional fitting techniques. For example, Ref. [13] began with the background-removed atom density profiles (blue curves in Fig. 2) described in Sec. II A, then identified the deepest depletion (orange dashed line), and fit to a Gaussian function (a physically motivated, but heuristic choice) centered near the deepest depletion. This yielded physical information including soliton width, depth, and position. Unfortunately, this simple approach is failure prone, as for example in Fig. 2(b-ii), where the deepest depletion is far from the actual soliton. Moreover, it detects only single solitonic features, making human intervention necessary when many excitations are present. Rather than finding the deepest minimum, our framework first uses an OD (described in Sec. II B) to provide an initial estimate of all solitonic excitations positions, and then uses a skewed Mexican hat fit function (Sec. II C) that accurately describes their density profiles. The resulting fit coefficients serve two purposes: qualitative likelihood assessment and fine-grained categorization.

A. Data

Our framework is trained and initialized using a revised dataset consisting of about 5.5×10^3 manually labeled experimental images of BECs with and without solitonic excitations [23, 28]. The experimental setup and preprocessing techniques are described in [13].

Figure 2 shows six selected sample images from the labeled dataset. The dataset includes labels for five classes: "no solitonic excitation," images that do not contain any excitations; "single solitonic excitation," images containing one solitonic excitation; "other excitations," images not in the preceding classes (including those with multiple solitonic excitations, high degrees of noise, and those annotators could not agree up (on); "mislabeled", data determined to be potentially mislabeled during curation process; and "unlabeled," images that have not been manually annotated. Additionally, for the single excitation class the dataset includes the horizontal position of excitations within BEC.

Figure 2(a) displays an image from the no excitation class, which lacks the pronounced stripes present in the remaining examples. In (b), we show three elements of the single excitation class, each containing a single dark vertical fringe: (b-i) a longitudinal soliton; (b-ii) an off-center single longitudinal soliton; and (b-iii) a solitonic vortex (see Sec. II C 2). In (c), we show two elements of the other excitations class containing more than one vertical fringe.

Horizontal 1D profiles (bottom row of Fig. 2) also have features associated with vertically aligned solitonic excitations and are amenable to least squares fitting. We obtain these profiles by first summing the pixel values vertically to compress 2D images to 1D; this sum can be over all (green curves) or part (see Sec. II C 2) of the vertical extent of the image. We then fit a 1D Thomas-Fermi (TF) model

$$n^{\mathrm{TF}}(i) = n_0 \max\left\{\left[1 - \left(\tfrac{i-i_0}{R_0}\right)^2\right], 0\right\}^2 + \delta_n \qquad (1)$$

to each summed 1D profile, where i is the horizontal pixel index, and n_0, i_0, R_0, and δ_n are fitting parameters repre-

senting peak density, center position, TF radius, and an overall offset, respectively. This fit (black curves) serves as an overall background that we subtract from the 1D profiles, leaving behind the 1D density fluctuations (blue curves). The orange dashed lines represent the location of deepest depletion in the 1D fluctuations.

B. ML Modules

Our previous dark soliton classifier [22] consisted of a CNN model that returned one of the three predefined classes: no solitonic excitation, single solitonic excitation, or other excitations. However, this detector did not locate the excitations. To compare with experimental data, we located the soliton by identifying the deepest depletion and fitting to a Gaussian, as described above. This algorithm has two limitations: (1) The soliton may not be the deepest depletion [as in Fig. 2(b-ii)]; and (2) multiple solitons cannot be located [as in Fig. 2(c)]. Here we retain the CNN classifier to globally organize the data, but inspired by a highly successful recent result using an OD to locate vortices in numerically simulated 2D BECs [30], we employ an OD to locate solitonic excitations in experimental images of highly elongated BECs.

The OD complements the CNN classifier in two ways: (1) it identifies soliton positions rather than classifying; and (2) even thought it is trained with single-soliton data, it can locate multiple excitations in the same image. We employ a neural network based OD with six convolution layers and four max-pooling layers but no fully connected layers (see App. A for more detail). The OD has an order of magnitude fewer trainable parameters than our previous CNN (7×10^4 versus $\sim 10^6$ parameters), accelerating the training process and making it lightweight to deploy. Because the OD simply requires a dataset with many representative instances of the object to be detected, it requires far less training data than the CNN classifier (which by design required substantial data from all considered classes).

In our data, the solitonic excitations are roughly 4 pixels in width. Since our images are 164 pixels wide we designed our OD to aggregate the image into 41 spatial cells, each with 2 outputs in the range $\in [0, 1]$; the OD therefore returns a 41×2 array $\widetilde{\mathbf{Y}}$. For our dataset this aggregation guarantees that each output cell can describe the state of at most one soliton. $\widetilde{Y}_{\ell,1}$ is a probability estimate that cell ℓ contains a soliton, and $\widetilde{Y}_{\ell,2}$ is the fractional position of the soliton center within that cell, where 0 or 1 correspond to the left or right edge of the cell, respectively. The OD considers any cell with $\widetilde{Y}_{\ell,1} > 0.5$ as containing an excitation, and then obtains its position from $\widetilde{Y}_{\ell,2}$.

When comparing to the training dataset with labels denoted by $\mathbf{Y}$, we use the cost function [30]

$$F = \sum_{\ell=1}^{41} \begin{cases} -w_1 \log(\widetilde{Y}_{\ell,1}) + w_2 (Y_{\ell,2} - \widetilde{Y}_{\ell,2})^2, & \text{if } Y_{\ell,1} = 1 \\ -\log(1 - \widetilde{Y}_{\ell,1}), & \text{if } Y_{\ell,1} = 0 \end{cases} \tag{2}$$

for each training image, where the label $Y_{\ell,1}$ identifying the presence of an excitation in a cell is fully confident, i.e., either 0 or 1. The coefficients w_1, w_2 are hyperparameters controlling the relative importance of each term. The log terms increase the cost function when the the OD misidentifies solitons, while the quadratic term contributes when a soliton is mislocated within a cell. Our training set uses images with at most one soliton, so cells with $Y_{\ell,1} = 1$ are much less frequent than those with $Y_{\ell,1} = 0$, as a result we expect that $w_1, w_2 \gg 1$ to give similar overall weight to the three terms in Eq. 2. We train the OD by minimizing the cost function summed over all training images, updating the predicted OD values $\widetilde{\mathbf{Y}}$ in each iteration. Because the cell size is comparable to the soliton size, a single soliton can span two cells. To prevent double counting, we merge detections occurring in adjacent cells and take the position to be their average.

We deem the OD's detection successful if our training data contains a labeled soliton close to the detected one (within 3 pixels in our implementation). The two failure modes are failing to detect a solitonic excitation and reporting an excitation that is not present.

C. Physics-based modules

In this subsection, we introduce our physics-based module that uses constrained least-squares fitting to estimate soliton parameters, and following a Yeo-Johnson transformation [26], produces a quality estimate giving the likelihood of a given feature being solitonic.

We fit the Ricker wavelet [32], i.e., a "Mexican hat" function

$$\begin{aligned} f(i) = \delta_n - \; & n^{\mathrm{TF}}(i_c) A \exp\left[-\tfrac{1}{2}\left(\tfrac{i-i_c}{\sigma}\right)^2\right] \\ & \times \left[1 - a\left(\tfrac{i-i_c}{\sigma}\right)^2 + b\left(\tfrac{i-i_c}{\sigma}\right)\right], \end{aligned} \tag{3}$$

to the 1D density fluctuations described Sec. II A, where $n^{\mathrm{TF}}(i_c)$ is evaluated with $\delta_n = 0$. The function takes six parameters: normalized logarithmic amplitude A, center position i_c, width σ, logarithmic symmetrical shoulder height a, asymmetrical shoulder height b, and an offset δ. When a and b are zero this function is a simple Gaussian, making a non-zero adds symmetric shoulders to the distribution and b introduces an asymmetry. Our solitonic features are well described by this function; since our excitations manifest as density depletions, the second term in Eq. 3 is negative.

Our constrained least squares fit requires initial guesses for all of these parameters. The guess for the center position i_c also provides the initial guess for A by setting

it equal to the 1D density fluctuations evaluated at i_c. We found the initial values $\sigma = 4$, $a = 0.2$, $b = 0$, and $\delta = 0$ to lead to convergent fits across the whole dataset. In order to produce reliable fits we apply the following constraints: i_c must remain within three pixels from the initial guess, $10^{-13} < A < 10^4$, and $10^{-13} < a < 10^4$ to prevent numerical fitting errors.

1. *Physics-informed excitation classifier*

Many candidate solitonic excitations are not vertically symmetric as might be expected, see e.g., Fig. 2(b-iii). The location of the largest "shoulder" in top half of the excitation is reversed with respect to the bottom half; in addition, the location of the minimum is slightly displaced going from the top half to the bottom. Inspired by these differences, we bisect each image into top and bottom halves (labeled by + and −, respectively) and separately apply the Mexican hat fit to fluctuations in these data, giving vectors $\Theta^{\pm}$. Using this observation, we develop a physics-informed excitation (PIE) classifier based on the single-soliton dataset and discover that correlations between these vectors allow for a more fine-grained excitation classification.

Figure 3 shows the distribution of parameters from a single soliton dataset that were useful for classifying excitations. No meaningful correlations were found for parameters $\sigma^{\pm}$ and $a^{\pm}$, thus these did not assist in classification. The markers in the top panel show the amplitude ratio $\rho_A = A^+/A^-$ versus the top-bottom position difference $\delta i_c = i_c^+ - i_c^-$, and show that they are not correlated. By contrast, the bottom panel shows that the asymmetric shoulder height difference $\delta b = b^+/\sigma^+ - b^-/\sigma^-$ is clearly anti-correlated with δi_c. Both panels are colored based on the cut-off points discussed in Sec. III B (see also Fig. 5).

This distribution and its correlation guide the classification rules described in Sec. III B, yielding a PIE classifier based on cutoffs defined by human examination of the data.

2. *Quality estimation*

Here we describe a quality estimate that a candidate excitation in an image is solitonic. We derive the likelihood that a vector of fit outcomes $\Theta = [A, i_c, \sigma, a, b]$ is drawn from a $k = 5$ dimensional prior distribution spanning the set of representative solitonic excitations [33]. Ideally this distribution would be an uncorrelated multivariate normal distribution, but it is not. As a result, we developed the following procedure to bring the distribution into this desired form.

We first fit a Yeo-Johnson power transformation [26] to each separate parameter distribution (having summed the 5D distribution along the remaining parameters) to transform them into independent zero-mean 1D Gaussian distributions with unit variance. Note that this treatment cannot transform the parameter distributions into perfect Gaussians, nevertheless each resulting distribution is balanced, contains a single-peak, and has long tails. The covariance matrix Σ_k is uncorrelated after this treatment and the distribution is qualitatively Gaussian in shape.

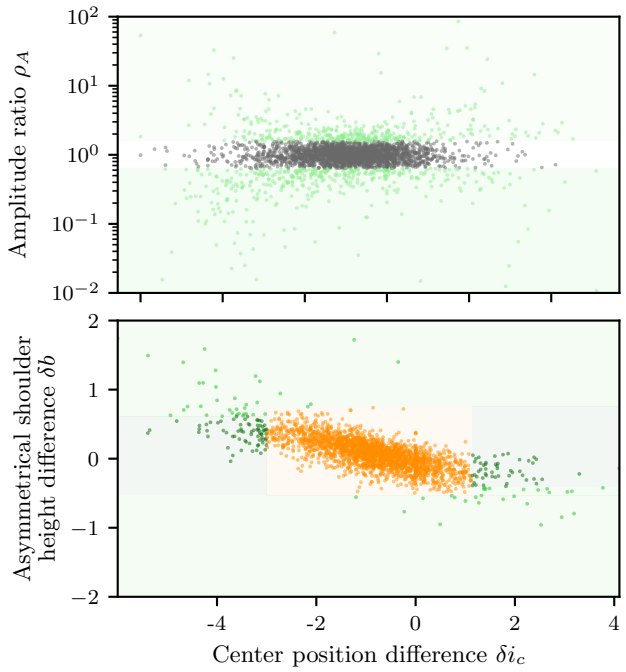

FIG. 3. Correlations between parameters implemented in PIE classifier. The top panel shows the distribution of center position difference versus the amplitude ratio (on a logarithmic scale). The bottom panel shows the correlation between the center position difference and the asymmetrical shoulder height difference for the gray points from top panel. Both panels are colored based on the cut-off points discussed in Sec. III B.

To calculate the quality estimate for a candidate excitation detected in an image, we:

1. Fit the subtracted background 1D profile to Mexican hat function 3 giving Θ.

2. Use the established power transformation on Θ to obtain Θ'.

3. Return the quality estimate: $M(\Theta') = 1 - \chi_k^2\left(D^2(\Theta')\right)$, the likelihood between 0 and 1 that the excitation is solitonic.

The chi-squared cumulative distribution function $\chi_k^2(p)$ relates the Mahalanobis distance [34] $D^2(\Theta') = \Theta'^{\dagger}\Sigma_k^{-1}\Theta'$ to the likelihood that an outcome was drawn from the specified distribution [35]. $D(\Theta')$ is unbounded above and decreases to zero as Θ' approaches $\langle\Theta'\rangle$, the average over the prior distribution.

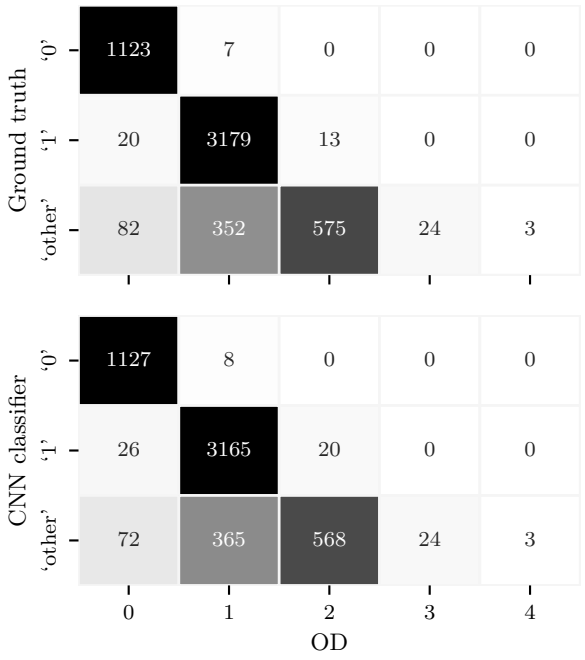

FIG. 4. OD performance compared to ground truth (top), and the CNN classifier prediction (bottom), For ground truth and CNN classifier, the ticks "0", "1", "other" represent no, single, and other excitation classes. For OD, ticks represent the total number of positive excitations within an image.

III. RESULTS

A. ML modules

We train both the CNN classifier and the OD using the refined dataset with added soliton position labels (see Ref. [28]). The CNN classifier is trained using the full dataset while the OD training uses only the no solitonic excitation and single solitonic excitation classes. We assess the performance of both modules using 5-fold cross validation, that is using 80 % of the data to train a given module and the remaining 20 % to test it, and repeating the process 5 times to fully cover the dataset (see App. A for training details).

The results are summarized in the two cumulative confusion matrices plotted in Fig. 4. The top panel compares the outcome of the OD to the initial labels, showing near perfect delineation between no excitations and single excitations classes. However, the OD further subdivides the other excitations class, counting anywhere from 0 to 4 candidate solitonic excitations within it. This results from the existence of excitations in this class that are not solitonic, as well as the possibility of having multiple solitons in the same image. The analogous comparison to CNN classification labels in the bottom panel is nearly indistinguishable from the one presented in the top panel, evidencing the quality of the CNN predictions.

Together, these ML tools effectively classify these data and locate excitations, however, they do not provide any fine-grained information on the nature nor the quality of the identified excitations. This is addressed in the following subsections.

B. PIE classifier

The PIE classifier operates by applying a sequence of "cuts" driven by different combinations of the top-bottom fit outcomes $\Theta^{\pm}$. The exact parameter values described below are arrived at manually by exploring the data accepted and rejected by the cut to minimize the number of false positive longitudinal soliton identifications.

The following cuts are applied sequentially, and the PIE classifier stops as soon as a classification is assigned.

A cut: The amplitude parameters $A^{\pm}$, and their ratio ρ_A allow us to identify excitations that do not span the whole cloud. Data with $\rho_A > 1.57$ are classified as "top partial excitation" and those with $1/\rho_A > 1.57$ are classified as "bottom partial excitation". This threshold identifies large fractional jumps in depth between the top and bottom that likely are off-axis solitonic vortices. Applying A cuts first is important because partial excitations interfere with the subsequent steps.

δb cut: Figure 2(b-iii) illustrates a case with large shoulder height difference δb; Ref. [27] showed that such data result from solitonic vortices. As a result, we classify data with $\delta b > 0.75$ as "counterclockwise solitonic vortex" and $\delta b < -0.53$ as "clockwise solitonic vortex".

δi_c cut: Since longitudinal solitons have a vertically aligned density depletion [36], we classify data with $-3.0 < \delta i_c < 1.14$ as "longitudinal soliton."

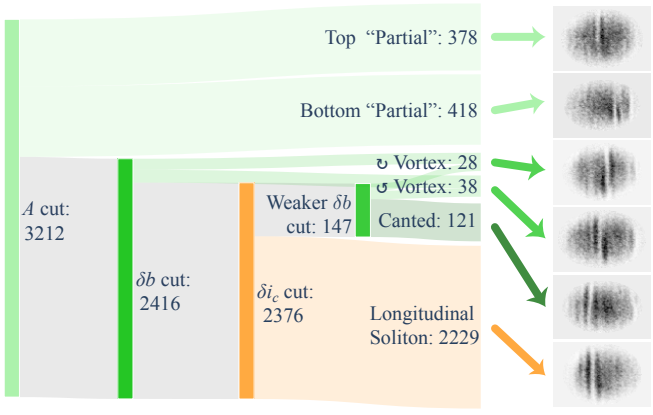

FIG. 5. The flow of the PIE classifier with example images for classification categories. Flow pathways and nodes are square-root scaled.

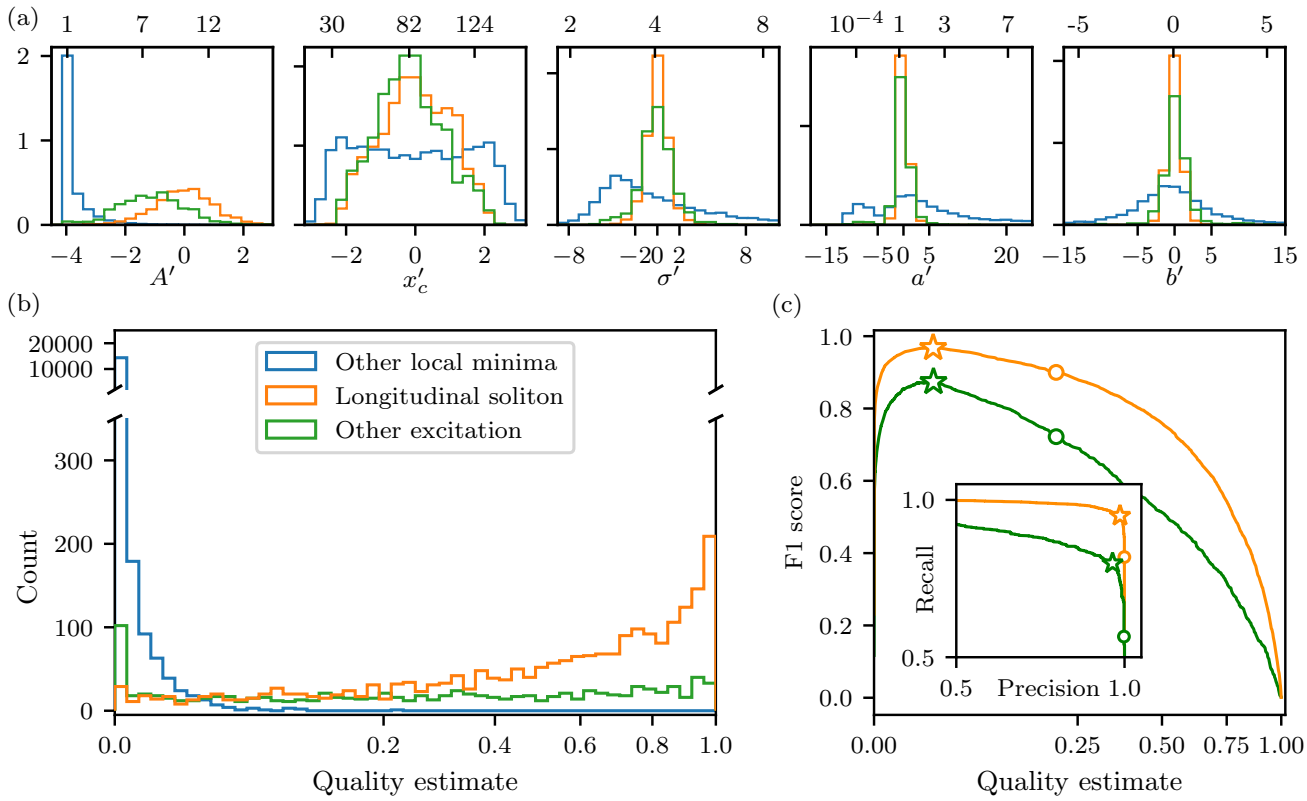

FIG. 6. Quality estimate performance on no excitation and single excitation classes. In all cases we use the following color scheme: longitudinal solitons (orange), all other solitonic excitations (green), and all non-solitonic local minima (blue). (a) Power transformed fit coefficient distributions, with untransformed variables labeled on the top axis. (b) Distribution of quality estimate. (c) Performance of quality estimate quantified by F1 score, the stars indicate the optimal F1 value and the circles mark the threshold we use for classification. The inset shows performance / recall curves.

Weaker δb cut: Figure 3 shows that differences δi_c and $\delta b = b^+/\sigma^+ - b^-/\sigma^-$ are anti-correlated, indicating that asymmetries in position and shoulder height are related. A closer look at Fig. 2(b-iii) indicates that it is such a case, with $\delta i_c < 0$ and $\delta b > 0$. We therefore add images with $\delta i_c < -3.0$ and $\delta b > 0.61$ to the "counter-clockwise solitonic vortex" class and those with $\delta i_c > 1.14$ and $\delta b < -0.41$ to the "clockwise solitonic vortex" class.

Other data: The remaining images have $\delta i_c \neq 0$ but $\delta b \approx 0$ are labeled as "canted excitations", likely kink solitons in the process of decay.

The flow chart in Fig. 5 shows the application of this classifier to a single-soliton dataset. We found that of the initial 3 212 images about 1/3 failed a cut and were rejected as longitudinal soliton candidates.

This classification was also used in the preparation of Ref. [28] in which we present a refined soliton dataset, which includes improved single longitudinal soliton labels. The cuts above are fairly aggressive to avoid false positives in the longitudinal soliton classification. This implies possible misclassification in the other categories in order to ensure a high quality longitudinal soliton subset and a reliability of the quality metric.

C. Quality estimator

The quality estimator is initialized on the subset of the single excitation class identified as longitudinal soliton using the PIE classifier. Figure 6(a) shows the power-transformed distribution of Mexican hat fit coefficients Θ', with non-transformed coordinates marked on the top axis for reference. As would be expected, the data from the initialization dataset (orange) are nearly-normally distributed; interestingly, the remaining elements of the single excitation class (partial solitons, canted excitations, and solitonic vortices, as labeled by the PIE filter) collectively follow very similar distributions (green). By contrast, the coefficients from every local minimum [37] in the initialization set *except* solitonic excitations (blue curve) obey a qualitatively different distribution.

Using this initialization, we compare quality estimates M obtained from the single excitation class in Fig. 6(b). The orange data show M for longitudinal solitons, and

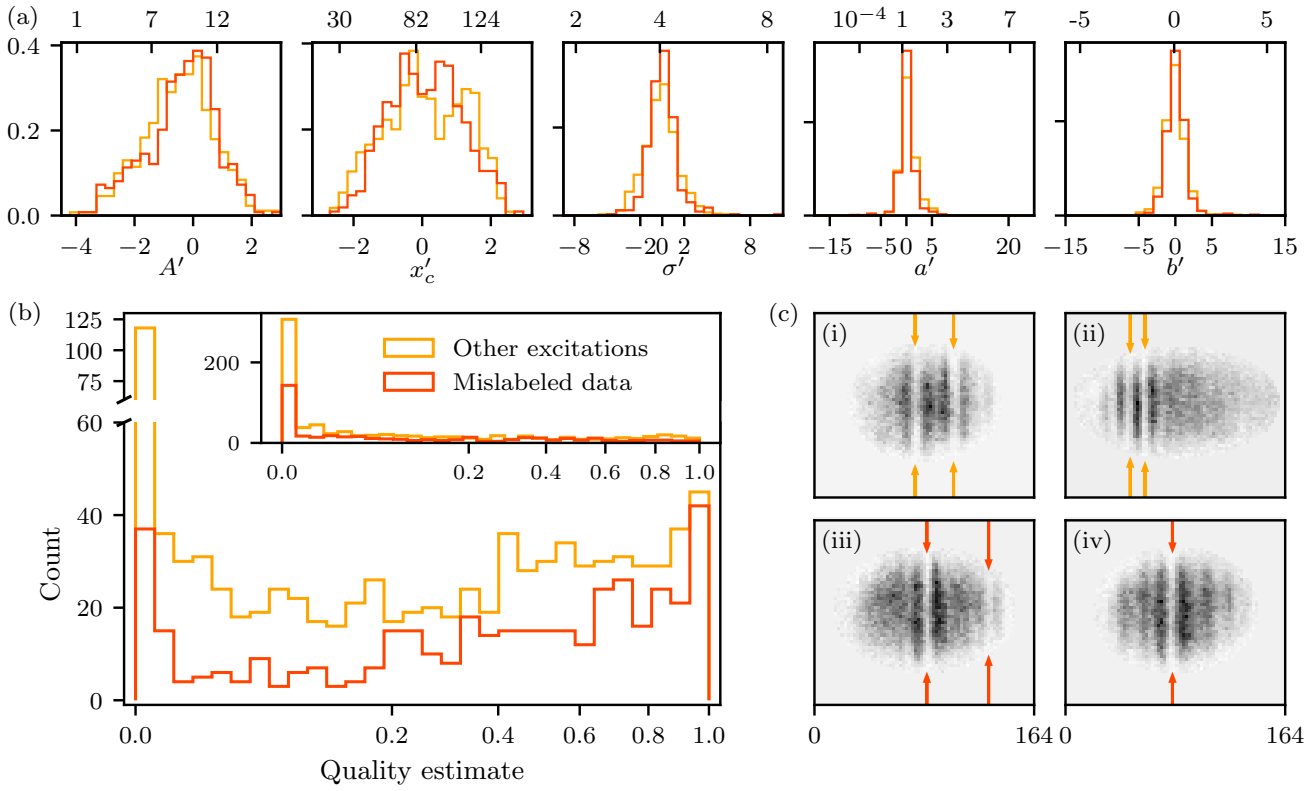

FIG. 7. Performance of quality estimate on other excitation (orange) and mislabeled (red) classes. (a) Power transformed fit coefficient distributions, with untransformed variables labeled on the top axis. (b) Distribution of quality estimate of all longitudinal solitons. (c) Representative images from the other excitation (i-ii) and mislabeled (iii-iv) classes, with OD+PIE identified longitudinal soliton marked with arrows. The quality estimate for these excitations is as follows : $M_{(i)} = [0.74, 0.86]$, $M_{(ii)} = [0.00, 0.01]$, $M_{(iii)} = [0.92, 0.02]$ (all from left to right), and $M_{(iv)} = 0.82$.

as intended the majority of this data is associated with larger values of M. The green data for the remaining solitonic excitations are nearly uniformly distributed, and the non-soliton minima (blue) are highly concentrated at small M. We note that the small peak in longitudinal soliton distribution near-zero M contains a negligible fraction of the longitudinal soliton dataset (about 1.3 %). However, this peak is more pronounced for the remaining excitations, which is not surprising because the power transform was initialized using longitudinal soliton data. These distributions demonstrate the ability of the quality estimator to discriminate between solitonic excitations and other features in the data, reinforcing the importance of the PIE filter for fine-grained classification.

We quantify the performance of the quality estimator in terms of the F1 scores plotted in Fig. 6(c), for longitudinal solitons (orange) and all other solitonic excitations (green). The F1 score for longitudinal solitons is maximized with a threshold of just $M = 0.02$ (stars), however, in practice we minimized false positives and assign a feature to be solitonic when $M > 0.2$ (circles). This choice gives only small change in the F1 score, however, it gives a marked increase in precision with only a small reduction in recall, as shown in the inset. The performance of the quality estimate on the other solitonic excitations, while far better than random, is subpar; this reemphasizes the importance of the PIE classifier in our framework.

D. Application to other excitation and mislabeled data class

Here we discuss the performance of our SolDet framework applied to two classes of data from the the dark soliton dataset: other excitations (1 036 images) and mislabeled data (879 images). These classes consist of images with multiple solitonic excitations, such as shown in Fig. 2(c), as well as confusing structures that made human annotation difficult. As such, they are an ideal test dataset since they defeated previous labeling attempts.

As a reminder, after the CNN classification step, the framework first uses the OD to locate all soliton candidates that are then sorted by the PIE classifier. Here, we focus only on features identified as longitudinal solitons. Figure 7(a) plots the frequency of transformed Mexican hat fit outcomes Θ', giving distributions that for both classes are qualitatively the same as those in Fig. 6(a) for the labeled single solitons. By contrast, histograms

of the quality estimate for longitudinal solitons detected in these two classes [panel (b)] have important differences. For the other excitations class ($N_{\text{longitudinal}} = 877$, $N_{\text{images}} = 669$), the distribution is nearly uniform, with a potential increase for the higher quality estimates ($M > 0.4$). For the mislabeled data ($N_{\text{longitudinal}} = 415$, $N_{\text{images}} = 398$), on the other hand, the quality estimate distribution follows a trend consistent with that observed in Fig. 6(b).

To better understand this discrepancy it is important to consider more carefully the differences between the two classes. According to the OD module, nearly 78 % of images in the other excitation class contains two or more excitations. While for excitation spaced apart within the BEC, as in Fig. 7(c-i), the individual fits to Mexican hat do not affected one another, the contrary holds for excitation captured in a close proximity, as shown in Fig. 7(c-ii). Qualitative differences between these images are quantified by the quality estimate. The quality estimate for the two well separated excitation in image (i) is 0.74 and 0.86. In image (ii), in contrast, even though both excitations are reminiscent of a longitudinal solitons, they are assigned a low quality, with $M_{(ii)} = [0.00, 0.01]$ from left to right. This is likely because the overlap in the adjacent shoulders significantly affects the relative fits. Given that majority of data in this class contains multiple excitations, the unusually high frequency of the low quality is to be expected.

The mislabeled class, on the other hand, consists of images determined to be potentially mislabeled during the manual annotation (see Ref. [28] for details about the data curation process). These include: over 320 images that the annotators found confusing (but in which ODs consistently found exactly one candidate excitation); over 190 images removed during curation from the single excitation class; and about 30 images originally assigned to the no excitation class (but in which the ODs also consistently found exactly one candidate excitations). Unsurprisingly, in almost 83 % of these images the OD module found only one excitations. Two representative images from this set are shown in Fig. 7(c-iii,iv), with $M_{(iii)} = [0.92, 0.02]$ and $M_{(iv)} = 0.82$. The distribution of non-longitudinal soliton quality estimate, shown in in the inset in Fig. 7(b), is consistent with that depicted in Fig. 6(b).

The performance on these qualitatively different test sets emphasizes the power of SolDet. By combining the CNN and OD modules, SolDet autonomously and reliably locates multiple excitations within the BECs, which goes beyond the traditional state-of-the-art deepest-depletion-based approach. The PIE classifier enables further systematic validation that the desired type of excitation—here, longitudinal solitons—has been observed, which previously required visual inspection of each acquired image. Finally, the quality metric provides a quantitative assessment of the excitation quality, further reinforcing the classification reliability. Put together, these tools provide a robust and reliable analysis framework, capable of processing data significantly more complex than possible given the current traditional state-of-the-art approaches.

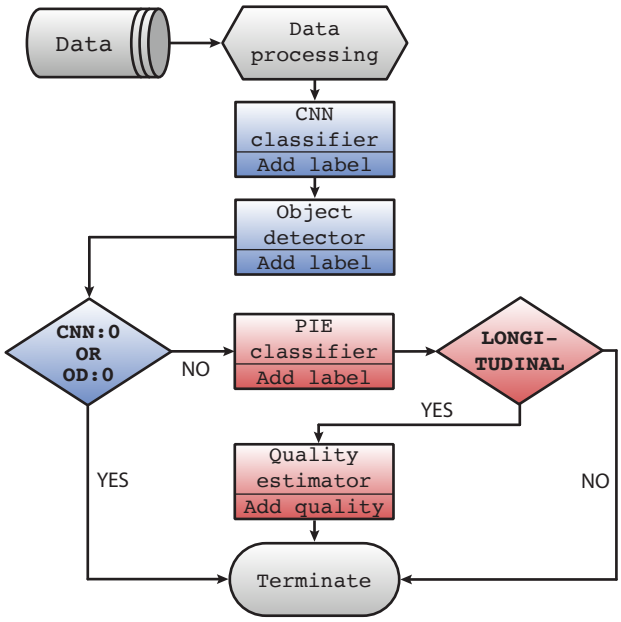

FIG. 8. The SolDet flow chart. The black line follows the SolDet dataflow and contains the labels added by each module (rectangles). Blue blocks represents ML modules, red blocks represent physics-based modules.

E. SolDet: Open-source Python package for solitonic excitation detection

In this section, we describe our software package SolDet that integrates both the ML modules (CNN classifier and OD) with the fitting physics-based modules (PIE classifier and quality estimator), as we described in previous sections. The above discussion showed that the ML modules classify images effectively and can accurately locate one or many candidate solitons. The physics-based modules can sort these candidates into subclasses and provide a quality estimate for longitudinal soliton candidates. Therefore, the ML and physics-based modules contribute to the task of soliton detection in different ways, and the SolDet infrastructure leverages their complementing strengths. We emphasize that soliton detection is one of a larger class of feature identification in quantum gases and that SolDet was designed to be broadly applicable.

The SolDet distribution includes a CNN classifier, OD, PIE classifier, and quality estimator trained and initialized using the soliton dataset [23]. In addition, we provide training scripts to enable the ready application to user-defined data with custom preprocessors, ML models, fitting functions, and even the overall process flow.

Figure 8 illustrates a single use of SolDet for the spe-

cific example of longitudinal soliton detection, where the individual blocks operate as follows:

Data processing: Preprocess raw data into 164×132 image format that just enclose the elliptical atom clouds [22]. The preprocessing particulars are not generic and instead are specific to both our task as well as the experimental parameters.

CNN classifier: Apply a trained CNN classifier to processed data, yield labels no excitation, single excitation, or other excitations.

Object detection: Apply trained OD to processed data, yield a list of positions of solitonic excitations.

CNN:0 OR OD:0: If either the CNN classifier or OD finds no soliton, SolDet terminates.

PIE classifier: The PIE classifier is applied to each solitonic excitation.

Quality estimator: The quality estimator is applied to each excitation identified as "longitudinal soliton" by the PIE classifier.

This algorithm is designed to be usable in a laboratory environment where one needs real-time identification, as well as for automated labeling of large datasets, as in Ref. [28].

IV. DISCUSSION AND CONCLUSION

Here we described a new framework that adds to the growing ML quantum science and technology toolkit, with additional recent developments including: noise characterization [38, 39]; quantum state detection [22, 30, 40–48]; parameter space exploration and optimization [49–54]; and quantum control [55, 56]. Together, these results show that ML techniques can extract information from ambiguous data, efficiently search large parameter spaces, and optimally control quantum systems.

Our high level framework combines ML methods with physics-based analysis, providing an integrated platform for studying experimental data. Our implementation of this framework, SolDet, currently targets the identification, classification, and tracking of features in image data generated by cold atom experiments. We demonstrated its initialization and performance using a publicly available dark soliton dataset [28]. This investigation focused only on properties of individual images, however, the dataset also includes a label giving time elapsed since the excitation's were created. This opens the door for studies correlating system control parameters and the SolDet labels.

While our initialization used only the no excitation and single excitation classes, SolDet's feature detection successfully generalizes the learned patterns. This is confirmed by its performance on the other excitations and mislabeled classes that were not part of training, where the CNN classifier gave ambiguous results and human classifiers often disagreed. Going beyond simple classification tasks, SolDet allowed us to identify unexpected structure in the data, enabling a fine-grained division of the single excitation class into physically-relevant subclasses, including solitonic vortices and partial solitons.

Moreover, for the multiple excitations class, the distribution of the quality metric in Fig. 7 reveals a possible correlation between the quality metric and the excitations relative proximity. These observations illustrate the power of our combined framework as a data analysis tool for discovery.

An interesting application of SolDet would be an offline optimization of the experimental setup. Such optimization strategy—successfully implemented to, e.g., improve fabrication of quantum dot devices [1]—requires an efficient analysis of large volumes of data to find the appropriate correlations in a high dimensional parameter space. The ML toolbox described in our manuscript allows automatically locate multiple solitonic excitations in the same cloud and produces a fine classification that goes beyond longitudinal solitons. An analysis of the correlations between the various control parameter ranges used in our experiments and the resulting class of data (as determined by SolDet) could enable a controlled generation of a desired number, type, and configurations of excitations, with SolDet integrated on-line to provide real-time data analysis and control feedback. Another interesting extension of this work would be to train an OD on a dataset containing a single subclass found by the PIE classifier, e.g., longitudinal solitons, or solitonic vortices.

An emerging area of ML is the derivation of effective hydrodynamic equations of motion for biological, colloidal and active fluids based on time-series data [57]. Owing to the complexity of full 3D simulations of nonzero temperature BECs, this data-driven approach could also be applied to create effective kinetic theory of solitons as well as the hydrodynamics of the underling fluid.

Going beyond solitonic excitations, the wakefield for sub- and supersonic impurities moving in atomic superfluids have characteristic patterns that could be identified by ML techniques [58–61]. This might be implemented using a template based method such as used in the Laser Interferometer Gravitational-Wave Observatory (LIGO) where a large set of numerical simulations provide a library of patterns to correlated with the data [62]. This pattern matching is a form of object detection, and in our context a CNN based object detector could also be trained on such a template set. In this way, our methodology could be employed with a trained OD followed by a LIGO-like algorithm playing the role of our quality estimator and PIE classifier.

From the ML perspective, adding modules based on unsupervised [63], active learning [64], and synthetic data generation with generative models [65] may further enhance the performance of the SolDet framework.

ACKNOWLEDGEMENTS

This work was partially supported by NIST and NSF through the Physics Frontier Center at the JQI. The views and conclusions contained in this paper are those of the authors and should not be interpreted as representing the official policies, either expressed or implied, of the U.S. Government. The U.S. Government is authorized to reproduce and distribute reprints for Government purposes notwithstanding any copyright noted herein.

Appendix A: Parameters of Machine Learning Models

Both machine learning modules are built and trained using the TensorFlow (v.2.5.0) Keras Python API [66]. Fig. 9(a) and (b) show the visualization of the network architecture for the OD and the CNN classifier, respectively. The model parameters of OD are presented in Tab. I. The model parameters for the CNN classifier are presented in the Appendix of Ref. [22].

As can be seen in Fig. 9, there are three main differences between the two architectures: (1) the OD outputs 41 local probabilities and positions while the CNN classifier only outputs 1 of 3 possible classes; (2) the CNN classifier contains three fully-connected layers, which dramatically increase the number of trainable parameters, while OD does not; (3) the OD has asymmetric pool size and strides for vertical and horizontal directions, which are customized to the features in our dataset; the pool size and strides are symmetric for the CNN classifier. As a result, the OD has more than an order of magnitude fewer trainable parameters (7×10^4) than the CNN classifier (10^6).

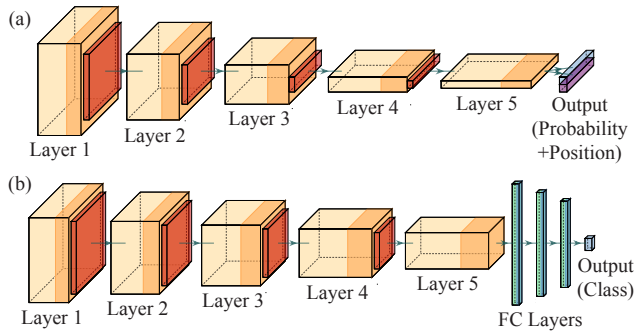

FIG. 9. Illustration of (a) OD and (b) CNN classifier neural network architectures. Yellow-orange boxes show convolutional layers while orange-red boxes show max-pooling layers. The horizontal lengths of boxes represent number of filters and the other two dimensions represent the image sizes. The horizontal blue and purple rectangles in (a) denote output vectors. Each cell of the blue vector describes the probability that it contains a soliton and and the purple vector contains the position of a soliton within the cell. And the vertical blue-green rectangles in (b) are three fully connected layers and the output layer. The lengths of edges are logarithmically scaled.

TABLE I. The OD architecture parameters. The top four rows are for for the convolutional 2D layers and the three bottom rows are for maxpooling 2D layers.

Layer	1	2	3	4	5	output
Filter	8	16	32	64	128	2
Kernel	5×5	5×5	5×5	1×5	1×5	1×5
Padding	same	same	same	same	same	same
Activation	ReLu	ReLu	ReLu	ReLu	ReLu	sigmoid
Pool size	4×2	4×2	4×1	2×1	N/A	N/A
Strides	4×2	4×2	4×1	2×1	N/A	N/A
Padding	valid	valid	same	same	N/A	N/A

[1] A. B. Mei, I. Milosavljevic, A. L. Simpson, V. A. Smetanka, C. P. Feeney, S. M. Seguin, S. D. Ha, W. Ha, and M. D. Reed. Optimization of quantum-dot qubit fabrication via machine learning. *Appl. Phys. Lett.*, 118(20):204001, May 2021.

[2] J R Abo-Shaeer, C Raman, J M Vogels, and W. Ketterle. Observation of Vortex Lattices in Bose-Einstein Condensates. *Science*, 292(5516):476–479, April 2001.

[3] V. Schweikhard, I. Coddington, P. Engels, V. P. Mogendorff, and E. A. Cornell. Rapidly rotating bose-einstein condensates in and near the lowest landau level. *Phys. Rev. Lett.*, 92(4):40404, January 2004.

[4] Y. J. Lin, R. L. Compton, K. Jiménez-García, J. V. Porto, and I. B. Spielman. Synthetic magnetic fields for ultracold neutral atoms. *Nature*, 462(7273):628–632, 12 2009.

[5] Christoph Becker, Simon Stellmer, Parvis Soltan-Panahi, Sören Dörscher, Mathis Baumert, Eva-Maria Richter, Jochen Kronjäger, Kai Bongs, and Klaus Sengstock. Oscillations and interactions of dark and dark–bright solitons in Bose–Einstein condensates. *Nature Physics*, 4(6):496–501, May 2008.

[6] Lauren M. Aycock, Hilary M. Hurst, Dmitry K. Efimkin, Dina Genkina, Hsin-I Lu, Victor M. Galitski, and I. B. Spielman. Brownian motion of solitons in a bose-einstein condensate. *Proceedings of the National Academy of Sciences*, 114(10):2503–2508, 2017.

[7] L E Sadler, J M Higbie, S. R. Leslie, M. Vengalattore, and D. M. Stamper-Kurn. Spontaneous symmetry breaking in a quenched ferromagnetic spinor Bose–Einstein condensate. *Nature*, 443(7109):312–315, September 2006.

[8] M. Vengalattore, J. Guzman, S. R. Leslie, F. Serwane, and D. M. Stamper-Kurn. Periodic spin textures in a degenerate $f = 1$ ^{87}rb spinor bose gas. *Phys. Rev. A*, 81(5):53612, May 2010.

[9] S De, D L Campbell, R M Price, A Putra, Brandon M Anderson, and I. B. Spielman. Quenched binary Bose-Einstein condensates: Spin-domain formation and coarsening. *Phys. Rev. A*, 89(3):33631, March 2014.

[10] Matthias Tarnowski, Marlon Nuske, Nick Fläschner, Benno Rem, Dominik Vogel, Lukas Freystatzky, Klaus Sengstock, Ludwig Mathey, and Christof Weitenberg. Observation of topological bloch-state defects and their merging transition. *Phys. Rev. Lett.*, 118:240403, June 2017.

[11] A. M. Legendre. *Nouvelles méthodes pour la détermination des orbites des cometes.* F. Didot, 1805.

[12] W. Ketterle, D. S. Durfee, and D. M. Stamper-Kurn. Making, probing and understanding bose-einstein condensates. *arXiv:cond-mat/9904034*, 1999.

[13] A. R. Fritsch, M. Lu, G. H. Reid, A. M. Piñeiro, and I. B. Spielman. Creating solitons with controllable and near-zero velocity in Bose-Einstein condensates. *Phys. Rev. A*, 101(5):053629, 2020.

[14] T. P. Purdy, K. E. Grutter, K. Srinivasan, and J. M. Taylor. Quantum correlations from a room-temperature optomechanical cavity. *Science*, 356(6344):1265–1268, 2017.

[15] F. Huang, Z. Cao, J. Guo, S.-H. Jiang, S. Li, and Z. Guo. Comparisons of heuristic, general statistical and machine learning models for landslide susceptibility prediction and mapping. *Catena*, 191:104580, 2020.

[16] S. Ghosh, M. R Malgireddy, V. Chaudhary, and G. Dhillon. A new approach to automatic disc localization in clinical lumbar mri: combining machine learning with heuristics. In *2012 9th IEEE International Symposium on Biomedical Imaging (ISBI)*, pages 114–117. IEEE, 2012.

[17] J. Sakhnini, H. Karimipour, and A. Dehghantanha. Smart grid cyber attacks detection using supervised learning and heuristic feature selection. In *2019 IEEE 7th International Conference on Smart Energy Grid Engineering (SEGE)*, pages 108–112. IEEE, 2019.

[18] M. Greiner, O. Mandel, T. Esslinger, T.W. Hänsch, and I. Bloch. Quantum phase transition from a superfluid to a mott insulator in a gas of ultracold atoms. *Nature*, 415:39–44, 2002.

[19] T. Bothwell, D. Kedar, E. Oelker, J. M. Robinson, S. L. Bromley, W. L. Tew, J. Ye, and C. J. Kennedy. JILA SrI optical lattice clock with uncertainty of 2.0×10^{-18}. *Metrologia*, 56(6):065004, 2019.

[20] S. Burger, K. Bongs, S. Dettmer, W. Ertmer, K. Sengstock, A Sanpera, G. V. Shlyapnikov, and M. Lewenstein. Dark Solitons in Bose-Einstein Condensates. *Phys. Rev. Lett.*, 83(25):5198–5201, 1999.

[21] J. Denschlag, J. E. Simsarian, D. L. Feder, C. Clark, L. A. Collins, J. Cubizolles, L. Deng, E. Hagley, K. Helmerson, W. P. Reinhardt, S. L. Rolston, B. I. Schneider, and W. D. Phillips. Generating Solitons by Phase Engineering of a Bose-Einstein Condensate. *Science*, 287(5450):97–101, 2000.

[22] S. Guo, A. R. Fritsch, C. Greenberg, I. B. Spielman, and J. P. Zwolak. Machine-learning enhanced dark soliton detection in Bose-Einstein condensates. *Mach. Learn.: Sci. Technol.*, 2:035020, 2021.

[23] J. Zwolak. Dark solitons in BECs dataset. National Institute of Standards and Technology, 2020.

[24] A. M. Mateo and J Brand. Stability and dispersion relations of three-dimensional solitary waves in trapped bose–einstein condensates. *New J. Phys.*, 17(12):125013, 2015.

[25] A. Voulodimos, N. Doulamis, A. Doulamis, and E. Protopapadakis. Deep learning for computer vision: A brief review. *Comput. Intell. Neurosci.*, 2018:7068349, 2018.

[26] I.-K. Yeo and R. A. Johnson. A New Family of Power Transformations to Improve Normality or Symmetry. *Biometrika*, 87(4):954–959, 2000.

[27] S. Donadello, S. Serafini, M. Tylutki, L. P. Pitaevskii, F. Dalfovo, G. Lamporesi, and G. Ferrari. Observation of Solitonic Vortices in Bose-Einstein Condensates. *Phys. Rev. Lett.*, 113(6):065302, 2014.

[28] A. R. Fritsch, S. M. Koh, S. Guo, I. B. Spielman, and J. P. Zwolak. Dark Solitons in Bose-Einstein Condensation: Real Dataset for Many-Body Physics Research. (in preparation).

[29] SolDet Team, 2021.

[30] F. Metz, J. Polo, N. Weber, and T. Busch. Deep learning based quantum vortex detection in atomic Bose-Einstein condensates. *Mach. Learn.: Sci. Technol.*, 2:035019, 2021.

[31] D. Leykam, I. Rondon, and D. G. Angelakis. Dark soliton detection using persistent homology. *arXiv:2107.14594*, 2021.

[32] N. Ricker. Further developments in the wavelet theory of seismogram structure. *Seismol. Soc. Am., Bull.*, 33(3):197–228, 1943.

[33] We found that δ was strongly correlated with the remaining five parameters and did not improve the the quality estimate performance.

[34] P. C. Mahalanobis. On the generalized distance in statistics. National Institute of Science of India, 1936.

[35] This argument assumes no prior knowledge about the distribution of fit outcomes for structures that are not solitonic excitations.

[36] Our images are slightly rotated with respect to the vertical and horizontal axes leading to a small angle in our data.

[37] We require that the local minima be at least 7 pixels wide, i.e., a minimum at pixel i must obey $n^{1D}_{i\pm j} < n^{1D}_{i\pm(j+1)}$ for $j = 0, 1, 2$.

[38] R. Harper, S. T. Flammia, and J. J. Wallman. Efficient learning of quantum noise. *Nat. Phys.*, 16:1184–1188, 2020.

[39] J. Ziegler, T. McJunkin, E. S. Joseph, S. S. Kalantre, B. Harpt, D. E. Savage, M. G. Lagally, M. A. Eriksson, J. M. Taylor, and J. P. Zwolak. Toward robust autotuning of noisy quantum dot devices. *Phys. Rev. Applied*, 17:024069, Feb 2022.

[40] J. Carrasquilla and R. G. Melko. Machine learning phases of matter. *Nat. Phys.*, 13(5):431–434, 2017.

[41] Y. Zhang and E.-A. Kim. Quantum Loop Topography for Machine Learning. *Phys. Rev. Lett.*, 118(21):216401, 2017.

[42] G. Torlai, G. Mazzola, J. Carrasquilla, M. Troyer, R. Melko, and G. Carleo. Neural-network quantum state tomography. *Nat. Phys.*, 14(5):447–450, 2018.

[43] J. Venderley, V. Khemani, and E.-A. Kim. Machine learning out-of-equilibrium phases of matter. *Phys. Rev. Lett.*, 120(25):257204, 2018.

[44] B. S. Rem, N. Käming, M. Tarnowski, L. Asteria, N. Fläschner, C. Becker, K. Sengstock, and C. Weitenberg. Identifying quantum phase transitions using artificial neural networks on experimental data. *Nat. Phys.*, 15(9):917–920, 2019.

[45] C. Miles, A. Bohrdt, R. Wu, C. Chiu, M. Xu, G. Ji, M. Greiner, K. Q. Weinberger, E. Demler, and E.-A. Kim. Correlator Convolutional Neural Networks: An Interpretable Architecture for Image-like Quantum Matter Data. *Nat. Commun.*, 12:3905, 2020.

[46] P. Cha, P. Ginsparg, F. Wu, J. Carrasquilla, P. L. McMahon, and E.-A. Kim. Attention-based Quantum Tomography. *arXiv:2006.12469*, 2020.

[47] J. Venderley, M. Matty, K. Mallayya, M. Krogstad, J. Ruff, G. Pleiss, V. Kishore, D. Mandrus, D. Phelan, L. Poudel, A. G. Wilson, K. Weinberger, P. Upreti, M. R. Norman, S. Rosenkranz, R. Osborn, and E.-A. Kim. Harnessing Interpretable and Unsupervised Machine Learning to Address Big Data from Modern X-ray Diffraction. *arXiv:2008.03275*, 2021.

[48] N. Maskara, M. Buchhold, M. Endres, and E. van Nieuwenburg. A learning algorithm with emergent scaling behavior for classifying phase transitions. *arXiv:2103.15855*, 2021.

[49] P. B. Wigley, P. J. Everitt, A. van den Hengel, J. W. Bastian, M. A. Sooriyabandara, G. D. McDonald, K. S. Hardman, C. D. Quinlivan, P. Manju, C. C. N. Kuhn, I. R. Petersen, A. N. Luiten, J. J. Hope, N. P. Robins, and M. R. Hush. Fast machine-learning online optimization of ultra-cold-atom experiments. *Sci. Rep.*, 6(1):25890, 2016.

[50] A. D. Tranter, H. J. Slatyer, M. R. Hush, A. C. Leung, J. L. Everett, K. V. Paul, P. Vernaz-Gris, P. K. Lam, B. C. Buchler, and G. T. Campbell. Multiparameter optimisation of a magneto-optical trap using deep learning. *Nat. Commun.*, 9(1):4360, 2018.

[51] S. S. Kalantre, J. P. Zwolak, S. Ragole, X. Wu, N. M. Zimmerman, M. D. Stewart, and J. M. Taylor. Machine learning techniques for state recognition and auto-tuning in quantum dots. *npj Quantum Inf.*, 5(1):1–10, 2019.

[52] J. P. Zwolak, T. McJunkin, S. S. Kalantre, J.P. Dodson, E.R. MacQuarrie, D.E. Savage, M.G. Lagally, S.N. Coppersmith, M. A. Eriksson, and J. M. Taylor. Autotuning of double-dot devices in situ with machine learning. *Phys. Rev. Appl.*, 13:034075, 2020.

[53] A. J. Barker, H. Style, K. Luksch, S. Sunami, D. Garrick, F. Hill, C. J. Foot, and E. Bentine. Applying machine learning optimization methods to the production of a quantum gas. *Mach. Learn.: Sci. Technol.*, 1(1):015007, 2020.

[54] H. Saito. Creation and Manipulation of Quantized Vortices in Bose–Einstein Condensates Using Reinforcement Learning. *J. Phys. Soc. Jpn.*, 89(7):074006, 2020.

[55] Y. Baum, M. Amico, S. Howell, M. Hush, M. Liuzzi, P. Mundada, T. Merkh, A. R. R. Carvalho, and M. J. Biercuk. Experimental Deep Reinforcement Learning for Error-Robust Gateset Design on a Superconducting Quantum Computer. *arXiv:2105.01079*, 2021.

[56] Mi.-Z. Ai, Y. Ding, Y. Ban, J. D. Martín-Guerrero, J. Casanova, J.-M. Cui, Y.-F. Huang, X. Chen, C.-F. Li, and G.-C. Guo. Experimentally Realizing Efficient Quantum Control with Reinforcement Learning. *arXiv:2101.09020*, 2021.

[57] Rohit Supekar, Boya Song, Alasdair Hastewell, Gary P. T. Choi, Alexander Mietke, and Jörn Dunkel. Learning hydrodynamic equations for active matter from particle simulations and experiments, 2021.

[58] I. Carusotto, S. X. Hu, L. A. Collins, and A. Smerzi. Bogoliubov-Čerenkov radiation in a bose-einstein condensate flowing against an obstacle. *Phys. Rev. Lett.*, 97:260403, Dec 2006.

[59] Yu. G. Gladush, G. A. El, A. Gammal, and A. M. Kamchatnov. Radiation of linear waves in the stationary flow of a bose-einstein condensate past an obstacle. *Phys. Rev. A*, 75:033619, Mar 2007.

[60] T.-L. Horng, S.-C. Gou, T.-C. Lin, G. A. El, A. P. Itin, and A. M. Kamchatnov. Stationary wave patterns generated by an impurity moving with supersonic velocity through a bose-einstein condensate. *Phys. Rev. A*, 79:053619, May 2009.

[61] A. M. Kamchatnov and L. P. Pitaevskii. Stabilization of solitons generated by a supersonic flow of bose-einstein condensate past an obstacle. *Phys. Rev. Lett.*, 100:160402, Apr 2008.

[62] P. Ajith, S. Babak, Y. Chen, M. Hewitson, B. Krishnan, A. M. Sintes, J. T. Whelan, B. Brügmann, P. Diener, N. Dorband, J. Gonzalez, M. Hannam, S. Husa, D. Pollney, L. Rezzolla, L. Santamaría, U. Sperhake, and J. Thornburg. Template bank for gravitational waveforms from coalescing binary black holes: Nonspinning binaries. *Phys. Rev. D*, 77:104017, May 2008.

[63] M Emre Celebi and Kemal Aydin. *Unsupervised learning*

algorithms. Springer, 2016.

[64] Li-Li Sun and Xi-Zhao Wang. A survey on active learning strategy. In *2010 International Conference on Machine Learning and Cybernetics*, volume 1, pages 161–166. IEEE, 2010.

[65] J. Gui, Z. Sun, Y. Wen, D. Tao, and J. Ye. A review on generative adversarial networks: Algorithms, theory, and applications. *arXiv:2001.06937*, 2020.

[66] M. Abadi, A. Agarwal, P. Barham, E. Brevdo, Z. Chen, C. Citro, G. S. Corrado, A. Davis, J. Dean, M. Devin, S. Ghemawat, I. Goodfellow, A. Harp, G. Irving, M. Isard, Y. Jia, R. Jozefowicz, L. Kaiser, M. Kudlur, J. Levenberg, D. Mané, R. Monga, S. Moore, D. Murray, C. Olah, M. Schuster, J. Shlens, B. Steiner, I. Sutskever, K. Talwar, P. Tucker, V. Vanhoucke, V. Vasudevan, F. Viégas, O. Vinyals, P. Warden, M. Wattenberg, M. Wicke, Y. Yu, and X. Zheng. TensorFlow: Large-scale machine learning on heterogeneous systems, 2015. Software available from tensorflow.org.

Bibliography

[1] Charles H Bennett and David P DiVincenzo. Quantum information and computation. nature, 404(6775):247–255, 2000.

[2] Frank Arute, Kunal Arya, Ryan Babbush, Dave Bacon, Joseph C Bardin, Rami Barends, Rupak Biswas, Sergio Boixo, Fernando GSL Brandao, David A Buell, et al. Quantum supremacy using a programmable superconducting processor. Nature, 574 (7779):505–510, 2019.

[3] Han-Sen Zhong, Hui Wang, Yu-Hao Deng, Ming-Cheng Chen, Li-Chao Peng, Yi-Han Luo, Jian Qin, Dian Wu, Xing Ding, Yi Hu, et al. Quantum computational advantage using photons. Science, 370(6523):1460–1463, 2020.

[4] Jens Eisert, Mathis Friesdorf, and Christian Gogolin. Quantum many-body systems out of equilibrium. Nature Physics, 11(2):124–130, 2015.

[5] Bas Hensen, Hannes Bernien, Anaïs E Dréau, Andreas Reiserer, Norbert Kalb, Machiel S Blok, Just Ruitenberg, Raymond FL Vermeulen, Raymond N Schouten, Carlos Abellán, et al. Loophole-free bell inequality violation using electron spins separated by 1.3 kilometres. Nature, 526(7575):682–686, 2015.

[6] Victor Galitski and Ian B Spielman. Spin–orbit coupling in quantum gases. Nature, 494(7435):49–54, 2013.

[7] Alessio Celi, Pietro Massignan, Julius Ruseckas, Nathan Goldman, Ian B Spielman, G Juzeliūnas, and M Lewenstein. Synthetic gauge fields in synthetic dimensions. Physical review letters, 112(4):043001, 2014.

[8] Benjamin P Abbott, Richard Abbott, TD Abbott, MR Abernathy, Fausto Acernese, Kendall Ackley, Carl Adams, Thomas Adams, Paolo Addesso, RX Adhikari, et al. Observation of gravitational waves from a binary black hole merger. Physical review letters, 116(6):061102, 2016.

[9] Daniel Carney, Gordan Krnjaic, David C Moore, Cindy A Regal, Gadi Afek, Sunil Bhave, Benjamin Brubaker, Thomas Corbitt, Jonathan Cripe, Nicole Crisosto, et al. Mechanical quantum sensing in the search for dark matter. Quantum Science and Technology, 6(2):024002, 2021.

[10] Romana Schirhagl, Kevin Chang, Michael Loretz, and Christian L Degen. Nitrogen-vacancy centers in diamond: nanoscale sensors for physics and biology. Annual review of physical chemistry, 65:83–105, 2014.

[11] Giuseppe E Santoro and Erio Tosatti. Optimization using quantum mechanics: quantum annealing through adiabatic evolution. Journal of Physics A: Mathematical and General, 39(36):R393, 2006.

[12] Iulia M Georgescu, Sahel Ashhab, and Franco Nori. Quantum simulation. Reviews of Modern Physics, 86(1):153, 2014.

[13] Nicolas Gisin and Rob Thew. Quantum communication. Nature photonics, 1(3): 165–171, 2007.

[14] Christian L Degen, F Reinhard, and Paola Cappellaro. Quantum sensing. Reviews of modern physics, 89(3):035002, 2017.

[15] John Preskill. Quantum computing in the nisq era and beyond. Quantum, 2:79, 2018.

[16] Howard M Wiseman and Gerard J Milburn. Quantum measurement and control. Cambridge university press, 2009.

[17] Giuseppe Carleo, Ignacio Cirac, Kyle Cranmer, Laurent Daudet, Maria Schuld, Naftali Tishby, Leslie Vogt-Maranto, and Lenka Zdeborová. Machine learning and the physical sciences. Reviews of Modern Physics, 91(4):045002, 2019.

[18] Shangjie Guo, Yidan Wang, Thomas Purdy, and Jacob Taylor. Beyond spontaneous emission: Giant atom bounded in the continuum. Physical Review A, 102 (3):033706, 2020.

[19] Hilary M Hurst, Shangjie Guo, and IB Spielman. Feedback induced magnetic phases in binary bose-einstein condensates. Physical Review Research, 2(4):043325, 2020.

[20] Shangjie Guo, Amilson R Fritsch, Craig Greenberg, Ian Spielman, and Justyna P Zwolak. Machine-learning enhanced dark soliton detection in bose-einstein condensates. Machine Learning: Science and Technology, 2021.

[21] Shangjie Guo, Sophia M Koh, Amilson R Fritsch, IB Spielman, and Justyna P Zwolak. Combining machine learning with physics: A framework for tracking and sorting multiple dark solitons. arXiv preprint arXiv:2111.04881, 2021.

[22] J. Zwolak. Dark solitons in BECs dataset. National Institute of Standards and Technology, 2020. URL https://data.nist.gov/od/id/mds2-2363.

[23] A. R. Fritsch, S. M. Koh, S. Guo, I. B. Spielman, and J. P. Zwolak. Dark Solitons in Bose-Einstein Condensation: Real Dataset for Many-Body Physics Research. (in preparation).

[24] SolDet Team, 2021.

[25] T. P. Purdy, K. E. Grutter, K. Srinivasan, and J. M. Taylor. Quantum correlations from a room-temperature optomechanical cavity. Science, 356(6344):1265–1268, 2017.

[26] A. González-Tudela, C. S. Muñoz, and J. I. Cirac. Engineering and Harnessing Giant Atoms in High-Dimensional Baths: A Proposal for Implementation with Cold Atoms. Phys. Rev. Lett., 122:203603, May 2019. doi: 10.1103/PhysRevLett.122.203603. URL https://link.aps.org/doi/10.1103/PhysRevLett.122.203603.

[27] Y. Wang, M. J. Gullans, A. Browaeys, J. V. Porto, D. E. Chang, and A. V. Gorshkov. Single-photon bound states in atomic ensembles.

[28] C Laflamme, D Yang, and P Zoller. Continuous measurement of an atomic current. Phys. Rev. A, 95(4):043843, 2017.

[29] Kristof T Schütt, Stefan Chmiela, O Anatole von Lilienfeld, Alexandre Tkatchenko, Koji Tsuda, and Klaus-Robert Müller. Machine learning meets quantum physics. Lecture Notes in Physics, 2020.

[30] J. P. Zwolak, T. McJunkin, S. S. Kalantre, J.P. Dodson, E.R. MacQuarrie, D.E. Savage, M.G. Lagally, S.N. Coppersmith, M. A. Eriksson, and J. M. Taylor. Autotuning of double-dot devices in situ with machine learning. Phys. Rev. Appl., 13:034075, 2020. doi: 10.1103/PhysRevApplied.13.034075. URL https://link.aps.org/doi/10.1103/PhysRevApplied.13.034075.

[31] P. B. Wigley, P. J. Everitt, A. van den Hengel, J. W. Bastian, M. A. Sooriyabandara, G. D. McDonald, K. S. Hardman, C. D. Quinlivan, P. Manju, C. C. N. Kuhn, I. R. Petersen, A. N. Luiten, J. J. Hope, N. P. Robins, and M. R. Hush. Fast machine-learning online optimization of ultra-cold-atom experiments. Sci. Rep., 6(1):25890, 2016. ISSN 2045-2322. doi: 10.1038/srep25890. URL http://www.nature.com/articles/srep25890.

[32] Yuval Baum, Mirko Amico, Sean Howell, Michael Hush, Maggie Liuzzi, Pranav Mundada, Thomas Merkh, Andre RR Carvalho, and Michael J Biercuk. Experimental deep reinforcement learning for error-robust gate-set design on a superconducting quantum computer. PRX Quantum, 2(4):040324, 2021.

[33] H.-P. Breuer, E.-M. Laine, J. Piilo, and B. Vacchini. Colloquium: Non-Markovian dynamics in open quantum systems. Rev. Mod. Phys., 88:021002, Apr 2016. doi: 10.1103/RevModPhys.88.021002. URL https://link.aps.org/doi/10.1103/RevModPhys.88.021002.

[34] C. W. Hsu, B. Zhen, A. D. Stone, J. D. Joannopoulos, and M. Soljacic. Bound states in the continuum. Nat. Rev. Mater., 1(9):16048, 2016. ISSN 2058-8437. doi: 10.1038/natrevmats.2016.48. URL https://doi.org/10.1038/natrevmats.2016.48.

[35] Anton Frisk Kockum. Quantum optics with giant atomsí Ôthe first five years. In International Symposium on Mathematics, Quantum Theory, and Cryptography, pages 125–146. Springer Singapore, 2021.

[36] Göran Wendin. Quantum information processing with superconducting circuits: a review. Reports on Progress in Physics, 80(10):106001, 2017.

[37] R. Manenti, A. F. Kockum, A. Patterson, T. Behrle, J. Rahamim, G. Tancredi, F. Nori, and P. J. Leek. Circuit quantum acoustodynamics with surface acoustic waves. Nat. Commun., 8(1):975, 2017. ISSN 2041-1723. doi: 10.1038/s41467-017-01063-9. URL https://doi.org/10.1038/s41467-017-01063-9.

[38] Mike H Anderson, Jason R Ensher, Michael R Matthews, Carl E Wieman, and Eric A Cornell. Observation of bose-einstein condensation in a dilute atomic vapor. science, 269(5221):198–201, 1995.

[39] Todd A Brun. A simple model of quantum trajectories. American Journal of Physics, 70(7):719–737, 2002.

[40] Jing Zhang, Yu-xi Liu, Re-Bing Wu, Kurt Jacobs, and Franco Nori. Quantum feedback: theory, experiments, and applications. Phys. Rep., 679:1–60, 2017.

[41] Jesus Rogel-Salazar. The gross–pitaevskii equation and bose–einstein condensates. European Journal of Physics, 34(2):247, 2013.

[42] Lauren M Aycock, Hilary M Hurst, Dmitry K Efimkin, Dina Genkina, Hsin-I Lu, Victor M Galitski, and I. B. Spielman. Brownian motion of solitons in a bose–einstein condensate. Proc. Natl. Acad. Sci., 114(10):2503–2508, 2017.

[43] A. R. Fritsch, Mingwu Lu, G. H. Reid, A. M. Piñeiro, and I. B. Spielman. Creating solitons with controllable and near-zero velocity in Bose-Einstein condensates. Phys. Rev. A, 101:053629, May 2020. doi: 10.1103/PhysRevA.101.053629. URL https://link.aps.org/doi/10.1103/PhysRevA.101.053629.

[44] A. Ask, M. Ekström, P. Delsing, and G. Johansson. Cavity-free vacuum-Rabi splitting in circuit quantum acoustodynamics. Phys. Rev. A, 99:013840, Jan 2019. doi: 10.1103/PhysRevA.99.013840. URL https://link.aps.org/doi/10.1103/PhysRevA.99.013840.

[45] L. Guo, A. F. Kockum, F. Marquardt, and G. Johansson. Oscillating bound states for a giant atom.

[46] G. Calajó, Yao-LungL. Fang, H. U. Baranger, and F. Ciccarello. Exciting a Bound State in the Continuum through Multiphoton Scattering Plus Delayed Quantum Feedback. Phys. Rev. Lett., 122:073601, Feb 2019. doi: 10.1103/PhysRevLett.122.073601. URL https://link.aps.org/doi/10.1103/PhysRevLett.122.073601.

[47] R. Singh and T. P. Purdy. Detecting Thermal Acoustic Radiation with an Optomechanical Antenna.

[48] L. Guo, A. Grimsmo, A. F. Kockum, M. Pletyukhov, and G. Johansson. Giant acoustic atom: A single quantum system with a deterministic time delay. Phys. Rev. A, 95:053821, May 2017. doi: 10.1103/PhysRevA.95.053821. URL https://link.aps.org/doi/10.1103/PhysRevA.95.053821.

[49] G. Andersson, B. Suri, L. Guo, T. Aref, and P. Delsing. Non-exponential decay of a giant artificial atom. Nat. Phys., 15(11):1123, 2019. ISSN 1745-2481. doi: 10.1038/s41567-019-0605-6. URL https://doi.org/10.1038/s41567-019-0605-6.

[50] S. S. Szigeti, M. R. Hush, A. R. R. Carvalho, and J. J. Hope. Continuous measurement feedback control of a bose-einstein condensate using phase-contrast imaging. Phys. Rev. A, 80:013614, Jul 2009.

[51] Immanuel Bloch, Jean Dalibard, and Wilhelm Zwerger. Many-body physics with ultracold gases. Rev. Mod. Phys., 80:885–964, Jul 2008.

[52] Markus Greiner, Olaf Mandel, Tilman Esslinger, Theodor W Hänsch, and Immanuel Bloch. Quantum phase transition from a superfluid to a mott insulator in a gas of ultracold atoms. Nature, 415(6867):39–44, 2002.

[53] Dmitry A. Abanin, Ehud Altman, Immanuel Bloch, and Maksym Serbyn. Colloquium: Many-body localization, thermalization, and entanglement. Rev. Mod. Phys., 91:021001, May 2019.

[54] S. Burger, K. Bongs, S. Dettmer, W. Ertmer, K. Sengstock, A. Sanpera, G. V. Shlyapnikov, and M. Lewenstein. Dark solitons in Bose-Einstein condensates. Phys. Rev. Lett., 83:5198–5201, Dec 1999. doi: 10.1103/PhysRevLett.83.5198. URL https://link.aps.org/doi/10.1103/PhysRevLett.83.5198.

[55] Diego AR Dalvit, Jacek Dziarmaga, and Roberto Onofrio. Continuous quantum measurement of a bose-einstein condensate: A stochastic gross-pitaevskii equation. Phys. Rev. A, 65(5):053604, 2002.

[56] Seth Lloyd. Coherent quantum feedback. Physical Review A, 62(2):022108, 2000.

[57] MR Hush, SS Szigeti, ARR Carvalho, and JJ Hope. Controlling spontaneous-emission noise in measurement-based feedback cooling of a bose–einstein condensate. New J. Phys., 15(11):113060, 2013.

[58] Stuart S Szigeti, Michael R Hush, Andre RR Carvalho, and Joseph J Hope. Feedback control of an interacting bose-einstein condensate using phase-contrast imaging. Phys. Rev. A., 82(4):043632, 2010.

[59] Howard M Wiseman, Dominic W Berry, Stephen D Bartlett, Brendon L Higgins, and Geoffrey J Pryde. Adaptive measurements in the optical quantum information laboratory. IEEE Journal of Selected Topics in Quantum Electronics, 15(6):1661–1672, 2009.

[60] Pablo Solano, Yiheng Duan, Yu-Ting Chen, Alyssa Rudelis, Cheng Chin, and Vladan Vuletić. Strongly correlated quantum gas prepared by direct laser cooling. Phys. Rev. Lett., 123:173401, Oct 2019.

[61] P Öhberg and L Santos. Dark solitons in a two-component bose-einstein condensate. Phys. Rev. Lett., 86(14):2918, 2001.

[62] Oludare Isaac Abiodun, Aman Jantan, Abiodun Esther Omolara, Kemi Victoria Dada, Nachaat AbdElatif Mohamed, and Humaira Arshad. State-of-the-art in artificial neural network applications: A survey. Heliyon, 4(11):e00938, 2018.

[63] A. Voulodimos, N. Doulamis, A. Doulamis, and E. Protopapadakis. Deep learning for computer vision: A brief review. Comput. Intell. Neurosci., 2018:7068349, 2018. URL `https://doi.org/10.1155/2018/7068349`.

[64] Waseem Rawat and Zenghui Wang. Deep Convolutional Neural Networks for Image Classification: A Comprehensive Review. Neural Computation, 29(9):2352–2449, September 2017. ISSN 0899-7667. doi: 10.1162/neco_a_00990. Conference Name: Neural Computation.

[65] V. Weisskopf and E. Wigner. Berechnung der natürlichen Linienbreite auf Grund der Diracschen Lichttheorie. Z. Phys., 63(1-2):54, Jan 1930. doi: 10.1007/BF01336768.

[66] P. W. Milonni. Why spontaneous emission? Am. J. Phys., 52(4):340, 1984. doi: 10.1119/1.13886. URL `https://doi.org/10.1119/1.13886`.

[67] H. Walther, B. T H Varcoe, B.-G. Englert, and T. Becker. Cavity quantum electrodynamics. Rep. Prog. Phys., 69(5):1325, apr 2006. doi: 10.1088/0034-4885/69/5/r02. URL https://doi.org/10.1088%2F0034-4885%2F69%2F5%2Fr02.

[68] T. Niemczyk, F. Deppe, H. Huebl, E. P. Menzel, F. Hocke, M. J. Schwarz, J. J. Garcia-Ripoll, D. Zueco, T. Hümmer, E. Solano, A. Marx, and R. Gross. Circuit quantum electrodynamics in the ultrastrong-coupling regime. Nat. Phys., 6(10):772, 2010. ISSN 1745-2481. doi: 10.1038/nphys1730. URL https://doi.org/10.1038/nphys1730.

[69] X. Gu, A. F. Kockum, A. Miranowicz, Y. Liu, and F. Nori. Microwave photonics with superconducting quantum circuits. Phys. Rep., 718:1, 2017. ISSN 0370-1573. doi: https://doi.org/10.1016/j.physrep.2017.10.002. URL http://www.sciencedirect.com/science/article/pii/S0370157317303290.

[70] H. Zheng, D. J. Gauthier, and H. U. Baranger. Waveguide QED: Many-body bound-state effects in coherent and Fock-state scattering from a two-level system. Phys. Rev. A, 82:063816, Dec 2010. doi: 10.1103/PhysRevA.82.063816. URL https://link.aps.org/doi/10.1103/PhysRevA.82.063816.

[71] Yao-LungL. Fang and H. U. Baranger. Waveguide QED: Power spectra and correlations of two photons scattered off multiple distant qubits and a mirror. Phys. Rev. A, 91:053845, May 2015. doi: 10.1103/PhysRevA.91.053845. URL https://link.aps.org/doi/10.1103/PhysRevA.91.053845.

[72] F. Dinc, I. Ercan, and A. M. Brańczyk. Exact Markovian and non-Markovian time dynamics in waveguide QED: collective interactions, bound states in continuum, superradiance and subradiance. Quantum, 3:213, Dec 2019. doi: 10.22331/q-2019-12-09-213. URL https://doi.org/10.22331/q-2019-12-09-213.

[73] R. H. Dicke. Coherence in Spontaneous Radiation Processes. Phys. Rev., 93:99, Jan 1954. doi: 10.1103/PhysRev.93.99. URL https://link.aps.org/doi/10.1103/PhysRev.93.99.

[74] M. Gross and S. Haroche. Superradiance: An essay on the theory of collective spontaneous emission. Phys. Rep., 93(5):301, 1982. ISSN 0370-1573. doi: https://doi.org/10.1016/0370-1573(82)90102-8. URL http://www.sciencedirect.com/science/article/pii/0370157382901028.

[75] S. Datta. Surface Acoustic Wave Devices . Englewood Cliffs, N.J. : Prentice-Hall, 1986.

[76] A. F. Kockum, G. Johansson, and F. Nori. Decoherence-Free Interaction between Giant Atoms in Waveguide Quantum Electrodynamics. Phys. Rev. Lett., 120:140404, Apr 2018. doi: 10.1103/PhysRevLett.120.140404. URL https://link.aps.org/doi/10.1103/PhysRevLett.120.140404.

[77] K. Sinha, P. Meystre, E. A. Goldschmidt, F. K. Fatemi, S. L. Rolston, and P. Solano. Non-Markovian collective emission from macroscopically separated emitters.

[78] P.-O. Guimond, A. Roulet, H. N. Le, and V. Scarani. Rabi oscillation in a quantum cavity: Markovian and non-Markovian dynamics. Phys. Rev. A, 93:023808, 2016. doi: 10.1103/PhysRevA.93.023808. URL https://link.aps.org/doi/10.1103/PhysRevA.93.023808.

[79] L. Qiao and C.-P. Sun. Atom-photon bound states and non-Markovian cooperative dynamics in coupled-resonator waveguides. Phys. Rev. A, 100:063806, Dec 2019. doi: 10.1103/PhysRevA.100.063806. URL https://link.aps.org/doi/10.1103/PhysRevA.100.063806.

[80] C. Gonzalez-Ballestero, F. J. García-Vidal, and E. Moreno. Non-Markovian effects in waveguide-mediated entanglement. New Journal of Physics, 15(7):073015, 2013.

[81] S. Garmon, T. Petrosky, L. Simine, and D. Segal. Amplification of non-Markovian decay due to bound state absorption into continuum. Fortschritte der Phys., 61(2í 3): 261, 2013. doi: 10.1002/prop.201200077. URL https://onlinelibrary.wiley.com/doi/abs/10.1002/prop.201200077.

[82] F. Dinc and A. M. Brańczyk. Non-markovian super-superradiance in a linear chain of up to 100 qubits. Phys. Rev. Research, 1:032042, Dec 2019. doi: 10.1103/PhysRevResearch.1.032042. URL https://link.aps.org/doi/10.1103/PhysRevResearch.1.032042.

[83] L. R. Sletten, B. A. Moores, J. J. Viennot, and K. W. Lehnert. Resolving Phonon Fock States in a Multimode Cavity with a Double-Slit Qubit. Phys. Rev. X, 9: 021056, Jun 2019. doi: 10.1103/PhysRevX.9.021056. URL https://link.aps.org/doi/10.1103/PhysRevX.9.021056.

[84] B. A. Moores, L. R. Sletten, J. J. Viennot, and K. W. Lehnert. Cavity Quantum Acoustic Device in the Multimode Strong Coupling Regime. Phys. Rev. Lett., 120: 227701, May 2018. doi: 10.1103/PhysRevLett.120.227701. URL https://link.aps.org/doi/10.1103/PhysRevLett.120.227701.

[85] K. J. Satzinger, Y. P. Zhong, H.-S. Chang, G. A. Peairs, A. Bienfait, M.-H. Chou, A. Y. Cleland, C. R. Conner, É. Dumur, J. Grebel, I. Gutierrez, B. H. November, R. G. Povey, S. J. Whiteley, D. D. Awschalom, D. I. Schuster, and A. N. Cleland. Quantum control of surface acoustic-wave phonons. Nature, 563(7733):661, 2018. ISSN 1476-4687. doi: 10.1038/s41586-018-0719-5. URL https://doi.org/10.1038/s41586-018-0719-5.

[86] A. Noguchi, R. Yamazaki, Y. Tabuchi, and Y. Nakamura. Single-photon quantum regime of artificial radiation pressure on a surface acoustic wave resonator.

[87] A. Noguchi, R. Yamazaki, Y. Tabuchi, and Y. Nakamura. Qubit-Assisted Transduction for a Detection of Surface Acoustic Waves near the Quantum Limit. Phys. Rev. Lett., 119:180505, Nov 2017. doi: 10.1103/PhysRevLett.119.180505. URL https://link.aps.org/doi/10.1103/PhysRevLett.119.180505.

[88] T. Aref, P. Delsing, M. K. Ekström, A. F. Kockum, M. V. Gustafsson, G. Johansson, P. J. Leek, E. Magnusson, and R. Manenti. Quantum Acoustics with Surface Acoustic Waves, page 217. Springer International Publishing, Cham, 2016. ISBN 978-3-319-24091-6. doi: 10.1007/978-3-319-24091-6_9. URL https://doi.org/10.1007/978-3-319-24091-6_9.

[89] A. FriskKockum, P. Delsing, and G. Johansson. Designing frequency-dependent relaxation rates and Lamb shifts for a giant artificial atom. Phys. Rev. A, 90:013837, 2014. doi: 10.1103/PhysRevA.90.013837. URL https://link.aps.org/doi/10.1103/PhysRevA.90.013837.

[90] G. De Nittis and M. Lein. Linear Response Theory: An Analytic-Algebraic Approach. 2017.

[91] M. J. A. Schuetz, E. M. Kessler, G. Giedke, L. M. K. Vandersypen, M. D. Lukin, and J. I. Cirac. Universal Quantum Transducers Based on Surface Acoustic Waves. Phys. Rev. X, 5:031031, Sep 2015. doi: 10.1103/PhysRevX.5.031031. URL https://link.aps.org/doi/10.1103/PhysRevX.5.031031.

[92] D. Royer and E. Dieulesaint. Elastic Waves in Solids I Free and Guided Propagation. 1996.

[93] R. Igreja and C. J. Dias. Analytical evaluation of the interdigital electrodes capacitance for a multi-layered structure. Sens. Actuators A Phys., 112(2-3):291, 2004.

[94] R. Stoneley. The propagation of surface elastic waves in a cubic crystal. Proc. R. Soc. A, 232(1191):447, 1955.

[95] F. H. Stillinger and D. R. Herrick. Bound states in the continuum. Phys. Rev. A, 11:446, Feb 1975. doi: 10.1103/PhysRevA.11.446. URL https://link.aps.org/doi/10.1103/PhysRevA.11.446.

[96] D. Suter and G. A. Álvarez. Colloquium: Protecting quantum information against environmental noise. Rev. Mod. Phys., 88:041001, Oct 2016. doi: 10.1103/RevModPhys.88.041001. URL https://link.aps.org/doi/10.1103/RevModPhys.88.041001.

[97] D. A. Lidar, I. L. Chuang, and K. B. Whaley. Decoherence-Free Subspaces for Quantum Computation. Phys. Rev. Lett., 81:2594, Sep 1998. doi: 10.1103/PhysRevLett.81.2594. URL https://link.aps.org/doi/10.1103/PhysRevLett.81.2594.

[98] V. Paulisch, H. J. Kimble, and A. González-Tudela. Universal quantum computation in waveguide QED using decoherence free subspaces. New J. Phys., 18(4):043041, apr 2016. doi: 10.1088/1367-2630/18/4/043041. URL https://doi.org/10.1088%2F1367-2630%2F18%2F4%2F043041.

[99] S. Kim, X. Xu, J. M. Taylor, and G. Bahl. Dynamically induced robust phonon transport and chiral cooling in an optomechanical system. Nat. Commun., 8(1): 205, 2017. ISSN 2041-1723. doi: 10.1038/s41467-017-00247-7. URL https://doi.org/10.1038/s41467-017-00247-7.

[100] J Ignacio Cirac and Peter Zoller. Goals and opportunities in quantum simulation. Nature Physics, 8(4):264–266, 2012.

[101] I. M. Georgescu, S. Ashhab, and Franco Nori. Quantum simulation. Rev. Mod. Phys., 86:153–185, Mar 2014.

[102] SS Hodgman, RG Dall, AG Manning, KGH Baldwin, and AG Truscott. Direct measurement of long-range third-order coherence in bose-einstein condensates. Science, 331(6020):1046–1049, 2011.

[103] Christian Gross and Immanuel Bloch. Quantum simulations with ultracold atoms in optical lattices. Science, 357(6355):995–1001, 2017.

[104] Torsten V. Zache, Thomas Schweigler, Sebastian Erne, Jörg Schmiedmayer, and Jürgen Berges. Extracting the field theory description of a quantum many-body system from experimental data. Phys. Rev. X, 10:011020, Jan 2020.

[105] M. Bartenstein, A. Altmeyer, S. Riedl, S. Jochim, C. Chin, J. Hecker Denschlag, and R. Grimm. Collective excitations of a degenerate gas at the bec-bcs crossover. Phys. Rev. Lett., 92:203201, May 2004.

[106] Thomas Bourdel, Lev Khaykovich, Julien Cubizolles, Jun Zhang, Frédéric Chevy, M Teichmann, L Tarruell, SJJMF Kokkelmans, and Christophe Salomon. Experimental study of the bec-bcs crossover region in lithium 6. Phys. Rev. Lett., 93(5): 050401, 2004.

[107] Y-J Lin, K Jiménez-García, and I. B. Spielman. Spin-orbit-coupled bose-einstein condensates. Nature, 471(7336):83–86, 2011.

[108] Renate Landig, Lorenz Hruby, Nishant Dogra, Manuele Landini, Rafael Mottl, Tobias Donner, and Tilman Esslinger. Quantum phases from competing short-and long-range interactions in an optical lattice. Nature, 532(7600):476, 2016.

[109] J. P. Ronzheimer, M. Schreiber, S. Braun, S. S. Hodgman, S. Langer, I. P. McCulloch, F. Heidrich-Meisner, I. Bloch, and U. Schneider. Expansion dynamics of interacting bosons in homogeneous lattices in one and two dimensions. Phys. Rev. Lett., 110:205301, May 2013.

[110] Thomas Kohlert, Sebastian Scherg, Xiao Li, Henrik P. Lüschen, Sankar Das Sarma, Immanuel Bloch, and Monika Aidelsburger. Observation of many-body localization in a one-dimensional system with a single-particle mobility edge. Phys. Rev. Lett., 122:170403, May 2019.

[111] Anatoli Polkovnikov, Krishnendu Sengupta, Alessandro Silva, and Mukund Vengalattore. Colloquium: Nonequilibrium dynamics of closed interacting quantum systems. Rev. Mod. Phys., 83(3):863, 2011.

[112] Markus Heyl. Dynamical quantum phase transitions: a review. Rep. Prog. Phys., 81 (5):054001, 2018.

[113] Sebastian Diehl, A Micheli, A Kantian, B Kraus, HP Büchler, and P Zoller. Quantum states and phases in driven open quantum systems with cold atoms. Nat. Phys., 4 (11):878–883, 2008.

[114] B. Kraus, H. P. Büchler, S. Diehl, A. Kantian, A. Micheli, and P. Zoller. Preparation of entangled states by quantum markov processes. Phys. Rev. A, 78:042307, Oct 2008.

[115] Frank Verstraete, Michael M Wolf, and J Ignacio Cirac. Quantum computation and quantum-state engineering driven by dissipation. Nat. Phys., 5(9):633–636, 2009.

[116] Marcos Rigol. Breakdown of thermalization in finite one-dimensional systems. Phys. Rev. Lett., 103:100403, Sep 2009.

[117] T. Mawson, T. C. Petersen, J. K. Slingerland, and T. P. Simula. Braiding and fusion of non-abelian vortex anyons. Phys. Rev. Lett., 123:140404, Oct 2019.

[118] J Zhang, PW Hess, A Kyprianidis, P Becker, A Lee, J Smith, G Pagano, I-D Potirniche, Andrew C Potter, A Vishwanath, et al. Observation of a discrete time crystal. Nature, 543(7644):217–220, 2017.

[119] Marek Trippenbach, Krzysztof Góral, Kazimierz Rzazewski, Boris Malomed, and YB Band. Structure of binary bose-einstein condensates. J Phys B At Mol Opt Phys., 33(19):4017, 2000.

[120] Yuki Kawaguchi and Masahito Ueda. Spinor bose-einstein condensates. Phys. Rep., 520(5):253–381, 2012.

[121] Dan M Stamper-Kurn and Masahito Ueda. Spinor bose gases: Symmetries, magnetism, and quantum dynamics. Rev. Mod. Phys., 85(3):1191, 2013.

[122] S. A. Haine, A. J. Ferris, J. D. Close, and J. J. Hope. Control of an atom laser using feedback. Phys. Rev. A, 69:013605, Jan 2004.

[123] S. D. Wilson, A. R. R. Carvalho, J. J. Hope, and M. R. James. Effects of measurement backaction in the stabilization of a bose-einstein condensate through feedback. Phys. Rev. A, 76:013610, Jul 2007.

[124] Andrew C. J. Wade, Jacob F. Sherson, and Klaus Mølmer. Squeezing and entanglement of density oscillations in a bose-einstein condensate. Phys. Rev. Lett., 115: 060401, Aug 2015.

[125] Ebubechukwu O Ilo-Okeke and Tim Byrnes. Theory of single-shot phase contrast imaging in spinor bose-einstein condensates. Phys. Rev. Lett., 112(23):233602, 2014.

[126] Shi Wang and Tim Byrnes. Quantum feedback control of atomic ensembles and spinor bose-einstein condensates. Phys. Rev. A, 94:033620, Sep 2016.

[127] Andrew C. J. Wade, Jacob F. Sherson, and Klaus Mølmer. Manipulation of collective quantum states in bose-einstein condensates by continuous imaging. Phys. Rev. A, 93:023610, Feb 2016.

[128] M. R. Andrews, D. M. Kurn, H.-J. Miesner, D. S. Durfee, C. G. Townsend, S. Inouye, and W. Ketterle. Propagation of sound in a bose-einstein condensate. Phys. Rev. Lett., 79:553–556, Jul 1997.

[129] Hilary M. Hurst and I. B. Spielman. Measurement-induced dynamics and stabilization of spinor-condensate domain walls. Phys. Rev. A, 99(5):053612, 2019.

[130] In this work we use $\overline{\cdot}$ to denote a statistical average and $\langle\cdot\rangle$ to denote a quantum-mechanical expectation value. $\tilde{m}_{s,k}$ indicates the Fourier transform of $m_s(x)$.

[131] Lev Pitaevskii and Sandro Stringari. Bose-Einstein condensation. Oxford university press, 2003.

[132] Y-J Lin, Rob L Compton, Karina Jiménez-García, James V Porto, and Ian B Spielman. Synthetic magnetic fields for ultracold neutral atoms. Nature, 462(7273): 628–632, 2009.

[133] Nathan Goldman, G Juzeliūnas, Patrik Öhberg, and I. B. Spielman. Light-induced gauge fields for ultracold atoms. Rep. Prog. Phys., 77(12):126401, 2014.

[134] Victor Galitski and I. B. Spielman. Spin-orbit coupling in quantum gases. Nature, 494(7435):49–54, 2013.

[135] Ronen M Kroeze, Yudan Guo, and Benjamin L Lev. Dynamical spin-orbit coupling of a quantum gas. Phys. Rev. Lett., 123(16):160404, 2019.

[136] K. Jiménez-García, L. J. LeBlanc, R. A. Williams, M. C. Beeler, A. R. Perry, and I. B. Spielman. Peierls substitution in an engineered lattice potential. Phys. Rev. Lett., 108:225303, May 2012.

[137] H.-I Lu, M. Schemmer, L. M. Aycock, D. Genkina, S. Sugawa, and I. B. Spielman. Geometrical pumping with a bose-einstein condensate. Phys. Rev. Lett., 116: 200402, May 2016.

[138] A. Aurisano, A. Radovic, D. Rocco, A. Himmel, M.D. Messier, E. Niner, G. Pawloski, F. Psihas, A. Sousa, and P. Vahle. A convolutional neural network neutrino event classifier. Journal of Instrumentation, 11(09):P09001–P09001, sep 2016. doi: 10.1088/1748-0221/11/09/p09001. URL https://doi.org/10.1088/1748-0221/11/09/p09001.

[139] R. Acciarri, C. Adams, R. An, J. Asaadi, and M. Auger *et al*. Convolutional neural networks applied to neutrino events in a liquid argon time projection chamber. Journal of Instrumentation, 12(03):P03011–P03011, mar 2017. doi: 10.1088/1748-0221/12/03/p03011. URL https://doi.org/10.1088/1748-0221/12/03/p03011.

[140] Michael Kagan. Image-based jet analysis. arXiv preprint arXiv:2012.09719, 2020.

[141] Artem Golovatiuk, Giovanni De Lellis, and Andrey Ustyuzhanin. Deep learning for directional dark matter search. Journal of Physics: Conference Series, 1525:012108, apr 2020. doi: 10.1088/1742-6596/1525/1/012108. URL https://doi.org/10.1088/1742-6596/1525/1/012108.

[142] Charanjit K Khosa, Lucy Mars, Joel Richards, and Veronica Sanz. Convolutional neural networks for direct detection of dark matter. Journal of Physics G: Nuclear and Particle Physics, 47(9):095201, jul 2020. doi: 10.1088/1361-6471/ab8e94. URL https://doi.org/10.1088/1361-6471/ab8e94.

[143] S. S. Kalantre, Justyna P. Zwolak, Stephen Ragole, Xingyao Wu, Neil M. Zimmerman, M. D. Stewart, and Jacob M. Taylor. Machine learning techniques for state recognition and auto-tuning in quantum dots. npj Quantum Information, 5(6):1–10, 2017. doi: 10.1038/s41534-018-0118-7. URL https://www.nature.com/articles/s41534-018-0118-7.

[144] A. R. Mills, M. M. Feldman, C. Monical, P. J. Lewis, K. W. Larson, A. M. Mounce, and J. R. Petta. Computer-automated tuning procedures for semiconductor quantum dot arrays. Applied Physics Letters, 115(11):113501, 2019. doi: 10.1063/1.5121444. URL https://doi.org/10.1063/1.5121444.

[145] Justyna P. Zwolak, Thomas McJunkin, Sandesh S. Kalantre, J.P. Dodson, E.R. MacQuarrie, D.E. Savage, M.G. Lagally, S.N. Coppersmith, Mark A. Eriksson, and

Jacob M. Taylor. Autotuning of double-dot devices in situ with machine learning. Phys. Rev. Applied, 13:034075, Mar 2020. doi: 10.1103/PhysRevApplied.13.034075. URL https://link.aps.org/doi/10.1103/PhysRevApplied.13.034075.

[146] Muhammad Usman, Yi Zheng Wong, Charles D. Hill, and Lloyd C. L. Hollenberg. Framework for atomic-level characterisation of quantum computer arrays by machine learning. npj Computational Materials, 6(1):1–8, 2020. doi: 110.1038/s41524-020-0282-0. URL https://doi.org/10.1038/s41524-020-0282-0.

[147] Zhuo Cao, Yabo Dan, Zheng Xiong, Chengcheng Niu, Xiang Li, Songrong Qian, and Jianjun Hu. Convolutional neural networks for crystal material property prediction using hybrid orbital-field matrix and magpie descriptors. Crystals, 9(4):191, 2019.

[148] Mohammadreza Karamad, Rishikesh Magar, Yuting Shi, Samira Siahrostami, Ian D. Gates, and Amir Barati Farimani. Orbital graph convolutional neural network for material property prediction. Phys. Rev. Materials, 4:093801, Sep 2020. doi: 10.1103/PhysRevMaterials.4.093801. URL https://link.aps.org/doi/10.1103/PhysRevMaterials.4.093801.

[149] JE Gubernatis and T Lookman. Machine learning in materials design and discovery: Examples from the present and suggestions for the future. Physical Review Materials, 2(12):120301, 2018.

[150] David K Duvenaud, Dougal Maclaurin, Jorge Iparraguirre, Rafael Bombarell, Timothy Hirzel, Alán Aspuru-Guzik, and Ryan P Adams. Convolutional networks on graphs for learning molecular fingerprints. Advances in neural information processing systems, 28:2224–2232, 2015.

[151] Keith T Butler, Daniel W Davies, Hugh Cartwright, Olexandr Isayev, and Aron Walsh. Machine learning for molecular and materials science. Nature, 559(7715):547–555, 2018.

[152] Robin Winter, Floriane Montanari, Frank Noé, and Djork-Arné Clevert. Learning continuous and data-driven molecular descriptors by translating equivalent chemical representations. Chemical Science, 10(6):1692–1701, 2019.

[153] B. S. Rem, N. Käming, M. Tarnowski, L. Asteria, N. Fläschner, C. Becker, K. Sengstock, and C. Weitenberg. Identifying quantum phase transitions using artificial neural networks on experimental data. Nat. Phys., 15(9):917–920, 2019. ISSN 1745-2481. doi: 10.1038/s41567-019-0554-0. URL https://www.nature.com/articles/s41567-019-0554-0.

[154] Gal Ness, Anastasiya Vainbaum, Constantine Shkedrov, Yanay Florshaim, and Yoav Sagi. Single-exposure absorption imaging of ultracold atoms using deep learning.

Phys. Rev. Applied, 14:014011, Jul 2020. doi: 10.1103/PhysRevApplied.14.014011. URL https://link.aps.org/doi/10.1103/PhysRevApplied.14.014011.

[155] S. Pilati and P. Pieri. Supervised machine learning of ultracold atoms with speckle disorder. Scientific Reports, 9:5613, Jul 2019. doi: 10.1038/s41598-019-42125-w. URL https://doi.org/10.1038/s41598-019-42125-w.

[156] Friederike Metz, Juan Polo, Natalya Weber, and Thomas Busch. Deep learning based quantum vortex detection in atomic bose-einstein condensates. Machine Learning: Science and Technology, 2021.

[157] J. S. Russel. Report of the Committee on Waves, pages 417–468. British reports VI, 1837. plus plates 1í Ó8.

[158] A. R. Osborne and T. L. Burch. Internal solitons in the andaman sea. Science, 208 (4443):451–460, 1980.

[159] M. Lakshmanan. Solitons, Tsunamis and Oceanographical Applications of, pages 8506–8521. Springer New York, New York, NY, 2009. ISBN 978-0-387-30440-3. doi: 10.1007/978-0-387-30440-3_509. URL https://doi.org/10.1007/978-0-387-30440-3_509.

[160] J. Denschlag, J. E. Simsarian, D. L. Feder, Charles W. Clark, L. A. Collins, J. Cubizolles, L. Deng, E. W. Hagley, K. Helmerson, W. P. Reinhardt, S. L. Rolston, B. I. Schneider, and W. D. Phillips. Generating solitons by phase engineering of a Bose-Einstein condensate. Science, 287(5450):97–101, 2000. ISSN 0036-8075. doi: 10.1126/science.287.5450.97. URL https://science.sciencemag.org/content/287/5450/97.

[161] Akira Hasegawa and Frederick Tappert. Transmission of stationary nonlinear optical pulses in dispersive dielectric fibers. ii. normal dispersion. Applied Physics Letters, 23(4):171–172, 1973. doi: 10.1063/1.1654847. URL https://doi.org/10.1063/1.1654847.

[162] L. F. Mollenauer, R. H. Stolen, and J. P. Gordon. Experimental observation of picosecond pulse narrowing and solitons in optical fibers. Phys. Rev. Lett., 45:1095–1098, Sep 1980. doi: 10.1103/PhysRevLett.45.1095. URL https://link.aps.org/doi/10.1103/PhysRevLett.45.1095.

[163] K. Stasiewicz, P. K. Shukla, G. Gustafsson, S. Buchert, B. Lavraud, B. Thidé, and Z. Klos. Slow magnetosonic solitons detected by the cluster spacecraft. Phys. Rev. Lett., 90:085002, Feb 2003. doi: 10.1103/PhysRevLett.90.085002. URL https://link.aps.org/doi/10.1103/PhysRevLett.90.085002.

[164] Yasuo Hashizume. Nonlinear pressure waves in a fluid-filled elastic tube. Journal of the Physical Society of Japan, 54(9):3305–3312, 1985. doi: 10.1143/JPSJ.54.3305. URL https://doi.org/10.1143/JPSJ.54.3305.

[165] Sigeo Yomosa. Solitary waves in large blood vessels. Journal of the Physical Society of Japan, 56(2):506–520, 1987. doi: 10.1143/JPSJ.56.506. URL https://doi.org/10.1143/JPSJ.56.506.

[166] A. Weller, J. P. Ronzheimer, C. Gross, J. Esteve, M. K. Oberthaler, D. J. Frantzeskakis, G. Theocharis, and P. G. Kevrekidis. Experimental observation of oscillating and interacting matter wave dark solitons. Phys. Rev. Lett., 101:130401, Sep 2008. doi: 10.1103/PhysRevLett.101.130401. URL https://link.aps.org/doi/10.1103/PhysRevLett.101.130401.

[167] D J Frantzeskakis. Dark solitons in atomic Bose–Einstein condensates: from theory to experiments. Journal of Physics A: Mathematical and Theoretical, 43(21):213001, may 2010. doi: 10.1088/1751-8113/43/21/213001. URL https://doi.org/10.1088%2F1751-8113%2F43%2F21%2F213001.

[168] Linn F. Mollenauer and James P. Gordon. Solitons in Optical Fibers. Academic Press, Burlington, 2006. ISBN 978-0-12-504190-4. doi: https://doi.org/10.1016/B978-012504190-4/50002-5. URL http://www.sciencedirect.com/science/article/pii/B9780125041904500025.

[169] A. Hasegawa. Soliton-based optical communications: an overview. IEEE Journal of Selected Topics in Quantum Electronics, 6(6):1161–1172, 2000. doi: 10.1109/2944.902164.

[170] Lauren M. Aycock, Hilary M. Hurst, Dmitry K. Efimkin, Dina Genkina, Hsin-I Lu, Victor M. Galitski, and I. B. Spielman. Brownian motion of solitons in a Bose–Einstein condensate. Proceedings of the National Academy of Sciences, 114 (10):2503–2508, 2017. ISSN 0027-8424. doi: 10.1073/pnas.1615004114. URL https://www.pnas.org/content/114/10/2503.

[171] Waseem Rawat and Zenghui Wang. Deep convolutional neural networks for image classification: A comprehensive review. Neural computation, 29(9):2352–2449, 2017.

[172] Y. Castin and R. Dum. Bose-einstein condensates in time dependent traps. Phys. Rev. Lett., 77(27):5315–5319, December 1996.

[173] F. Pedregosa, G. Varoquaux, A. Gramfort, V. Michel, B. Thirion, O. Grisel, M. Blondel, P. Prettenhofer, R. Weiss, V. Dubourg, J. Vanderplas, A. Passos, D. Cournapeau, M. Brucher, M. Perrot, and E. Duchesnay. Scikit-learn: Machine learning in Python. Journal of Machine Learning Research, 12:2825–2830, 2011.

[174] Moloud Abdar, Farhad Pourpanah, Sadiq Hussain, Dana Rezazadegan, Li Liu, Mohammad Ghavamzadeh, Paul Fieguth, Abbas Khosravi, U Rajendra Acharya, Vladimir Makarenkov, et al. A review of uncertainty quantification in deep learning: Techniques, applications and challenges. arXiv preprint arXiv:2011.06225, 2020.

[175] Scott Thiebes, Sebastian Lins, and Ali Sunyaev. Trustworthy artificial intelligence. Electronic Markets, pages 1–18, 2020.

[176] Burr Settles. Active learning literature survey. Technical report, University of Wisconsin-Madison Department of Computer Sciences, 2009.

[177] Xu Ji, João F Henriques, and Andrea Vedaldi. Invariant information clustering for unsupervised image classification and segmentation. In Proceedings of the IEEE International Conference on Computer Vision, pages 9865–9874, 2019.

[178] C. Miles, A. Bohrdt, R. Wu, C. Chiu, M. Xu, G. Ji, M. Greiner, K. Q. Weinberger, E. Demler, and E.-A. Kim. Correlator Convolutional Neural Networks: An Interpretable Architecture for Image-like Quantum Matter Data. Nat. Commun., 12: 3905, 2020.

[179] F. Metz, J. Polo, N. Weber, and T. Busch. Deep learning based quantum vortex detection in atomic Bose-Einstein condensates. Mach. Learn.: Sci. Technol., 2: 035019, 2021. URL http://arxiv.org/abs/2012.13097.

[180] J. Venderley, M. Matty, K. Mallayya, M. Krogstad, J. Ruff, G. Pleiss, V. Kishore, D. Mandrus, D. Phelan, L. Poudel, A. G. Wilson, K. Weinberger, P. Upreti, M. R. Norman, S. Rosenkranz, R. Osborn, and E.-A. Kim. Harnessing Interpretable and Unsupervised Machine Learning to Address Big Data from Modern X-ray Diffraction. arXiv:2008.03275, 2021. URL http://arxiv.org/abs/2008.03275.

[181] J. Carrasquilla and R. G. Melko. Machine learning phases of matter. Nat. Phys., 13 (5):431–434, 2017. ISSN 1745-2473, 1745-2481. doi: 10.1038/nphys4035. URL http://www.nature.com/articles/nphys4035.

[182] S. Guo, A. R. Fritsch, C. Greenberg, I. B. Spielman, and J. P. Zwolak. Machine-learning enhanced dark soliton detection in Bose-Einstein condensates. Mach. Learn.: Sci. Technol., 2:035020, 2021. URL http://arxiv.org/abs/2101.05404.

[183] A. J. Barker, H. Style, K. Luksch, S. Sunami, D. Garrick, F. Hill, C. J. Foot, and E. Bentine. Applying machine learning optimization methods to the production of a quantum gas. Mach. Learn.: Sci. Technol., 1(1):015007, 2020. ISSN 2632-2153. doi: 10.1088/2632-2153/ab6432. URL https://doi.org/10.1088/2632-2153/ab6432.

[184] H. Saito. Creation and Manipulation of Quantized Vortices in Boseí ÓEinstein Condensates Using Reinforcement Learning. J. Phys. Soc. Jpn., 89(7):074006, 2020. ISSN 0031-9015. doi: 10.7566/JPSJ.89.074006. URL https://journals.jps.jp/doi/10.7566/JPSJ.89.074006.

[185] A. D. Tranter, H. J. Slatyer, M. R. Hush, A. C. Leung, J. L. Everett, K. V. Paul, P. Vernaz-Gris, P. K. Lam, B. C. Buchler, and G. T. Campbell. Multiparameter optimisation of a magneto-optical trap using deep learning. Nat. Commun., 9(1): 4360, 2018. ISSN 2041-1723. doi: 10.1038/s41467-018-06847-1. URL https://www.nature.com/articles/s41467-018-06847-1.

[186] S. S. Kalantre, J. P. Zwolak, S. Ragole, X. Wu, N. M. Zimmerman, M. D. Stewart, and J. M. Taylor. Machine learning techniques for state recognition and auto-tuning in quantum dots. npj Quantum Inf., 5(1):1–10, 2019. ISSN 2056-6387. doi: 10.1038/s41534-018-0118-7. URL https://www.nature.com/articles/s41534-018-0118-7.

[187] Y. Baum, M. Amico, S. Howell, M. Hush, M. Liuzzi, P. Mundada, T. Merkh, A. R. R. Carvalho, and M. J. Biercuk. Experimental Deep Reinforcement Learning for Error-Robust Gateset Design on a Superconducting Quantum Computer. arXiv:2105.01079, 2021. URL http://arxiv.org/abs/2105.01079.

[188] Mi.-Z. Ai, Y. Ding, Y. Ban, J. D. Martˆn-Guerrero, J. Casanova, J.-M. Cui, Y.-F. Huang, X. Chen, C.-F. Li, and G.-C. Guo. Experimentally Realizing Efficient Quantum Control with Reinforcement Learning. arXiv:2101.09020, 2021. URL http://arxiv.org/abs/2101.09020.

[189] N. Maskara, M. Buchhold, M. Endres, and E. van Nieuwenburg. A learning algorithm with emergent scaling behavior for classifying phase transitions. arXiv:2103.15855, 2021. URL http://arxiv.org/abs/2103.15855.

[190] J. Venderley, V. Khemani, and E.-A. Kim. Machine learning out-of-equilibrium phases of matter. Phys. Rev. Lett., 120(25):257204, 2018. ISSN 0031-9007, 1079-7114. doi: 10.1103/PhysRevLett.120.257204. URL http://arxiv.org/abs/1711.00020.

[191] Tamil Arasan Bakthavatchalam, Suriyadeepan Ramamoorthy, Malaikannan Sankarasubbu, Radha Ramaswamy, and Vijayalakshmi Sethuraman. Bayesian Optimization of Bose-Einstein Condensates. Scientific Reports, 11(1):5054, March 2021. ISSN 2045-2322. doi: 10.1038/s41598-021-84336-0. URL https://www.nature.com/articles/s41598-021-84336-0. Number: 1 Publisher: Nature Publishing Group.

[192] R. Harper, S. T. Flammia, and J. J. Wallman. Efficient learning of quantum noise. Nat. Phys., 16:1184–1188, 2020. ISSN 1745-2473, 1745-2481. doi: 10.1038/s41567-020-0992-8.

[193] P. Cha, P. Ginsparg, F. Wu, J. Carrasquilla, P. L. McMahon, and E.-A. Kim. Attention-based Quantum Tomography. arXiv:2006.12469, 2020. URL http://arxiv.org/abs/2006.12469.

[194] G. Torlai, G. Mazzola, J. Carrasquilla, M. Troyer, R. Melko, and G. Carleo. Neural-network quantum state tomography. Nat. Phys., 14(5):447–450, 2018. ISSN 1745-2473, 1745-2481. doi: 10.1038/s41567-018-0048-5. URL http://www.nature.com/articles/s41567-018-0048-5.

[195] Y. Zhang and E.-A. Kim. Quantum Loop Topography for Machine Learning. Phys. Rev. Lett., 118(21):216401, 2017. ISSN 0031-9007, 1079-7114. doi: 10.1103/PhysRevLett.118.216401. URL http://link.aps.org/doi/10.1103/PhysRevLett.118.216401.

[196] W. Ketterle, D. S. Durfee, and D. M. Stamper-Kurn. Making, probing and understanding Bose-Einstein condensates. In M. Inguscio, S. Stringari, and C. E. Wieman, editors, Bose-Einstein condensation in atomic gases, Proceedings of the International School of Physics "Enrico Fermi", Course CXL, pages 67–176. IOS Press, Amsterdam, 1999.

[197] A. R. Fritsch, M. Lu, G. H. Reid, A. M. Piñeiro, and I. B. Spielman. Creating solitons with controllable and near-zero velocity in Bose-Einstein condensates. Phys. Rev. A, 101(5):053629, 2020. doi: 10.1103/PhysRevA.101.053629. URL https://link.aps.org/doi/10.1103/PhysRevA.101.053629.

[198] F. Huang, Z. Cao, J. Guo, S.-H. Jiang, S. Li, and Z. Guo. Comparisons of heuristic, general statistical and machine learning models for landslide susceptibility prediction and mapping. Catena, 191:104580, 2020.

[199] S. Ghosh, M. R Malgireddy, V. Chaudhary, and G. Dhillon. A new approach to automatic disc localization in clinical lumbar mri: combining machine learning with heuristics. In 2012 9th IEEE International Symposium on Biomedical Imaging (ISBI), pages 114–117. IEEE, 2012.

[200] J. Sakhnini, H. Karimipour, and A. Dehghantanha. Smart grid cyber attacks detection using supervised learning and heuristic feature selection. In 2019 IEEE 7th International Conference on Smart Energy Grid Engineering (SEGE), pages 108–112. IEEE, 2019.

[201] T. Bothwell, D. Kedar, E. Oelker, J. M. Robinson, S. L. Bromley, W. L. Tew, J. Ye, and C. J. Kennedy. JILA SrI optical lattice clock with uncertainty of 2.0×10^{-18}. Metrologia, 56(6):065004, 2019.

[202] Kean Loon Lee, Nils B Jørgensen, Lars J Wacker, Magnus G Skou, Kristoffer T Skalmstang, Jan J Arlt, and Nick P Proukakis. Time-of-flight expansion of binary

bose–einstein condensates at finite temperature. New Journal of Physics, 20(5): 053004, 2018.

[203] S. Burger, K. Bongs, S. Dettmer, W. Ertmer, K. Sengstock, A Sanpera, G. V. Shlyapnikov, and M. Lewenstein. Dark Solitons in Bose-Einstein Condensates. Phys. Rev. Lett., 83(25):5198–5201, 1999.

[204] J. Denschlag, J. E. Simsarian, D. L. Feder, C. Clark, L. A. Collins, J. Cubizolles, L. Deng, E. Hagley, K. Helmerson, W. P. Reinhardt, S. L. Rolston, B. I. Schneider, and W. D. Phillips. Generating Solitons by Phase Engineering of a Bose-Einstein Condensate. Science, 287(5450):97–101, 2000.

[205] A Muñoz Mateo and J Brand. Stability and dispersion relations of three-dimensional solitary waves in trapped bose–einstein condensates. New Journal of Physics, 17 (12):125013, 2015.

[206] Youzi Xiao, Zhiqiang Tian, Jiachen Yu, Yinshu Zhang, Shuai Liu, Shaoyi Du, and Xuguang Lan. A review of object detection based on deep learning. Multimed Tools Appl, 79(33):23729–23791, September 2020. ISSN 1573-7721. doi: 10.1007/s11042-020-08976-6. URL https://doi.org/10.1007/s11042-020-08976-6.

[207] Saeid Asgari Taghanaki, Kumar Abhishek, Joseph Paul Cohen, Julien Cohen-Adad, and Ghassan Hamarneh. Deep semantic segmentation of natural and medical images: a review. Artif Intell Rev, 54(1):137–178, January 2021. ISSN 1573-7462. doi: 10.1007/s10462-020-09854-1. URL https://doi.org/10.1007/s10462-020-09854-1.

[208] Hamed Alqahtani, Manolya Kavakli-Thorne, and Gulshan Kumar. Applications of Generative Adversarial Networks (GANs): An Updated Review. Arch Computat Methods Eng, 28(2):525–552, March 2021. ISSN 1886-1784. doi: 10.1007/s11831-019-09388-y. URL https://doi.org/10.1007/s11831-019-09388-y.

[209] S. Donadello, S. Serafini, M. Tylutki, L. P. Pitaevskii, F. Dalfovo, G. Lamporesi, and G. Ferrari. Observation of Solitonic Vortices in Bose-Einstein Condensates. Phys. Rev. Lett., 113(6):065302, 2014. ISSN 0031-9007, 1079-7114. doi: 10.1103/PhysRevLett.113.065302. URL http://arxiv.org/abs/1404.4237.

[210] D. Leykam, I. Rondon, and D. G. Angelakis. Dark soliton detection using persistent homology. arXiv:2107.14594, 2021.

[211] M. Abadi, A. Agarwal, P. Barham, E. Brevdo, Z. Chen, C. Citro, G. S. Corrado, A. Davis, J. Dean, M. Devin, S. Ghemawat, I. Goodfellow, A. Harp, G. Irving, M. Isard, Y. Jia, R. Jozefowicz, L. Kaiser, M. Kudlur, J. Levenberg, D. Mané, R. Monga, S. Moore, D. Murray, C. Olah, M. Schuster, J. Shlens, B. Steiner, I. Sutskever, K. Talwar, P. Tucker, V. Vanhoucke, V. Vasudevan, F. Viégas, O. Vinyals, P. Warden,

M. Wattenberg, M. Wicke, Y. Yu, and X. Zheng. TensorFlow: Large-scale machine learning on heterogeneous systems, 2015. URL https://www.tensorflow.org/. Software available from tensorflow.org.

[212] N. Ricker. Further developments in the wavelet theory of seismogram structure. Seismol. Soc. Am., Bull., 33(3):197–228, 1943.

[213] I.-K. Yeo and R. A. Johnson. A New Family of Power Transformations to Improve Normality or Symmetry. Biometrika, 87(4):954–959, 2000. ISSN 0006-3444. URL https://www.jstor.org/stable/2673623.

[214] P. C. Mahalanobis. On the generalized distance in statistics. National Institute of Science of India, 1936.

[215] M Emre Celebi and Kemal Aydin. Unsupervised learning algorithms. Springer, 2016.

[216] Li-Li Sun and Xi-Zhao Wang. A survey on active learning strategy. In 2010 International Conference on Machine Learning and Cybernetics, volume 1, pages 161–166. IEEE, 2010.

[217] J. Gui, Z. Sun, Y. Wen, D. Tao, and J. Ye. A review on generative adversarial networks: Algorithms, theory, and applications. arXiv:2001.06937, 2020.